Superconducting Quantum Routers, Modules, Gates, and Measurements Based on Charge-pumped Parametric Interactions

by

Chao Zhou

Bachelor of Science, University of Science and Techonology of China, 2017

Master of Science, University of Pittsburgh, 2018

Submitted to the Graduate Faculty of

the Dietrich School of Arts & Sciences in partial fulfillment

of the requirements for the degree of

Doctor of Philosophy

University of Pittsburgh

2023

UNIVERSITY OF PITTSBURGH

DIETRICH SCHOOL OF ARTS AND SCIENCES

This dissertation was presented

by

Chao Zhou

It was defended on

August 21, 2023

and approved by

Michael Hatridge, Department of Physics and Astronomy

Gurudev Dutt, Department of Physics and Astronomy

Tao Han, Department of Physics and Astronomy

Wensheng Vincent Liu, Department of Physics and Astronomy

Alex Jones, Department of Electrical and Computer Engineering

Superconducting Quantum Routers, Modules, Gates, and Measurements Based on Charge-pumped Parametric Interactions

Chao Zhou, PhD

University of Pittsburgh, 2023

Superconducting quantum circuits have emerged as very promising platforms for quantum information processing. As the field navigates the Noisy Intermediate-Scale Quantum era, we can now achieve high-fidelity quantum gates across hundreds of physical qubits. Nonetheless, evolving from NISQ machines to fault-tolerant quantum computers still requires numerous advancements in both science and engineering.

In this dissertation, I aim to contribute solutions to the challenge of realizing large-scale quantum computers by exploring new ways to employ parametric interactions in superconducting quantum circuits. Specifically, the parametric charge-pumping scheme, activated by directly applying microwave drives to a coupler device that is coupled to one or multiple fixed frequency qubits, offers the versatility to execute a variety of both single-qubit and multi-qubit quantum operations. Moreover, the parametric coupling scheme also facilitates innovative qubit connection architectures and potential new error correction schemes.

The thesis starts with an introduction to the theory of charge-pumped parametric interactions and the classical electronics setup necessary for such operations. Building on this foundation, I showcase the potential of parametric interactions using two experimental works conducted during my PhD. Firstly, we have realized a prototype modular structure superconducting quantum computer with parametric interactions. The design centrals a microwave quantum state router that realizes all-to-all couplings among four independent and detachable quantum modules. We have performed full mode characterization, gate calibration, inter- and intra-module photon transfer, pairwise entanglements, and even parallel operation of simultaneous iSWAP gates. This experiment illustrates the potential of parametric interactions for building high-efficiency qubit inter-connections.

Secondly, I demonstrate the versatility of parametric interactions by performing a parametric transverse component readout on a transmon qubit. This experiment utilizes the idea

of ‘multi-parametric interactions’, in which multiple parametric drives are applied simultaneously to a set of quantum modes, and shows that a three-wave mixing coupler device can not only be used for quantum gates, but can also be used to perform novel qubit readouts that can be potentially very useful in qubit error correction schemes.

In the concluding chapter, I discuss the future of the parametric coupling scheme in larger-scale modular devices and ongoing efforts to enhance parametric coupler performance.

To my parents.

Table of Contents

List of Tables

List of Figures

Acknowledgments

At the conclusion of the incredible journey of my PhD dissertation, I want to take this opportunity to extend a huge "thank you" to the amazing people who have generously helped me every step of the way. Their assistance extends beyond just guidance and support in my research; they have also graced me with life lessons, shared moments of laughter, and stood by me during life's ups and downs. Your support means more than words can express.

First and foremost, I would like to express my deepest gratitude to my advisor, Professor Michael Hatridge. He introduced me to this exciting and thriving field of superconducting quantum computing, provided me with so many opportunities to meet with great scientists and learn invaluable skills, and has guided me through this whole research journey with his insights and expertise in every aspect of this field. His passion for good science and for educating students has profoundly shaped not only this dissertation but also my entire approach to research. Most significant is his unwavering belief in my capabilities, which I value even more than the knowledge and opportunities he has provided to me. It was under his encouragement and through the achievements we have realized together that I regained the confidence that one can truly accomplish great things if they believe in themselves and are willing to put in the work. I am certain that this lesson will serve as a guiding light throughout the rest of my life, helping me to achieve even more.

Next, I'd like to extend my heartfelt gratitude to my committee members — Prof. Gurudev Dutt, Prof. Tao Han, Prof. Wensheng Vincent Liu, and Prof. Alex Jones—for their insightful feedback during my committee meetings and on my thesis. Their expertise, time, and insightful guidance have been invaluable throughout my PhD journey. A special acknowledgment is due to Prof. Alex Jones, my initial guiding mentor in FPGA programming. Our collaborative works on quantum gates and modular architecture co-design projects have been incredibly enriching for me. I thoroughly enjoy working on these projects and have gained a wealth of knowledge through this partnership. I can't wait to see how Evan and the "team-treexotics" will work together and turn all our dreams of novel gates and modular structure devices into reality.

During my PhD, I was also incredibly fortunate to collaborate with several outstanding professors. First, I'd like to acknowledge our theory collaborators from Pitt, Prof. David

Pekker and Prof. Roger Mong. Together, we conceived the idea for our first-generation quantum router device, and they have been invaluable in supporting us on the theoretical aspects of parametric controls. I'm extremely grateful for David's patience in helping me verify my preliminary derivations and for explaining complex theories in accessible terms with clear physical pictures. Roger's innovative ideas in the applications of parametric processes have opened a whole new horizon in my understanding of parametric operations, and I truly appreciate all the calculation notes he has shared with us; they have been extremely valuable learning resources for me, offering insights far beyond what textbooks provide. Next, I want to thank Prof. Wolfgang Pfaff, who have been extremely helpful in teaching us about experimental parametric control and quality coding practices. I will never forget the coding sessions we had during the COVID lockdowns, which have taught me so much about the philosophy of how well-designed control systems should be written. Furthermore, Wolfgang has generously shared insights on navigating a scientific career during our numerous fruitful conversations, wisdom I anticipate will guide me throughout the rest of my career.

Moving forward, I would like to extend my appreciation to the group of people that I have shared the most time with in the past six years, my awesome labmates. I will start from the "OG core 4" of the Hatlab, Xi Cao, Tzu-Chiao Chien, Olivia Lanes, and Gangqiang Liu. They have taught me so many lessons on how to do basically everything in the lab, from simulation to fabrication, from how to make a magnet to how to measure a qubit. I still miss doing Hamiltonian derivations with Xi on the whiteboard, and learning all the "sneaky" fab tricks from Tzu-Chiao Olivia and Gang have not only been a wealth of knowledge in quantum experiments, but they have also separately offered me valuable advice on navigating career paths in the quantum industry and academia, respectively. Their advice have been incredibly helpful in my search for post-graduate positions. Next up is Pinlei Lu, my closest collaborator throughout this PhD journey. Words can't capture how much I've valued our partnership and mutual learning. There were times we could literally read each other's minds, simply by watching the other type out a function name. Together we have had so much fun doing hardware and software developments, fabricating desperately for the right qubits, and performing all the measurements on the "Tree". Pinlei has an uncanny ability to generate new ideas when we're stuck on experiments, a skill from which I've learned immensely.

Even after his graduation, when I find myself stuck on a measurement, I often ask, “what would Pinlei do at this point?”, and the afterimage of his innovative ideas continues to offer invaluable guidance to me. Next, I want to recognize Maria Mucci, the first Hatlaber I met even before joining the lab. Maria is the backbone of our lab infrastructure, having set up the fridge lines that make all of our experiments possible. She’s also the person I can always count on for meticulous attention to detail. I’ll fondly remember our time working together and miss her candid comments on matters that I, too, found frustrating but couldn’t figure out a good way to vocalize.

Next, the three younger members who joined the lab after me, Ryan Kaufman, Mingkang Xia, and Param Patel. Ryan is our first true expert of electronics. I really appreciate all the efforts he put in developing custom control devices for our lab and carried the torch in building novel parametric amplifiers following the graduation of Tzu-Chiao and Olivia. Ryan has a kindness that I won’t forget—he was the one who offered to take a walk with me when he noticed I was having a particularly stressful moment in the lab. That gesture of compassion will always stay with me. Mingkang joined as the third member of the ’treexotics’ team and rapidly became as an vital and irreplaceable member. He is such a fast learner and deep thinker. I have really enjoyed and benefited a lot from our many fruitful discussions on theoretical calculations and design ideas. I have no doubt that, building on the foundation we’ve established together, he’ll take our modular parametric device projects to heights that we’ve yet to imagine. Param has such a relentless dedication to making good qubits, and I’m truly grateful for his tireless work in developing new fab recipes and taking over the job of PLASSYS maintenance. Besides, Param’s knack for organizing March Meeting activities has been really enjoyable, something I’ll sorely miss.

Israa Yusuf and Boris Mesits are the newer members of Hatlab. While we haven’t collaborated much on projects, I’ll always cherish my conversations with Israa about the challenges and experiences of being an international student in the U.S., as well as all the insightful questions she’s asked about qubit experiments. Boris is such a man of dedication with an uncanny ability to maintain an exceptional work-life balance. It’s almost as if he has extra hours in his day for both work and personal life, something I truly hope to learn how to achieve for myself. Evan McKinney, our amazing computer scientist collaborator, has been an incredible resource for me in the realms of coding and computer networking. I'll always remember the late-night brainstorming sessions we've had in the lab, where we've come up with new ideas for building quantum gates and modular computer structures. Those were exciting moments where I really feel the thrill of "co-design".

I feel so lucky to have had Jacob Repicky, our mighty new postdoc, joining the lab during my final PhD year. Finally, someone has arrived who can take decisive action on a host of projects that are beneficial for the lab but had been sidelined due to lack of time or energy. Jake has such a delightful character I really enjoyed working with, and I'm particularly grateful for his dedication to elevating two crucial elements for the betterment of the lab: the quality of our qubits, and our coffee.

Finally, a shoutout to the newest members of Hatlab: Maria Nowicki,Girish Kumbhar, Chun-Che Wang, and Steven Shum. The last few moths of working with Girish has been a real pleasure to me. I've been really impressed by his amazing learning ability—especially as a first-year student. After just an hour of walking him through our parametric measurement experiment and some basics on the code, he was able to carry out this whole complicated experiment on his own. This was really a lifesaver for me during the madness of thesis writing. With his strong foundation and keen ability to learn, I can't wait to see what he'll accomplish in his coming PhD years.

At the very end, I would like to thank my family and best friends for supporting me through this whole PhD journey. First, I owe an enormous debt of gratitude to my parents, who have shaped me into the person I am today. Looking back, I realize that my love for science and my problem-solving abilities stem from the activities you encouraged me to participate in during my childhood. Your unwavering support and encouragement have truly made me who I am today. Next, I want to give a heartfelt shoutout to my "good old friends", Tianze Li and Yuan Sun. Your emotional support has been my lifeline during my low points. Our conversations are among the few moments when I can truly let my tension down and relax. Both of you have an incredible knack for grounding me when I'm overwhelmed by issues that, in hindsight, seem trivial. I honestly can't envision completing my PhD journey without your unwavering support.

1.0 Introduction to quantum computing with superconducting circuits

1.1 Quantum Computing's potential

Just as classical computers that operate based on algorithms that manipulate classical bits, quantum computers function on algorithms that manipulate quantum bits, or qubits. Unlike classical bits, which can exist in one of two states - either 0 or 1, qubits, being coherent two-level quantum systems, can exist in a superposition of both states simultaneously. Another unique property of the qubit systems, entanglement, describes the quantum phenomenon that the state of one qubit becomes inherently linked to the state of another, and measuring the state of one qubit affects the state of the other. These unique quantum properties offer new computational resources, which, as eloquently put by Nielsen and Chuang [1], represent *"iron to the classical world's bronze age"*. By harnessing these quantum properties, quantum algorithms, such as Shor's algorithm [2] for factorization and Grover's search algorithm [3], have been developed. These algorithms allow quantum computers to solve specific computational problems at a significantly faster speed than their classical counterparts, leading to what is commonly referred to as "quantum advantage" [4].

In addition to enhanced computational speed, the potential of quantum computers extends to simulating complex physical systems [5]. Constructed based on the principles of quantum mechanics, quantum computers are intrinsically capable of emulating other quantum systems. This is particularly beneficial in fields such as materials science and chemistry [6]. For example, to understand the properties of complex molecules or high-temperature superconductors, simulating quantum mechanics is required. Due to the 'curse of dimensionality', these tasks pose a great challenge to classical computers, as the complexity of computations escalates exponentially with the size of the system. Quantum computers, on the other hand, can be designed/programmed to examine these properties effectively by harnessing their inherent quantum nature.

Finally, the unique attributes of quantum mechanics open up exciting opportunities for information security. Quantum encryption or quantum cryptography exploits the principles of quantum mechanics to establish unbreakable security systems. Quantum Key Distribution (QKD), for instance, ensures secure communication channels capable of detecting any eavesdropping attempts [7].

Uncovering the full potential of what quantum computers can accomplish remains an open question, as the development of quantum algorithms is a non-trivial task that may itself benefit from the capabilities of a quantum computer. This open question makes the theoretical and experimental pursuit of quantum computing even more intriguing for quantum physicists, and the research endeavors in the field of quantum computing also leads us to have a reinterpretation of computer functions from a more physical perspective. As we progress in this endeavor, we anticipate the discovery of innovative quantum algorithms that could significantly expand our understanding and utilization of quantum computation.

1.2 Building quantum processors with superconducting circuits

The physical realization of a quantum computer requires us to build reproducible quantum systems that we can isolate and precisely manipulate and measure. Various physical systems have been considered as candidates for qubits, each offering distinct advantages and challenges. Examples include spins in semiconductors[8, 9], trapped ions[10, 11, 12] and neutral atoms[13], photonic systems[14, 15], and superconducting (SC) circuits[16, 17]. Among the various platforms, superconducting qubits possess several distinct advantages. First, their fabrication processes align well with the techniques used in the well-developed microelectronics industry, which makes large scale integration promising. Second, being artificial quantum systems, SC qubits can be made with high degree of flexibility in device parameters, which allows us to build tailored devices to meet specific needs. Lastly, superconducting qubits can be operated using full microwave control, leveraging the advancements in the established microwave industry. This compatibility with existing technologies presents considerable advantages for the implementation of quantum computing.

To build an artificial two-level system with superconducting circuits, non-linearity need to be introduced to the system. The most commonly used non-linear device in superconducting circuit is the Josephson Junction (JJ). The Josephson junction generally consist of two or more superconductors coupled by a weak link. The weak link can be a thin insulating barrier (known as a superconductor–insulator–superconductor junction, or S-I-S), a short section of non-superconducting metal (S-N-S), or a physical constriction that weakens the superconductivity at the point of contact (S-c-S). The inductive energy of the Josephson Junction has a special Cosinusoidal relation with the superconducting phase variable through the junction, which gives the junction Hamiltonian an large inductance component and series of even-order non-linear terms. Based on the 4th order nonlinearity, the JJ can be combined with a large capacitor to built a charge qubit device with reduced sensitivity to charge noise, the transmon qubit [18]. Being a modified charge qubit, the transmon can have strong dipole coupling with external electronic magnetic field, which allows its state to be easily manipulated with external microwave drives. The readout of a transmon qubit can be performed by coupling the qubit to an ancillary mode whose state depends strongly on the qubit state [19, 20, 21]. The Josephson Junction can also be used to build other superconducting elements that are necessary for the operation of quantum processors, which include quantum limited parametric amplifiers[22, 23, 24] that enables high-fidelity qubit readout, coupler devices for multi-qubit gates[25, 26], or even cryogenic control devices for generating qubit control pulses[27, 28].

With all these developments in the construction, control, and measurement of superconducting qubits, the field of superconducting quantum computing has made substantial progress over the past few decades. As a result of extensive research and development, building and operating medium-scale quantum processors with superconducting circuits is now a reality. This has brought us into the so-called Noisy Intermediate-Scale Quantum (NISQ) era, where fairly high-fidelity universal quantum gates can be performed between tens [4, 29, 30] (or hundreds [31, 32]) of qubits, showing the immense potential of quantum computing for performing complex computation or simulation tasks that are beyond the capabilities of classical computers[4, 29, 33].

1.2.1 Remaining challenges in building a scalable quantum computer with superconducting circuits

Despite this progress on NISQ algorithms and continually increasing qubit counts, present quantum machines are still not capable of performing actual large scale quantum algorithms, since quantum information tends to degrade too rapidly in larger systems due to error accumulation. Therefore, transforming NISQ machines to fault-tolerant quantum computers with thousands of logical qubits remains a challenging research topic that must be addressed. Achieving this goal will require continued improvements in qubit coherence, gate fidelities and measurement fidelities. Moreover, as we proceed with large-scale integration of superconducting qubits, we also encounters more challenges. As the number of qubits increases, the complete control over the quantum processor necessitates more sophisticated and extensive classical control electronics. This leads us to explore the development of multiplexed qubit control and readout schemes, as well as to advance classical electronics to meet these needs. Another critical aspect that demands consideration is the type of connection architecture suitable for large-scale superconducting quantum circuits. These challenges, inherent in the large-scale integration of superconducting qubits, have shaped the focus of my PhD research. We aim to contribute solutions based on the central concept of exploiting parametric interactions in superconducting qubit systems. Namely, parametric interactions can be used for performing qubit operations that enables full microwave, multiplexed control. This control scheme places specific requirements on the control electronics used in the experiments, which is an area I devoted substantial time to developing. Furthermore, parametric interactions pave the way for constructing quantum processors in a modular manner. This modular design allows us to replace faulty components and test sub-units separately, significantly easing the demand for flawless fabrication. Moreover, this approach fosters novel qubit-qubit connection topologies, shortening the communication distance between qubits and potentially enabling new quantum error correction schemes.

1.3 Overview of thesis

This thesis is organized as follows. Chapter 2 introduces the fundamental theory of charge-pumped parametric interactions, the single- and multi-qubit gates that such interactions enable, and how to realize these interactions using Josephson Junction based parametric couplers. The discussion in this chapter lays the theoretical foundation for the subsequent chapters.

Chapter 3 provides a detailed introduction to the microwave electronics utilized in the operation of superconducting quantum processors. Although these microwave electronics have already been widely used since the beginning of superconducting qubit research, as a researcher who has spent a significant amount of time programming and testing these electronics from the very basic layer (hardware description language), I believe a summary of the knowledge I have acquired throughout my research will be beneficial for newcomers in this field. Moreover, this chapter also provides a thorough analysis of the requirements for implementing paramateric quantum operations among many qubits and cavities using these electronics — an important topic which, in my observation, has not been thoroughly discussed in the literature

In Chapter 4 I present our work on building parametrically-controlled, prototype modular structure quantum processors with superconductor qubits. This chapter delves into the design, fabrication, characterization, and full operation of a four-port quantum state router, complemented by four quantum modules. The parametric gates introduced in Chapter 2 are extensively employed in this experiment, demonstrating the versatility and efficacy of parametric quantum operations. Following the successful realization of the quantum router device, I further discuss the expansion of the modular architecture. This includes the design of a 4-qubit quantum module and the exploration of other potential modular coupling schemes.

Chapter 5 explores the topic of multi-parametric interactions, providing several illustrative examples of unique quantum operations enabled by the concurrent activation of multiple parametric processes. A noteworthy highlight of this chapter is the presentation of an innovative approach to measuring the transverse components of a transmon qubit, based on the three-wave mixing ‘gain-conversion’ interaction, with preliminary experimental data. This chapter further demonstrates the vast potential of parametric interaction in performing quantum operations that extend beyond conventional gate operations. Lastly, Chapter 6 summarizes the key findings and concepts explored throughout this dissertation and discusses future prospects of parametric quantum operations and modular quantum computers.

2.0 Quantum Operations with Charge-pumped Parametric Interactions

In gate-based quantum computing, universal single-qubit and two-qubit gates are necessary for compiling an arbitrary quantum algorithm [34, 1]. For superconducting qubit systems, single-qubit gates can be conveniently implemented by applying microwave drives at the qubit frequency via a port that is capacitively coupled to the qubit [35, 36]. On the other hand, two-qubit gates are generally more challenging to realize. One of the primary reasons for this is that, unlike single-qubit gates where the qubit-filed interaction can be rapidly turned on and off via straightforward control of the microwave drive, the two-qubit gates require us to coherently and rapidly control the qubit-qubit interaction with a high on/off ratio.

To achieve two-qubit gates with high fidelities, a wide variety of approaches have been proposed and experimentally implemented. Reference [36] provides a comprehensive review of these different approaches. Broadly speaking, these approaches can be categorized based on two criteria: 1) whether there is a dedicated coupler device between the two qubits, and 2) whether it requires fast flux lines for rapid frequency tuning. For example, an iSWAP gate can be performed between two directly-coupled frequency-tunable qubits by tuning the two qubits on- and off-resonance with each other via fast flux lines [37, 38], or using a mediating tunable coupler [39]. Alternatively, the tunable coupler can be used between fixed frequency qubits,where the gate can be parametrically activated by rapidly modulating the frequency of the coupler [40, 41, 42, 43], i.e. the flux-pumping schemes. The fast flux lines used in these schemes requires additional device and input line designs beyond the conventional microwave control, and the frequency tunability also opens the system to additional dephasing. On the other hand, two-qubit gates can also be performed via "fully microwave" methods, for example, the cross-resonance gate [44, 45, 46] can be performed between two fixed-frequency qubits with direct coupling. The speed of the cross-resonance gate is reduced when the qubit-qubit detuning is larger than the transmon anharmonicity.

Another fully microwave-controlled method is the parametric charge-pumping scheme, which is performed by directly applying microwave drives to a coupler device between two qubits[47, 48, 49, 50, 51, 52]. This scheme offers the versatility to execute both single-qubit gates and a variety of two-qubit gates (see Sec. 2.2). Additionally, the gate's speed is determined by both the pump strength and the coupling strength between the qubits and the coupler mode. This allows us to design systems with very low static qubit-qubit couplings, while still being able to perform fast gate operations via strong external pumps, thereby realizing gates with a very high on-off ratio.

In this section, I will provide detailed derivation of the theory behind charged-pumped parametric interactions, as well as explore the gates enabled by these interactions. In addition, I will introduce the coupler devices that provides the non-linearity needed in these interactions. The experiment implementation of such parametric quantum operations will be presented in Chapter 4 and 5.

2.1 Theory of charge-pumped parametric interactions

In this section, I will provide a detailed derivation on how parametric quantum processes can be activated by applying external electromagnetic drives on a non-linear mode in a coupled quantum system. Specifically, we will focus on harmonic to moderately anharmonic modes like cavities and transmons, where the system can be well-described by the creation and annihilation operators, $\hat{a}^\dagger$ and $\hat{a}$, i.e. the Hamiltonian after second quantization. While the process of deriving such a quantized Hamiltonian from a superconducting circuit exceeds the scope of our current discussion, there are excellent resources that provide comprehensive coverage of this topic, with my favored ones being [53, 54, 36]. For our discussion of charge-pumped parametric processes, we will utilize some of the results derived from these well-established theories. The key points to note are:

- The Hamiltonian of a harmonic oscillator mode (or linear mode) can be written as:

  $$\hat{\mathcal{H}}_{lin}/\hbar = \omega_a \hat{a}^\dagger \hat{a}, \tag{1}$$

  where ω_a is the mode frequency.

- The Hamiltonian of a Josephson Junction based non-linear mode can generally be written as:
$$\hat{\mathcal{H}}_{non-lin}/\hbar = \omega_a \hat{a}^\dagger \hat{a} + \sum_{n=3}^{\infty} g_n (\hat{a} + \hat{a}^\dagger)^n, \tag{2}$$
in which g_n denotes the coefficient of the n_{th} order non-linear term, which is determined by the device parameters and could potentially be tunable via external parameters such as flux threading a superconducting loop.
- The coupling term between two capacitively coupled modes, A and B, can be written as:
$$\hat{\mathcal{H}}_{couple}/\hbar = g_{ab}(\hat{a}^\dagger \hat{b} + \hat{a}\hat{b}^\dagger), \tag{3}$$
in which g_{ab} is the coupling strength between the two modes, which we assume to be real here; $\hat{a}/\hat{a}^\dagger$ and $\hat{b}/\hat{b}^\dagger$ are the annihilation/creation operators of mode A and B, respectively.
- An external microwave drive that is coupled to the charge variable of mode A via electronic ($\boldsymbol{E}$) field can be written as:
$$\hat{\mathcal{H}}_{drive}/\hbar = \left[\varepsilon(t) e^{-i\omega_d t} - \varepsilon^*(t) e^{i\omega_d t}\right] \left(\hat{a}^\dagger - \hat{a}\right) \tag{4}$$
in which $\varepsilon(t)$ is the (slowly varying) time dependent amplitude of the drive. The drive envelope $\varepsilon(t)$ is related to the amplitude of the field at the pump port $\mathcal{A}(t)$ via $\varepsilon(t) = \sqrt{\kappa_a}\mathcal{A}(t)$, with κ_a being the coupling strength between the A mode and the port. The angular frequency of the pump is denoted as ω_d. There are few extra points to note in this driving term Hamiltonian:
  - The external drive $\mathcal{A}(t)$ is typically generated with arbitrary waveform generators (AWGs), which can provide both phase and amplitude modulation. Therefore, $\varepsilon(t)$ is generally a complex variable whose real and imaginary part can be controlled individually. This allows us to create optimized pulse shapes that can reduce unwanted transitions induced by the drive[55, 52, 56].
  - When the drive is only amplitude modulated with fixed frequency ω_d and phase ϕ_d, Equation 4 can be simplified as [57, 36]:
$$\hat{\mathcal{H}}_{drive}/\hbar = i2\varepsilon(t)\cos(\omega_d t + \phi_d)\left(\hat{a}^\dagger - \hat{a}\right), \tag{5}$$
in which a $\pi/2$ phase is absorbed in ϕ_d.

– Another commonly seen form of the driving term is typically written as[36]:

$$\hat{\mathcal{H}}_{drive}/\hbar = \varepsilon(t)\left(e^{-i(\omega_d t+\phi_d)}\hat{a}^\dagger + e^{i(\omega_d t+\phi_d)}\hat{a}\right) \tag{6}$$

This a further simplified version of Eq. 4, which is valid only when the drive frequency ω_d is close to the mode frequency ω_a, allowing the fast rotating terms in Eq. 4 to be neglected under rotating-wave approximation (RWA).

Based on this foundation, we can derive the emergence of parametric quantum processes activated by external drives. As an illustrative example, let's consider a coupling system depicted in Fig. 1. In this system, two harmonic oscillators A and B are both coupled to a central mode, S, who has a third-order non-linearity. The total static Hamiltonian can be written as:

$$\hat{\mathcal{H}}_0/\hbar = \omega_a\hat{a}^\dagger\hat{a} + \omega_b\hat{b}^\dagger\hat{b} + \omega_s\hat{s}^\dagger\hat{s} + g_3(\hat{s}+\hat{s}^\dagger)^3 + g_{as}(\hat{a}^\dagger\hat{s}+\hat{a}\hat{s}^\dagger) + g_{bs}(\hat{b}^\dagger\hat{s}+\hat{b}\hat{s}^\dagger) \tag{7}$$

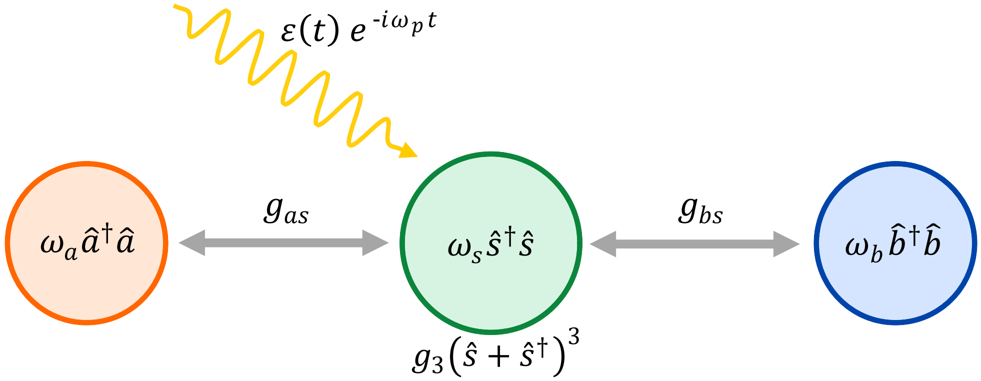

Figure 1: **Example of three mode coupling system.** Two linear modes A (labeled in orange) and B (labeled in blue) are coupled to a central non-linear mode S (labeled in green) with coupling coefficients g_{as} and g_{bs} respectively. The S mode as third order non-linearity with coefficient g_3. An external microwave pump is applied at the S mode with effective time-dependent amplitude $\epsilon(t)$ and angular frequency ω_p.

We define Δ_{xy} to be the frequency difference (detuning) between two modes X and Y, e.g. $\Delta_{xy} = \omega_x - \omega_y$. In the on-resonance case, $\Delta = 0$, the eigenstates of the system become the maximally entangled states of the two modes, which implies that each original mode by it self is no longer an eigenstate, and so if prepared in this state will promptly leave it. Therefore, for quantum information processing, we generally work in the 'dispersive regime' [53, 54, 36], in which the direct coupling strength, g_{xy}, is much smaller than the detuning Δ_{xy}. Here we define the hybridization strength between two modes X and Y as

$$\lambda_{xy} = \left(\frac{g}{\Delta}\right)_{xy} \tag{8}$$

In our 3-mode system depicted in Fig. 1, we will work in the dispersive regime where $|\lambda_{as}| = |g/\Delta|as \ll 1$ and $|\lambda_{bs}| = |g/\Delta|_{bs} \ll 1$. Next, we will analyze the dynamics of this 3-mode system under an external drive applied to the non-linear mode with amplitude $\varepsilon(t)$, frequency ω_p, and phase ϕ_p. To achieve this, we will employ a series of unitary transformations on the original Hamiltonian and make approximations based on this assumption of dispersive coupling.

2.1.1 Bogoliubov transformation

The Hamiltonian in Eq. 7 can be separated into two parts, the linear part $H_{0,L}$ and the non-linear part $H_{0,NL}$

$$\hat{\mathcal{H}}_{0,L} = \omega_a \hat{a}^\dagger \hat{a} + \omega_b \hat{b}^\dagger \hat{b} + \omega_s \hat{s}^\dagger \hat{s} + g_{as}(\hat{a}^\dagger \hat{s} + \hat{a}\hat{s}^\dagger) + g_{bs}(\hat{b}^\dagger \hat{s} + \hat{b}\hat{s}^\dagger) \tag{9}$$

$$\hat{\mathcal{H}}_{0,NL} = g_3(\hat{s} + \hat{s}^\dagger)^3 \tag{10}$$

To assess the impact of the non-linearity of the S mode on the three-mode system resulting from its coupling with the two linear modes, we need to first perform a Bogoliubov transformation that diagonalizes the linear part of the system's Hamiltonian, $H_{0,L}$.

2.1.1.1 Diagonalization of a two-mode system

Reference [36] provides a complete solution for diagonalizing the Hamiltonian of a two mode system with a Bogoliubov transformation. Specifically, for two linear modes X and Y with frequencies ω_x and ω_y, and coupling strength g_{xy}, the linear Hamiltonian can be written as:

$$\hat{\mathcal{H}}_{xy}/\hbar = \omega_x \hat{x}^\dagger \hat{x} + \omega_y \hat{y}^\dagger \hat{y} + g_{xy}(\hat{x}^\dagger \hat{y} + \hat{x}\hat{y}^\dagger). \tag{11}$$

The Bogoliubov transformation unitary that diagonalizes this Hamiltonian is [1]:

$$\hat{U}_{B,xy} = \exp\left[\Lambda_{xy}(\hat{x}^\dagger \hat{y} - \hat{x}\hat{y}^\dagger)\right], \tag{12}$$

in which

$$\Lambda_{xy} = \frac{1}{2}\arctan(2\lambda_{xy}) = \frac{1}{2}\arctan\left(2\frac{g_{xy}}{\omega_x - \omega_y}\right). \tag{13}$$

The annihilation operators after the Bogoliubov transformation can be derived using the Baker-Campbell-Hausdorff formula, which yields:

$$\hat{x}' = \hat{U}_{B,xy}\ \hat{x}\ \hat{U}^\dagger_{B,xy} = \cos(\Lambda_{xy})\hat{x} - \sin(\Lambda_{xy})\hat{y} \tag{14a}$$

$$\hat{y}' = \hat{U}_{B,xy}\ \hat{y}\ \hat{U}^\dagger_{B,xy} = \cos(\Lambda_{xy})\hat{y} + \sin(\Lambda_{xy})\hat{x}, \tag{14b}$$

and the Hamiltonian after transformation will have the diagonal form:

$$\begin{aligned}\hat{\mathcal{H}}'_{xy} &= \hat{U}_{B,xy}\ \hat{\mathcal{H}}_{xy}\ \hat{U}^\dagger_{B,xy} \\ &= \hbar\omega_x \hat{x}'^\dagger \hat{x}' + \hbar\omega_y \hat{y}'^\dagger \hat{y}' + g_{xy}(\hat{x}'^\dagger \hat{y}' + \hat{x}'\hat{y}'^\dagger) \\ &= \hbar\omega'_x \hat{x}^\dagger \hat{x} + \hbar\omega'_y \hat{y}^\dagger \hat{y},\end{aligned} \tag{15}$$

with the ‘dressed’ frequencies:

$$\omega'_x = \omega_x + \frac{\Delta_{xy}}{2}\left(\sqrt{1+4\lambda^2_{xy}} - 1\right) \tag{16a}$$

$$\omega'_y = \omega_y - \frac{\Delta_{xy}}{2}\left(\sqrt{1+4\lambda^2_{xy}} - 1\right). \tag{16b}$$

---

[1] Note that we are using different notations for Δ and the application of unitary transformations compared to those in Ref. [36].

Note that the formulas in Eq. 11 to 16 are derived in exact form without any approximation applied. In the dispersive regime, $|\lambda_{xy}| = \left|\frac{g}{\Delta}\right|_{xy} \ll 1$; $\Lambda_{xy} \sim \lambda_{xy}$. To first-order in λ_{xy}, Eq. 14 and Eq. 16 can be simplified to:

$$\hat{x}' \approx \hat{x} - \lambda_{xy}\hat{y} = \hat{x} - \left(\frac{g}{\Delta}\right)_{xy} \hat{y} \tag{17a}$$

$$\hat{y}' \approx \hat{y} + \lambda_{xy}\hat{x} = \hat{y} + \left(\frac{g}{\Delta}\right)_{xy} \hat{x}, \tag{17b}$$

and

$$\omega_x' \approx \omega_x + \lambda_{xy}g_{xy} = \omega_x + \left(\frac{g^2}{\Delta}\right)_{xy} \tag{18a}$$

$$\omega_y' \approx \omega_y - \lambda_{xy}g_{xy} = \omega_y - \left(\frac{g^2}{\Delta}\right)_{xy}. \tag{18b}$$

The results derived in Eq.17 and Eq.18 provide simple expressions for the dressed mode operators and frequencies following the Bogoliubov transformation in a dispersively coupled system. More importantly, these equations also give us an intuitive understanding of how the dressed operators and frequencies are related to the coupling coefficients and mode detunings. Essentially, each dressed operator will carry a $\sim g/\Delta$ portion of the other mode's bare mode operator, and the two frequencies will be shifted apart from each other by $\sim 2g^2/\Delta$. These formulas will serve as important references for analyzing the share of non-linearity in multi-mode systems that we will discuss in later sections. In the following text of this section, I will elaborate how these results can be extrapolated to multi-mode systems with dispersive couplings.

2.1.1.2 General formalism for a multi-mode system

In general, the Bogoliubov transformation can be applied to a quantum system of n linear modes with all-to-all couplings. The system Hamiltonian can be written as:

$$\hat{\mathcal{H}}/\hbar = \sum_{i=1}^{i} \omega_n \hat{a}_i^\dagger \hat{a}_i + \sum_{i=1}^{n} \sum_{j=i+1}^{n} g_{ij}(\hat{a}_i^\dagger \hat{a}_j + \hat{a}_i \hat{a}_j^\dagger), \tag{19}$$

which can be re-written in a matrix form:

$$\begin{aligned} \hat{\mathcal{H}}/\hbar &= \mathbf{\Psi}^\dagger \mathbf{H} \mathbf{\Psi} \\ &= \begin{bmatrix} \hat{a}_1^\dagger & \hat{a}_2^\dagger & \cdots & \hat{a}_n^\dagger \end{bmatrix} \begin{bmatrix} \omega_1 & g_{12} & \cdots & g_{1n} \\ g_{12} & \omega_2 & \cdots & a_{2n} \\ \vdots & \vdots & \ddots & \vdots \\ g_{1n} & g_{2n} & \cdots & \omega_n \end{bmatrix} \begin{bmatrix} \hat{a}_1 \\ \hat{a}_2 \\ \vdots \\ \hat{a}_n \end{bmatrix} \end{aligned} \tag{20}$$

Here, we denote $\mathbf{\Psi}$ as a column vector that consists of the annihilation operators $(\hat{a}_1, ..., \hat{a}_n)$ for each linear mode, and $\mathbf{H}$ is a numeric matrix (not an operator) that contains the bare mode frequencies $(\omega_1, ..., \omega_n)$ and the coupling coefficients g_{ij}. By nature, $\mathbf{H}$ is always a Hermitian matrix, and we assume that all the mode frequencies are distinct from each other. Then, there should always exist a unitary matrix $\mathbf{U}$ (the eigenvector matrix of $\mathbf{H}$) that can diagonally decompose $\mathbf{H}$, i.e.

$$\begin{aligned} \mathbf{H} &= \mathbf{U}\mathbf{H}'\mathbf{U}^\dagger \\ &= \begin{bmatrix} u_{11} & u_{12} & \cdots & u_{1n} \\ u_{21} & u_{22} & \cdots & u_{2n} \\ \vdots & \vdots & \ddots & \vdots \\ u_{n1} & u_{n2} & \cdots & u_{nn} \end{bmatrix} \begin{bmatrix} \omega_1' & 0 & \cdots & 0 \\ 0 & \omega_2' & \cdots & 0 \\ \vdots & \vdots & \ddots & \vdots \\ 0 & 0 & \cdots & \omega_n' \end{bmatrix} \begin{bmatrix} u_{11} & u_{21}^* & \cdots & u_{n1}^* \\ u_{12} & u_{22} & \cdots & u_{n2}^* \\ \vdots & \vdots & \ddots & \vdots \\ u_{1n} & u_{2n} & \cdots & u_{nn} \end{bmatrix} \end{aligned} \tag{21}$$

The diagonal elements in $\mathbf{H}'$ correspond to eigenvalues of $\mathbf{H}$, which equal to the dressed mode frequencies. Therefore, finding the Bogoliubov transformation that diagonalizes the system Hamiltonian $\hat{\mathcal{H}}$ is equivalent to finding the unitary operator $\hat{U}_B$ that transforms the annihilation operators such that:

$$\hat{a}_i' = \hat{U}_B \; \hat{a}_i \; \hat{U}_B^\dagger = \begin{bmatrix} u_{i1} & u_{i2} & \cdots & u_{in} \end{bmatrix} \begin{bmatrix} \hat{a}_1 \\ \hat{a}_2 \\ \vdots \\ \hat{a}_n \end{bmatrix} \tag{22}$$

which gives dressed annihilation operator vector:

$$\mathbf{\Psi}' = \begin{bmatrix} \hat{a}_1' \\ \hat{a}_2' \\ \vdots \\ \hat{a}_n' \end{bmatrix} = \begin{bmatrix} u_{11} & u_{12} & \cdots & u_{1n} \\ u_{21} & u_{22} & \cdots & u_{2n} \\ \vdots & \vdots & \ddots & \vdots \\ u_{n1} & u_{n2} & \cdots & u_{nn} \end{bmatrix} \begin{bmatrix} \hat{a}_1 \\ \hat{a}_2 \\ \vdots \\ \hat{a}_n \end{bmatrix} = \mathbf{U\Psi}. \tag{23}$$

Under the transformation represented by $\hat{U}_B$, the transformed Hamiltonian $\mathcal{H}'$ can be written by substituting the original annihilation and creation operators, $\hat{a}_i$ and $\hat{a}_i^\dagger$, with their corresponding dressed operators $\hat{a}_i'$ and $\hat{a}_i'^\dagger$, respectively. Note that the numeric matrix $\mathbf{H}$ will remain unchanged during this transformation, as the elements of $\mathbf{H}$ essentially act as coefficients for the operators and will be directly transferred onto the new operators. Using the matrix notation that we introduced in Eq. 20, and the results we have in Eq. 21 and 23, we can derive the dressed Hamiltonian:

$$\begin{aligned} \hat{\mathcal{H}}'/\hbar &= \hat{U}_B \; \hat{\mathcal{H}} \; \hat{U}_B^\dagger \\ &= \mathbf{\Psi}'^\dagger \mathbf{H} \mathbf{\Psi}' \\ &= \left(\mathbf{\Psi}^\dagger \mathbf{U}^\dagger\right) \left(\mathbf{U} \mathbf{H}' \mathbf{U}^\dagger\right) \left(\mathbf{U\Psi}\right) \\ &= \mathbf{\Psi}^\dagger \mathbf{H}' \mathbf{\Psi} \\ &= \sum_{i=1}^{n} \omega_n' \hat{a}_i^\dagger \hat{a}_i, \end{aligned} \tag{24}$$

Equation 24 shows that the unitary operator $\hat{U}_B$ indeed transforms original system Hamiltonian into a diagonal form with dressed frequencies ω_i'.

In the case of a two-mode system, the explicit expression for the Bogoliubov transformation unitary is given by Equations 12 and 13. For a more generalized multi-mode system, however, deriving an explicit expression for $\hat{U}_B$ based on Equations 21 and 22 becomes more complex and nontrivial. Regardless, the derivations above have shown that computing the transformed Hamiltonian and the dressed mode frequencies doesn't necessarily require us to use the explicit expression of $\hat{U}_B$. Instead, we simply need to diagonally decompose the characteristic matrix $\mathbf{H}$ as in Equation 21, then, the eigenvalues will represent the dressed mode frequencies, and the eigenvector matrix $\mathbf{U}$ will serve as the transformation matrix for the creation and annihilation operators (as in Equation 23), which can then be used to calculate the transformed Hamiltonian. Moreover, in the dispersive coupling regime, where $\left|\frac{g_{ij}}{\omega_i - \omega_j}\right| \ll 1$, the computation of Eq. 21 can be further simplified using perturbation methods, which I will discuss in the next section with our 3-mode example system.

2.1.1.3 Approximation method for the three-mode system under dispersive coupling

Back to our three-mode system depicted in Fig. 1. The Hamiltonian in Eq. 9 can be re-written as:

$$\hat{\mathcal{H}}_{0,L} = \mathbf{\Psi}_0^\dagger \mathbf{H_0} \mathbf{\Psi_0} = \begin{bmatrix} \hat{s}^\dagger & \hat{a}^\dagger & \hat{b}^\dagger \end{bmatrix} \begin{bmatrix} \omega_s & g_{as} & g_{bs} \\ g_{as} & \omega_a & 0 \\ g_{bs} & 0 & \omega_b \end{bmatrix} \begin{bmatrix} \hat{s} \\ \hat{a} \\ \hat{b} \end{bmatrix} \tag{25}$$

In the dispersive regime where $|\lambda_{as}| = |g/\Delta|as \ll 1$ and $|\lambda_{bs}| = |g/\Delta|_{bs} \ll 1$, the eigenvalues and eigenvectors of $\mathbf{H}_0$ can be calculated using the perturbation method[2]. To perform the perturbation method calculation, we write $\mathbf{H}_0$ in two separate parts: the diagonal (unperturbed) part $\mathbf{H}_{0,D}$ and the perturbation part $\mathbf{H}_{0,P}$

$$\mathbf{H_0} = \mathbf{H}_{0,D} + \mathbf{H}_{0,P} = \begin{bmatrix} \omega_s & 0 & 0 \\ 0 & \omega_a & 0 \\ 0 & 0 & \omega_b \end{bmatrix} + \begin{bmatrix} 0 & g_{as} & g_{bs} \\ g_{as} & 0 & 0 \\ g_{bs} & 0 & 0 \end{bmatrix} \tag{26}$$

Given that the eigenvector matrix of the unperturbed matrix $\mathbf{H}_{0,D}$ is the Identity matrix, and the diagonal elements of the perturbation matrix $\mathbf{H}_{0,P}$ are zero, we find that the first-order correction to the eigenvalues is zero. The first-order correction to the eigenvectors,

---

[2] Note that in this context we are not applying the quantum perturbation theory on quantum states, instead, we are just using the perturbation method for the diagonalization of the matrix $\mathbf{H}_0$

however, is non-zero and can be calculated as:

$$V_i^{(1)} = \sum_{j\neq i} \frac{g_{ij}}{\omega_i - \omega_j} V_j^{(0)} = \sum_{j\neq i} \lambda_{ij} V_j^{(0)}, \tag{27}$$

where $V_j^{(0)}$ is the j^{th} eigenvector of the unperturbed matrix $\mathbf{H}_{0,D}$, which is essentially the j^{th} column of an Identity matrix. The second-order correction to the eigenvalues is given by:

$$E_i^{(2)} = \sum_{j\neq i} \frac{g_{ij}^2}{\omega_i - \omega_j} = \sum_{j\neq i} \lambda_{ij} g_{ij} \tag{28}$$

Therefore, to the lowest order of energy and eigenvector corrections, the characteristic matrix $\mathbf{H}_0$ can be diagonally decomposed as:

$$\begin{aligned}&\mathbf{H}_0 \approx \mathbf{U}_0 \mathbf{H}_0' \mathbf{U}^{\dagger}{}_0 \\ &= \begin{bmatrix} 1 & \lambda_{as} & \lambda_{bs} \\ -\lambda_{as} & 1 & 0 \\ -\lambda_{bs} & 0 & 1 \end{bmatrix} \begin{bmatrix} \omega_s - \lambda_{as} g_{as} - \lambda_{bs} g_{bs} & 0 & 0 \\ 0 & \omega_a + \lambda_{as} g_{as} & 0 \\ 0 & 0 & \omega_b + \lambda_{bs} g_{bs} \end{bmatrix} \begin{bmatrix} 1 & -\lambda_{as} & -\lambda_{bs} \\ \lambda_{as} & 1 & 0 \\ \lambda_{bs} & 0 & 1 \end{bmatrix},\end{aligned} \tag{29}$$

which indicates that the Bogoliubov transformation that diagonalizes the Hamiltonian $\hat{\mathcal{H}}_{0,L}$ will transform the annihilation operators as:

$$\begin{bmatrix} \hat{s}' \\ \hat{a}' \\ \hat{b}' \end{bmatrix} \approx \mathbf{U}_0 \begin{bmatrix} \hat{s} \\ \hat{a} \\ \hat{b} \end{bmatrix} = \begin{bmatrix} 1 & \lambda_{as} & \lambda_{bs} \\ -\lambda_{as} & 1 & 0 \\ -\lambda_{bs} & 0 & 1 \end{bmatrix} \begin{bmatrix} \hat{s} \\ \hat{a} \\ \hat{b} \end{bmatrix}, \tag{30}$$

and give the diagonalized Hamiltonian:

$$\begin{aligned} \hat{\mathcal{H}}_{0,L}'/\hbar &= \hat{U}_{B,0} \hat{\mathcal{H}}_{0,L} \hat{U}_{B,0}^{\dagger}/\hbar \\ &= \omega_s' \hat{s}^{\dagger}\hat{s} + \omega_a' \hat{a}^{\dagger}\hat{a} + \omega_b' \hat{b}^{\dagger}\hat{b}, \end{aligned} \tag{31}$$

with the dressed mode frequencies:

$$\omega_s' \approx \omega_s - \lambda_{as} g_{as} - \lambda_{bs} g_{bs} \tag{32a}$$

$$\omega_a' \approx \omega_a + \lambda_{as} g_{as} \tag{32b}$$

$$\omega_b' \approx \omega_b + \lambda_{bs} g_{bs} \tag{32c}$$

Equations 30 and 32 resemble the form of Eq. 17 and 18, but are extended to our three-mode system. Essentially, the dressed S mode operator incorporates both a λ_{as} portion of the bare A mode operator and a λ_{bs} portion of the bare B mode operator. In fact, the derivation presented above (from Eq. 25 to Eq. 32) can be generalized to a multi-mode, dispersively coupled system with a 'star-shape' coupling diagram, where multiple modes are all coupled to one central mode. The properties of this generalized case will be discussed in Sec. 2.1.1.5

2.1.1.4 The emergence of multi-wave mixing term

Now with the linear part of our 3-mode system Hamiltonian diagonalized, we can move forward and see what the Bogoliubov transformation does to the non-linear part of the Hamiltonian:

$$\begin{aligned}\hat{\mathcal{H}}'_{0,NL}/\hbar &= \hat{U}_{B,0}\hat{\mathcal{H}}_{0,NL}\hat{U}^{\dagger}_{B,0}/\hbar \\ &= \frac{1}{\hbar}\hat{\mathcal{H}}_{0,NL}|_{s\to s'} \\ &= g_3\left(\hat{s}' + \hat{s}'^{\dagger}\right)^3 \\ &= g_3\left(\hat{s} + \lambda_{as}\hat{a} + \lambda_{bs}\hat{b} + \hat{s}^{\dagger} + \lambda_{as}\hat{a}^{\dagger} + \lambda_{bs}\hat{b}^{\dagger}\right)^3\end{aligned} \tag{33}$$

The expansion of Eq. 33 contains all the possible third-order products of the three modes' annihilation and creation operators, these terms are usually referred as the "3-wave-mixing terms". Each of these terms corresponds to a specific parametric process that we can activate by applying external pumps on the modes at specific frequencies. Specifically, the existence of the term: $\hat{s}\hat{a}\hat{b}^{\dagger} + \hat{s}^{\dagger}\hat{a}^{\dagger}\hat{b}$ enables us to activate exchange interaction between the A and B modes by pumping the S mode at frequency $\omega_p = \omega_b - \omega_a$. The strength of the exchange interaction will be promotional to the coefficient of this three wave mixing term, which, in this case equals to $6g_3\lambda_{as}\lambda_{bs}$ (the factor '6' is the binomial coefficient from the third-order expansion). The dynamic of this process will be elaborated in Sec. 2.1.2.

2.1.1.5 Dilution and propagation of non-linearity

Before we proceed from Eq. 33 and examine the effect of the external pump on the non-linear mode, let us take a brief detour to explore the effect of Bogoliubov transformation on some other coupling schemes. Specifically, we will consider a) the 'star-shaped' coupling diagram (as depicted in Fig. 2a) to study how the strength of a multi-wave mixing terms is 'diluted' by the addition of extra modes coupled to a central non-linear mode, and b) the 'chained' coupling scheme (as depicted in Fig. 2b) to study how the non-linearity is propagated to modes that are indirectly coupled to the non-linear mode.

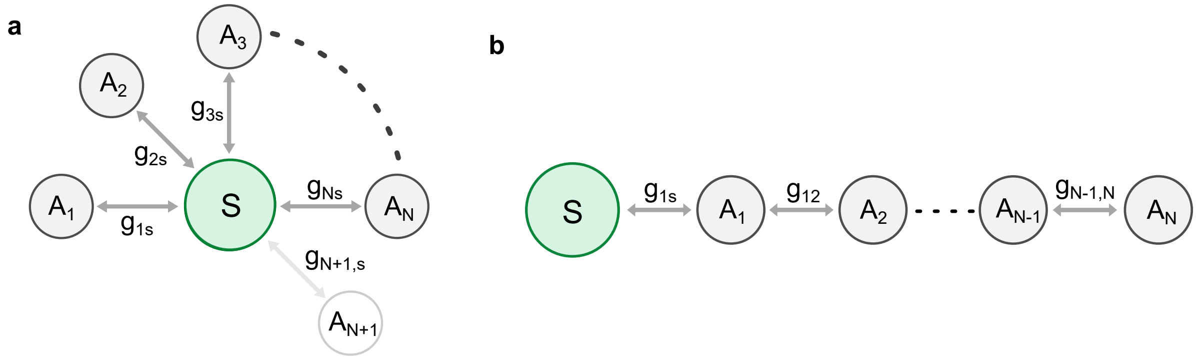

Figure 2: **'Star-shaped' and 'chained' coupling diagrams.. a)** 'Star-shaped' coupling scheme between a central non-linear mode S and multiple other modes $A_1 - A_n$. Each mode A_i is directly coupled to the S mode with coefficient g_{is}. **b)** 'Chained' coupling scheme. Mode A_1 is directly coupled with the S mode with coefficient g_{1s}, while the $A_2 - A_n$ modes are coupled with each other consecutively with coefficients $g_{i,i+1}$.

Dilution of non-linearity. In the star-shaped coupling scheme, multiple linear modes $(A_1 - A_N)$ are coupled to one central non-linear mode S. The linear part of the system Hamiltonian can be written as:

$$\hat{\mathcal{H}}_{star,L}/\hbar = \omega_s \hat{s}^\dagger \hat{s} + \sum_{i=1}^{N} \omega_i \hat{a}_i^\dagger \hat{a}_i + \sum_{i=1}^{N} g_{is}(\hat{a}_i^\dagger \hat{s} + \hat{a}_i \hat{s}^\dagger), \tag{34}$$

which gives the characteristic matrix of the coupling system:

$$\mathbf{H}_{star} = \begin{bmatrix} \omega_s & g_{1s} & g_{2s} & \cdots & g_{Ns} \\ g_{1s} & \omega_1 & 0 & \cdots & 0 \\ g_{2s} & 0 & \omega_2 & \cdots & 0 \\ \vdots & \vdots & \vdots & \ddots & 0 \\ g_{Ns} & 0 & 0 & 0 & \omega_{_N} \end{bmatrix} \tag{35}$$

Assuming all couplings are within the dispersive regime, i.e. $|\lambda_{is}| = \left|\frac{g_{is}}{\omega_i - \omega_s}\right| \ll 1$, we can apply the perturbation method to derive the diagonal decomposition of $\mathbf{H}_{star}$, as previously demonstrated in Sec. 2.1.1.3. In this context, to illustrate the impact of the reduction in the strength of the non-linear term due to the incorporation of additional linear modes, we take into account the second-order correction for the eigenvectors of the $\mathbf{H}_{star}$ matrix. This results in the eigenvector matrix:

$$\mathbf{U}_{star} \approx \begin{bmatrix} 1 - \frac{1}{2}\sum_{i=1}^{N} \lambda_{is}^2 & \lambda_{1s} & \cdots & \lambda_{Ns} \\ -\lambda_{1s} & 1 & \cdots & 0 \\ \vdots & \vdots & \ddots & \vdots \\ -\lambda_{Ns} & 0 & 0 & 1 \end{bmatrix}, \tag{36}$$

and the dressed mode frequencies:

$$\begin{aligned} \omega_s' &\approx \omega_s - \sum_{i=1}^{N} \lambda_{is} g_{is} \\ \omega_i' &\approx \omega_i + \lambda_{is} g_{is}. \end{aligned} \tag{37}$$

Based on the eigenvector matrix given in Eq. 36, the dressed S mode annihilation operator after the Bogoliubov transformation can be written as:

$$\hat{s}' \approx \left(1 - \frac{1}{2}\sum_{i=1}^{N} \lambda_{is}^2\right) \hat{s} + \sum_{i=1}^{N} \lambda_{is} \hat{a}_i. \tag{38}$$

Assuming the S mode has a n^{th} order non-linearity, $g_n(\hat{s}+\hat{s}^\dagger)^n$, then, after the transformation, we will have multi-wave mixing terms like :

$$\hat{\mathcal{H}}_{NWM,star}(k,l,m) = \hbar\, C_{klm} g_n \left[\left(1 - \frac{1}{2}\sum_{i=1}^{N} \lambda_{is}^2\right)^k \lambda_{is}^l \lambda_{js}^m\right] \hat{s}^k \hat{a}_i^l \hat{a}_j^m + h.c., \tag{39}$$

in which $k + l + m = n$, and C_{klm} is the binomial coefficient from the expansion of the non-linear term. Therefore, if an addition linear mode (A_{N+1}) is coupled to the S mode, the coefficient for the multi-wave mixing term $\hat{\mathcal{H}}_{NWM}(k, l, m)$ will be decreased (diluted) by a factor of $\sim \frac{1}{2^k}\lambda_{N+1,s}^{2k} = \frac{1}{2^k}\left(\frac{g_{N+1}}{\omega_{N+1}-\omega_s}\right)^{2k}$.

Propagation of non-linearity. In the chained coupling scheme, the non-linear mode S is directly coupled with one linear mode A_1, and the linear modes ($A_1 - A_N$)are consecutively coupled with each other in sequence. The system Hamiltonian can be written as:

$$\hat{\mathcal{H}}_{chain,L}/\hbar = \omega_s \hat{s}^\dagger \hat{s} + \sum_{i=1}^{N} \omega_i \hat{a}_i^\dagger \hat{a}_i + g_{1s}\left(\hat{a}_1^\dagger \hat{s} + \hat{a}_i \hat{s}^\dagger\right) + \sum_{i=1}^{N-1} g_{i,i+1}\left(\hat{a}_i^\dagger \hat{a}_{i+1} + \hat{a}_i \hat{a}_{i+1}^\dagger\right), \tag{40}$$

and the characteristic coupling matrix takes the form of a symmetric ‘tridiagonal’ matrix:

$$\mathbf{H}_{chain} = \begin{bmatrix} \omega_s & g_{1s} & 0 & 0 & \cdots & 0 \\ g_{1s} & \omega_1 & g_{12} & 0 & \cdots & 0 \\ 0 & g_{12} & \omega_2 & g_{23} & \cdots & 0 \\ 0 & 0 & g_{23} & \ddots & \ddots & 0 \\ \vdots & \vdots & \vdots & \ddots & \omega_{N-1} & g_{N-1,N} \\ 0 & 0 & 0 & 0 & g_{N-1,N} & \omega_N \end{bmatrix} \tag{41}$$

Once again, we assume that all the couplings are within the dispersive regime, i.e., $|\lambda_{1s}| = \left|\frac{g_{is}}{\omega_i - \omega_s}\right| \ll 1$ and $|\lambda_{i,i+1}| = \left|\frac{g_{i,i+1}}{\omega_i - \omega_{i+1}}\right| \ll 1$. The eigenvectors of the matrix $\mathbf{H}_{chain}$ can be calculated by iteratively applying the perturbation method. To determine the participation of the last linear mode A_n in the dressed S mode, we perform the perturbation calculation up to the N^{th} order, which yields:

$$\hat{s}' \approx \hat{s} + \sum_{i=1}^{N}\left(\lambda_{1s}\prod_{j=1}^{i-1}\lambda_{j,j+1}\right)\hat{a}_i \tag{42}$$

Therefore, in the multi-wave-mixing term derived from the original non-linearity of the S mode (i.e. the terms from the expansion of $g_n(\hat{s} + \hat{s}^\dagger)^n$), the modes further down the chain share less non-linearity from the S mode. Each additional step of concatenation, for example from the N^{th} mode to $(N+1)^{\text{th}}$ mode, decreases the strength of the multi-wave-mixing term by approximately $\lambda_{N,N+1} = \frac{g_{N,N+1}}{\omega_N - \omega_{N+1}}$.

The coupling diagrams depicted in Fig. 2 contains the basic patterns that are commonly used in large scale dispersively coupled quantum systems. Therefore, by decomposing a large system into these patterns and combing the results from Eq. 38 and 42, we can conveniently estimate the coefficient for any given multi-wave mixing term in the system Hamiltonian. This approach will be frequently used in our discussion of designing and building the parametrically controlled multi-mode devices in Chapter 4. In general, coupling too many modes to the SNAIL tends to dilute the system's nonlinearity, while using a chained coupling approach alleviates stress on the SNAIL but doesn't allow the nonlinearity to propagate effectively down the chain. In our quantum router and module experiments, we employ both schemes: the SNAILs are directly coupled to only a few modes, and a single intermediate coupling step is introduced when needed.

2.1.2 Displacement transformation

To activate parametric processes based on the multi-wave mixing terms, external microwave pumps are generally applied to the non-linear mode at specific frequencies. To illustrative this effect, we move back to the three-mode system depicted in Fig. 1. The pumping term can be generally written as:

$$\hat{\mathcal{H}}_{pump,S}/\hbar = \left[\varepsilon(t)e^{-i\omega_p t} - \varepsilon^*(t)e^{i\omega_p t}\right]\left(\hat{s}^\dagger - \hat{s}\right), \tag{43}$$

in which $\varepsilon(t)$ and ω_p are the effective amplitude and angular frequency of the pump, respectively. Combining with the result from Eq. 31 and 33, we get the total Hamiltonian of the system under the external drive:

$$\begin{aligned}\hat{\mathcal{H}}_p/\hbar &= \left(\hat{\mathcal{H}}'_{0,L} + \hat{\mathcal{H}}'_{0,NL} + \hat{\mathcal{H}}_{pump,S}\right)/\hbar \\ &= \omega_s\hat{s}^\dagger\hat{s} + \omega_a\hat{a}^\dagger\hat{a} + \omega_b\hat{b}^\dagger\hat{b} + g_3\left(\hat{s} + \lambda_{as}\hat{a} + \lambda_{bs}\hat{b} + h.c.\right)^3 \\ &\quad + \left[\varepsilon(t)e^{-i\omega_p t} - \varepsilon^*(t)e^{i\omega_p t}\right]\left(\hat{s}^\dagger - \hat{s}\right),\end{aligned} \tag{44}$$

In which we have made the approximation that the pump is applied only on the dressed S mode, and replaced the notation for the dressed mode frequencies ω' with ω for simplicity of future calculation.

To examine the dynamics activated by the external pump, we apply a displacement transformation that eliminates the S mode driving term and transfers its effect into the multi-wave mixing term. The transformation operator is written as:

$$\hat{U}_D = \exp\bigl(zs^\dagger - z^* s\bigr), \tag{45}$$

with

$$z = \frac{\varepsilon(t)}{\omega_s - \omega_p} e^{-i\omega_p t} - \frac{\varepsilon^*(t)}{\omega_s + \omega_p} e^{i\omega_p t} \tag{46}$$

A full derivation for calculating this specific form of z can be found in Appendix A. After this transformation, the transformed operators of the S mode will take the displaced form:

$$\begin{aligned} \hat{s}' &= \hat{U}_D \hat{s} \hat{U}_D^\dagger = \hat{s} - z \\ \hat{s}'^\dagger &= \hat{U}_D \hat{s}^\dagger \hat{U}_D^\dagger = \hat{s}^\dagger - z^*, \end{aligned} \tag{47}$$

and the transformed Hamiltonian will be:

$$\begin{aligned} \hat{\mathcal{H}}_D/\hbar &= \hat{U}_D \hat{\mathcal{H}}_p \hat{U}_D^\dagger/\hbar + i\dot{\hat{U}}_D \hat{U}_D^\dagger \\ &= \omega_s \hat{s}^\dagger \hat{s} + \omega_a \hat{a}^\dagger \hat{a} + \omega_b \hat{b}^\dagger \hat{b} + g_3 \left(\hat{s} + \lambda_{as}\hat{a} + \lambda_{bs}\hat{b} - z + h.c.\right)^3 \end{aligned} \tag{48}$$

The $(-z - z^*)$ component in the 3rd-order term can be rearranged based on the positive and negative frequency components:

$$\begin{aligned} -z - z^* &= -\frac{\varepsilon(t)}{\omega_s - \omega_p} e^{-i\omega_p t} + \frac{\varepsilon^*(t)}{\omega_s + \omega_p} e^{i\omega_p t} - \frac{\varepsilon^*(t)}{\omega_s - \omega_p} e^{i\omega_p t} + \frac{\varepsilon(t)}{\omega_s + \omega_p} e^{-i\omega_p t} \\ &= \frac{2\omega_p \varepsilon(t)}{\omega_p^2 - \omega_s^2} e^{-i\omega_p t} + \frac{2\omega_p \varepsilon^*(t)}{\omega_p^2 - \omega_s^2} e^{i\omega_p t} \\ &= \eta e^{-i\omega_p t} + \eta^* e^{i\omega_p t}, \end{aligned} \tag{49}$$

in which we have defined:

$$\eta = \frac{2\omega_p \varepsilon(t)}{\omega_p^2 - \omega_s^2} \tag{50}$$

So the transformed Hamiltonian in Eq. 48 can be re-written as:

$$\hat{\mathcal{H}}_D/\hbar = \omega_s \hat{s}^\dagger \hat{s} + \omega_a \hat{a}^\dagger \hat{a} + \omega_b \hat{b}^\dagger \hat{b} + g_3 \left(\hat{s} + \lambda_{as}\hat{a} + \lambda_{bs}\hat{b} + \eta e^{-i\omega_p t} + h.c.\right)^3 \tag{51}$$

After the displacement transformation, the impact of the external pump is incorporated into the non-linear term that involves all three modes in the system. However, the Hamiltonian in Eq. 51 still contains both the system dynamics attributable to the static system Hamiltonian and the dynamics activated by the external pump. Therefore, to concentrate on the effect of the external pump, we perform another transformation that effectively "removes" the static Hamiltonian components. Namely, we apply a rotating frame transformation at all three modes' resonance frequencies.

2.1.3 Rotating frame transformation and rotating-wave approximation (RWA)

The rotating frame transformation takes the form:

$$\hat{U}_R = \exp\left[i\omega_a t\hat{a}^\dagger\hat{a} + i\omega_b t\hat{b}^\dagger\hat{b} + i\omega_s t\hat{s}^\dagger\hat{s}\right] \tag{52}$$

After then transformation, the annihilation operators of the three modes will be transformed as:

$$\begin{aligned}\hat{a}' &= \hat{U}_R\hat{a}\hat{U}_R^\dagger = \hat{a}e^{-i\omega_a t}\\ \hat{b}' &= \hat{U}_R\hat{b}\hat{U}_R^\dagger = \hat{b}e^{-i\omega_b t}\\ \hat{s}' &= \hat{U}_R\hat{s}\hat{U}_R^\dagger = \hat{s}e^{-i\omega_s t},\end{aligned} \tag{53}$$

while the creation operators can be calculated by taking the Hermitian conjugates of the above expressions. This specific rotating frame transformation is effectively equivalent to moving to the interaction picture, and the effective Hamiltonian after transformation is given by:

$$\begin{aligned}\hat{\mathcal{H}}_I/\hbar &= \hat{U}_R\hat{\mathcal{H}}_D\hat{U}_R^\dagger/\hbar + i\dot{\hat{U}}_R\hat{U}_R^\dagger\\ &= g_3\left(\hat{s}e^{-i\omega_s t} + \lambda_{as}\hat{a}e^{-i\omega_a t} + \lambda_{bs}\hat{b}e^{-i\omega_b t} + \eta e^{-i\omega_p t} + h.c.\right)^3,\end{aligned} \tag{54}$$

where the subscript I denotes the interaction picture.

The expansion of Eq. 54 contains all possible third-order products of $\hat{a}$, $\hat{b}$, $\hat{s}$, η, and their Hermitian conjugates. Each third-order term is accompanied by a corresponding time-dependent oscillating phase factor. The evolution of the quantum system state under the Hamiltonian $\hat{\mathcal{H}}_I$ is governed by the time evolution operator $\hat{U}_{\mathcal{H}} = \exp\left(-\frac{i}{\hbar}\int\hat{\mathcal{H}}_I dt\right)$. Terms in $\hat{\mathcal{H}}_I$ with rapidly oscillating phases tend to cancel out in the time integral and can therefore be neglected. This phenomenon is commonly referred to as the rotating-wave approximation (RWA). By carefully choosing the pumping frequency, we can selectively determine which terms survive under RWA, thereby activating the desired dynamics. For example, by setting $\omega_p = \omega_b - \omega_a$, the term $\eta^* \hat{a}^\dagger \hat{b} + \eta \hat{a}\hat{b}^\dagger$ will have zero oscillating phase and, assuming no other frequency collision effects, will be the only term remaining in the Hamiltonian after RWA. The effective Hamiltonian under this pump can be written as:

$$\begin{aligned} \hat{\mathcal{H}}^{eff} &= 6g_3 \lambda_{as} \lambda_{bs} \left(\eta^* \hat{a}^\dagger \hat{b} + \eta \hat{a}\hat{b}^\dagger \right) \\ &= g^{eff} \left(\hat{a}^\dagger \hat{b} e^{i\phi_p} + \hat{a}\hat{b}^\dagger e^{-i\phi_p} \right), \end{aligned} \tag{55}$$

in which we have defined the effective interaction strength $g^{eff} = 6g_3 \lambda_{as} \lambda_{bs} |\eta|$, and $\phi_p = \arg(\eta*)$ is essentially the phase of the external pump. This effective Hamiltonian activates the exchange interaction between the A and B modes. When A and B are both linear modes (harmonic oscillators), this dynamic is usually referred to as a beam-splitter interaction [51, 50, 48, 58] for its obvious resemblance to the optical component of the same name. In contrast, when A and B modes are both two-level systems (qubits), this effective Hamiltonian with various pump lengths create a continuous series of iSWAP family gates, which will be discussed in detail in Sec. 2.2.2.

2.1.4 Summary of main results

Sections 2.1.1 through 2.1.3 provide a comprehensive derivation of the dynamics of charge-pumped parametric interactions, based on the bare mode frequencies, couplings strengths and the pump parameters. Here, we distill these extensive derivations into a concise summary of the principal results. Using these results, we devise a simplified approach for identifying the possible parametric processes given a multi-wave mixing term, and provides simple formulas for estimating the strength of the parametrically activated interaction.

- In a dispersively coupled multi-mode system, the operator of the dressed non-linear mode (S) contains linear combinations of the operators of other modes ($A_1, ..., A_N$) that are (directly or indirectly) coupled to the S mode:

$$\hat{s}' \approx \hat{s} + \sum_{i}^{N} p_i \hat{a}_i, \tag{56}$$

in which $\hat{a}_i$ is the annihilation operator of mode A_i, and p_i corresponds to the participation of mode A_i in the dressed S mode. For modes that are directly coupled to the S mode, p_i can be estimated as

$$p_i = \lambda_{is} = \left(\frac{g}{\Delta}\right)_{is}, \tag{57}$$

in which g_{ij} and Δ_{ij} are the coupling strength and frequency difference between mode A_i and S, respectively. For a mode A_i that is indirectly coupled to the S mode via m intermediate modes $B_{i,1}, ..., B_{i,m}$, p_i can be estimated as:

$$p_i = \lambda_{b_1 s} \left(\prod_{k=1}^{m-1} \lambda_{b_k, b_{k+1}} \right) \lambda_{b_m, a_i} = \left(\frac{g}{\Delta}\right)_{b_1 s} \left(\frac{g}{\Delta}\right)_{b_1 b_2} \cdots \left(\frac{g}{\Delta}\right)_{b_{m-1} b_m} \left(\frac{g}{\Delta}\right)_{b_m a_i}, \tag{58}$$

in which $g_{b_k, b_{k+1}}$ and $\Delta_{b_k, b_{k+1}}$ are the coupling strength and frequency difference between two adjacent intermediate modes $B_{i,k}$ and $B_{i,k+1}$.

- By substituting the dressed non-linear mode operator $\hat{s}'$ into the original non-linear term $g_n(\hat{s} + \hat{s}^\dagger)^n$ (with $n \geq 3$), we can get the dressed non-linear term:

$$\hat{\mathcal{H}}'_{NL} = g_n \left(\hat{s} + \sum_{i}^{N} p_i \hat{a}_i + h.c. \right)^n \tag{59}$$

- After applying the external pump on the S mode and performing both the displacement transformation and rotating frame transformation, we get the new system Hamiltonian in the interaction picture:

$$\hat{\mathcal{H}}_I = g_n \left(\hat{s} e^{-i\omega_s t} + \sum_{i}^{N} p_i \hat{a}_i e^{-i\omega_i t} + \eta e^{-i\omega_p t} + h.c. \right)^n, \tag{60}$$

where ω_i represents the frequency of mode A_i, ω_s is the frequency of the coupler mode S, ω_p is the pump frequency, and $\eta = \frac{2\omega_p \varepsilon(t)}{\omega_p^2 - \omega_s^2}$, as defined in Eq. 50.

- From the pool of n^{th} order terms that emerge from the expansion of Eq. 60, we can pick the term that encapsulates our desired dynamic and includes at least one pump component η. The desired dynamic can then be activated by pumping the S mode at the frequency that allows the desired dynamic to persist under the rotating wave approximation (RWA), i.e.:

  $$k\omega_p = \omega_{\text{rot}} \tag{61}$$

  in which k is the number of η/η^* terms involved in the multi-wave mixing process, and ω_{rot} is the overall rotating frequency of the desired dynamic. The strength of the desired interaction can generally be estimated as:

  $$g^{eff} = C g_n \eta^k \prod_i p_i \tag{62}$$

  in which C is the binomial coefficient from the n^{th} order expansion, g_n is the coefficient of the original n^{th} order non-linearity of the S mode, and the p_i terms represent the participation factors of the interaction-involved modes in the dressed S mode, as can be estimated using Eq. 57 and 58.

Predicting possible parametric interactions from multi-wave mixing terms. The expansion of Eq. 59 contains terms like:

$$\hat{s}^\dagger\hat{s}^\dagger\hat{a}_1,\ \hat{s}^\dagger\hat{a}_1^\dagger\hat{a}_2,\ \hat{s}^\dagger\hat{s}^\dagger\hat{a}_1^\dagger\hat{a}_2,\ \hat{s}^\dagger\hat{a}_1^\dagger\hat{a}_2\hat{a}_3,\ etc \tag{63}$$

We usually refer to these terms as multi-wave mixing terms since each of these terms corresponds to a parametric process that can be activated by applying external pump(s). It is worth noting that, in fact, none of these terms themselves will survive after RWA, since by design we usually want to avoid the multi-wave mixing process to activate spontaneously without any external control. However, from Eq. 47-51 we see that the existence of, for example, $\hat{s}^\dagger\hat{a}_1^\dagger\hat{a}_2$ term actually indicates that $\eta^*\hat{a}_1^\dagger\hat{a}_2$ term (with the same coefficient) will emerge after applying the external pump and performing the displacement transformation, which consequently can produce the desired $(\hat{a}_1^\dagger\hat{a}_2 + h.c.)$ interaction when the pump is applied at the right frequency $\omega_p = \omega_2 - \omega_1$. For this reason, the $\hat{s}^\dagger\hat{a}_1^\dagger\hat{a}_2$ term is also sometimes written as $\langle s\rangle \hat{a}_1^\dagger \hat{a}_2$ when considering the multi-wave mixing parametric process, with $\langle s\rangle = |\eta|$ representing the effective "pump photon" number we put into the non-linear mode S via the external off-resonance pump.

2.2 Parametric single and multi-qubit gates

Based on the formalism we summarized in Sec. 2.1.4, we can explore what other single- and two-qubit gates are available from multi-wave-mixing processes.

2.2.1 Single-qubit sub-harmonic gates

Consider a qubit mode (denoted as Q) with frequency ω_q that is dispersively coupled to a non-linear mode S with n^{th} order non-linearity $g_n(\hat{s}+\hat{s}^\dagger)^n$, as depicted in Fig. 3a. Using Eq. 59 we get the dressed non-linear term in system:

$$\hat{\mathcal{H}}_{QS,NL} = g_n\left(\hat{s} + \lambda_{qs}\hat{\sigma_-} + \hat{s}^\dagger + \lambda_{qs}\hat{\sigma_+}\right)^n , \tag{64}$$

in which $\lambda_{qs} = \frac{g_{qs}}{\omega_q - \omega_s}$ is the hybridization strength between the two modes. The annihilation and creation operators of the qubit are written in the form of Pauli ladder operators $\hat{\sigma_-}$ and $\hat{\sigma_+}$, respectively, as consider the qubit as an ideal two-level system here. The expansion of this Hamiltonian contains the multi-wave-mixing term:

$$\hat{\mathcal{H}}_{QS,subH} = n g_n \lambda_{qs}\left(\hat{s}^{n-1}\hat{\sigma_+} + (\hat{s}^\dagger)^{n-1}\hat{\sigma_-}\right) , \tag{65}$$

in which the coefficient "n" comes from the binomial expansion. This term indicates that by pumping on the S mode at frequency $\omega_p = \frac{1}{n-1}\omega_q$, we can create the effective Hamiltonian:

$$\hat{\mathcal{H}}_{QS}^{eff} = n g_n \lambda_{qs}\eta^{n-1}\left(\hat{\sigma_+}e^{-i(n-1)\phi_p} + \hat{\sigma_-}e^{i(n-1)\phi_p}\right) , \tag{66}$$

in which $\eta = \frac{2\omega_p}{\omega_p^2 - \omega_s^2}\varepsilon(t)$, with $\varepsilon(t)$ being the amplitude of the external pump, and ϕ_p the phase of the pump. This Hamiltonian effectively mirrors an on-resonance drive on the qubit mode, which thereby can create arbitrary single-qubit rotations (gates) by controlling the

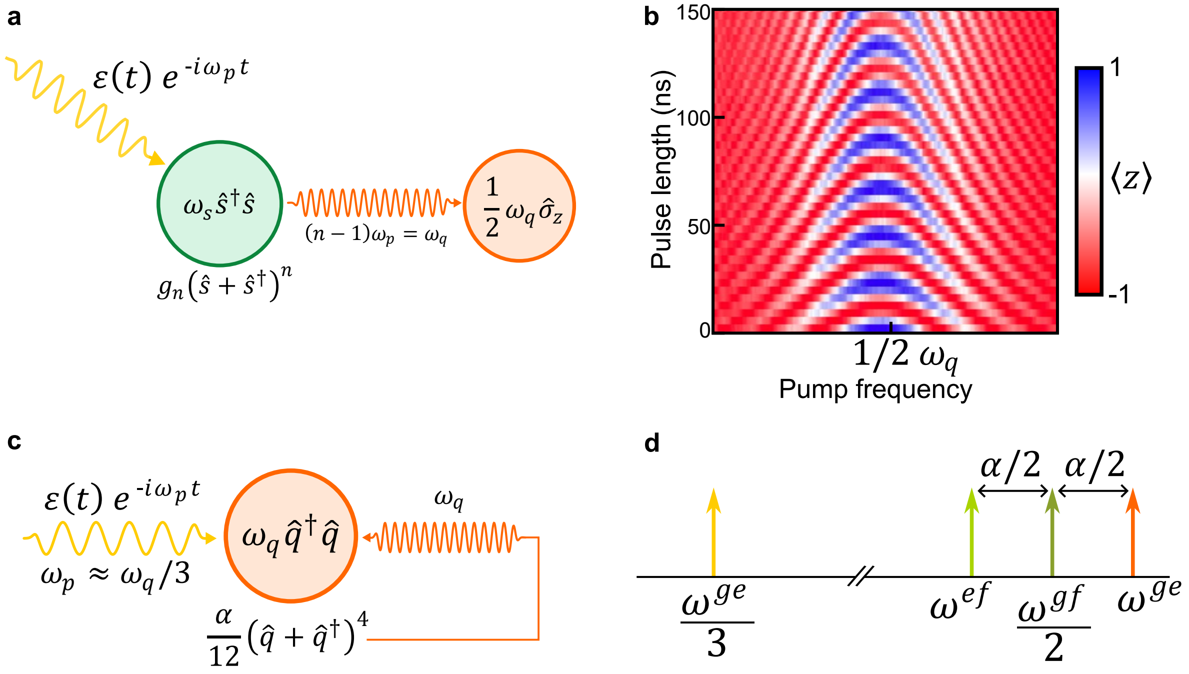

Figure 3: **Sub-harmonic single-qubit control via a non-linear coupler and in a single transmon.** **a)** Coupling diagram between a non-linear coupler (labeled in green) with n^{th} non-linearity and a qubit mode (labeled in orange) with frequency ω_q. The sub-harmonic qubit control can be performed by applying an external pump on the coupler mode with frequency $\omega_p = \omega_q/(n-1)$. **b)** "Chevron" plot obtained from the experiment that shows the Rabi oscillation of the qubit under the sub-Harmonic drive, which indicates the sub-harmonic driving scheme's ability to perform arbitrary single qubit control. **c)** Sub-harmonic control scheme using the 4^{th} order non-linearity of the transmon qubit itself. The pump is directly applied on the qubit at frequency $\omega_p \approx \omega_q/3$. **d)** Spectrum of the mode frequencies and potential driving frequencies for single qubit control of a transmon. The commonly observed transitions, namely the two-photon $|g\rangle - |f\rangle$ transition and the $|e\rangle - |f\rangle$ transition, are both relatively close to the major $|g\rangle - |e\rangle$ transition. In contrast, the three photon $|g\rangle - |e\rangle$ transition lies much further below in frequency, therefore has usually been overlooked.

length and phase of the external pump. The speed of the single qubit gate is then determined by the interaction coefficient:

$$g^{eff} = ng_n\eta^{n-1}\lambda_{qs} \tag{67}$$

Figure 3b shows an example single qubit sub-Harmonic Rabi-oscillation data that is taken from our 4-qubit module device, which I will introduce in Sec. 4.4.1. In comparison with the traditional on-resonance qubit drive, this sub-harmonic driving scheme has the interesting property that the gate speed is proportional to the $(n-1)^{\text{th}}$ power of the pump amplitude, i.e. $g^{eff} \propto \varepsilon(t)^{n-1}$, rather than being linearly proportional to the pump amplitude. Also, the phase of the gate is set by $(n-1)\phi_p$, as opposed to simply being ϕ_p as in the case of on-resonance drive.

Interestingly, such sub-harmonic single qubit gates can also be implemented in a even simpler setup - a transmon qubit by itself [56]! The transmon qubit inherently possesses a 4^{th} order non-linearity [18]:

$$\hat{\mathcal{H}}_{tr,NL} = \frac{\alpha}{12}\left(\hat{q} + \hat{q}^\dagger\right)^4, \tag{68}$$

in which α is generally known as the "anharmonicity" of the qubit, as this 4^{th} order term contains an always-on Kerr component:

$$\hat{\mathcal{H}}_{tr,anh} = \frac{\alpha}{2}\hat{q}^\dagger\hat{q}^\dagger\hat{q}\hat{q}, \tag{69}$$

which gives the transmon the unevenly spaced energy level with $\omega_q^{ef} - \omega_q^{ge} = \alpha$. For a transmon qubit, the value of α is usually around -300 to $-50\,\text{MHz}$. From the perspective of parametric process, this term also indicates that we can activate the $|g\rangle \leftrightarrow |f\rangle$ transition of the transmon by applying a pump directly to the qubit at frequency $\omega_p = (\omega_q^f - \omega_q^g)/2 = \omega_q^{ge} + \frac{\alpha}{2}$. This transition is $\frac{\alpha}{2}/2\pi$ (generally $\sim -100\,\text{MHz}$) away from the qubit's $|g\rangle \leftrightarrow |e\rangle$ transition frequency, therefore is commonly observed in transmon spectroscopy experiments[59]. However, there is another term from the expansion of Eq. 68 that is typically neglected after RWA when the external drive is applied near-resonance, but can be leveraged for sub-harmonic driving scheme. That term is:

$$\hat{\mathcal{H}}_{tr,subH} = \frac{\alpha}{3}\left(\hat{q}^\dagger\hat{q}^\dagger\hat{q}^\dagger\hat{q} + \hat{q}^\dagger\hat{q}\hat{q}\hat{q}\right) \tag{70}$$

This term suggests that the qubit $|g\rangle \leftrightarrow |e\rangle$ transition can also be activated by pumping at[3] $\omega_p \approx \omega_q^{ge}/3$, as illustrated in Fig. 3c,d. This sub-harmonic driving scheme gives an effective Rabi rate of:

$$g^{eff} = \frac{\alpha}{3}\eta^3, \tag{71}$$

in which $\eta = \frac{\omega_p}{\omega_p^2 - \omega_q^2}\varepsilon(t)$. Despite the transmon's longstanding popularity as a superconducting qubit, this hidden drive channel has not been thoroughly explored. In our recent preprint[56], we experimentally demonstrated the complete capability of this sub-harmonic driving scheme for full control over a standard transmon qubit. Furthermore, this driving scheme offers the advantage of separating the qubit's loss and control channels in the frequency domain, which thereby enabling more optimal qubit input line configurations that can reduce the heat load on the dilution refrigerator, potentially alleviating the fridge cooling power overhead in the large-scale integration of superconducting qubits[60].

2.2.2 Parametric two-qubit gates

In Section 2.1, we derived the Hamiltonian for the three-mode system that includes two linear modes, A and B, and a non-linear mode, S, with third-order non-linearity. Under the external pump on the S mode, the effective system Hamiltonian was given by Eq.54. When both A and B are two-level systems (qubits), the same derivation can be applied, allowing us to rewrite Eq.54 as:

$$\hat{\mathcal{H}}_{I,QSQ}/\hbar = g_3\left(\hat{s}e^{-i\omega_s t} + \lambda_{as}\sigma_{a,-}e^{-i\omega_a t} + \lambda_{bs}\sigma_{b,-}e^{-i\omega_b t} + \eta e^{-i\omega_p t} + h.c.\right)^3, \tag{72}$$

in which we basically replaced the annihilation and creation operators for mode A and B in Eq.54 with Pauli ladder operators. The definitions of the other variables remain the same as in Eq.54. With this Hamiltonian as our foundation, we can explore what two-qubit gates can be activated by applying external pumps to the S mode.

Continuous *i*SWAP family gates. As briefly discussed in Sec. 2.1.3, when the external pump is applied at frequency $\omega_p = \omega_b - \omega_a$, we can activate the exchange interaction between the A and B modes. Here, when A and B are both qubits, the external pump

---

[3] The approximation is due to the ac-Stark shift effect that occurs during the pump.

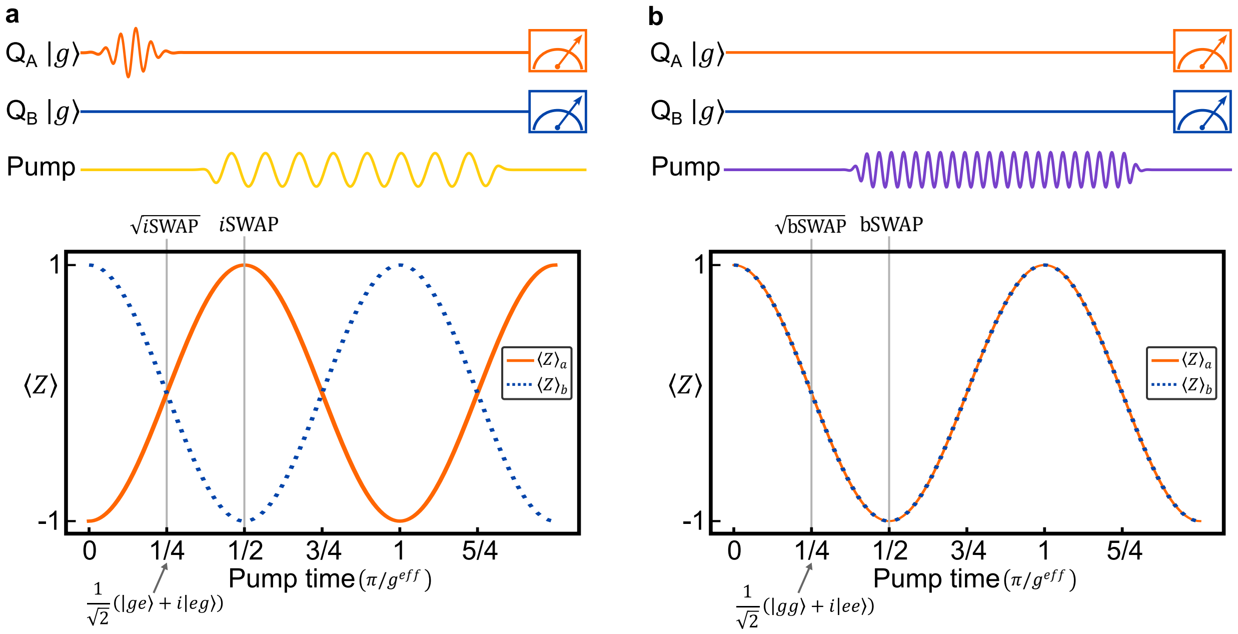

Figure 4: ***i*****SWAP and bSWAP exchange interactions between two qubits. a)** Pulse sequence and photon population of two qubit Q_A and Q_B under the iSWAP interaction. Qubit A is first prepared to the excited state with a $\pi-$pulse, then the pump on the coupler is turned on at the frequency difference between Q_A and Q_B. Under pumps of various lengths, the initial Fock state photon oscillates between the two qubits, enabling the execution of a family of $(i\text{SWAP})^\alpha$ gates. **b)** Pulse sequence and photon population of two qubit Q_A and Q_B under the bSWAP interaction. With both qubits starting from their ground states, the pump at the sum frequency of Q_A and Q_B makes both qubits undergo a simultaneous Rabi oscillation between their ground and excited states. Similar to the iSWAP interaction, a continuous family of $(\text{bSWAP})^\alpha$ gates can be created by controlling the length of the sum frequency pump.

can actually create a Rabi-like oscillation between the $|ge\rangle$ and $|eg\rangle$ states in this two-qubit system, as shown in Fig. 4a. The effective Hamiltonian can be written as:

$$\hat{\mathcal{H}}^{eff}_{\text{iSWAP}}/\hbar = g^{eff}\left(\sigma_{a,+}\sigma_{b,-}e^{i\phi_p} + \sigma_{a,-}\sigma_{b,+}e^{-i\phi_p}\right), \tag{73}$$

with $g^{eff} = 6g_3\lambda_{as}\lambda_{bs}|\eta|$, as described in Sec. 2.1.3. By changing the length of the external pump, we can create a continuous family of two qubit gates whose operator can be explicitly written down as:

$$\hat{U}^{\theta}_{i\mathrm{SWAP}} = \exp\Big[-i\hat{\mathcal{H}}^{eff}_{i\mathrm{SWAP}}t/\hbar\Big] = \begin{bmatrix} 1 & 0 & 0 & 0 \\ 0 & \cos(\theta) & -i\sin(\theta)e^{-i\phi_p} & 0 \\ 0 & -i\sin(\theta)e^{i\phi_p} & \cos(\theta) & 0 \\ 0 & 0 & 0 & 1 \end{bmatrix}, \tag{74}$$

in which $\theta = g^{eff}t$. Such gates are known as the iSWAP family gates[61, 62], with each θ corresponds to a partial version of the full iSWAP gate. By setting the pumping time $t = \frac{\pi}{2}/g^{eff}$ and pump phase $\phi_p = \pi$, we can generate the full-iSWAP gate:

$$\hat{U}_{i\mathrm{SWAP}} = \begin{bmatrix} 1 & 0 & 0 & 0 \\ 0 & 0 & i & 0 \\ 0 & i & 0 & 0 \\ 0 & 0 & 0 & 1 \end{bmatrix} \tag{75}$$

The iSWAP gate operator looks very similar to a SWAP gate, with the key difference being that the two central off-diagonal elements are 'i's rather than '1's. This seemingly minor distinction significantly alters the gate's behavior. While the SWAP gate is a non-entangling gate that simply exchanges the states of two qubits, the iSWAP gate executes the state exchange with an additional "non-Hermitian" phase[4] of i, which makes it an entangling gate. In fact, the iSWAP gate is an universal two-qubit gate that can serve as a basis for compiling any other needed gates between two qubits. It is important to note that the iSWAP gate cannot be transformed into a SWAP gate by simply changing the phase of the external pump. As shown in Eq. 74, the phase introduced by the pump is added to the central off-diagonal elements in a Hermitian way, while the two 'i's at those positions are inherently non-Hermitian. In fact, to construct a SWAP gate from iSWAP gates, we will need three iSWAP gates combined with multiple single qubit gates [63].

---

[4] Here by "non-Hermitian", we mean that the $|ge\rangle \rightarrow |eg\rangle$ and $|eg\rangle \rightarrow |ge\rangle$ transitions have the same, instead of conjugate, added phase.

Another special member of the iSWAP family gates is the root-iSWAP $\left(\sqrt{i\text{SWAP}}\right)$gate, which can be generated by setting the pumping time $t = \frac{\pi}{4}/g^{eff}$ and pump phase $\phi_p = \pi$. The $\sqrt{i\text{SWAP}}$ gate operator is written as:

$$\hat{U}_{\sqrt{i\text{SWAP}}} = \begin{bmatrix} 1 & 0 & 0 & 0 \\ 0 & \frac{1}{\sqrt{2}} & \frac{i}{\sqrt{2}} & 0 \\ 0 & \frac{i}{\sqrt{2}} & \frac{1}{\sqrt{2}} & 0 \\ 0 & 0 & 0 & 1 \end{bmatrix}, \tag{76}$$

The $\sqrt{i\text{SWAP}}$ gate can be employed to generate an odd Bell state from a two-qubit product state $|ge\rangle$, as follows:

$$\hat{U}_{\sqrt{i\text{SWAP}}} |ge\rangle = \frac{1}{\sqrt{2}} \left(|ge\rangle + i\,|eg\rangle\right) \tag{77}$$

The $\sqrt{i\text{SWAP}}$ gate is also an universal two-qubit entangling gate, which is actually more powerful than the iSWAP gate in terms of compiling arbitrary other two-qubit gates [62]. Moreover, since the pump duration required to generate the $\sqrt{i\text{SWAP}}$ gate is half that needed for the full-iSWAP gate, the $\sqrt{i\text{SWAP}}$ gate is inherently faster. Therefore, it can be used as a versatile and easy-to-construct basis gate in parametrically controlled multi-qubit quantum systems.

Continuous bSWAP family gates. Similar to the iSWAP family gates in which the pump was applied at the frequency difference between the two modes, if the external pump is applied at the frequency sum of the two modes, i.e. $\omega_p = \omega_b + \omega_a$, then the surviving term after RWA becomes

$$\hat{\mathcal{H}}^{eff}_{\text{bSWAP}}/\hbar = g^{eff} \left(\sigma_{a,+}\sigma_{b,+}e^{-i\phi_p} + \sigma_{a,-}\sigma_{b,-}e^{i\phi_p}\right), \tag{78}$$

This Hamiltonian activates the monochromatic two-photon excitation of the two qubit modes, i.e. the $|gg\rangle \leftrightarrow |ee\rangle$ transition, as shown in Fig. 4b. Again, by changing the length of the pulse, we get another continuous family of two qubit gates whose operator can be written as:

$$\hat{U}_{\text{bSWAP}^\theta} = \exp\left[-i\hat{\mathcal{H}}^{eff}_{\text{bSWAP}}t/\hbar\right] = \begin{bmatrix} \cos(\theta) & 0 & 0 & -i\sin(\theta)e^{i\phi_p} \\ 0 & 1 & 0 & 0 \\ 0 & 0 & 1 & 0 \\ -i\sin(\theta)e^{-i\phi_p} & 0 & 0 & \cos(\theta) \end{bmatrix}, \tag{79}$$

in which $\theta = g^{eff}t$. The gates described by this operator are also know as the "bSWAP" family gates [64, 65]. When $t = \frac{\pi}{2}/g^{eff}$ and $\phi_p = \pi$, we get the "bSWAP" gate:

$$\hat{U}_{\text{bSWAP}} = \begin{bmatrix} 0 & 0 & 0 & i \\ 0 & 1 & 0 & 0 \\ 0 & 0 & 1 & 0 \\ i & 0 & 0 & 0 \end{bmatrix} \tag{80}$$

The "bSWAP" gate, like the iSWAP gate, is also an universal two-qubit gate, meaning it can serve as a basis gate for compiling any other two-qubit gates. Additionally, the $\sqrt{\text{bSWAP}}$ gate can be used to generate an even Bell state, $\frac{1}{\sqrt{2}}\left(|gg\rangle + i\,|ee\rangle\right)$, from a product state $|gg\rangle$. In fact, the bSWAP family gates are "locally equivalent" [66, 67, 62] to the iSWAP family of gates. This means that one can construct a bSWAP$^{\theta}$ gate by combining a single iSWAP$^{\theta}$ gate with single qubit gates. The specific decomposition is as follows:

$$\hat{U}_{\text{bSWAP}^{\theta}} = \hat{R}_{x,a}(\pi)\; \hat{U}_{\text{iSWAP}^{\theta}}\; \hat{R}_{x,a}(-\pi), \tag{81}$$

in which $\hat{R}_{x,a}(\pm\pi)$ represents a rotation of angle $\pm\pi$ along the x axis on qubit A. This local equivalence property suggests that the bSWAP family of gates possesses the same capability for compiling other two-qubit gates as the iSWAP family of gates. However, when the bSWAP and iSWAP interactions are activated simultaneously in the system (by applying two pumps at the two frequencies concurrently), we can generate gates that are intrinsically different than the iSWAP family gates. The detailed discussion involves the use of the "Weyl Chamber" concept and will be addressed in Sec. 5.1.1.

Discrete CZ gate for transmon qubits. While the $\sqrt{i\text{SWAP}}$ gate is a universal and easy-to-construct gate in parametrically controlled quantum systems, it is not the most commonly used basis gate for most quantum algorithms. Instead, many existing quantum algorithms are written with CNOT gates. Given the iSWAP family gates as our basis gates, the CNOT gate can be constructed using either two $\sqrt{i\text{SWAP}}$ gates [62] or two iSWAP gates [63], combined with single qubit gates. However, when the qubit systems are made with transmons (or other qubits with accessible higher energy levels), we can leverage the

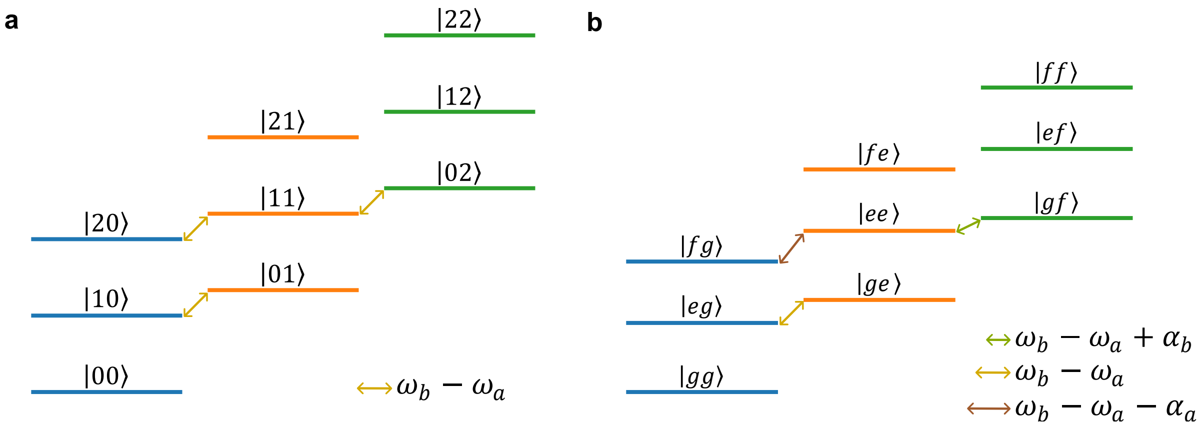

Figure 5: **Energy level structures of two harmonic oscillators and two transmons.** **a)** Energy level structure of two harmonic oscillators. The transitions of $|10\rangle \leftrightarrow |01\rangle$, $|20\rangle \leftrightarrow |11\rangle$ and $|11\rangle \leftrightarrow |02\rangle$ all has the same frequency. **b)** Energy level structure of two transmon qubits. The similar transitions now have different frequencies due to the anharmonicity of the two qubits.

higher-energy-level parametric transitions to directly generate a CZ gate between the two qubits [68], which is locally equivalent to the CNOT gate.

When the two modes involved in the parametric exchange interaction are harmonic oscillators, the dynamic described by Eq. 55 can bring the initial state $|11\rangle$ to state $\frac{1}{\sqrt{2}}(|02\rangle - |20\rangle)$ after one beam-splitter (BS) gate, and back to $-|11\rangle$ state after another BS gate. In the qubit system, such transition is forbidden when pumping at frequency $\omega_p^{ge\to eg} = \omega_b - \omega_a$, since the energy required to go from $|ee\rangle$ to $|gf\rangle$ state is $\hbar\omega_p^{ee\to gf} = \hbar(\omega_b - \omega_a + \alpha_b)$, and the energy required to go from $|ee\rangle$ to $|fg\rangle$ state is $\hbar\omega_p^{ee\to fg} = \hbar(\omega_b - \omega_a - \alpha_a)$, in which α_a and α_b are the anharmonicity of the two transmons, respectively, as depicted in Fig. 5. This unique spectrum allows us to create a CZ gate between the two qubits by pumping at either $\omega_p^{ee\to gf}$ or $\omega_p^{ee\to fg}$. After a full exchange period, in the $\{|gg\rangle, |ge\rangle, |eg\rangle, |ee\rangle\}$ subspace of the two-qubit system, only the $|ee\rangle$ state will undergo the exchange interaction with the $|gf\rangle / |fg\rangle$ state, and will come back with a negative sign (π phase shift). Thus, we get the effective CZ gate operator:

$$\hat{U}_{CZ} = \begin{bmatrix} 1 & 0 & 0 & 0 \\ 0 & 1 & 0 & 0 \\ 0 & 0 & 1 & 0 \\ 0 & 0 & 0 & -1 \end{bmatrix} \tag{82}$$

The CZ gate can be easily converted to a CNOT gate using the decomposition:

$$\hat{U}_{\text{CNOT}} = \hat{R}_{y,b}(\pi/2)\ \hat{U}_{\text{CZ}}\ \hat{R}_{y,b}(-\pi/2), \tag{83}$$

in which $\hat{R}_{y,b}(\pm\pi/2)$ represents a rotation of angle $\pm\pi/2$ along the y axis on qubit B.

2.3 Superconducting parametric couplers

The two-qubit gate discussion in Sec. 2.2.2 has been based on the 3-wave mixing processes introduced by the third-order non-linearity of the S mode. However, as shown in the analysis in Sec. 2.1, the same effective Hamiltonian can also be activated using different order non-linear terms. For instance, given a 4-wave mixing term $\left(\hat{s}\hat{s}\hat{a}\hat{b}^\dagger + \hat{s}^\dagger\hat{s}^\dagger\hat{a}^\dagger\hat{b}\right)$, we can apply a pump to the S mode at $\omega_p = (\omega_b - \omega_a)/2$, or two pumps whose frequencies satisfy $\omega_{p_1} + \omega_{p_2} = (\omega_b - \omega_a)/2$, to activate the same effective exchange interaction as in Eq. 55. This leads us to consider the following questions: What is the optimal non-linearity order for activating a desired parametric process? And how can we construct such a non-linear term with superconducting quantum circuits?

2.3.1 Four-wave mixing with single Josephson Junction devices (transmon)

In superconducting qubit devices, the most common method to introduce non-linearity is through the use of a Josephson Junction (JJ). The potential energy of a single Josephson Junction is related to the flux Φ across the junction via:

$$U_J = -E_J \cos(2\pi\Phi/\Phi_0) = -E_J \cos(\varphi), \tag{84}$$

where Φ_0 is the magnetic flux quantum, E_J is the Josephson energy, and $\varphi = 2\pi\Phi/\Phi_0$ denotes the Josephson phase variable. After combing the JJ with a capacitor and performing the second quantization [53, 54, 36], the phase variable can be expressed in terms of the annihilation and creation operators:

$$\varphi = \left(\frac{2E_C}{E_J}\right)^{\frac{1}{4}} (\hat{a}^\dagger + \hat{a}) = \varphi_{ZPF}(\hat{a}^\dagger + \hat{a}), \tag{85}$$

where E_C is the captive energy, and $\varphi_{ZPF} = \left(\frac{2E_C}{E_J}\right)^{\frac{1}{4}}$ is the phase zero-point-fluctuation (ZPF). Substituting Eq.85 back into Eq.84, we obtain the Hamiltonian term:

$$\hat{\mathcal{H}}_J = -E_J \cos\left[\varphi_{ZPF}(\hat{a}^\dagger + \hat{a})\right] = -E_J \sum_{n=0}^{\infty} \frac{(-1)^n \varphi_{ZPF}^{2n}}{(2n)!} \left(\hat{a}^\dagger + \hat{a}\right)^{2n} \tag{86}$$

Equation 86 shows that the JJ can naturally provide all the even-order non-linear terms to the quantum system, with the leading non-linear term being fourth order. Therefore, a simple transmon, which is usually made of a single JJ combined with a capacitor, can be readily used as a four-wave mixing coupler for constructing parametric two-qubit gates in superconducting multi-mode systems [47, 48, 50]. In Sec. 4.2.4.2, I will also present an example usage of such transmon-based four-wave mixing process for exchanging photons between the qubit and a high-Q resonator.

2.3.2 Issues of the four-wave mixing process

While 4-wave mixing couplers are relatively straightforward to implement, they do come with inherent issues. The two primary problems are the AC-Stark shift effects and the static ZZ interaction between the modes in the system. Moreover, in comparison with the minimal third-order non-linearity, the fourth-order non-linearity introduces a significantly larger number of possible parametric processes, which can potentially cause frequency collisions in parametric interactions.

The AC-Stark shift effect. Following the same derivation we did in Sec. 2.1, if the coupler mode S in Fig.1 has a fourth-order non-linearity, then the effective system Hamiltonian under external pump can be expressed as:

$$\hat{\mathcal{H}}_I/\hbar = g_4 \left(\hat{s}e^{-i\omega_s t} + \lambda_{as}\hat{a}e^{-i\omega_a t} + \lambda_{bs}\hat{b}e^{-i\omega_b t} + \eta e^{-i\omega_p t} + h.c.\right)^4, \tag{87}$$

where the variable and operator notations follows the same definitions as in Eq. 54. From the expansion of this Hamiltonian, we will have the always-non-rotating terms:

$$\hat{\mathcal{H}}_{Stark} = 24g_4|\eta|^2 \left(\hat{s}^\dagger\hat{s} + \lambda_{as}^2\hat{a}^\dagger\hat{a} + \lambda_{bs}^2\hat{b}^\dagger\hat{b}\right) \tag{88}$$

These terms indicate that when an external pump is applied to a fourth-order non-linear coupler, all the modes in the system will be subject to a frequency shift proportional to the power of the external pump. Given that each parametric process is addressed by a specific pumping frequency related to the mode frequencies, such frequency shifts can greatly complicate the tuning process of parametric gates (see Sec. 4.2.4.2 for an example experiment). Moreover, it makes it hard to prevent frequency collisions in multi-mode systems, i.e., situations where two modes or two parametric transitions coincide in frequency.

Static ZZ interaction. The expansion of Eq 87 also contains the non-rotating Kerr terms that are not related to the external pump η:

$$\hat{\mathcal{H}}_{Kerr} = 24g_4|\eta|^2 \left(\lambda_{as}^2\hat{s}^\dagger\hat{s}\hat{a}^\dagger\hat{a} + \lambda_{bs}^2\hat{s}^\dagger\hat{s}\hat{b}^\dagger\hat{b} + \lambda_{as}^2\lambda_{bs}^2\hat{a}^\dagger\hat{a}\hat{b}^\dagger\hat{b}\right) \tag{89}$$

These terms resemble the form of the cross-Kerr terms used in qubit dispersive readout and are generally referred to as static ZZ interactions between modes. The existence of these terms means that even without the external pump (when the system is in the static state), the change in photon number in one mode will influence the state of the other modes. The first two components in Eq. 89 indicate that the stray photons in the coupler mode S will decohere the two computational modes A and B, while the last indirectly introduced cross-Kerr term between the A and B modes can cause cross-talk and spectator qubit errors [69, 70, 71]. Although it is possible to eliminate such undesirable interactions via dynamical methods[72, 73] or by engineering the coupler design [74, 68], it is more preferable for the coupler mode not to rely on a strong cross-Kerr term for its operation.

Frequency crowding of parametric interactions. Except for these always-non-rotating terms, the majority of the terms from the expansion of Eq. 87 correspond to the possible parametric interactions that can be activated by the external pump. Using the formalism introduced in Appendix B, we can systematically identify and list the pumping frequencies corresponding to all these potential parametric interactions. By considering a set of example mode frequencies: $\omega_a/2\pi = 3.5\,\mathrm{GHz}$, $\omega_b/2\pi = 5\,\mathrm{GHz}$, and $\omega_s/2\pi = 4\,\mathrm{GHz}$, we can plot the transition frequency spectrum for all the 4-wave mixing processes, as shown in Fig. 6a. For comparison, we also performed this calculation for the same 3-mode system but with third-order non-linearity (i.e. the Hamiltonian in Eq. 54), and the result is shown in Fig. 6b.

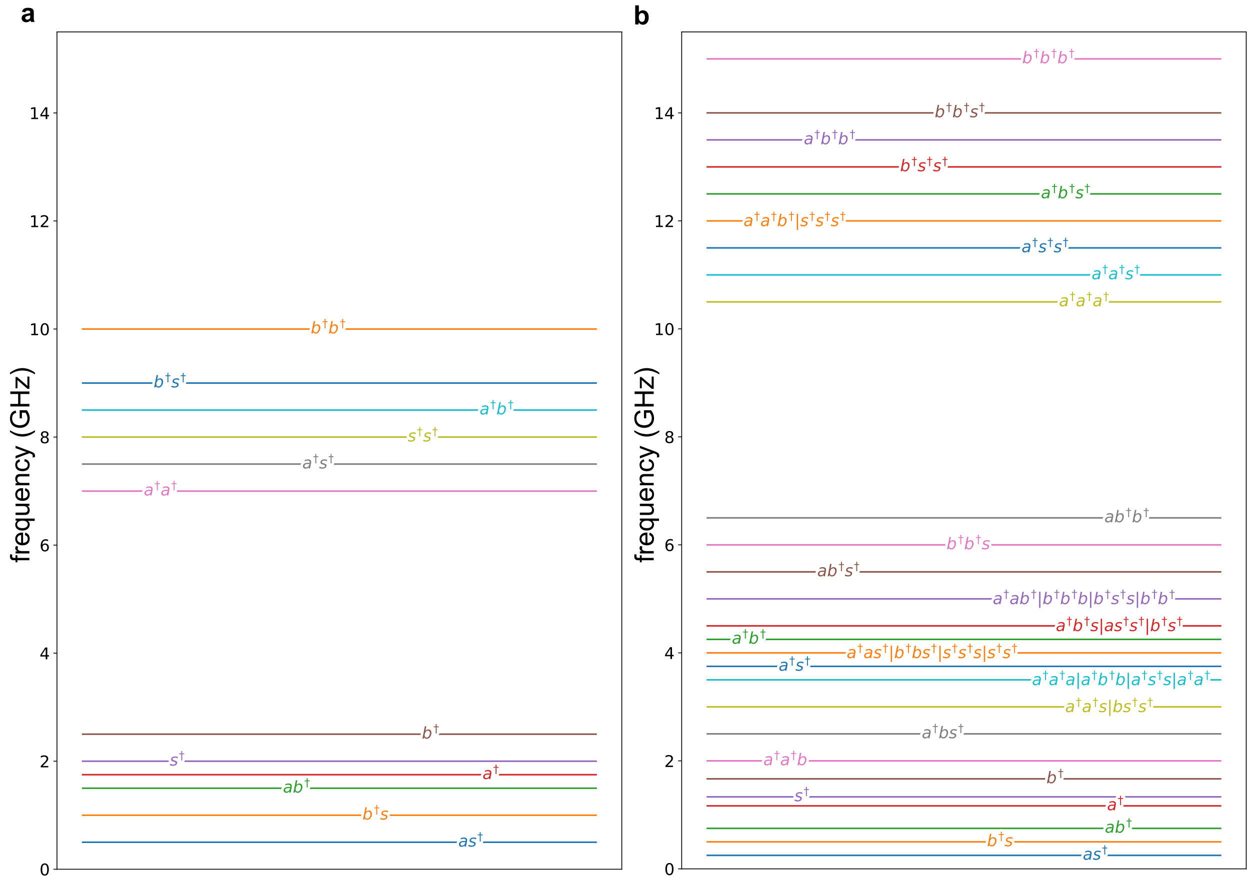

Figure 6: **Parametric transition frequency spectrum in a 3-mode system with 3^{rd} or 4^{th} order non-linearity.** **a)** The parametric transitions and their required pumping frequencies for the three-wave mixing interactions. **b)** The same figure for the four-wave mixing interactions. While the latter clearly presents a larger number of possible parametric processes that can be activated, it also possesses a considerably denser frequency spectrum, making it harder to prevent frequency collisions among the parametric processes.

It is worth notating that the above calculation only considers a monochromatic (single frequency) external pump. When multiple pumps are applied at different frequencies, the same parametric processes listed in these figures can also be activated as long as the overall rotating frequencies of the pumping terms match with the parametric transition frequencies. In that case, we will not have a closed-form constraint for choosing the frequency of each specific pump, but we must make sure that non of the pumping frequencies coincide with the monochromatic transition frequencies listed above. The comparison between Fig. 6a and b clearly shows that the fourth-order non-linearity enables more parametric processes that can be activated by the external pump, but it also results in a denser spectrum. This packed spectrum raises the possibility for two transitions to collide in frequency, which will make it impossible to address each process individually. This effect is commonly known as “frequency crowding” in parametrically controlled quantum systems. Note that this frequency crowding effect is not specific to the four-wave mixing processes only. With higher-order non-linearity, it is not hard to imagine that we will have even more parametric interactions available, with an even denser spectrum for the pumping frequencies.

In gate-based quantum computing, it is generally not necessary to have an excessive number of available interactions. Instead, the minimal requirement is to have a set of universal basis gates that can compile the entire quantum circuit[1]. In this context, it is preferable to have a small set of basis gates that can be easily calibrated to high fidelity, rather than having a dense transition frequency spectrum that makes tuning the basis gate difficult. For this reason, we would like to use the minimal-order non-linearity that is sufficient for performing universal two-qubit gates. As illustrated in Sec. 2.2.2, the third-order non-linear term is more than sufficient for this job. Additionally, the third-order non-linearity does not introduce extra AC-Stark shift effects and ZZ interactions as the fourth-order non-linearity does. Therefore, three-wave mixing-based parametric processes can be considered preferable to higher order mixing processes for constructing quantum gates.

2.3.3 Three-wave-mixing with the "superconducting non-linear asymmetric inductive element" (SNAIL)

The superconducting non-linear asymmetric inductive element" (SNAIL) [26, 75, 76] is a dipole element with third-order non-linearity that can be easily built as a coupler device for three-wave mixing parametric operations. Figure 7 shows the circuit diagram and example pictures of a SNAIL device. Basically, the central part of the SNAIL circuit contains a superconducting loop with $M(M > 1)$ larger identical Josephson Junctions (JJs) with Josephson Energy E_J, and one smaller JJ with Josephson energy βE_J on the other arm. The Hamiltonian of the SNAIL is dependent on the external flux Φ_{ext} applied to the SNAIL loop. The total potential energy of the SNAIL can be written as:

$$U_s(\varphi) = -\beta E_J \cos(\varphi) - M E_J \cos\left(\frac{\varphi_{\text{ext}} - \varphi}{M}\right), \tag{90}$$

in which φ is the superconducting phase across the small junction. This superconducting phase φ is related to the flux Φ across the junction via $\varphi = \Phi/\phi_0$, where $\phi_0 = \frac{\Phi_0}{2\pi} = \frac{\hbar}{2e}$ is the reduced magnetic flux quantum. Similarly, $\varphi_{\text{ext}} = \Phi_{\text{ext}}/\phi_0$ denotes the superconducting phase in the SNAIL loop induced by the external magnetic flux Φ_{ext}.

The mixing capability of the SNAIL device can be analyzed by performing Taylor expansion around the potential minimal point (at $\varphi = \varphi_{\text{min}}$). For each given each external applied flux, the value of φ_{min} can be calculated numerically using:

$$\frac{dU_s}{d\phi}\bigg|_{\varphi=\varphi_{\text{min}}} = \beta E_J \sin(\varphi_{\text{min}}) + E_J \sin\left(\frac{\varphi_{\text{min}} - \varphi_{\text{ext}}}{M}\right) = 0 \tag{91}$$

Equation 91 has a single solution when $\beta < 1/M$. To avoid hysteresis and unstable behavior, we always design the SNAIL circuit in this regime when using it as a coupler device. The Taylor expansion of the SNAIL potential energy around $\varphi = \varphi_{\text{min}}$ can be written as follows:

$$U_s(\varphi) = c_2\tilde{\varphi}^2 + c_3\tilde{\varphi}^3 + c_4\tilde{\varphi}^4 + \dots, \tag{92}$$

in which we have defined $\tilde{\varphi} \equiv \varphi - \varphi_{\text{min}}$, and c_i are the Taylor coefficients. Here, we list the expressions for the coefficients up to the fifth order, which have been simplified based on the condition in Eq. 91.

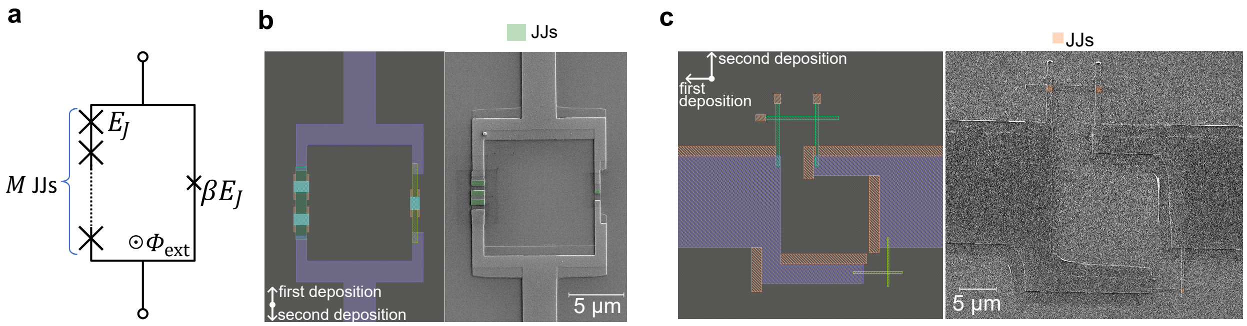

Figure 7: **Circuit diagram and SEM pictures of the SNAIL device.** **a)** Circuit diagram of a SNAIL device. The superconducting loop contains M large Josephson Junctions (JJs) on one arm, and one smaller JJ one the other arm. Each large junction has Josephson energy E_J, while the small junction has Josephson energy βE_J. The device property can be tuned via external flux Φ_{ext}. **b)** GDS design and SEM image of a 3-large-junction SNAIL device made with Dolan style deposition. **c)** GDS design and SEM image of a 2-large-junction SNAIL device made with Manhattan style deposition.

$$\begin{aligned}
c_2 &= \frac{1}{2!}\frac{d^2U_s}{d\varphi^2}\bigg|_{\varphi=\varphi_{\min}} = \frac{E_J}{2}\left[\beta\cos(\varphi_{\min}) + \frac{1}{M}\cos\left(\frac{\varphi_{\min}-\varphi_{\mathrm{ext}}}{M}\right)\right] \\
c_3 &= \frac{1}{3!}\frac{d^3U_s}{d\varphi^3}\bigg|_{\varphi=\varphi_{\min}} = \frac{E_J}{6}\left[\frac{1-M^2}{M^2}\beta\sin(\varphi_{\min})\right] \\
c_4 &= \frac{1}{4!}\frac{d^4U_s}{d\varphi^4}\bigg|_{\varphi=\varphi_{\min}} = \frac{E_J}{24}\left[-\beta\cos(\varphi_{\min}) - \frac{1}{M^3}\cos\left(\frac{\varphi_{\min}-\varphi_{\mathrm{ext}}}{M}\right)\right] \\
c_5 &= \frac{1}{5!}\frac{d^5U_s}{d\varphi^5}\bigg|_{\varphi=\varphi_{\min}} = \frac{E_J}{120}\left[\frac{M^4-1}{M^4}\beta\sin(\varphi_{\min})\right]
\end{aligned} \tag{93}$$

The second order term in the expansion gives the inductive energy of the SNAIL. For a linear LC oscillator, the inductive energy is given by $E_L = \frac{\Phi^2}{2L} = \frac{\phi_0^2}{2L}\varphi^2$. Therefore, we can define the SNAIL inductance as:

$$L_{SN} = \frac{\phi_0^2}{2c_2} \tag{94}$$

When being used as a coupler device, the SNAIL is usually fabricated with a large antenna for creating coupling with other modes (see Fig. 27e for an example). This antenna forms a capacitance C, which produces the dominant part of the captive energy component in the SNAIL Hamiltonian. Therefore, the total SNAIL Hamiltonian can be written as:

$$\begin{aligned} H_s &= 4E_C\mathbf{N}^2 + U_s(\varphi) \\ &= 4E_C\mathbf{N}^2 + c_2\tilde{\varphi}^2 + c_3\tilde{\varphi}^3 + c_4\tilde{\varphi}^4 + \dots, \end{aligned} \tag{95}$$

in which $E_C = \frac{e^2}{2C}$ is the charging energy, $\mathbf{N}$ is the conjugate variable for the superconducting phase $\tilde{\varphi}$, and corresponds to the charge number (in units of Cooper pairs $2e$) across the capacitance [26, 76]. We can then apply the second quantization by letting:

$$\begin{aligned} \mathbf{N} &= -i\frac{1}{2\varphi_{_{ZPF}}}(\hat{s} - \hat{s}^\dagger) \\ \tilde{\varphi} &= \varphi_{_{ZPF}}(\hat{s} + \hat{s}^\dagger), \end{aligned} \tag{96}$$

in which

$$\varphi_{_{ZPF}} = \left(\frac{E_C}{c_2}\right)^{1/4} = \frac{1}{\phi_0}\sqrt{\frac{\hbar}{2}\sqrt{\frac{L_{_{SN}}}{C}}} \tag{97}$$

The quantize SNAIL Hamiltonian can then be written as:

$$\begin{aligned} \hat{\mathcal{H}}_s &= \hbar\omega_s\hat{s}^\dagger\hat{s} + \hat{\mathcal{H}}_{s,NL} \\ &= \hbar\omega_s\hat{s}^\dagger\hat{s} + \sum_{n=3}^{\infty} c_n\varphi_{_{ZPF}}^n(\hat{s} + \hat{s}^\dagger)^n \end{aligned} \tag{98}$$

in which the SNAIL mode frequency ω_s is given by:

$$\omega_s = \frac{1}{\hbar}4\sqrt{E_C\ c_2} = \sqrt{L_{_{SN}}C} \tag{99}$$

Thus, we get the coefficient g_n for the SNAIL's n^{th} order non-linear term:

$$g_n = \frac{1}{\hbar}c_n\varphi_{_{ZPF}}^n \tag{100}$$

Figure 8 shows the variation of the SNAIL frequency and the nonlinear coefficients $g_3 - g_5$ with respect to the external flux induced phase Φ_{ext}. The example parameters used in the plot are $\beta = 0.25$, $M = 3, E_J = 9.4 \times 10^{-23}\,\text{J}$ and $C = 0.4\,\text{pF}$.

From Fig. 8 we can see that there exist a special external flux bias point $\Phi_{\text{ext}} = \Phi_{\text{ext}}^{null}$ that nulls the fourth order non-linearity, i.e. $g_4 = 0$. In fact, all the even order non-linear

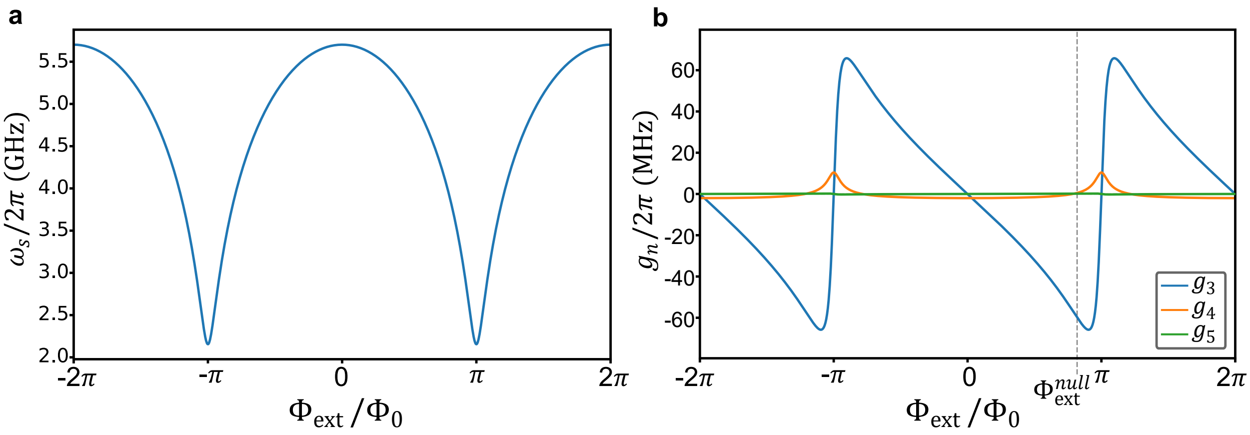

Figure 8: **SNAIL mode frequency and non-linear coefficients versus external flux.** **a)** Example of SNAIL mode frequency versus external flux. **b)** Example of a SNAIL mode's non-linear coefficients versus external flux. There exists a special external flux $\Phi_{\mathrm{ext}}^{null}$, under which the even-order non-linear terms are all equal to 0 and the third order non-linearity is close to maximum.

coefficients will be canceled at this bias point, and we get $g_3(\hat{s}+\hat{s}^\dagger)^3$ as the dominant non-linear term. Therefore, the SNAIL can be readily made as a three-wave mixing coupler device that can perform the parametric gates introduced in the earlier sections.

It is important to note that the calculation above only considers a single SNAIL device. When a SNAIL is coupled with other modes, the quantized phase variable $\tilde{\varphi}$ will contain the annihilation/creation operators of the other modes, i.e.:

$$\tilde{\varphi} = \varphi_{s,\mathrm{ZPF}}(\hat{s}+\hat{s}^\dagger) + \sum_{i=1}^{N} \varphi_{i,\mathrm{ZPF}}(\hat{a}_i + \hat{a}_i^\dagger), \tag{101}$$

where N represents the number of modes coupled to the SNAIL and $\varphi_{i,\mathrm{ZPF}}$ is the phase variable's zero point fluctuations for mode i. This expression takes the similar form as we have seen in the multi-mode system after Bogoliubov transformation (Eq. 38). In fact, $\varphi_{i,\mathrm{ZPF}}$ also reflects the participation of mode i's electromagnetic field in the SNAIL mode. In the dispersive regime, we have the relation: $\varphi_{i,\mathrm{ZPF}}/\varphi_{s,\mathrm{ZPF}} \approx \lambda_{is} = g_{is}/(\omega_i - \omega_s)$.

In the microwave design of a SNAIL-based multi-mode system, the SNAIL is typically treated as an inductive element with a lumped inductance L_{SN}. The value of $\varphi_{i,\mathrm{ZPF}}$ can be extracted using either the "Black-Box Quantization (BBQ)" method [77, 76] or the "Energy Participation Ratio (EPR)" method [78]. Subsequently, the physical parameters of the SNAIL device, including E_J, β and M can be incorporated to calculate the non-linear coefficients g_n, thereby allowing us to analyze the SNAIL-based parametric processes using the methods introduced in the previous sections of this chapter.

It is also worth noting that the SNAIL Hamiltonian calculated above does not account for the shunted linear inductance introduced by the antenna pads. When the magnitude of this inductance is comparable to the SNAIL inductance L_{SN}, the non-linearity of the SNAIL can be effectively 'diluted' by a non-negligible amount. For a comprehensive analysis of this effect, I kindly suggest delving into the thorough discussions presented in references [76, 79].

3.0 Microwave Electronics for Real-time Quantum Control

The control of superconducting qubits is typically performed using external microwave drives, represented by the $\varepsilon(t)$ term in Eq. 4. This term corresponds to the field applied to the quantum system and is directly related to the pulse generated by microwave electronics operating at room temperature. Therefore, the precision with which we can control the amplitude, phase, and frequency of these pulses directly determines the operational fidelity of our quantum processor.

Due to the rapid growth of the microwave telecommunication industry, there have been significant technology advancements in microwave control/characterization electronics, including equipment such as microwave signal generators, vector-network analyzers(VNAs), spectrum analyzers(SAs), etc. These electronics operate at frequencies that align with those of superconducting qubits/resonators, typically ranging from around 100 MHz to 10 GHz. Using these commercially available products, we can readily perform frequency domain characterization of superconducting qubit systems.

However, when it comes to precise time domain control of quantum systems for quantum computing, these electronics face additional requirements that are not typically encountered in their intended applications. For instance, real-time feed-forward control is often necessary in quantum error correction [1, 30, 80, 81]. Given the finite lifetimes of superconducting qubits, performing these feed-forward logic at the microsecond to nanosecond level becomes crucial. Furthermore, the parametric interactions introduced in the previous chapter impose additional demands on the phase coherence between different drive channels, which I will introduce in details in Sec. 3.3.

Field programmable gate arrays (FPGAs) integrated with digital-to-analog converters (DACs) and analog-to-digital converters (ADCs) offer an excellent solution to address these requirements. FPGAs can be programmed to execute digital logic that directly runs on the hardware at fixed clock rates of few hundred megahertz, which enables real-time readout of qubit states, thereby facilitating the determination and execution of qubit state-dependent, next-step operations within the same device with precise timing. Such digital logic can

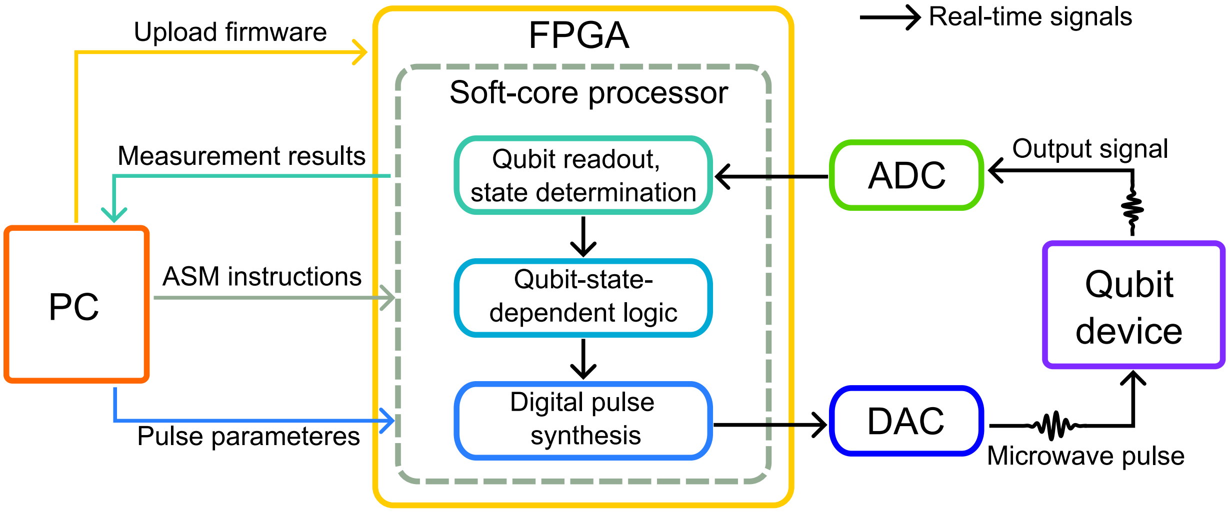

Figure 9: **Example workflow of a FPGA-based qubit control system.** The measurement PC communicate with the FPGA via “low-speed” interfaces, while the FPGA takes on the task of executing real-time qubit-state-dependent algorithms by directly processing the data from the ADC and controlling the output of the DAC.

be further expanded into a soft-core processor that enables the implementation of more complex and customizable logic functionalities at the software level, reducing the need for frequent reprogramming of the FPGA. Figure 9 shows the example workflow of a FPGA-based qubit control system, the digital logic can be pre-loaded from the PC to the FPGA in the form of assembly (ASM) instructions. Such FPGA-based arbitrary waveform generators (AWGs) and digitizers were first custom developed in university labs for controlling qubits systems[82, 83]. Subsequently, similar equipment has become commercially available from companies such as Keysight, Quantum Machines, Zurich Instruments, etc.

The first generation of these systems usually contain (partially programmable) FPGAs with relatively low sampling rate ($\sim 0.5 - 1\,\mathrm{GSa/s}$) DACs/ADCs, that need to be combined with up/down conversion circuits for qubit control/readout (see Sec. 3.2.1). Over the past three to four years, significant firmware and software advancements have been made in these commercial products, which greatly simplifies the execution of complex qubit control experiments that previously requires sophisticated FPGA/software programming [84]. However, we have also seen the trend that these commercial platforms are becoming more and more closed-source, which makes the development of new FPGA features and debugging the low-level errors harder for researchers in the lab.

In parallel with these quantum experiment oriented hardware developments, the major FPGA manufacturer, Xilinx, has introduced a new line of FPGA-based Radio Frequency System on Chip (RFSoC) hardware starting in 2017. These boards and chips feature high performance Xilinx FPGAs integrated with very high-sampling rate DACs/ADCs ($\sim 3-10\,\mathrm{GSa/s}$), which enables qubit pulse generation and readout signal demodulation with direct digital synthesis (DDS). Based on this powerful hardware platform, capable new open-source firmware + software tools have been developed for controlling quantum systems[85, 86]. In comparison to the previously introduced commercial products, these RFSoC-based control setups offer notable advantages. The high frequency DDS feature greatly reduces the requirement for ancillary hardware components in setting up control/measurement systems, which not only makes it much more cost-efficient than using the up/down conversion circuits, but also greatly simplifies the frequency and timing synchronization between different components. Additionally, the availability of open-source firmware and software enables users to have a comprehensive understanding of the pulse synthesis and readout signal demodulation sequence at a very low level, which facilitates easier debugging, as well as the simpler alteration and development of new features.

As a PhD student who works on experimental superconducting quantum computing during this thriving and dynamic era of quantum control systems, I have been fortunate to be actively involved in the development of quantum experiment firmware/software stacks for my laboratory with both types of FPGA platform. In this chapter, I will first present the basic hardware setup for generating qubit control pulses using both ‘slow’ and ‘fast’ pulse synthesis, and digital signal processing (DSP) algorithms for qubit readout signal demodulation. Following that, I will discuss the specific requirements of phase coherence for charge-pumped parametric interactions, the additional demands that the integration of phase coherence places on the microwave hardware and FPGA firmware, and finally the strategies we have employed to meet these demands effectively with both up-converted and

DDS pulse synthesis systems.

Despite the availability of pre-packaged hardware/software platforms that can readily execute qubit measurements, I still believe that understanding the underlying principles of these setups is crucial. Neglecting to fully grasp the workings of the control electronics can result in various errors in experiments, with the worst case being the propagation of misleading or false scientific findings. Given that quantum systems are inherently elusive and challenging to debug, if we fail to effectively manage our classical system, it can cause a cascade of complications. Therefore, my objective for this chapter is twofold: firstly, to provide an explanation of how microwave electronics functions for new quantum experimentalists who are venturing into this field, and secondly, to serve as a reference for future hardware/firmware developers, outlining the essential features required for microwave electronics in the context of quantum computing.

3.1 Basic concepts

3.1.1 Nyquist theorem and aliasing effect

The DAC and ADC both work with discrete-time sampling. The Nyquist sampling theorem states that a periodic signal must be sampled at more than twice the highest frequency component of the signal in order to accurately preserve all of the frequency content[87, 88]. Put another way, for a DAC/ADC device with sampling rate f_s, the maximum frequency component it can accurately produce/capture without aliasing (see below text) is $f_s/2$. The Nyquist frequency of a discrete-time sampling device is defined as:

$$f_{Nq} = f_s/2 \tag{102}$$

When the Nyquist sampling condition is not satisfied, an effect called ‘aliasing’ will happen. Basically, signals of different frequencies will look the same after sampling. Figure 10a shows examples of aliasing effects. When sampling with $f_s = 2\,\text{GHz}$, three continuous signals (either as desired outputs of a DAC or inputs we need to recognize with an ADC), with frequencies of $f_1 = 0.2\,\mathrm{GHz}$, $f_2 = f_s - f_1 = 1.8\,\mathrm{GHz}$ and $f_3 = f_s + f_1 = 2.2\,\mathrm{GHz}$, are sampled as the same digital signal (purple dots).

From this example we can see that aliasing occurs in a regular pattern based on the sampling frequency f_s. This pattern is described using 'Nyquist Zones' in the frequency domain, as depicted in Fig. 10b. The n_{th} Nyquist Zone is the frequency range spanning from $(n-1) * f_{Nq}$ to $n * f_{Nq}$. Each signal in the first Nyquist Zone with frequency f_1 has image tones in the higher Nyquist zones with frequencies $k * f_s - f_1$ and $k * f_s + f_1$.

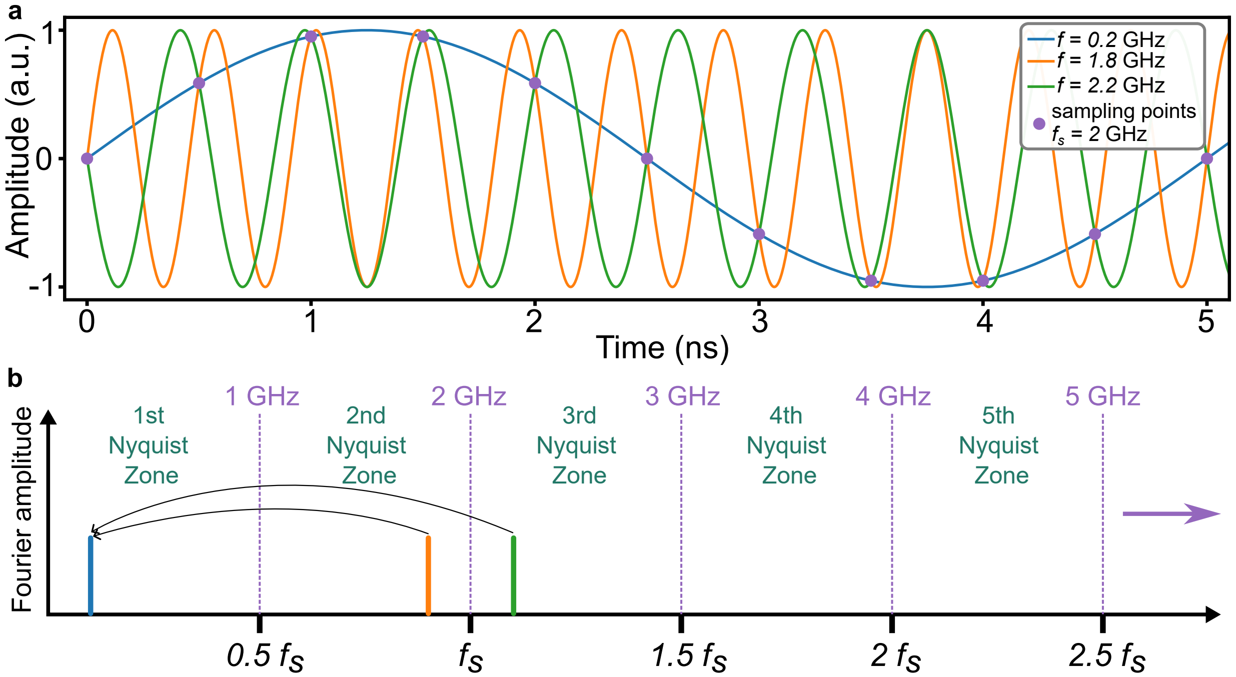

Figure 10: **Aliasing effect and Nyquist zones.** **a)** Aliasing effect. When the signal frequency f is higher than the sampling rate f_s, higher frequency signals (orange and green curves) will look the same as their images in the first Nyquist Zone (blue curve) after sampling (purple dots). **b)** Nyquist Zones. The n_{th} Nyquist Zone is the frequency range from $(n-1)f_s/2$ to $nf_s/2$.

For DACs, having this aliasing effect means that the output signal we defined with the purple dots will have image Fourier components in other Nyquist zones. For ADCs, the consequence is that all the input signals with frequencies above f_{Nq} will be 'folded' down to the first Nyquist Zone. In commercial AWG/digitizer devices, to ensure a well-defined output spectrum/input frequency resolution, the aliasing effects are usually removed with built-in low-pass filters on the DAC/ADC channels (see Sec. 3.2.1). However, in the RFSoC devices, where we have access to the bare DACs and ADCs, we can exploit the aliasing effects intentionally to generate/demodulate signals beyond the first Nyquist Zone (see Sec. 3.2.2.1 and 3.2.2.2).

3.1.2 Frequency mixing and types of analog mixers

The process of frequency mixing simply multiplies two signals in the time domain, thereby creating new signals at the sum and difference frequencies of the two input signals. If we consider two input signals with amplitudes represented by A_1 and A_2, frequencies f_1 and f_2, and phases ϕ_1 and ϕ_2, then the resulting output signal can be expressed using the trigonometric identity:

$$\begin{aligned} V_{out} &= V_{in,1} * V_{in,2} \\ &= A_1 \cos(2\pi f_1 t + \phi_1) * A_2 \cos(2\pi f_2 t + \phi_2) \\ &= \frac{A_1 A_2}{2} \left[\cos(2\pi(f_1 - f_2)t + (\phi_1 - \phi_2)) + \cos(2\pi(f_1 + f_2)t + (\phi_1 + \phi_2))\right] \end{aligned} \tag{103}$$

Equation 103 shows that the output signal after the mixing process consists of two frequency components $f_1 + f_2$ and $f_1 - f_2$, and both components inherit the amplitudes and phases from both input signals. Using this property, we can perform frequency up/down-conversion operations to generate signals at the desired frequencies, while still maintaining the information carried by the input signals. The mixing process can be performed via either digital algorithms or analog mixers. In superconducting qubit experiments, analog mixers are commonly used due to the limited analog bandwidth available in the real-time AWG and digitizer devices.

Regular 3-port mixer. A typical analog mixer usually has three ports, namely, the local oscillator(LO), radio frequency(RF) and intermediate frequency(IF) ports, as shown in Fig. 11. The LO port is usually fed by a continuous generator source with relatively higher frequency (f_L) and fixed amplitude.

In the case of frequency up-conversion, a relatively low-frequency signal (f_I) is sent to the IF port, which generates the up-converted signals on the upper sideband (USB) with frequency $f_R = f_L + f_I$ and on the lower sideband (LSB) with frequency $f_R = f_L - f_I$ on the RF port, as illustrated in Fig. 11a. On the other hand, in frequency down-conversion, the input signal (with frequency f_R) is fed to the RF port, while the LO frequency is set close to the RF frequency. As depicted in Fig. 11b, this configuration produces a down-converted signal at frequency $f_I = |f_R - f_L|$ on the IF port. Typically, the other mixing product $f_R + f_L$ is either automatically eliminated as it falls outside the bandwidth of the IF port, or can be easily removed using a low-pass filter (LPF).

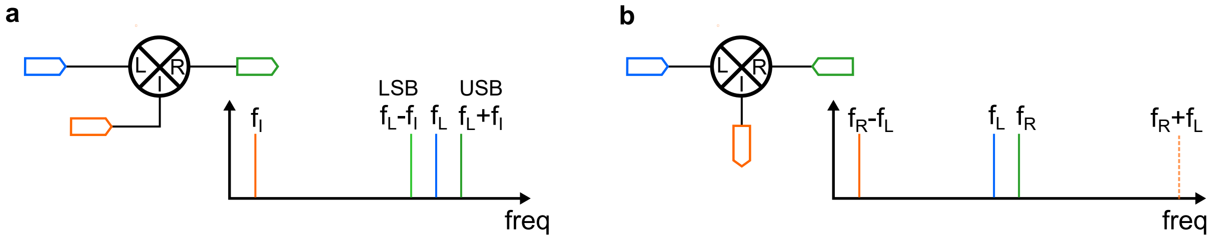

Figure 11: **Frequency up-/down-conversion with a regular 3-port analog mixer.** **a)** Frequency up-conversion setup. A low-frequency signal (f_I) is send to the IF port and mixed with a constant LO signal (f_L). Two up-converted signals at frequencies $f_L + f_I$ and $f_L - f_I$ are generated at the RF port. **b)** Frequency down-conversion setup. A high-frequency signal (f_R) is send to the RF port and mixed with a constant LO signal (f_L). Down-converted signal at frequency $|f_R - f_L|$ is generated at the IF port, while the other mixing product at $f_R + f_L$ is usually removed.

Both the up- and down-conversion operations using regular 3-port mixers have inherent issues. On the up-conversion side, since a practical analog mixer usually has leakage from LO to RF port, we will have three frequency components on the RF output: $f_L - f_I$, f_L and $f_L + f_I$, while only of of the three is the desired signal. Given that the up-conversion circuit is generally used for synthesizing control pulses for our quantum devices, it is necessary to remove these parasitic tones, as they may inadvertently activate unwanted quantum processes in the system [89, 90]. When the IF frequency is relatively high, the unwanted tones can be readily removed using analog low-pass or band-pass filters, as shown in Fig. 12a. However, when the maximum available frequency on the IF channel is limited to a few hundred megahertz (which is what most AWGs can provide), the unwanted signals will get too close to the desired signal, which makes them much more challenging to remove with analog filters; in this case, an In-phase/Quadrature (IQ) mixer will be needed.

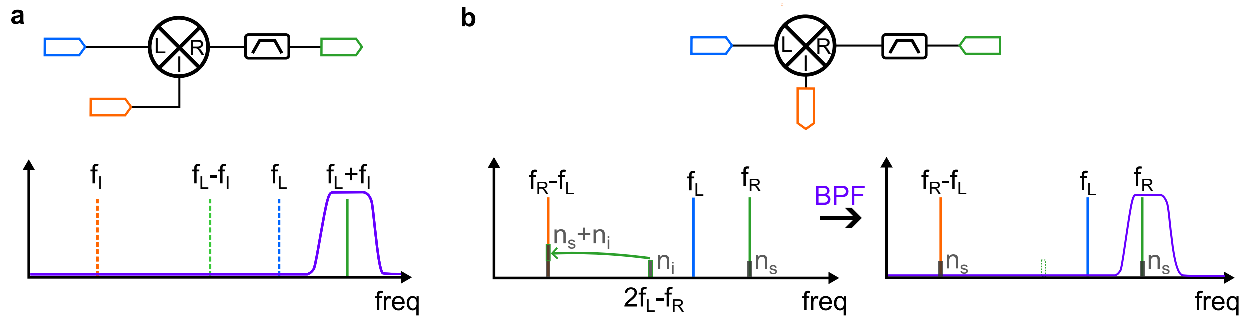

Figure 12: **Removing spurious signals/noise from 3-port mixers with filters. a)** In an up-conversion circuit, the spurious signals can be removed with a band-pass filter when the IF frequency is high enough. **b)** In the down-conversion circuit, the noise from the image sideband (n_i) can be removed by putting a band-pass filter on the RF input, so that the down-converted signal only contains the noise from the original signal (n_s).

The down-conversion circuit is typically used for shifting the high-frequency output signals from the quantum device to lower frequencies that fall within the bandwidth of the ADC. Although it is typically easy to remove the other spurious signals on the IF port and leave only $f_I = |f_R - f_L|$, we face the issue that the noise from the image frequency $2f_L - f_R$ ($2f_I$ away from the desired signal) will also be down-converted to f_I and added onto our down-converted signal, as illustrated in Fig. 12b. Assuming a white noise background, this effect will typically decrease our readout signal-to-noise-ratio (SNR) by a factor of 2, irrespective of the noise temperature of the incoming signal. Similarly to the up-conversion case, when the IF frequency f_I can be relatively high (limited by the analog input bandwidth of the digitizer/ADC), we can apply a LPF/BPF on the original signal to remove the image noise. Alternately, if a narrowband amplifier is used so that the noise of the desired signal is much higher than at the image frequency we can also avoid SNR degradation. However, when f_I needs to be small, another special mixer called ‘Image Reject’ (IR) mixer is generally needed.

In-phase/Quadrature (IQ) mixer. An In-phase/Quadrature (IQ) mixer is made by combining two 3-port mixers, whose LOs are provided by a shared source that goes through a 90° hybrid, a shown in Fig. 13a. The two IF ports are called In-phase (I) and Quadrature (Q) ports on the packaged device. When being used as an up-converter, the I and Q ports are usually fed with two signals that also have a 90° phase difference. As a result, one of the two frequency components ($f_L + f_I$ or $f_L - f_I$) from the two RF ports will have a 180° phase difference, and thus gets cancelled out at the combiner. Additionally, DC offsets ($V_{0,I/Q}$) can be added onto the I and Q channels to cancel out the LO leakage. Therefore, using an IQ mixer we can create up-converted signals with only one sideband frequency. When working with an analog IQ mixer, the relative amplitude (IQ scale) and relative phase (skew phase) on the IQ ports usually needs to be fine tuned to compensate for the practical IQ imbalances inherent in the device.

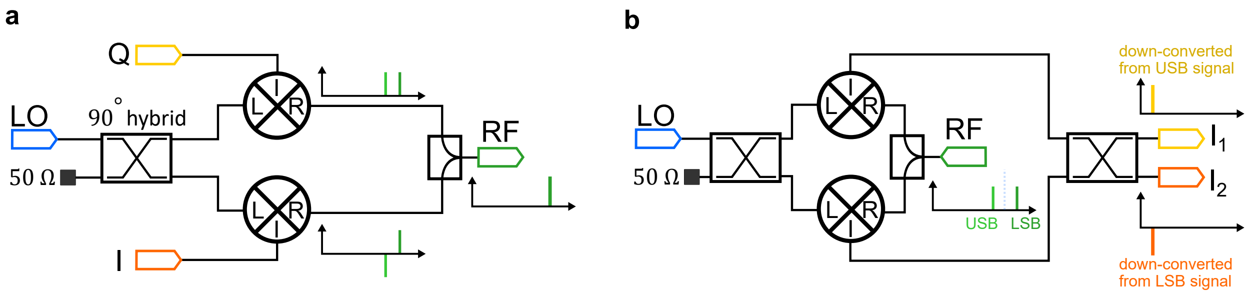

Figure 13: **IQ and IR mixers. a)** IQ mixer. When being used as up-converters, IQ mixers can be tuned to cancel the unwanted sideband signal. **b)** IR mixer. When being used as down converters, IR mixers can separate the USB and LSB RF inputs, thereby avoid adding image noise on the down-converted signals.

Image reject (IR) mixer. An Image Reject (IR) mixer, as shown in Fig. 13b adds an extra 90° hybrid on the I and Q ports of an IQ mixer. As a result, when being used as a down converter, the signal coming out from each IF port, I_1 and I_2, will exclusively contain the frequency component that originated from either only the upper-sideband ($f_R = f_L + f_I$)

or only the lower-sideband ($f_R = f_L - f_I$) input on the RF port. Therefore, each port also only contains the noise associated with its original sideband frequency, avoiding the SNR degradation of three-port mixers.

IR mixers can also be used as up-converters to produce single sideband up-converted signals. However, in a practical analog device, without the ability to fine tune the internal IQ scale and skew phase, it is very difficult to achieve sideband suppression of greater than 15 dBc (decibels relative to the desired signal), which is not ideal for generating a clean output spectrum for qubit control, and so 3-port mixers with large IF or IQ mixers are preferred for this task.

3.2 Basic hardware setup for single qubit control and readout

As an illustrative example of controlling a single superconducting qubit device, we consider a minimal example device that contains a fixed-frequency transmon [18] qubit with a stripline readout resonator [91]. The configuration of this device is depicted in Figure 14.

The transmon qubit usually has a $|g\rangle \leftrightarrow |e\rangle$ transition frequency of $\sim 3-6$ GHz [18],while the resonant frequency of the readout resonator falls within the $5 - 9$ GHz range. To have full control over the qubit, we need to generate microwave pulses at the qubit frequency with arbitrary pulse shape and phase. For reading out the qubit state, we consider the conventional dispersive readout scheme, which requires generating pulses at the cavity frequency, demodulating the output signal from the cavity, and extracting the phase information carried in that signal (we assume readout in reflection here, in other configurations there can be a general state-depdendent shift in the I-Q plane).

In order to generate the microwave pulses and precisely control their frequencies, waveforms, phases, and timing, the central instrument used is an arbitrary waveform generator (AWG), whose core component is a digital-analog converter(DAC). For the demodulation of the readout signal, the signal is typically processed through an analog down-conversion circuit and/or a set of amplifiers and filters, before being routed to the analog-digital converter (ADC). The subsequent demodulation is performed with digital signal processing (DSP)

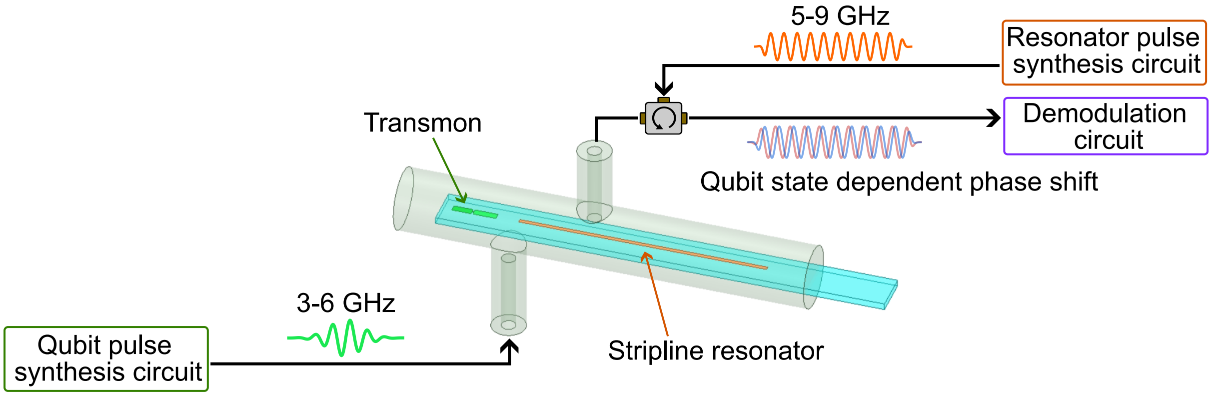

Figure 14: **Example single qubit control and measurement setup.** A transmon qubit and a stripline readout resonator are fabricated on a sapphire chip and housed within an aluminum tube. Qubit control is realized through a dedicated port (drawn at the bottom), which delivers microwave pulses at the qubit frequency, typically in the range of $3-6\,\mathrm{GHz}$. Qubit readout is performed by sending a drive through the resonator port (drawn at the top) and demodulating the changes in phase or amplitude of the reflected output signal. The resonator frequencies are typically around $5-9\,\mathrm{GHz}$.

algorithms on the FPGA. The configuration of the pulse synthesis and demodulation circuit varies according to the different sampling rates of the DACs/ADCs implemented in the setup.

3.2.1 Low-sampling rate devices with analog up/down–conversion circuits

A typical ‘low-sampling rate’ AWG + digitizer setup usually contains DACs with sampling rate of $f_s^{\mathrm{DAC}} \sim 1\,\mathrm{GSa/s}$, and ADCs with sampling rate of $f_s^{\mathrm{ADC}} \sim 500\,\mathrm{MSa/s}$. As shown in Fig. 15, both the AWG and the digitizer have built-in low-pass filters (LPFs) on the DAC and ADC channels to eliminated aliasing effects. These LPFs usually cut at frequencies slightly lower than the Nyquist frequencies ($f_{Nq} = f_s/2$) of the DACs/ADCs, thereby also determining the analog bandwidth of the AWG and the digitizer channels. For example, an $1\,\mathrm{GSa/s}$ AWG usually has an output bandwidth of $\sim 400\,\mathrm{MHz}$, meaning it can output signals of up to $\sim 400\,\mathrm{MHz}$ without distortion. Similarly, a $500\,\mathrm{MSa/s}$ usually has an analog input bandwidth of $\sim 150\,\mathrm{MHz}$. These frequencies are too low to be directly used as qubit control and readout. Thus analog up/down–conversion circuits are needed.

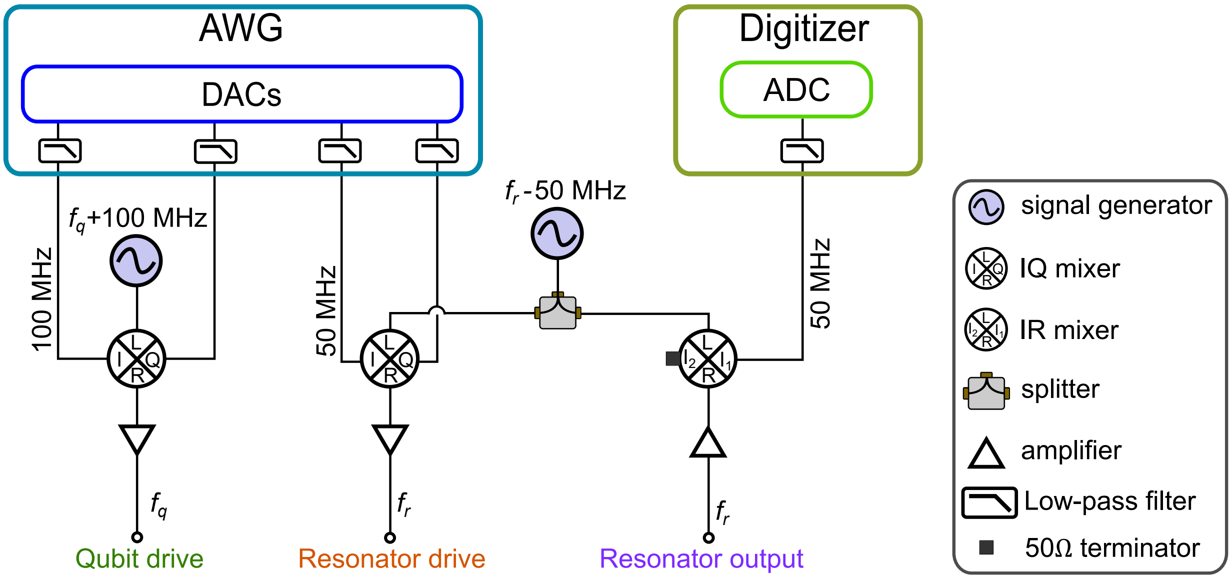

Figure 15: **Example up- and down-conversion circuit for single qubit control and readout.** The AWG signals are up-converted with in-phase/quadrature (IQ) mixers, whose local oscillators (LO) are provided by high frequency signal generators. On the readout side, the output signal from the resonator is down-converted with an image reject (IR) or a regular 3-port mixer, bringing the signal's frequency down to within the bandwidth of the ADC.

Figure 15 shows an example up/down- conversion circuit for single qubit control and readout. The qubit pulse synthesis circuit includes two AWG channels, an in-phase/quadrature (IQ) mixer, and a high-frequency signal generator. For low frequency signals, the AWG generates pulses of desired waveform ($A(t)$) and phase ($\phi_I(t)$) with a carrier frequency of $f_I = 100\,\mathrm{MHz}$, the voltage of the AWG output signal can be written as

$$V_I(t) = A(t)\cos(2\pi f_I t + \phi_I(t)) \tag{104}$$

Thus, each channel of the AWG can produce a fully arbitrary signal within its sampling bandwidth. However, as noted above, when we apply this signal to a 3-port mixer, we inevitably produce two tones separated by $2f_I$ and leakage from the LO port. To suppress these tones we produce pairs of signals (using pairs of channels) to the I and Q ports of the IQ mixer. The local oscillator (LO) of the mixer is provided by the generator, which produces a continuous sinusoidal signal at a frequency $f_L = f_q + 100\,\mathrm{MHz}$, in which f_q is the qubit frequency. The mixer functions as a multiplier of the LO and I/Q signals in the time domain, which adds/subtracts the signal frequencies in the frequency domain. By tuning the relative amplitude and phase, and adding DC offsets on the two AWG channels, the IQ mixer can generate signal on the radio frequency(RF) port with a single frequency that equals to difference of the LO and I/Q frequencies, i.e.

$$f_R = f_L - f_I = (f_q + 100) - 100 = f_q \tag{105}$$

Using this circuit we can generate pulses at the qubit frequency, and control its waveform and phase with the AWG.

The resonator drive setup has similar up-conversion circuit, with the only difference being the I/Q pulse frequencies are 50 MHz, and the LO generator is shared for up- and down- conversion using a splitter, and has a frequency of $f_L = f_r + 50\,\mathrm{MHz}$. This circuit generates arbitrary waveform at the resonator frequency f_r for qubit readout. The output signal from the resonator is mixed with the other LO copy using an image reject(IR) mixer, which creates down-converted signal at 50 MHz without adding noises from image frequency. This 50 MHz signal is then acquired by the ADC for digital demodulation. Note that the phase carried by the original output signal, which contains the qubit state information, is directly transferred to the down-converted signal, thus we can extract the qubit state by demodulating the digital signal from the ADC.

3.2.1.1 System stability discussion

The control and measurement system depicted in Fig. 15 contains several analog components. Due to their analog nature, the parameters of these components are susceptible to changes in environmental conditions, with temperature being the most significant factor. The changes of these parameters, including the amplifier's gain, the signal generator and

AWG's frequencies and phases, can directly affect the fidelity of quantum gates. As it is impractical to make these analog devices stay absolutely stable over time, we need to determine an acceptable degree of stability for each parameter based on the specific requirements of the quantum system and the desired level of fidelity.

In this section, we will conduct a detailed examination of how each parameter affects the fidelity of qubit gates. By establishing these relationships, we can compare the typical performance specifications of the instruments with the state-of-the-art qubit properties including coherence time, gate and readout fidelity, to identify which parameter drift is the primary cause of errors in the system, and prioritize efforts towards stabilizing and controlling that specific parameter to improve overall system performance.

- **Frequency drift.** The frequency of the qubit pulse is controlled by the frequencies of both the generator and the AWG. Both devices have internal phase-locked loops (PLLs) whose references can be provided via a common reference clock. In this configuration, the frequencies of both devices can generally be maintained to have drifts within the range of $\sim 100\,\mathrm{Hz}$ over days. Let us consider a typical qubit $\pi-$pulse time of $50\,\mathrm{ns}$, which corresponds to a Rabi rate of $\sim 10\,\mathrm{MHz}$. Assuming a qubit starts in the $|g\rangle$ state, then the probability of finding the qubit in $|e\rangle$ state after a detuned continuous drive is [92]:

  $$\mathcal{P}_{|e\rangle}(t) = \frac{\Omega^2 \sin^2(\frac{\sqrt{\Omega^2+\delta^2}}{2}t)}{\Omega^2+\delta^2}, \tag{106}$$

  where Ω is the on-resonance Rabi rate and δ is the drive detuning. Then, the probability of finding the qubit in $|e\rangle$ state after a detuned $\pi-$pulse is:

  $$\mathcal{P}_{|e\rangle}(t=\frac{\pi}{\Omega}) = \frac{\Omega^2 \sin^2(\frac{\pi\sqrt{\Omega^2+\delta^2}}{2\Omega})}{\Omega^2+\delta^2} = 1 - \left(\frac{\delta}{\Omega}\right)^2 + \mathcal{O}\left[\left(\frac{\delta}{\Omega}\right)^4\right]. \tag{107}$$

  Using this formula we can estimate the qubit gate error due to an $100\,\mathrm{Hz}$ shift on the pulse frequency: $(100/10^6)^2 = 10^{-8}$, which is far lower than the best state-of-the-art single qubit gate error, thus this absolute frequency drift pushing a pulse off resonance is not a concern.

- **Phase drift.** The phase of the pulse can be affected by many factors in the system, e.g. the phase drifts of the generator and AWG, the temperature change that changes the wave travelling time in the components, or even a wiggling cable. These changes usually happens at a rate of few degrees per minute (in a relatively bad case).

  For controlling a single qubit, the time scale we need to compare with is the coherence time of the qubit, i.e. the classical system should at least stay as stable as the qubit (that is, its phase should be stable for as long as the qubit can hold its state in each experiment sequence). Assuming a 0.1 degree phase drift per second (see example in Fig. 23), the gate error rate due to this pulse phase drift is roughly $0.1/180 * \pi \approx 0.0017/s$, while the gate error due to qubit decoherence is roughly $1 - e^{-t/T_2} \approx t/T_2$, where t is the time of the pulse in a experiment sequence and T_2 is the coherence time of the qubit. Thus, this slow phase drift error will not be a major concern until the qubit coherence time reaches $1/0.0017\,\mathrm{s} \approx 10\,\mathrm{min}$ level.

  Note that in this estimation we only consider the relative phase drift within each experiment sequence, and neglected the absolute phase accumulation on the instruments. This is valid for single qubit experiments, because the phase reference frame is always defined by the first pulse in each sequence, and the phases of the following pulses only need to stay coherent with the first one within the same sequence.

  However, for multi-qubit experiments, the absolute phase accumulation could be different on different drive channels, thereby causing the relative phase between different drive channels to vary at the beginning of each experiment. This relative phase between different channels actually determines the phase of parametrically pumped multi-qubit gates. Therefore, this relative phase change will lead to the tedious requirement of frequent re-calibration. The details of this effect and strategies for mitigating it will be discussed in section 3.3.

- **Amplitude drift.** The amplitude of the synthesized pulse is mainly determined by three factors:

  $$V_{out} = V_I * \sqrt{L_c * G_A}, \tag{108}$$

  in which the V_I is the output voltage from the AWG, L_c is the $I - R$ power conversion loss on the mixer, and G_A is the power gain of the amplifier. Note that the power of the signal generator is not considered here, as a typical mixer is first-order insensitive to a change in LO power provided it is within the mixer's operating range. Among these three factors, the most vulnerable to environmental condition change one is the gain of the amplifier. For example, for a Mini-Circuits ZVE-3W-83+ amplifier that we commonly use on qubit drive channels, we observed a $\sim 2\%$ of change in gain when the temperature changes by 1°C, as shown in Fig. 16a,b [56].

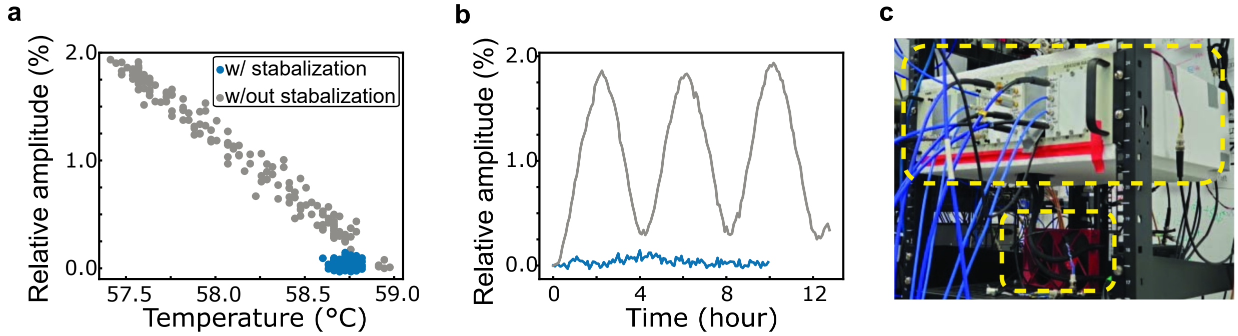

Figure 16: **Amplitude drift of up-converted signal and temperature stabilization setup. a)** Amplitude stability vs temperature before (grey circles and stars) and after stabilization (blue circles and red stars). **b)** Amplitude stability over time without stabilization (grey trace) and with stabilization (blue trace). (c) The up-conversion circuit is enclosed in a optical box (upper yellow dashed box), whose external walls are wrapped with Styrofoam for thermal isolation from the lab environment . A PID-controlled commercial liquid cooling head is mounted on the bottom plate of the box, and the cooing power is regulated by the speed of the fan attached to the cooler's heat sink (lower yellow dashed box).

The amplitude of a single qubit pulse determines the rotation angle of the qubit on the Bloch sphere, i.e. the Rabi rate Ω in Eq. 106 is directly proportional to the drive voltage. Thus, the gate fidelity of an on-resonance but slightly wrong amplitude $\pi-$pulse can be estimated using Eq. 106, by setting $\delta = 0$ and put in a new Rabi rate Ω':

$$\mathcal{P}_{|e\rangle}(t = \frac{\pi}{\Omega}) = \sin^2(\frac{\pi}{2}\frac{\Omega'}{\Omega}) = \sin^2(\frac{\pi}{2}\frac{V'}{V_0}) = 1 - \frac{\pi^2}{4}\left(\frac{\delta_V}{V_0}\right)^2 + \mathcal{O}\left[\left(\frac{\delta_V}{V_0}\right)^4\right], \tag{109}$$

in which V_0 is the correct pulse voltage, V' is the drifted voltage, and $\delta_V = V' - V_0$. From this equation we can see that the single qubit gate error is directly proportional to the power (voltage squared) drift of the pulse with a factor of $\frac{\pi^2}{4} * 2 \approx 5$, which means that 1% of gain change on the amplifier (caused by 1°C temperature change) will decrease the gate fidelity by $\sim 5\%$. Thus, the room air conditioner and airflow, and their associated amplitude drift, can be quite fatal to good qubit controls.

To solve this issue, we must stabilize the temperature of the control circuit. Fig. 16c shows a temperature stabilization box built by Boris Mesits from our lab[56]. This box encloses all the electronics involved in Fig. 15 except for the AWG and digitizer parts. The internal temperature is controlled via a cooling head attached to the outer bottom plate of the box, and the cooling power is regulated by a PID loop running on a Raspberry Pi. Using this setup, we were able to stabilized the overall output voltage drift to within 0.1% range.

3.2.2 High-sampling rate devices with direct digital synthesis (DDS)

The Xilinx RFSoC boards provide DAC and ADC channels with much higher sampling rate. For example, the ZCU-216 board provides maximum DAC sampling rate of 9.85 GSa/s and ADC sampling rate of 2.5 GSa/s. This allows us to use direct digital synthesis (DDS) to generate the high frequency qubit and cavity drive signals without using up conversion circuits (see Sec. 3.2.2.1). For signal demodulation and digitization, there are two options for processing the signal before sending it to the ADC. One approach is to down-convert the signal to fall within the first Nyquist zone of the ADC using a regular 3-port mixer, as shown in Fig. 17a. Alternatively, if the signal's frequency is within the ADC's analog input bandwidth, it can pass through a band-pass filter and be sent directly to the ADC for "aliasing readout", as shown in Fig. 17b. Further details on this technique will be discussed in Sec. 3.2.2.2.

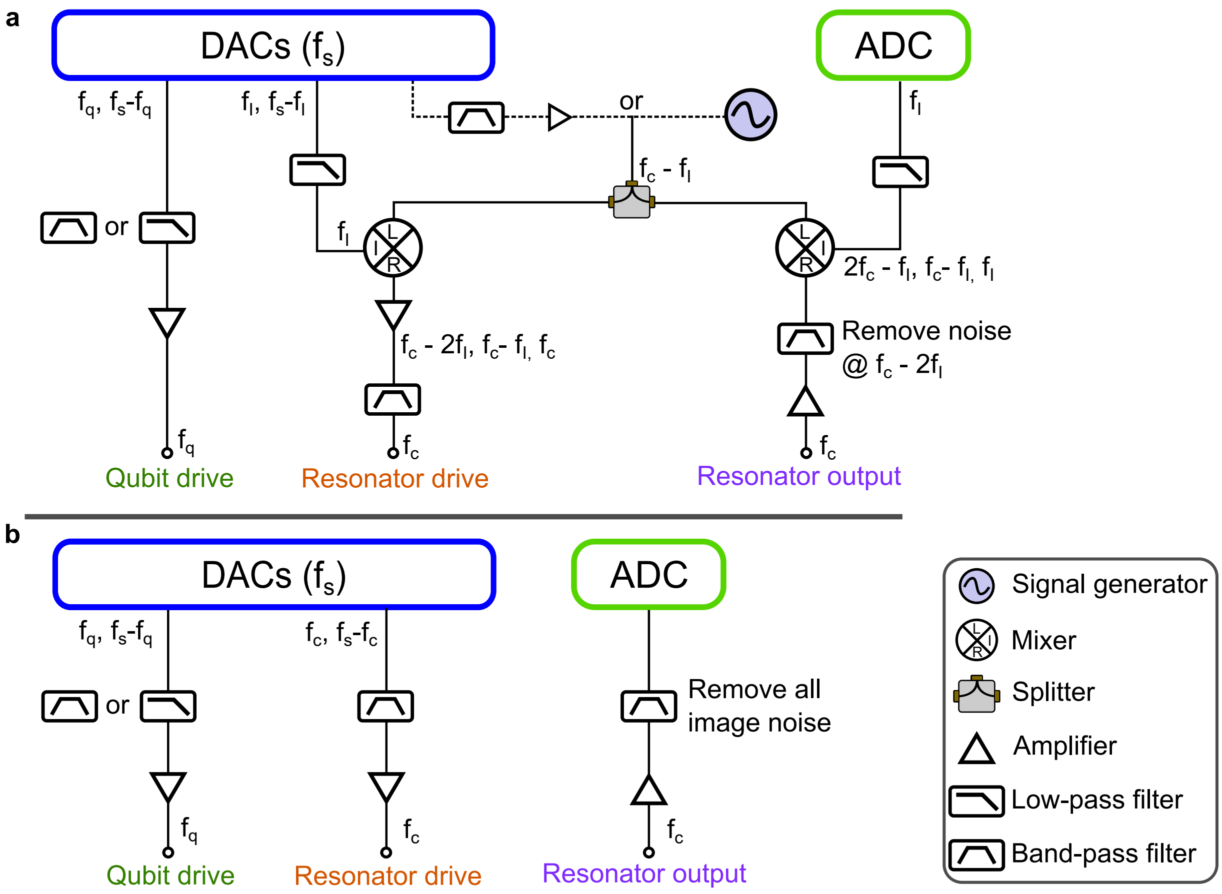

Figure 17: **Example circuits for single qubit control and readout using high-sampling rate DACs and ADCs.** The qubit drive pulses generally have relatively lower frequencies ($\lesssim$ 6 GHz), which can be produced using Direct Digital Synthesis (DDS). The resonator drive can either be also produced with DDS when the resonator frequency falls within the analog bandwidth of the DAC, as in **b)** , or, be synthesized with a up-convertion circuit, as in **a)** . The LO for the up-conversion can be provided either by an external generator or another DAC channel. The same idea applies to the ADC readout side. Note that the circuit in **a)** and **b)** can be mixed and matched, i.e. we can use DDS the for resonator drive but still use another DAC output only as the LO for the output signal down-conversion for the ADC readout.

3.2.2.1 Pulse synthesis in different DAC Nyquist zones

Figure 10a shows how a continuous signal is digitally sampled to discrete-time points. On the output of the DAC, these discrete points need to be converted to continuous analog signals, the conventional technique that DACs use is Zero-Order Hold (ZOH), in which the analog output simply holds the amplitude of samples between clock ticks, as shown in Fig. 18a.

Due to the difference between the ideal smooth signal and the staircase-like signal defined by ZOH, the output signal from the DAC will have frequency components in higher Nyquist Zones, as shown in in Fig. 18b. Also, the Fourier amplitude of the signal in the first Nyquist Zone will not be flat. In fact, the overall envelop of the signal amplitude versus frequency can be described by a sinc function [88, 87]:

$$A_{ZOH}(f) = \frac{\sin(\pi f/f_s)}{\pi f/f_s} = \mathrm{sinc}(f/f_s) \tag{110}$$

In the ZOH mode, the amplitudes of the image tones drop quickly in the 2nd and higher Nyquist Zones. Thus, conventional AWGs usually have built-in LPFs on the DAC channels that cut at around $f_s/2$. This LPF ensures a clean output spectrum, but also limits the output bandwidth of AWG.

To fully exploit the aliasing effect and get stronger signals from the 2nd Nyquist Zone, some DACs can be configured to work in the “Return to Complement” (RTC), or “Mixed” mode. In this mode, the DAC holds the sampled digital value during the first half of each clock period, and change to the inverse (complement) value on the second half of the clock period, as shown in Fig. 18c. The frequency spectrum of this operation mode is shown Fig. 18d, with the amplitude now described by:

$$A_{RTC}(f) = \frac{\sin^2(\pi f/2f_s)}{\pi f/2f_s} \tag{111}$$

Under this mode, the DAC output spectrum now has a much stronger and flatter Fourier amplitude in the 2nd Nyquist Zone. Combining the Mixed mode with band-pass filters (BPFs) that cut off at $f_s/2$ and f_s allows us to generate clean, strong signals in the second Nyquist Zone of the DAC.

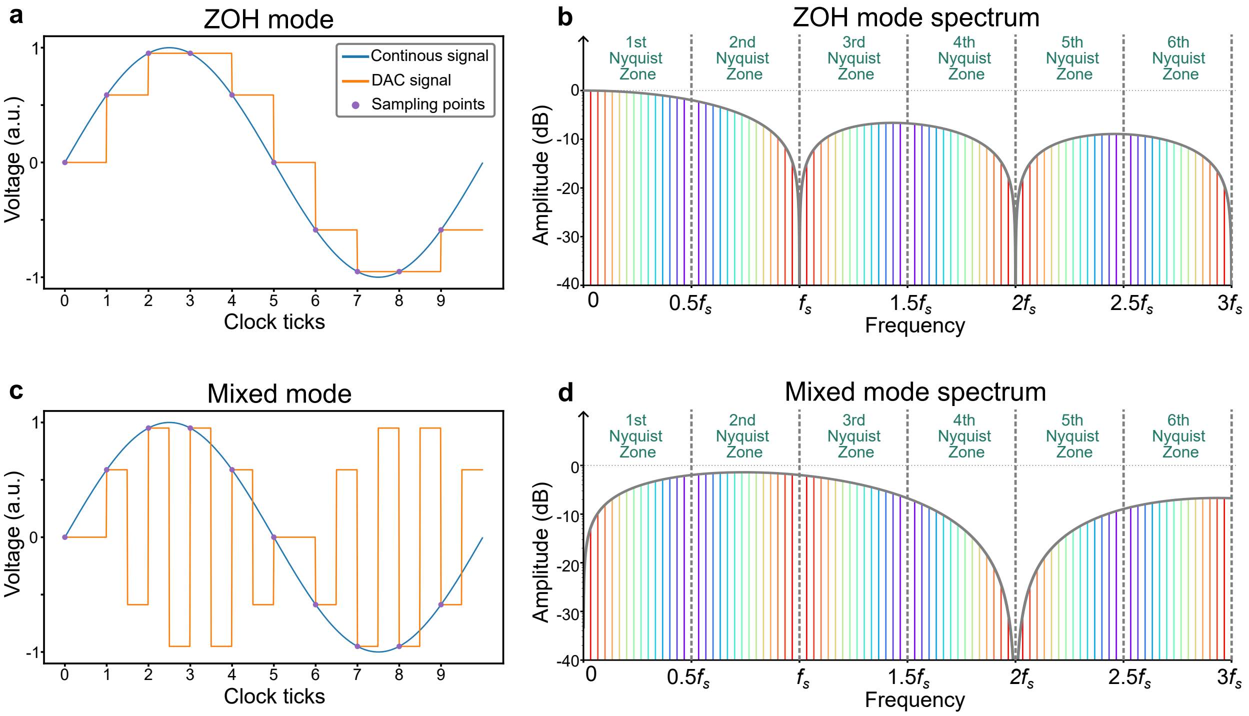

Figure 18: **ZOH and Mixed operation modes of the DAC. a)** DAC output voltage in the Zero-Order Hold (ZOH) mode. The voltage is held constant at the sampling point value over the sampling period. **b)** Frequency spectrum of the DAC output in the ZOH mode. The vertical lines of the same color corresponds to the Fourier amplitudes of the same signal in different Nyquist Zones, while different colors corresponds to different signals. The overall envelop of the spectrum has the shape of a 'sinc' function. **c)** DAC output voltage in the Mixed (or Return To Complement) mode. The voltage is held at the sampled value for the first half of each sampling period and changed to the inverse (complement) value for the second half of the sampling period. **d)** Frequency spectrum of the DAC output in the Mixed mode. The Fourier components in the 2nd Nyquist Zone have a much higher amplitude then in the ZOH mode, and is flatter versus different frequency.

The Xilinx RFSoC boards offer the capability to change the DAC operation mode between ZOH and Mixed via software APIs, and the DAC channels on these boards do not have built-in filters. This setup provide us with significant flexibility in choosing the output spectrum based on our desired frequencies. As illustrated in Fig. 17, for instance, assuming a DAC sampling rate of $f_s = 9.85\,\mathrm{GHz}$, when the qubit frequency is below 4.5 GHz, we can set the DAC to ZOH mode and use a LPF that cuts at around 4.9 GHz to generate qubit drive pulses with a clean spectrum; or when the qubit frequency is above $\sim 5.5\,\mathrm{GHz}$, the DAC can be set to Mixed mode and combined with a BPF to generate the desired signal. Note that the sampling rate of the DAC can also be changed by re-programming the FPGA firmware. Therefore, when the mode frequency falls in the proximity of $f_s/2 = 4.9\,\mathrm{GHz}$, resulting in image tones that are challenging to filter, we can re-program the FPGA to move down f_s, thereby moving the image frequencies further away from the desired signal and make them easier to filter.

To operate at even higher Nyquist Zones, additional DAC operation modes are theoretically available. However, their practical application is often constrained by the analog bandwidth limitations of the DACs. Therefore, for generating signals above the DAC sampling rate, such as a high-frequency resonator drive or parametric pump tone, up-conversion is still required. An example circuit is shown in Fig. 17a on the resonator drive line. It is worth noting that, in comparison to the scheme shown in Figure 15, the IQ mixers can be replaced with regular 3-port mixers in this scenario. This is because the intermediate frequency (IF) signals from the DAC can now be much higher, which makes it more practical to remove the image tones using filters. Additionally, the LO for the mixers can be provided using combinations of extra high frequency DAC channels with amplifiers, which enables easier phase locking than using an external signal generator.

3.2.2.2 Aliasing readout in higher ADC Nyquist zones

The aliasing effect in an ADC can be understood as a down-conversion mixing process. As shown in Figure 10, after ADC sampling, signals from higher Nyquist Zones (orange and green curves) will appear identical to how their images in the first Nyquist Zone (the blue curve) was sampled (the purple dots). This frequency folding effect is typically considered undesirable when our goal is to differentiate signals of different frequencies. However, in the qubit readout process, we know exactly the frequency of our signal - the readout resonator frequency, and all the information we need is encoded in the phase and/or amplitude of that signal. Note that in a down-conversion process, the phase and amplitude of the input signal will be directly transferred to the down-converted signal. Thus, we can leverage this aliasing effect to perform qubit readout with resonator output signals at frequencies much higher than the Nyquist frequency of the ADC.

Implementing this aliasing readout technique in firmware or software is delightfully straightforward. All we need to do is to perform the digital demodulation with a reference frequency that equals to the input signal's image frequency in the first Nyquist Zone. For a input signal with frequency f, this image frequency can be found by first identifying the Nyquist Zone in which the signal falls using:

$$n = \left\lceil f/\frac{f_s}{2} \right\rceil, \tag{112}$$

then the image frequency in the first Nyquist Zone can be calculated with:

$$f_i = \begin{cases} \frac{n}{2} f_s - f, & \text{if } n \text{ is even} \\ -\frac{n-1}{2} f_s + f, & \text{if } n \text{ is odd} \end{cases} \tag{113}$$

Note that when the Nyquist Zone number n is even , the down-converted signal is actually at $-f_i$. Thus the phase we extract from demodulation will actually be flipped (conjugated).

Practical limitations. The practical limitation of the highest frequency signal we can capture using this technique is determined by the analog input bandwidth of the ADC. In section 3.2.1 I mentioned that a conventional digitizer device usually has an input bandwidth slightly smaller than the Nyquist frequency ($f_s/2$) of the ADC, due to the presence of the built-in LPF. However, it is important to differentiate between the LPF-limited bandwidth of a digitizer and the actual analog input bandwidth of a bare ADC, which, in certain cases, can actually be few times higher than the sampling rate f_s. For example, the Xilinx ZU49DR Zynq RFSoC used on the ZCU216 board has maximum ADC sampling rate of $f_s = 2.5\,\text{GHz}$, while its analog input bandwidth is $6\,\text{GHz}$, meaning that we can use the aliasing readout technique to demodulate signals of up to $\sim 6\,\text{GHz}$ without significant signal degradation. Here, the analog input bandwidth is defined as: when the input amplitude response drops $3\,\text{dB}$ relative to a low-frequency reference point of 100 MHz. This analog input bandwidth limitation exists because practical ADCs do not operate as instantaneous samplers. Instead, they employ a “sample-and-hold” circuitry that effectively captures the averaged input voltage over a very short period of time. Thus, when the input frequency gets too high, the ADC will not be able to capture enough voltage from the input signal.

Interestingly, when a signal is well-filtered and its frequency is close to the ADC’s analog input bandwidth, the signal-to-noise ratio (SNR) may not necessarily degrade significantly even if the signal amplitude is attenuated. This is because both the signal and the noise are attenuated by the same factor, and the input noise temperature is generally much higher than the noise introduced by the ADC itself. However, when the signal frequency is significantly higher than the analog bandwidth that the signal got suppressed to a level comparable to the ADC added noise, down conversion circuit will be needed again to bring the signal back within the ADC’s effective range.

Filtering considerations. Another catch of this aliasing readout technique is that we must carefully filter out the noise at the image frequencies. As illustrated in Fig. 19a, the aliasing effect will also fold the noise from other Nyquist Zones to the first Nyquist Zone and add them on top of our down-converted signal. Thus, to avoid decreasing the signal-to-noise-ratio(SNR) of our qubit measurement, we need to remove these images using an analog band-pass filter(BPF) before sending the signal to the ADC. The original signal needs to stay within the pass-band of the filter, while all the image frequency components in other Nyquist Zones must be filtered out, as shown in Fig. 19b.

An exception to this behavior occurs when a narrow-band low-noise amplifier, such as a Josephson parametric amplifier (JPA) [93, 23], is used on the output line. In this case, in stead of having a white noise spectrum as depicted in yellow in Fig. 19, the noise at the signal frequency becomes significantly higher compared to the noise at other frequencies. As a result, extra filtering for removing the image noise is no longer necessary.

3.2.2.3 System stability discussion

The analog devices used in Fig. 17a are similar to the ones used in Fig. 15. Thus the device parameters are susceptible to the same environmental condition changes and internal

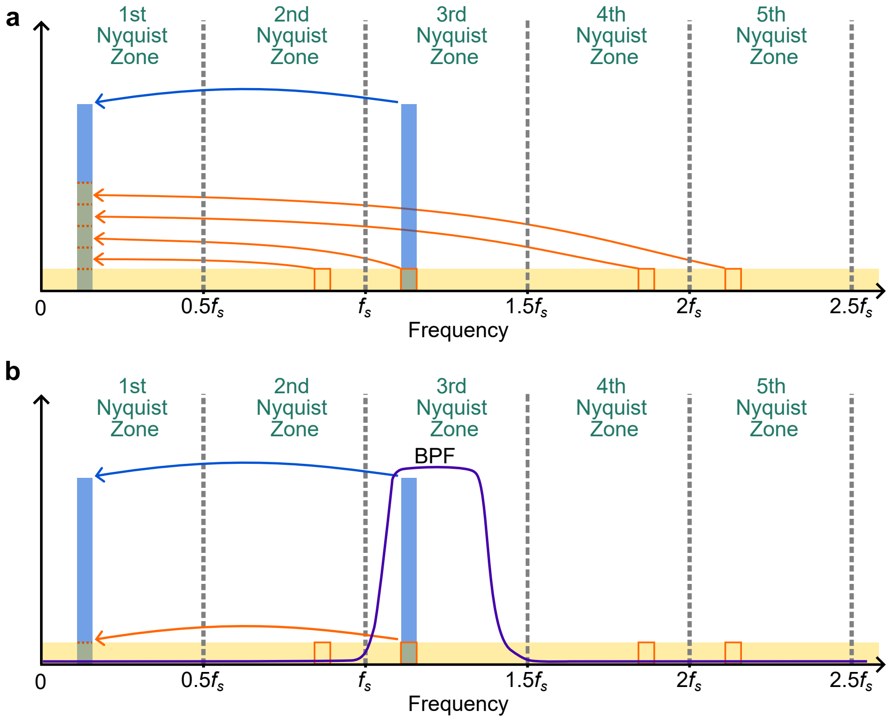

Figure 19: **Effect of added noise from other Nyquist Zones in ADC aliasing readout.** Here we assume a white noise background colored in yellow, and a desired signal in the 3rd Nyquist Zone (blue bar). **a)** The image noise from other Nyquist Zones is added onto the down-converted signal degrading its SNR provided these zones are within the analog bandwidth of the digitizer. **b)** These images can be effectively removed with an appropriate band-pass filter.

drifts. However, in comparison to the up-conversion pulse synthesis scheme, we do have an important additional advantage: the ability to maintain a highly stable relative phase between different drive channels and the digital demodulation reference. This advantage stems from the utilization of high-frequency DDS (direct digital synthesis) technique, which enables us to digitally define all microwave signals on the same board. As a result, we can easily reset the phase of each signal during any given clock cycle. This relative phase stability is essential for parametrically pumped multi-qubit gates, which will be discussed in the next section and later in sec 5.2.6. Furthermore, not having to worry about synchronizing the phase between different microwave sources significantly simplifies the experimental setup.

3.3 Phase coherent pulse generation for parametric quantum control

3.3.1 Formalism for analyzing drive added phase

Before we start the discussion on how the phase of each drive channel affect the state of a quantum system, let us first establish a consensus regarding how the phase of each drive channel itself evolves throughout an experiment.

Premise: As described in Eq. 114, the phase of each drive channel has three components. At the beginning of each experiment, each drive channel 'x' has an initial phase Φ_x, that may or may not be predictable/controllable. Next, over the course of the experiment, the drive channel's phase will have a continuously evolving component $\phi_{x,c}(t) = 2\pi f_x t$, where f_x is the drive frequency, and t is time relative to the start of the experiment. Additionally, for each specific pulse (i) in the sequence, an extra phase, $\phi_{x,i}$ can be added on top of this continuously evolving phase. This extra phase $\phi_{x,i}$ is fully controllable via the AWG or DAC. Therefore: the phase of pulse i at time t_i can be written as:

$$\phi_x(t_i) = 2\pi f_x t_i + \Phi_x + \phi_{x,i} \tag{114}$$

Here, to facilitate our later discussion, we refer to each drive channel 'x' based on its associated frequency f_x, instead of the physical hardware that generates the pulses. Therefore, the frequency of each channel can be considered as a predetermined, constant value[1].

The above premise is generally true for both up-converted and direct digital synthesised drive channels. Next, to examine the effect of drive added phase, it is helpful to consider the pulse induced Hamiltonian in the interaction picture, as this picture removes the system's "free evolution" under the qubit's static Hamiltonian and allows us to focus on the effect of the external drive.

Moving to the interaction picture is basically equivalent to performing a rotating frame transformation at the static mode frequencies in the system. For example, for a single

---

[1] In practice, f_x is susceptible to slow drift, and the impact of this drift will be discussed in section 3.3.2

qubit under an external drive that is applied at time t_i, the original (Schrödinger picture) Hamiltonian can be written as:

$$\hat{\mathcal{H}}_{qdrive,S}/\hbar = \frac{\omega_q}{2}\hat{\sigma}_z + \varepsilon\left(\hat{\sigma}_- e^{i(\omega_d(t-t_i)+\phi_d(t_i))} + \hat{\sigma}_+ e^{-i(\omega_d(t-t_i)+\phi_d(t_i))}\right), \tag{115}$$

in which ω_q is the angular frequency of the qubit's $|g\rangle \leftrightarrow |e\rangle$ transition, ε is the effective drive strength, $\omega_d = 2\pi f_d$ is the angular frequency of the drive, and $\phi_d(t_i)$ is the phase of the drive applied at time t_i, which follows the form specified in Eq. 114. The Pauli-Z operator is represented as $\hat{\sigma}_z$, while the lowering and raising operators are denoted as $\hat{\sigma}_-$ and $\hat{\sigma}_+$ respectively. After the rotating frame transformation at frequency ω_q, the operators will be transferred as:

$$\hat{\sigma}_- \rightarrow \hat{\sigma}_- e^{-i\omega_q t}; \quad \hat{\sigma}_+ \rightarrow \hat{\sigma}_+ e^{i\omega_q t}, \tag{116}$$

and the qubit's static Hamiltonian term $\frac{\omega_q}{2}\hat{\sigma}_z$ will be removed. Assuming the drive is applied on-resonance with the qubit frequency, i.e. $\omega_d = \omega_q$, then the Hamiltonian in the interaction picture can be written as:

$$\begin{aligned}\hat{\mathcal{H}}_{qdrive,I}/\hbar &= \varepsilon\left(\hat{\sigma}_- e^{i(-\omega_d t_i+\phi_d(t_i))} + \hat{\sigma}_+ e^{-i(-\omega_d t_i+\phi_d(t_i))}\right)\\ &= \varepsilon\left(\hat{\sigma}_- e^{i(\Phi_d+\phi_{d,i})} + \hat{\sigma}_+ e^{-i(\Phi_d+\phi_{d,i})}\right)\end{aligned} \tag{117}$$

Equation 117 shows that, in the interaction picture, the continuous evolving phase in the drive signal is eliminated. As a result, our attention can be directed towards the impact of the two phase offset components, namely Φ_d and $\phi_{d,i}$. Based on Eq. 117 we can write down the gate operator for a single qubit on-resonance drive applied for duration τ:

$$\hat{U}_{qdrive,I}(\tau) = \exp\left(-i\frac{\hat{\mathcal{H}}_{qdrive,I}}{\hbar}\tau\right) = \begin{bmatrix}\cos(\varepsilon\tau) & -i\sin(\varepsilon\tau)e^{-i(\Phi_d+\phi_{d,i})}\\ -i\sin(\varepsilon\tau)e^{i(\Phi_d+\phi_{d,i})} & \cos(\varepsilon\tau)\end{bmatrix} \tag{118}$$

According to the discussion we had in Sec. 3.2.1.1, in each pulse sequence, the phase drift of the drive channel is negligible, as each pulse sequence is generally much shorter than the timescale on which phase drift typically occurs. Thus, although the value of Φ_d may be different for each experiment run, we can assume it is a constant over the course of one experiment. This allows us to perform another unitary transformation that removes the constant phase offset in the gate operator.

$$\hat{U}_{\Phi_{shift}}(\Phi) = \begin{bmatrix} 1 & 0 \\ 0 & e^{-i\Phi} \end{bmatrix} \tag{119}$$

By applying this phase shift transformation with $\Phi = \Phi_d$, we have the final effective operator for a single qubit on-resonance drive, with amplitude ε, duration τ and phase $\phi_{d,i}$.

$$\begin{aligned} \hat{U}^{eff}_{qdrive,I}(\tau) &= \hat{U}_{\Phi_{off}}(\Phi_d)\hat{U}_{qdrive,I}(\tau)\hat{U}^{\dagger}_{\Phi_{off}}(\Phi_d) \\ &= \begin{bmatrix} \cos(\varepsilon\tau) & -i\sin(\varepsilon\tau)e^{-i(\phi_{d,i})} \\ -i\sin(\varepsilon\tau)e^{i(\phi_{d,i})} & \cos(\varepsilon\tau) \end{bmatrix} \end{aligned} \tag{120}$$

Equation 120 shows that, in a single qubit experiment, the initial phase of the drive channel has no observable impact on the applied gate. As a result, when considering each individual single qubit gate within the pulse sequence, we can simplify our analysis by assuming that the gate's phase is solely determined by the phase we introduce using the DAC, denoted as $\phi_{d,i}$. In this case, control over the initial phase of the drive channel, Φ_d, is not necessary.

However, this behavior will change for multi-qubit parametric gates. In the subsequent analysis, we will extend our interaction picture Hamiltonian analysis to parametrically pumped two-qubit gates, and will specifically investigate the impact of the initial phase of each drive channel on the quantum system's state. To guide our analysis, we will follow the steps outlined below:

1. In the interaction picture, write down the effective system Hamiltonian under each drive signal, with the phase of the drive included. Derive the phase-dependent gate operator induced by each pulse.

2. Sequentially apply the gate operators in the pulse sequence to the initial qubit state vector to obtain the final qubit state vector.

3. Examine how the initial phase Φ_x of each channel affects the final state.

4. Analyze the source of the Φ_x. For instance, in an up-converted control circuit, the phase could be the sum of the LO and IF phase components, $\Phi_x = \Phi_x^L + \Phi_x^I$. Examine how effectively we can control/stabilize the phase contributed by each part.

3.3.2 Phase coherent requirements for parametric multi-qubit gates

As an illustrative example, let us consider a 3-wave-mixing iSWAP gate between two qubits A and B. In the interaction picture of this two-qubit system, the Hamiltonian that activates the iSWAP interaction can be written as (see details in Sec. 2.1).

$$\hat{\mathcal{H}}_{i\mathrm{SWAP},I}/\hbar = g\left(\hat{\sigma}_{a,+}\hat{\sigma}_{b,-}e^{i\phi_p} + \hat{\sigma}_{a,-}\hat{\sigma}_{b,+}e^{-i\phi_p}\right), \tag{121}$$

in which g is the effective exchange interaction coefficient, and ϕ_p is the phase of the pump signal. The lowering and raising operators of qubit A/B are denoted as $\hat{\sigma}_{a/b,-}$ and $\hat{\sigma}_{a/b,+}$, respectively.

In a charged-pumped 3-wave-mixing process, the pump signal is typically applied at a frequency $\omega_p = 2\pi f_p = \omega_b - \omega_a + \delta$ (assuming $\omega_b > \omega_a$), where ω_a and ω_b represent the static angular frequencies of qubits A and B, respectively, and δ denotes the pump detuning. The pump detuning δ is typically necessary for compensating for the AC-Stark shift effect that arises during the parametric pump process [36, 52]. In Equation 121, the δ detuning does not appear explicitly in the exponent as $i\delta t$, because we have transformed to a new frame that rotates at the Stark-shifted frequencies of qubits A and B when the pulse is active. However, the pump phase in this Hamiltonian, denoted as ϕ_p, does depend on the timing of the pulse application within the experiment sequence. This is because, before the pulse is turned on, the pump channel has been accumulating the continuously involving phase $\phi_{p,c} = \omega_p t_i$, but the interaction picture transformation that we applied before this pulse is turned on only subtracts the phase $(\omega_b - \omega_a)t_i$ from it. Hence, the pump phase ϕ_p for a pulse applied at time t_i should be written as:

$$\begin{aligned}\phi_p(t_i) &= \omega_p t + \Phi_p + \phi_{p,i} - (\omega_b - \omega_a)t \\ &= \delta t_i + \Phi_p + \phi_{p,i}\end{aligned} \tag{122}$$

Using the Hamiltonian in Eq.121, we can derive the gate operator for a full iSWAP operation in the interaction picture of the two qubit system:

$$\hat{U}_{i\mathrm{SWAP},I}(t_i) = \exp\left(-i\frac{\hat{\mathcal{H}}_{i\mathrm{SWAP},I}}{\hbar}\frac{\pi}{2g}\right) = \begin{bmatrix} 1 & 0 & 0 & 0 \\ 0 & 0 & -ie^{-i(\delta t_i+\Phi_p+\phi_{p,i})} & 0 \\ 0 & -ie^{i(\delta t_i+\Phi_p+\phi_{p,i})} & 0 & 0 \\ 0 & 0 & 0 & 1 \end{bmatrix} \tag{123}$$

Here we neglected the phase accumulated during the pump, as it is a constant value that can be calibrated and fixed via single qubit virtual-Z gates [94, 95, 56]. Also, since δ and t_i are both predetermined constant values, the δt_i phase component can also be compensated via virtual-Z gates after the iSWAP gate. Therefore, the only remaining potentially uncontrollable phase in the iSWAP gate operator is the pump's initial phase Φ_p. Our question is: does the initial phase Φ_p matter, or is it essentially 'invisible' like in the one-qubit experiment case discussed in the previous section?

To answer this question, let us try to follow a similar analysis to the single qubit case. Since a typical multi-qubit experiment generally involves both single qubit control pulses and two qubit control pulses, we can first remove the initial phase components for the single qubit drive channels by applying the transformation:

$$\begin{aligned} \hat{U}_{\Phi_{shift}}(\Phi_a, \Phi_b) &= \hat{U}_{\Phi_{shift}}(\Phi_a) \otimes \hat{U}_{\Phi_{shift}}(\Phi_b) \\ &= \begin{bmatrix} 0 & 0 & 0 & 0 \\ 0 & e^{-i\Phi_b} & 0 & 0 \\ 0 & 0 & e^{-i\Phi_a} & 0 \\ 0 & 0 & 0 & e^{-i(\Phi_b+\Phi_b)} \end{bmatrix} \end{aligned} \tag{124}$$

After this transformation, the iSWAP operator becomes:

$$\begin{aligned} \hat{U}^{eff}_{i\mathrm{SWAP},I}(t_i) &= \hat{U}_{\Phi_{shift}}(\Phi_a, \Phi_b)\hat{U}_{i\mathrm{SWAP},I}(t_i)\hat{U}^{\dagger}_{\Phi_{shift}}(\Phi_a, \Phi_b) \\ &= \begin{bmatrix} 1 & 0 & 0 & 0 \\ 0 & 0 & -ie^{-i(\delta t_i+\Phi'_p+\phi_{p,i})} & 0 \\ 0 & -ie^{i(\delta t_i+\Phi'_p+\phi_{p,i})} & 0 & 0 \\ 0 & 0 & 0 & 1 \end{bmatrix}, \end{aligned} \tag{125}$$

in which $\Phi_p' = \Phi_p - (\Phi_b - \Phi_a)$. Equation 125 shows that, although the phase shift transformation can eliminate the initial phase components in the single qubit drive pulses, it effectively transfers these qubit drive channels' initial phases to the pump channel. In fact, there is no transformation that can completely remove all initial phase components in both the two single qubit drive channels and the parametric pump channel simultaneously. Therefore, in a two qubit experiment, to guarantee that the applied pulses always correspond to the same gate operators in different experiment runs, we must ensure that the this effective initial phase Φ_p' remains constant (or be predictable) for each experiment run, i.e.:

$$(\Phi_p - (\Phi_b - \Phi_a))|_{t=T_n} = \text{const} \tag{126}$$

in which T_n is the starting time of the n_{th} experiment run.

Equation 126 describes the general phase coherence requirement for two-qubit iSWAP family gates, and provides the answer to our question: It is the effective initial phase $\Phi_p' = \Phi_p - (\Phi_b - \Phi_a)$ that determines how the observable will be affected. When Φ_p' is not controllable or predictable, different experiment runs will create qubit final states with different phases. As a result, after repeating the same DAC pulse sequence numerous times and taking the averaged result, the phase information of the final state will be averaged out and the system will appear to be completely decohered. As an illustrative example of this effect, let's consider a simple experiment sequence that involves all three drive channels in a two-qubit system, as depicted in Fig.20.

The pulse sequence starts from both qubits in their $|g\rangle$ states. First, a $\pi/2-$pulse is applied on qubit A, then, a full iSWAP gate is applied between the two qubits. After that, another $\pi/2-$pulse is applied on qubit B, and finally the qubit B is measured along the Z axis. In this simple pulse sequence, we assume the controllable parts of each pulse's phase $\phi_{a,i}$, $\phi_{p,i}$ and $\phi_{b,i}$ have been tuned such that the only phase components left are the initial

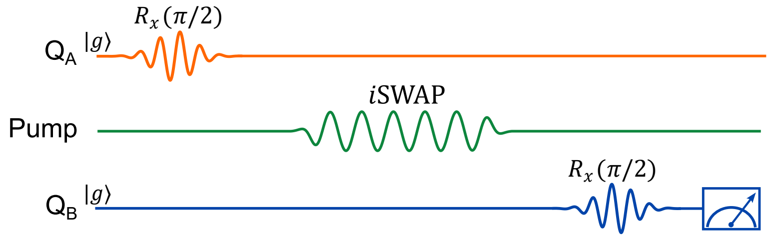

Figure 20: **Example two-qubit pulse sequence with iSWAP gate.** The qubit Q_A is first prepared to the $|-y\rangle$ state using a $\pi/2-$pulse along the x direction, then an iSWAP gate is performed between the two qubits. Finally, the qubit Q_B is measured along the y direction by applying a $\pi/2$ rotation around the x axis followed by a measurement in the z direction.

phase parts: Φ_a, Φ_b and Φ_p. So we have the overall operator of the pulse sequence.

$$\begin{aligned}
\hat{U}^{eff}_{tot} &= (\mathbb{I} \otimes \hat{U}^{eff}_{\pi/2,B})\ \hat{U}^{eff}_{i\text{SWAP}}\ (\hat{U}^{eff}_{\pi/2,A} \otimes \mathbb{I}) \\
&= \begin{bmatrix} \frac{1}{\sqrt{2}} & \frac{-i}{\sqrt{2}} & 0 & 0 \\ \frac{-i}{\sqrt{2}} & \frac{1}{\sqrt{2}} & 0 & 0 \\ 0 & 0 & \frac{1}{\sqrt{2}} & \frac{-i}{\sqrt{2}} \\ 0 & 0 & \frac{-i}{\sqrt{2}} & \frac{1}{\sqrt{2}} \end{bmatrix} \begin{bmatrix} 1 & 0 & 0 & 0 \\ 0 & 0 & -ie^{-i\Phi'_p} & 0 \\ 0 & -ie^{i\Phi'_p} & 0 & 0 \\ 0 & 0 & 0 & 1 \end{bmatrix} \begin{bmatrix} \frac{1}{\sqrt{2}} & 0 & \frac{-i}{\sqrt{2}} & 0 \\ 0 & \frac{1}{\sqrt{2}} & 0 & \frac{-i}{\sqrt{2}} \\ \frac{-i}{\sqrt{2}} & 0 & \frac{1}{\sqrt{2}} & 0 \\ 0 & \frac{-i}{\sqrt{2}} & 0 & \frac{1}{\sqrt{2}} \end{bmatrix} \qquad (127) \\
&= \frac{1}{2} \begin{bmatrix} 1 + ie^{-i\Phi'_p} & 0 & -i - e^{-i\Phi'_p} & 0 \\ -i - e^{-i\Phi'_p} & 0 & -1 - ie^{-i\Phi'_p} & 0 \\ 0 & -1 - ie^{i\Phi'_p} & 0 & -i - e^{i\Phi'_p} \\ 0 & -i - e^{i\Phi'_p} & 0 & 1 + ie^{i\Phi'_p} \end{bmatrix},
\end{aligned}$$

which gives us the final state of the two-qubit system:

$$|\psi\rangle_f = \hat{U}^{eff}_{tot}\, |g\rangle \otimes |g\rangle = \frac{1}{2} \begin{bmatrix} 1 + ie^{-i\Phi'_p} \\ -i - e^{-i\Phi'_p} \\ 0 \\ 0 \end{bmatrix}, \qquad (128)$$

and the final Z measurement result on qubit B will result:

$$\langle z \rangle_B = \langle \psi | \, \mathbb{I} \otimes \sigma_z \, | \psi \rangle_f = \sin\bigl(\Phi'_p\bigr) = \sin(\Phi_p - (\Phi_b - \Phi_a)) \tag{129}$$

Therefore, the final result we measured will depend on the effective initial phase Φ'_p. If Φ'_p undergoes unpredictable changes at the beginning each experiment run, the averaged result after numerous experiment repetitions will converge towards zero. To ensure that we can obtain a valid averaged result, we must either: a) maintain a constant value for Φ'_p across different experiment runs, or b) be able to predict the value of Φ'_p for each experiment run so that we can adjust the controllable parts of the pulse phases ($\phi_{a,i}$, $\phi_{b,i}$ and $\phi_{p,i}$) to compensate for that change. Next, I will discuss how these approaches can be realized using the up-converted and DDS pulse synthesis circuits.

3.3.3 Realizing phase coherence with up-converted signal

Figure 21a shows a general up-conversion pulse synthesis setup for generating control signals for a two-qubit system. The two qubit drives and the parametric pump channels each has a dedicated up-conversion circuit for generating the control pulses. Some of the filter and amplifier components are omitted here.

For a signal generated with up-converted circuit, the initial Φ_x phase of a drive channel 'x' is contributed by two components:

$$\Phi_x = \Phi_x^I + \Phi_x^L, \tag{130}$$

in which Φ_x^I is the phase contributed by the IF channel(s) of the up-conversion circuit, which is fully controllable by the DAC, while Φ_x^L comes from the LO channel, which is usually fed by a continuous signal generator. Therefore, the core part of the uncontrollable phase comes from the signal generators of each up-conversion circuit. At the beginning time of the n^{th} experiment run, $t = T_n$, the phase of the generator channel 'x' can be written as:

$$\Phi_x^L = \int_{-\infty}^{T_n} 2\pi f_x^L dt \tag{131}$$

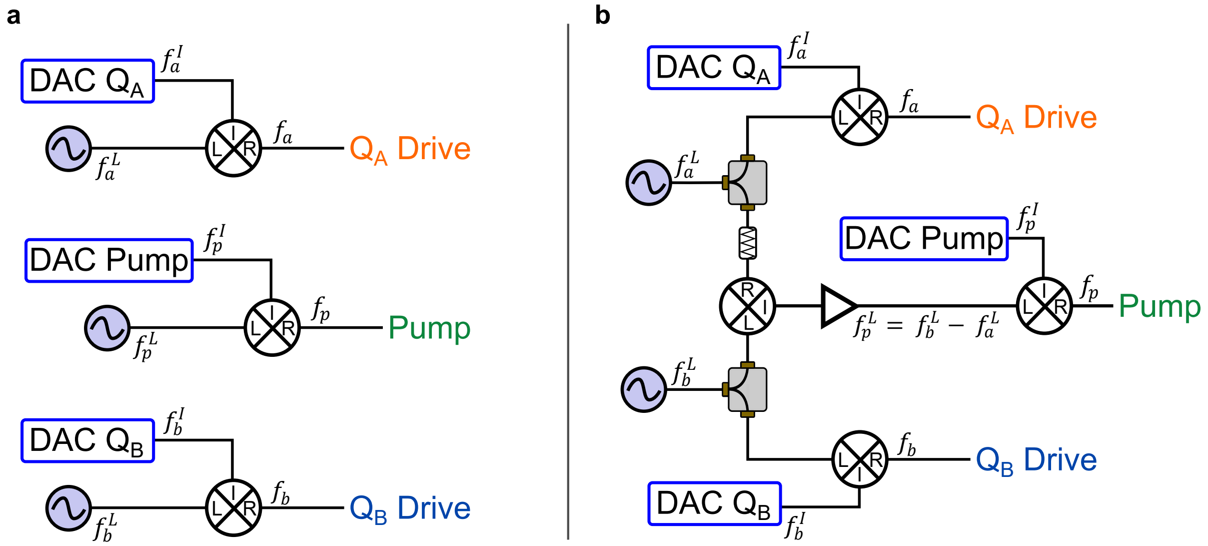

Figure 21: **Two-qubit control pulse generation with up-conversion circuits. a)** Each drive channel uses a dedicated set of signal generator, mixer and DAC. **b)** The Local Oscillator (LO) for the pump channel is provided by the mix product derived from the copies of the two qubits' generators. This configuration guarantees that $f_p^L - f_b^L + f_a^L = 0$, even when f_b^L and f_a^L are subject to random drifts.

Thus, the phase coherence condition in Eq. 126 can be re-written as:

$$\int_{-\infty}^{T_n} 2\pi(f_p^L - f_b^L + f_a^L)dt = \text{const} \tag{132}$$

When the timing of each repetition of the experiment sequence is controlled by the FPGA, the value of each T_n is a well-defined value. In this case, the change of the effective initial phase Φ_p' for each experiment run is actually predictable, so we can compensate for this phase change by adjusting the DAC-controlled phase components. However, adopting this approach significantly complicates the process of pulse programming. Moreover, it will not work when the experiment repetition is controlled by software, or when the signal generators are subject to frequency drifts over time. Therefore, this approach is not generally implemented. In fact, a much simpler solution would be to choose the LO channel frequencies such that

$$f_p^L - f_b^L + f_a^L = 0, \tag{133}$$

so that the phase accumulations due to the continuous evolving generators are completely removed. Note that these frequencies also need to satisfy the condition

$$\begin{cases} f_p^L + f_p^I = f_b - f_a + \delta \\ f_a^L + f_a^I = f_a \\ f_b^L + f_b^I = f_b \end{cases}, \tag{134}$$

in which f_b, f_a, and δ are determined by the physical system and the specific gate speed required (as δ is typically proportional to the pump power). Given that the DACs usually have analog bandwidths of at least few hundred megahertz, it is actually not hard to find f_x^L and f_x^I combinations that satisfy both Eq. 133 and Eq. 134.

The actual challenge of implementing this approach is to ensure that Eq. 133 is always satisfied, even when the LO channels experience slow frequency drifts. These frequency drifts will also break the condition in Eq. 134. However, this corresponds to driving the quantum process slightly off-resonance, and the resulting error is typically considered negligible (see discussion in Sec. 3.2.1.1). In contrast, when the condition in Eq. 133 is not satisfied, it will result in untraceable accumulation of the initial phase on each experiment run, which makes long-term averaging of the same experiment difficult and necessitates tedious frequent re-calibration of the pulse phases.

One way to solve this problem is to build the up-conversion circuit as in Fig. 21b. Instead of using a separate generator to provide the LO for the pump signal, we use another analog mixer that mixes the copies of the two qubit drive channels' LO frequencies. This mixing process creates a down-converted frequency that always equals to $f_b - f_a$, In this case, even if f_a^L and f_b^L are still subject to frequency drifts, the condition in Eq. 133 is guaranteed to be satisfied (assuming no mixer induced phase drift).

The circuit in Fig. 21b is basically sufficient for generating stable, phase coherent control signals for a two-qubit system. However, for a larger-scale system with n qubits, this setup is not quite practical, as we will need to mix the LO signals of the qubit drive channels for $\binom{n}{2} = n(n-1)/2$ times, which greatly increases the number of microwave components required and complicates the experiment setup.

3.3.4 Realizing phase coherence with DDS signal

The direct-digital-synthesis pulse generation circuit offers a much more straightforward approach to fulfill the phase coherence requirement expressed in Eq. 126. As shown in Fig. 22, here, the phase of each drive channel is completely controlled by the DAC, so we have full control over each channel's initial phase Φ_x with precise timing. To maintain phase coherence between different experiment runs, all we have to do is to reset the phase of all the drive channels simultaneously at the beginning of each experiment. Although the absolute frequency of each channel can still drift over time, their relative phase will always stay locked, which makes long-term relative phase stability easily realizable without frequent phase re-calibration.

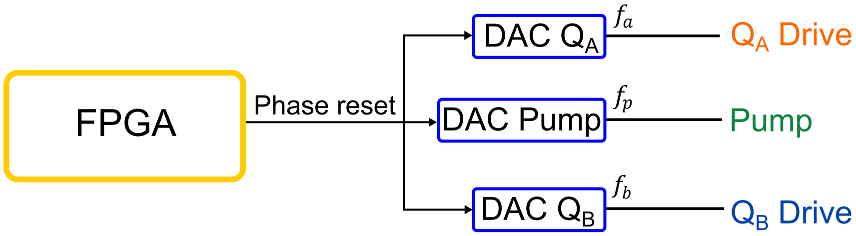

Figure 22: **Two-qubit control pulse generation with direct digital synthesis.** Some filters and amplifiers are omitted here. The qubit control pulses and the pump signal can be generated with direct digital synthesis (DDS) via the DAC. The DACs are controlled by the central FPGA, which can trigger the phase reset of all DAC channels simultaneously with well-defined timing.

The successful implementation of this technique resides in the FPGA firmware layer. The central soft-core processor must be able to send the phase-reset triggers to all the DAC channels simultaneously, while avoiding any jitter that might result in a potentially varying phase offset after each phase reset.

Figure 23 shows an example comparison of the relative phase stability measured using two different setups. In Fig. 23a, two signal generators are mixed to generate a 50 MHz signal, which is then sent to the digitizer for extracting the relative phase between the two generators. All three devices are locked to the same external Rubidium clock. In Fig. 23b's setup, two DAC channels on a RFSoC board are mixed, and the resultant signal is sent to an ADC on the same board to extract the phase information. The relative phase drift between the two signal channels is monitored for an hour and plotted in Fig. 23c,d.

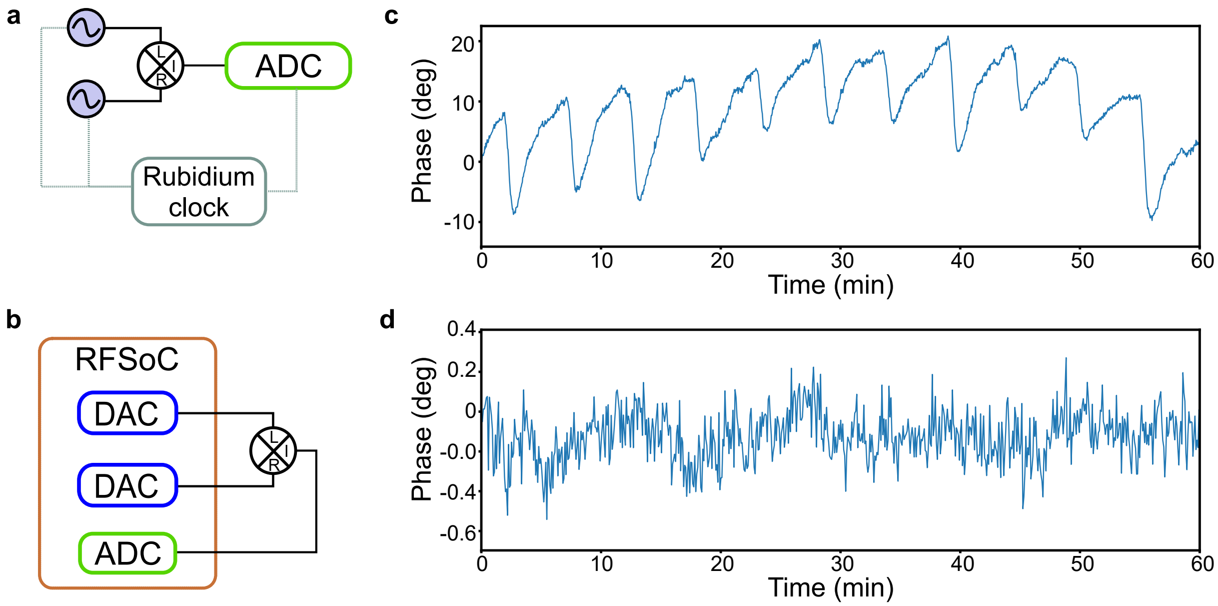

Figure 23: **Relative phase stability measurement with two different setups.** **a)** Setup for measuring the relative phase stability between two signal generators using a ADC that is locked to the same Rubidium clock with both generators. **b)** Setup for measuring the relative phase stability between two DAC channels with an ADC channel that is on the same RFSoC board with the DACs. **c)** and **d)** are the measured phase results from setup **a)** and **b)** .

The results presented in Fig. 23c show that the two generator channels, despite being synchronized to the same external reference clock, can have a relative phase drift of approximately 20° over a span of 5 minutes. This drift could lead to catastrophic impacts on the stability of two-qubit quantum gates. On the other hand, the results shown in Fig. 23d exhibit a phase variation of less than 0.5° over one hour of measurement, which provides compelling evidence of the relative phase stability offered by the RFSoC board with DDS pulse synthesis, demonstrating its excellent suitability for parametric quantum operations.

In section 5.2, I will present another example of system phase stability measured from an actual quantum experiment, which will clearly illustrate the crucial role played by RFSoC hardware in achieving practical realization of long-time experiment averages.

4.0 Building a Prototype Modular Quantum Computer with Parametric Interactions

This chapter is adapted in part from reference [52] and its supplementary material.

4.1 Modular structure for superconducting quantum processor

In the earlier chapters I have introduced the remarkable progress in the field of circuit QED, which has led to the development of mature techniques for building, controlling, and measuring superconducting qubits. As a result of this extensive research and development, building medium-scale quantum processors with superconducting circuits is now a reality. Currently, we are in the so-called Noisy Intermediate-Scale Quantum (NISQ) era, where fairly high-fidelity universal quantum gates can be performed between tens [4, 29, 30] (or hundreds [31, 32]) of qubits, showing the immense potential of quantum computing for tackling complex computation or simulation tasks that are beyond the capabilities of classical computers[4, 29, 33]. Despite this progress on NISQ algorithms and continually increasing qubit counts, these NISQ machines are still not capable of performing actual large scale quantum algorithms, since quantum information tends to degrade too rapidly in larger systems due to error accumulation. Therefore, scaling up NISQ machines to fault-tolerant quantum computers with thousands of logical qubits remains a challenging research topic that must be addressed. Achieving this goal will require continued improvements in qubit coherence and gate/measurement fidelities. Moreover, another critical aspect that must be considered is the type of connection architecture that should be constructed in large-scale superconducting quantum circuits.

The planar nature of Josephson junction-based quantum devices makes it a natural choice to construct multi-qubit processors on the 2D plane of a silicon or sapphire chip. This approach is commonly used in state-of-the-art medium-scale superconducting quantum processors, which utilize a 2D lattice structure. This structure consists of an array of qubits that are connected to their nearest neighbors using coupler devices. Recent examples of such processors include Google's 53-qubit chip depicted in Fig. 24a [4], as well as other devices of the same or similar topologies [96, 29, 30]. The 2D lattice structure has the advantage that its topology is well suited for direct implementation of the surface-code error correction scheme [97, 98, 99, 30], which offers an error-tolerant route to realizing fault-tolerant quantum computers, albeit at the price of very high numbers of physical qubits per logical qubit. However, in large-scale processors that rely on this monolithic fabric of nearest-neighbor interactions, the circuit must be designed carefully to prevent spectator qubit errors and long-range cross-talk[69, 70, 71]. Moreover, fabricating all components to perform flawlessly on a single die is another significant challenge that must be addressed[4].

To solve these issues, researchers have borrowed ideas from large-scale and distributed classical computers to design modular architectures for quantum processors. The modular design divides the processor into smaller, more manageable building blocks or modules, each containing a small number of qubits; modules are linked via quantum communication channels. Such designs allow us to replace faulty components and test sub-units separately, which can greatly ease requirements for flawless fabrication while also allowing distant qubits to communicate with many fewer intermediate steps, potentially enhancing fidelity in near-term quantum processors[102]. Moreover, sources of qubit decoherence (e.g. quasi-particles) and cross-talk errors can be more confined within a single module instead of propagating across the whole monolithic processor, making the mitigation of correlated errors in modular structure devices easier to engineer[103, 104].

Many of the early proposals for modular architectures are based on atomic qubit systems[105, 106, 107, 108] (Fig. 24b). In these systems, it is easy to move information over large distances via optical fibers, but challenging to collect light from individual atoms. Under these conditions, we cannot guarantee that light will be collected from a given shot. Therefore, remote inter-module communication must be realized by measurement based entanglement methods[109, 110, 111, 112, 113] which utilize external measurement events to counteract photon loss at the expense of reduced success probability. As noted, in these systems, the communication channel can simply be optical fibers and one can build programmable cross-connect switches to realize all-to-all communication between module pairs [106, 107, 100].

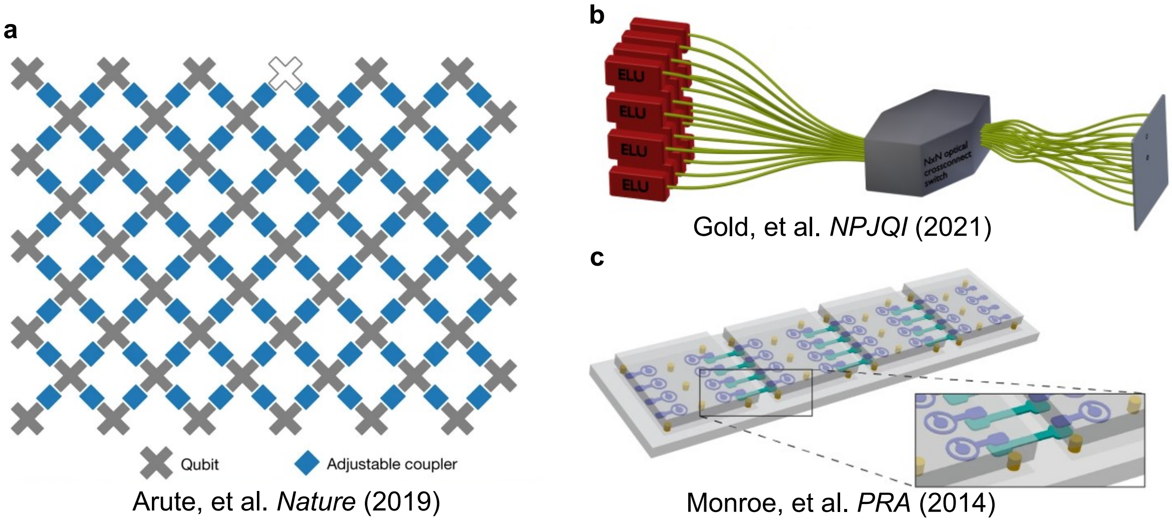

Arute, et al. *Nature* (2019)

Gold, et al. *NPJQI* (2021)

Monroe, et al. *PRA* (2014)

Figure 24: **2D lattice and modular structures for quantum processors. a)** Schematic of Google's 53-qubit superconducting (SC) quantum processor based 2D lattice structure [4], in which each qubit is coupled with its nearest neighbours via tunable couplers. **b)** Modular structure ion-trap quantum network proposed by Monroe, et al. [100]. Each elementary logic unit (ELU) consist of multiple ion-trap qubits. The ELUs are connected to an optical cross-connect switch, which is used to selectively create measurement based entanglement between arbitrary qubit pairs in the ELU array. **c)** Modular superconducting qubit chip connections built by Rigetti Computing [101], in which relatively small 2D SC qubit chips are connected via flip-chip bonds.

In superconducting circuits, there have also been several recent demonstrations of similar measurement-based protocols[114, 47, 115, 116], but only between a single pair of logical modes. The proposals and implementations for medium-scale modular structures are mostly based on building static couplings between pieces of 2D lattice devices [101, 32] (Fig. 24c).

However, superconducting circuits can also transfer states directly through a controllable communication bus. For this form of direct state exchange, we require strong, switchable couplings from module to the communication channel to enable rapid operations, low losses in the channel, and a dense, reconfigurable network of couplings among many modules.

Realizations to date have focused on pairs of quantum modules [117, 118, 119, 120, 121] or modes in a monolithic device [122, 40, 49, 123, 124]. They have utilized transmission-line based 'quantum bus' communication channels and controllable module-bus couplings based on the non-linearity of Josephson junctions or driven exchange via a non-linear coupling mode.

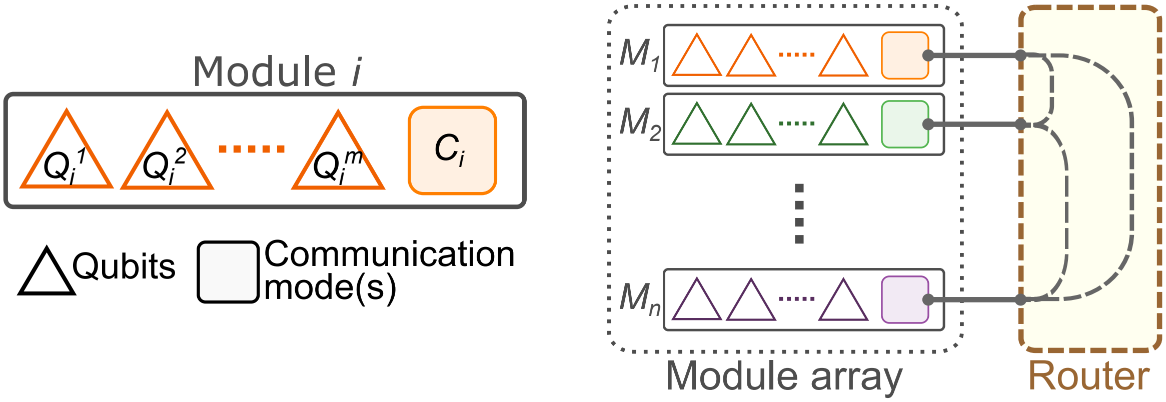

Figure 25: **Schematic representation of our proposed modular structure quantum computer.** Each module consists of multiple superconducting qubits that have all-to-all intra-module couplings. At least one of these qubits works as a communication mode that couples to the second element, the quantum router. The router can perform all-to-all operations between communication mode pairs in different modules.

In our work, we propose a new modular architecture for superconducting quantum processors that utilizes the idea of building a coherent communication bus that connects multiple quantum modules. The design schematic is shown in Fig. 25. Each quantum module includes multiple qubit modes represented by Q_i, as well as one or more additional modes used as communication mode(s)(C). Given a small number of modes in each module (less than ~ 6), it is feasible to build all-to-all intra-module connections between the qubits and communication mode(s) using the parametric interactions introduced in Ch. 2, while keeping the cross-talk effects under control and retaining unique drive frequencies for all interactions among qubits. The communication modes of all modules are coupled to the coherent communication bus that we call the quantum router. The quantum router utilizes similar parametric interactions between communication modes and manages the all-to-all communication among the quantum modules. Instead of using measurement to herald entanglement between modes, operations over the router can be thought of as direct, parametrically actuated gates between quantum communication modes in different modules. As an experimental demonstration of this structure, we have designed and built a prototype router-based superconducting quantum computer using 3D superconducting circuits. In the following sections, I will present the design, fabrication, characterization, and measurement processes for this device, as well as discussions on the further scaling schemes based on modular design.

4.2 Prototype modular quantum computer with a quantum router

4.2.1 Device design and fabrication

4.2.1.1 Design overview

Figure 26 shows the overall coupling scheme of our prototype modular quantum computer. A central quantum router is coupled to the communication modes of four quantum modules. Each quantum module is designed to host one communication mode C_i, one transmon qubit Q_i, and one readout cavity R_i.

I would like to highlight that the router's role extends beyond simply building connections among multiple quantum modes. It needs to distribute these connections across a large 3D space, and selectively activate interactions between any modes that couple with it. A standalone chip-based coupler would not be sufficient for this task, as the field of the coupler modes would be too localized, making it difficult to interact with module modes in 3D space. To address this, our design introduces intermediate modes ($W_1 - W_4$). These modes are combined with a central SNAIL coupler chip (S) to form a sizeable 3D non-linear object, the router. This structure helps distribute the non-linearity to different ports and create three-wave-mixing terms between the SNAIL mode and all the communication modes. As a result, we are able to perform parametric exchange operations between any pairs of communication modes that are coupled to the router.

In addition, we emphasize the "modularity" of our system in the additional sense that each module and the router itself exist as independent units which can operate individually, instead of the whole system forming a monolithic block. This offers a tremendous advantage in the laboratory, as defective components can be easily replaced, and the different components can be tested separately and then assembled.

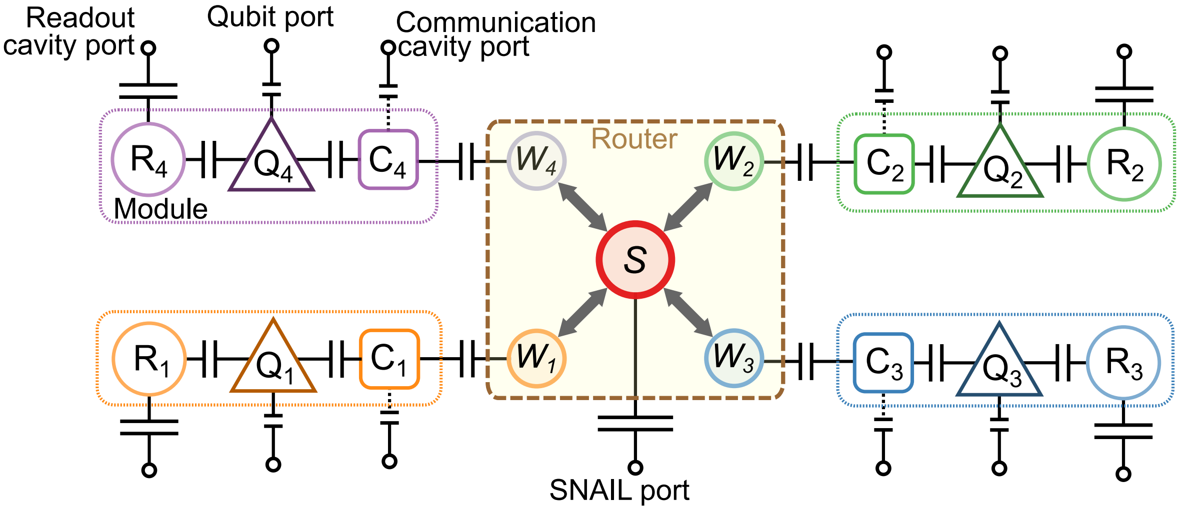

Figure 26: **Full coupling scheme of our prototype modular quantum computer.** The quantum router consists of a central 3-wave-mixing SNAIL coupler (S), and four intermediate modes ($W_1 - W_4$) to distribute the SNAIL's 3rd-order non-linearity to different ports. Each module ($i = 1 - 4$) includes a communication mode C_i that couples to a router port, a transmon qubit Q_i that couples to the communication mode, and a readout cavity R_i for reading out the qubit. Each mode in the system (except the intermediate modes in the router) has a dedicated control/readout port.

In our physical realization of the above coupling scheme, the communication modes we use are superconducting 3D cavities rather than qubits (Fig. 29), as they accommodate multiple qubit encoding schemes including the Fock encoding used in this work, cat states[125], binomial encodings[126], GKP-encodings[127], etc. This allows our router to be compatible with a wide array of future module designs.

Having the intermediate communication mode between the router and the qubits in each module also eases the design of the full device, as it serves as a separation point between the router and the modules and allows them to be simulated individually. Even in the current device where there is only one extra qubit and readout mode in each module, simulating the whole device of 1 router + 4 modules in one go is already very computationally demanding. The weak coupling between the router and the qubit modes allows us to separate the simulation into two steps: the router-communication mode system and each module system. Each module can be simulated as a three mode device, the communication mode, the qubit, and the readout mode. When simulating the router, the only extra modes we need to consider are the communication modes of the modules.

4.2.1.2 The quantum state router

In the router design, we use a SNAIL device that was introduced in Sec. 2.3.3 to bring 3rd-order non-linearity into the system, and the first four TE modes of a superconducting 3D waveguide to distribute the non-linearity across a large 3D space.

Choosing the SNAIL junction parameters. To enable fast parametric operation in the router, the SNAIL needs to be designed with a large g_3 coefficient. As introduced in Sec. 2.3.3, the g_3 coefficient is related to the large junction inductance L_j and total device capacitance C with:

$$g_3 \propto (L_j)^{-1/4}(C)^{-3/4} \tag{135}$$

At this point, one might think that this means we need to choose smaller L_j to achieve larger g_3 coefficient. However, in the router design, it is also important to keep the SNAIL frequency close to the waveguide mode frequencies to ensure enough hybridization strength. Since the SNAIL frequency $f_s \propto (L_jC)^{-1/2}$, we can rewrite Eq. 135 as:

$$g_3 \propto (L_j)^{1/2}(f_s)^{3/2} \tag{136}$$

In the following text, I will discuss our considerations for choosing the waveguide mode frequencies. Basically, we want the SNAIL mode to remain below the waveguide modes, and given a realistic waveguide size that can accommodate four quantum modules, the waveguide frequencies cannot be too high. Consequently, we will have limited space to increase the SNAIL mode frequency. Thus, to provide the SNAIL mode with a higher g_3, we must choose a higher L_j. Given a commonly used junction ratio of $\alpha = 0.25$ for a 3-large-junction SNAIL loop, we have selected the maximum L_j that made the smaller junction (with $L_{j,small} = Lj/\alpha$) easy to fabricate using Dolan bridge-style lithography, which was $L_j \sim 0.86$nH.

Given the fixed large junction inductance L_j, the SNAIL mode frequency can then be fine tuned by changing the antenna capacitance, which is primarily controlled by the capacitor pads located close to the junctions (Figure 27e, green region). Changing the width and the gap between the two pads allows us to tune the SNAIL frequency without significantly affecting the direct coupling strength between the SNAIL and the waveguide modes.

Choosing the waveguide dimensions. The waveguide used here is shorted on both ends (i.e. a 3D rectangular cavity resonator), which forms the standing wave $\mathrm{TE}_{mn\ell}$ modes with frequencies[128]:

$$f_{mn\ell} = \frac{c}{2\pi}\sqrt{\left(\frac{m\pi}{a}\right)^2 + \left(\frac{n\pi}{b}\right)^2 + \left(\frac{\ell\pi}{d}\right)^2} \tag{137}$$

where a, b and d are the three dimensions of the rectangular waveguide, as labeled in Fig. 27a, and c is the speed of light. Each mode is represented by three integer indices (m, n, ℓ), where at least two of the indices are positive, while the last one can start from 0. As these mode indices get larger, the frequency spectrum of the modes becomes denser, with neighboring modes getting closer to each other in frequency. Since each parametric process in the router is addressed by a specific frequency difference between two modes, to avoid activating unwanted processes and build a clean parametric coupling scheme we want to use the four lowest modes in the waveguide (where the mode frequencies are relatively well separated) as intermediate modes for non-linearity distribution, and the SNAIL will stay below all the waveguide modes so that the high-frequency modes are far detuned from it and have minimal effect on interfering with the desired parametric processes.

To enable efficient coupling between the SNAIL mode and the four lowest frequency waveguide modes, we choose the three waveguide dimensions such that $b < a < d$, which causes the first few lowest frequency modes to be $\mathrm{TE}_{10\ell}$ modes. As shown in Fig. 27b, these modes have electric fields all parallel to the x direction, which enables direct dipole couplings

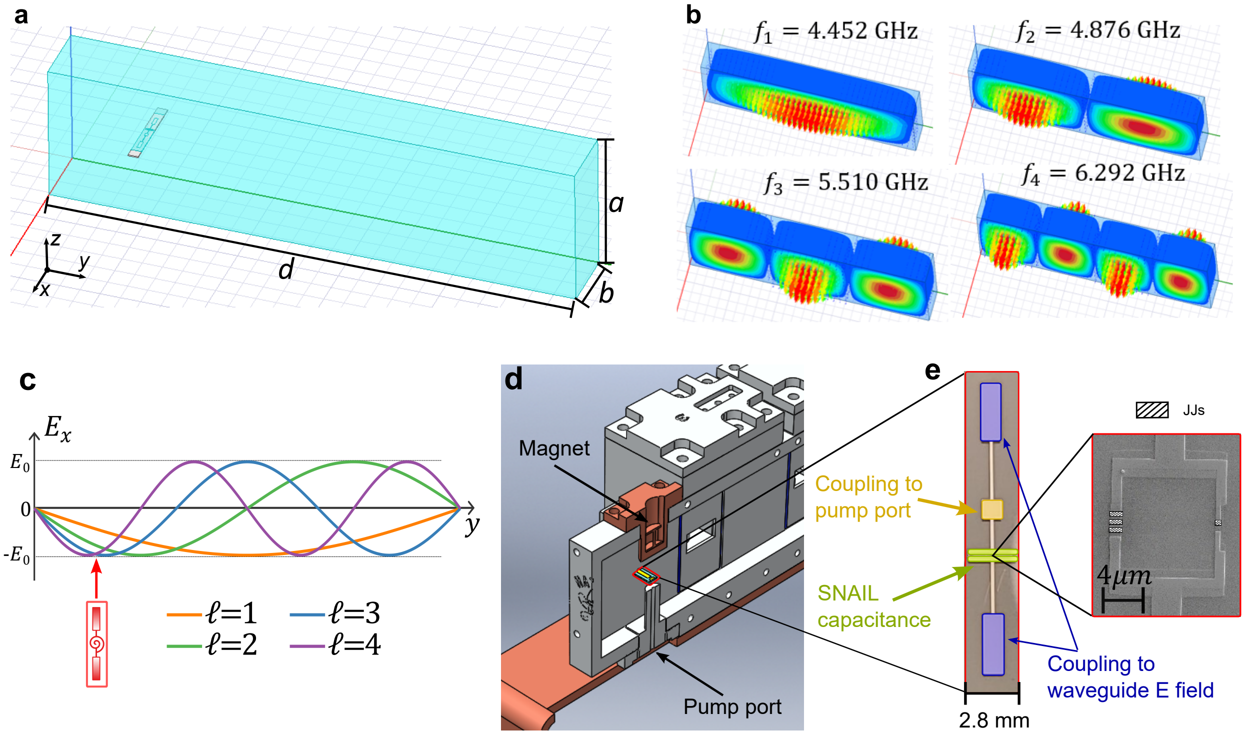

Figure 27: **Quantum state router design with the SNAIL and waveguide modes.** **a)** Our convention for labeling the Cartesian axis and the waveguide dimensions. **b)** Electronic field ($\boldsymbol{E}$) distribution for the first four lowest frequency waveguide modes in 3D space. **c)** $\boldsymbol{E}$-field component in the x direction as a function of the y coordinate on the $z = a/2$ plane for the first four lowest frequency modes, and a schematic drawing illustrating the location of the SNAIL chip. d) Computer-aided design (CAD) drawing of the SNAIL pump port and bias magnet. e) Color-labeled photograph of the SNAIL chip and scanning electron microscope (SEM) image of the SNAIL loop.

between the SNAIL mode and multiple waveguide modes.

Under the constraint $b < a < d$, the next thing we consider is that we want to make sure the $\text{TE}_{10\ell}$ modes in the waveguide that are close to the SNAIL mode frequency do not interfere with the final SNAIL controlled communication cavity exchange interactions. For example, for a given communication cavity pair c_i and c_j, we want to make sure that $|f_{c_i} - f_{c_j}|$

is far detuned from $|f_{c_i} - f_{\mathrm{w}_\ell}|$ and $|f_{c_j} - f_{\mathrm{w}_\ell}|$, where f_{w_ℓ} is the frequency of the waveguide $\mathrm{TE}_{10\ell}$ mode, so that the cavity photon will not leak into the waveguide modes during the exchange interaction. This requires us to think ahead, assuming each communication cavity mode is going to be ~ 70 MHz detuned from the intermediate waveguide mode it couples to, and then carefully choose the a and d dimensions such that all the possible unwanted transitions are at least ~ 50 MHz from all the $\binom{4}{2} = 6$ possible cavity transition frequencies. Here, this ~ 50 MHz minimum detuning is chosen such that it is much greater than the maximum exchange interaction speed that we expect to activate, which is around 5 MHz (100 ns iSWAP gate time).

Using the waveguide frequency formula in Eq. 137, we can easily run a brute-force 2D sweep of possible a and d dimensions, and find the feasible region where the possible frequency collisions are all avoided (bright region in Fig. 28). Meanwhile, we also want to keep the maximum $C - C$ exchange pumping frequency, $f_p^{\max}$, substantially below the router mode frequencies, so that we can use a low-pass filter on the SNAIL port to protect the router modes while allowing the pump tone to pass through (see Sec. 4.2.2). Furthermore, we want the minimum pumping frequency, $f_p^{\min}$, to stay above few hundred MHz, to ensure the efficient delivery of pump photons to the SNAIL mode. These two extra constraints are represented by the green and blue lines in Fig. 28. These three lines define an optimal region on the top right corner of Fig. 28. Note that this region doesn't always exist for arbitrary choices of waveguide-communication cavity detunings. In creating Fig. 28, we choose the four cavity detunings to be: [-70, -70, +70, -70] MHz from their dedicated waveguide modes.

We then settle on a point centrally positioned within this optimal region, with dimensions $a = 34.8$ mm and $d = 130.6$ mm, as marked by the red triangle in Fig. 28. The final dimension, $b = 15.8$mm, is selected to ensure that the waveguide is sufficiently wide to accommodate the SNAIL chip, while also preserving the first few lowest frequency modes as we defined in Fig. 27b. These dimensions give us the bare waveguide mode frequencies of the four lowest $\mathrm{TE}_{10\ell}$ modes $f_{\mathrm{w}_1} = 4.452$ GHz, $f_{\mathrm{w}_2} = 4.876$ GHz, $f_{\mathrm{w}_3} = 5.510$ GHz and $f_{\mathrm{w}_4} = 6.292$ GHz. These modes form the bare waveguide mode Hamiltonian we consider in the router device:

$$\hat{\mathcal{H}}_{WG}/\hbar = \sum_{i=1}^{4} \omega_{\mathrm{w}_i} \hat{\mathrm{w}}_i^\dagger \hat{\mathrm{w}}_i \tag{138}$$

In practice, incorporating the SNAIL mode, along with its associated pump port and magnet into the waveguide, will inevitably affect the waveguide mode frequencies. Thus, we need to then fine-tune the dimensions of each object as well as the SNAIL mode parameters to ensure that the constraints defined in Fig. 28 are still satisfied.

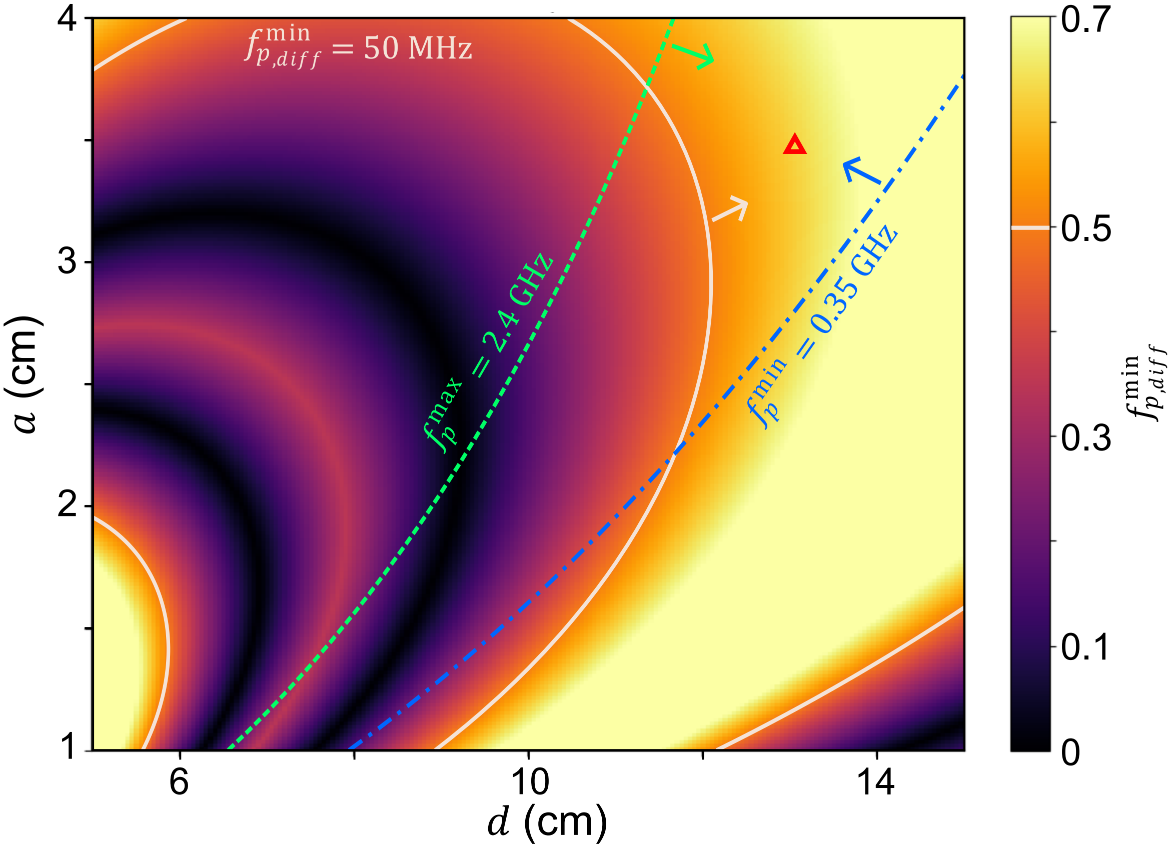

Figure 28: **Finding the optimized waveguide dimensions.** We define the minimum difference between the possible $C-C$ exchange pumping frequencies and any possible unwanted transition frequencies as $f_{p,diff}^{\min}$. This plot shows how $f_{p,diff}^{\min}$ changes as we sweep through the possible waveguide dimensions a and b. As discussed in the text, we want to stay in the region where $f_{p,diff}^{\min} \geq 50$ MHz, the boundary of which is represented by the white line in the figure. Combing this color plot with the two addition constraints on the minimum ($f_p^{\min}$) and maximum ($f_p^{\max}$) desired pumping frequencies, we find the optimal region for waveguide dimensions confined by these three lines. As a preliminary estimate for the optimized waveguide dimensions, we select a point centrally located within this region, marked by the red triangle.

Engineering the waveguide-SNAIL coupling strength. As mentioned earlier, the parallel $\boldsymbol{E}$ fields of the $\mathrm{TE}_{10\ell}$ modes allow us to build direct dipole coupling between the SNAIL and each waveguide mode, giving the bare SNAIL - waveguide coupling term in the router:

$$\hat{\mathcal{H}}_{R,\mathrm{coup}}/\hbar = \sum_{i=1}^{4} g_{\mathrm{w}_i s}(\hat{\mathrm{w}}_i^\dagger \hat{s} + \hat{\mathrm{w}}_i \hat{s}^\dagger) \tag{139}$$

in which $g_{\mathrm{w}_i s}$ is the direct coupling strength between the SNAIL and the waveguide mode i.

The coupling strength $g_{\mathrm{w}_i s}$ is determined by the strength of the waveguide $\boldsymbol{E}$ field across the SNAIL junction, which we can tune with two control knobs: the shape of the SNAIL antenna, and the location of the SNAIL inside the waveguide.

To achieve a strong coupling strength $g_{\mathrm{w}_i s}$, the SNAIL was designed with a long antenna and extra pads on the far ends to draw more $\boldsymbol{E}$ field across the junctions, as shown in Figure 27e (purple region). By changing the size of these extra pads, we can adjust the SNAIL-waveguide couplings without significantly affecting the other SNAIL parameters (e.g. SNAIL frequency), as the SNAIL mode capacitance is dominantly controlled by the green region in Fig. 27e.

In terms of SNAIL chip location, for a given (y, z) coordinate inside the waveguide, the $\boldsymbol{E}$ field of the $\mathrm{TE}_{10\ell}$ modes are uniform along the x direction, with strength:

$$E_x(y, z) = E_0 \sin\frac{\pi z}{a} \sin\frac{\ell \pi y}{d}, \tag{140}$$

where E_0 is the normalized $\boldsymbol{E}$ field strength based on the total energy stored in each mode. The SNAIL is thus placed on the $z = a/2$ plane inside the waveguide, with its antenna in parallel with the x direction to maximize overall coupling. Figure 27c shows E_x as a function of the y coordinate on the $z = a/2$ plane for $\ell = 1, 2, 3, 4$. Since each mode has a different $\boldsymbol{E}$ field distribution and different frequency, we can find a position on the y axis to place the SNAIL, where it has similar amount of hybridization strength $(g/\Delta)_{\mathrm{w}_i s}$ to each waveguide mode, in which $\Delta_{\mathrm{w}_i s}$ is the frequency difference between the SNAIL and waveguide mode i. By fine tuning the size of the SNAIL antenna and the y location and run the EPR simulation [78], we can tune $(g/\Delta)_{\mathrm{w}_i s}$ to be around $0.1-0.3$ for all the four waveguide modes we use in the router. This moderate hybridization strength enables the waveguide modes to share a sufficient amount of non-linearity from the SNAIL for the following 3-wave-mixing operations, while also allowing the waveguide modes to have lifetimes that are tens of times longer then the SNAIL mode, neglecting the complicating effects of spatially non-uniform loss (see discussion in Sec. 4.2.1.4).

Additional elements for SNAIL operation. As mentioned in Sec. 2.3.3, the SNAIL needs a tunable external flux bias to operate at the Kerr-free point. In our router design, we achieve this by using a magnetic coil, which is wrapped around a copper spindle and inserted into a copper shield which in turn is inserted into the waveguide body (Fig. 27d). By applying current through the coil, we can flux bias the SNAIL to a point where only the third-order non-linearity dominates, and give the approximate SNAIL Hamiltonian:

$$\hat{\mathcal{H}}_S/\hbar \approx \omega_s \hat{s}^\dagger \hat{s} + g_{sss}(\hat{s} + \hat{s}^\dagger)^3 \tag{141}$$

To deliver enough pump power to the SNAIL for fast parametric interaction, the SNAIL pump port was inserted from the bottom of the waveguide and couples directly to the SNAIL. Additionally, an extra square piece was added to the SNAIL antenna directly above the pump port to further enhance the coupling strength (Figure 27e, yellow region).

The copper holder and the pump port both form low Q modes in the router that actually limit the waveguide and SNAIL mode lifetimes. However, in Section 4.3, we will discuss how these limitations were improved in the updated design.

Total router Hamiltonian. By summing the Hamiltonian terms in Eq.138, 139 and 141, we get the total bare Hamiltonian of the router system:

$$\begin{aligned}\hat{\mathcal{H}}_R/\hbar &= \hat{\mathcal{H}}_{WG}/\hbar + \hat{\mathcal{H}}_{R,\mathrm{coup}}/\hbar + \hat{\mathcal{H}}_S/\hbar \\ &= \omega_s \hat{s}^\dagger \hat{s} + \sum_i \omega_{\mathrm{w}_i} \hat{\mathrm{w}}_i^\dagger \hat{\mathrm{w}}_i + \sum_i g_{\mathrm{w}_i s}(\hat{\mathrm{w}}_i^\dagger \hat{s} + \hat{\mathrm{w}}_i \hat{s}^\dagger) + g_{sss}(\hat{s} + \hat{s}^\dagger)^3.\end{aligned} \tag{142}$$

Using the non-linearity propagation formula that was introduced in Sec. 2.1.1.5. We get the waveguide-SNAIL 3-wave-mixing terms in the router:

$$\hat{\mathcal{H}}_R^{\rm 3wm}/\hbar = \sum_{i\neq j} g_{{\rm w}_i{\rm w}_j s}(\hat{\rm w}_i^\dagger \hat{\rm w}_j \hat{s} + \hat{\rm w}_i \hat{\rm w}_j^\dagger \hat{s}^\dagger), \tag{143}$$

In which the effective three-wave interaction strengths are given by $g_{{\rm w}_i{\rm w}_j s} \approx 6g_{sss}(\frac{g}{\Delta})_{{\rm w}_i s}(\frac{g}{\Delta})_{{\rm w}_j s}$.

4.2.1.3 The single qubit module

As a prototype demonstration of our proposed the modular structure quantum computer, we design and build single qubit modules that couple to the router. Each module contains a high-Q 3D coaxial cavity [129] as communication mode (C), one transmon qubit (Q) as computational mode, and another 3D coaxial cavity (R) for qubit readout. The design schematic and photograph of the real device is shown in Fig. 29.

The antenna of the transmon spans both cavities, resulting in dispersive coupling terms between the qubit and both cavity modes in the module:

$$\hat{\mathcal{H}}_M^{coup}/\hbar = g_{qc}(\hat{q}^\dagger \hat{c} + \hat{q}\hat{c}^\dagger) + g_{qr}(\hat{q}^\dagger \hat{r} + \hat{q}\hat{r}^\dagger), \tag{144}$$

where g_{qc} and g_{qr} are the coupling strengths between the qubit and communication mode and the readout mode, respectively. These couplings give rise to the total effective module Hamiltonian with both $Q-C$ and $Q-R$ cross-Kerr terms:

$$\hat{\mathcal{H}}_M^{\rm eff}/\hbar = \omega_c \hat{c}^\dagger \hat{c} + \omega_r \hat{r}^\dagger \hat{r} + \omega_q \hat{q}^\dagger \hat{q} + \frac{\alpha_q}{2}\hat{q}^\dagger \hat{q}^\dagger \hat{q}\hat{q} + \chi_{qc}\hat{q}^\dagger \hat{q}\hat{c}^\dagger \hat{c} + \chi_{qr}\hat{q}^\dagger \hat{q}\hat{r}^\dagger \hat{r}, \tag{145}$$

where $\omega_{c,q,r}$ are the angular frequencies of the communication, qubit, and readout mode, respectively. α_q is the anharmonicity of the qubit, and χ_{qc} and χ_{qr} are the strengths of the cross-Kerr between the qubit and communication and readout cavity modes, respectively. By adjusting the shape of the qubit antenna and the relative z-position of the two cavities, we can set χ_{qr} and χ_{qc} both to around 1 MHz to enable dispersive readout and four-wave-mixing qubit-communication cavity exchange interactions (see Ref. [47, 117, 50] and Sec. 4.2.4.2).

Each mode in the module has a dedicated control/readout port, as shown in Fig. 29b and c. The readout cavity port (purple) goes from the top of the cavity, and is over-coupled to the

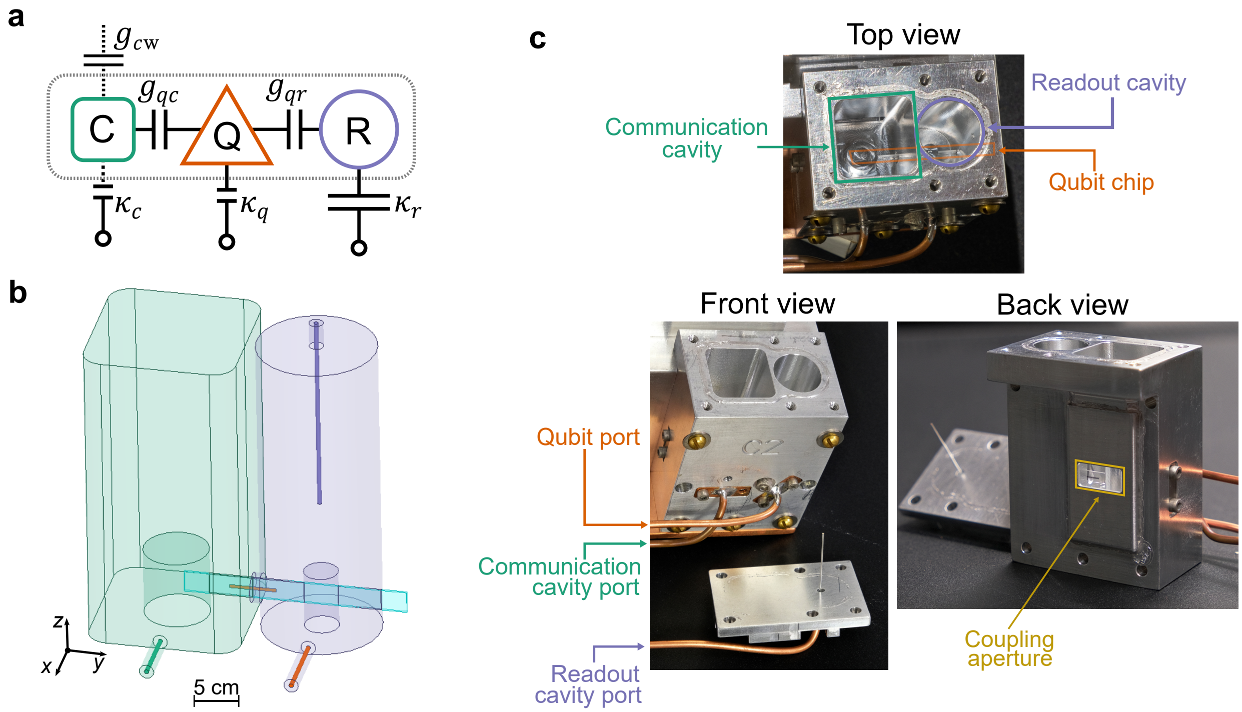

Figure 29: **Single qubit module design. a)** Coupling scheme in the single qubit module. The communication cavity mode (C) is coupled to both the external waveguide mode in the router with coupling strength g_{cw} and the internal transmon qubit mode (Q) with strength g_{qc}. The qubit is also coupled to a readout cavity (R) with coupling strength g_{qr}. Each mode has a dedicated external port. **b)** Device design in microwave simulator (HFSS). The rectangular coaxial cavity on the left is the communication cavity, while the cavity on the right is the readout cavity. The qubit is located on the sapphire chip (colored in blue) that goes through both cavities. **c)** Photograph of the device, in which the physical ports are also shown.

to the readout mode with rate $\kappa_r \sim 1$ MHz for optimized qubit state separation in dispersive readout, i.e. $\kappa_r/\chi_{qr} \sim 1$. The qubit readout is performed via reflective measurement from this port. The communication cavity port (green) is designed to be under-coupled to the communication mode. This port is only used in the coherent state exchange experiments that will be introduced in section 4.2.4.1, and will be removed to maximize the coherence of the communication mode in the Fock state experiments, where the communication modes will serve as intermediary modes that only store (but do not compute on or read out) quantum states, and enable the photon exchange between modules via the router controlled exchange interactions. To avoid introducing extra external loss to the communication cavity, the qubit control port (orange) was machined on the bottom of the readout cavity.

4.2.1.4 Full device coupling scheme

With the router and module devices separately designed, the next step is to couple the waveguide modes in the router to the communication modes of each module. This is realized by attaching the modules directly onto the sidewall of the waveguide and cutting a rectangular window on the shared wall between each communication cavity and the waveguide. As shown in Fig. 30b, the intrusion on the side of the communication cavity serves as part of the common wall between the module and the waveguide, and the coupling aperture is opened on this wall. These coupling apertures allow for direct $\boldsymbol{E}$ field overlap between each communication cavity mode and its corresponding waveguide mode, thereby creating the waveguide-communication mode coupling terms:

$$\hat{\mathcal{H}}_{RM,coup}/\hbar = \sum_{i=1}^{4} g_{c_i \mathrm{w}_i} (\hat{\mathrm{w}}_i^\dagger \hat{c}_i + \hat{\mathrm{w}}_i \hat{c}_i^\dagger). \tag{146}$$

Here, we assume each cavity is only effectively coupled to one waveguide mode. This assumption is valid because of two design choices we made. First, as shown in Fig. 30, the location of each communication cavity is chosen such that it faces the anti-node of its corresponding waveguide mode, so the $\boldsymbol{E}$ field overlap is designed to be strongest to the designated waveguide mode. Second, each cavity is only closely detuned from one waveguide mode by $\Delta_{\mathrm{w}c}/2\pi = |f_c - f_\mathrm{w}| \sim 70$ MHz. So, even though the couplings between the cavity and other waveguide modes can be of similar strengths (i.e. between communication cavity 1 and the waveguide mode 1 and 3), they are much further detuned (by $\sim$ GHz), which results in much lower hybridization strength g/Δ, and thus can be neglected. The size and z location of the coupling aperture are carefully tuned in simulation such that the coupling strength is around 7 MHz between the communication mode and its dedicated intermediate waveguide mode.

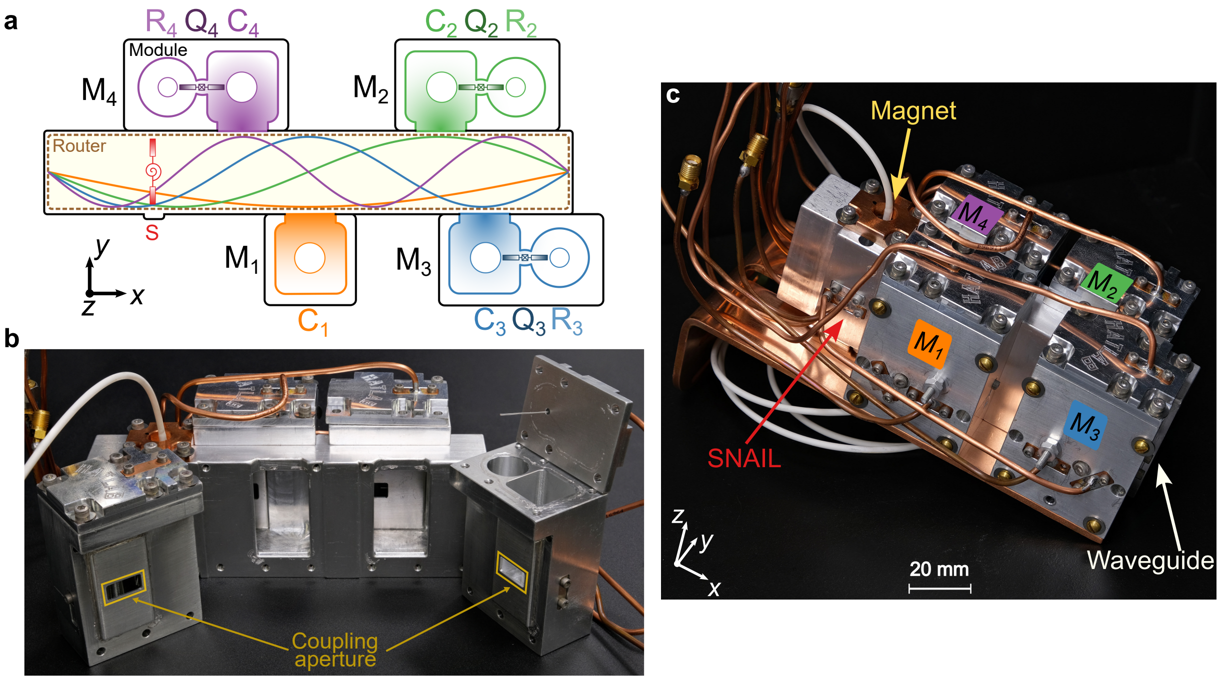

Figure 30: **Full coupling scheme of our prototype modular quantum processor and photograph of device. a)** Full device coupling scheme. The router uses one SNAIL chip and the four lowest modes in the waveguide. Modules 2-4 are single qubit modules that each contain a communication mode (C_i), a transmon qubit (Q_i) and a readout mode (R_i). Module 1's qubit is omitted. **b)** Picture of the device partially disassembled. The sidewalls of the communication cavities serve as parts of the waveguide sidewall; the two sides are joined with an indium wire. The small apertures (yellow boxes) on these sidewalls allow electromagnetic field overlap between the waveguide modes and the cavity modes, thereby creating the g_{cw} couplings. **c)** Photograph of the fully assembled device, with all the ports connected.

With the waveguide-cavity coupling terms in Eq. 146, we can once again use the nonlinearity propagation formula introduced in Sec. 2.1.1.5, and derive the communication cavity-SNAIL 3-wave-mixing terms in the full modular device:

$$\hat{\mathcal{H}}_{RC}^{\text{3wm}}/\hbar = \sum_{i\neq j} g_{c_i c_j s}(\hat{c}_i^\dagger \hat{c}_j \hat{s} + \hat{c}_i \hat{c}_j^\dagger \hat{s}^\dagger), \tag{147}$$

in which the effective three-wave interaction strengths are given by

$$g_{\text{c}_i\text{c}_j s} \approx g_{\text{w}_i\text{w}_j s}\left(\frac{g}{\Delta}\right)_{\text{w}_i c_i}\left(\frac{g}{\Delta}\right)_{\text{w}_j c_j} \approx 6g_{sss}\left(\frac{g}{\Delta}\right)_{\text{w}_i s}\left(\frac{g}{\Delta}\right)_{\text{w}_j s}\left(\frac{g}{\Delta}\right)_{\text{w}_i c_i}\left(\frac{g}{\Delta}\right)_{\text{w}_j c_j}, \tag{148}$$

Using these terms, we can apply pump on the SNAIL mode at the frequency difference between two cavity modes, i.e. $f_p = |f_{c_i} - f_{c_j}|$, and selectively activate the exchange (or beam-splitter) interaction between two communication cavity modes (Eq. 149), thereby performing inter-module gates across the router.

$$\hat{\mathcal{H}}_{CC}^{\text{eff}}/\hbar = g_{c_i c_j}^{\text{eff}} \hat{c}_i^\dagger \hat{c}_j + g_{c_i c_j}^{\text{eff}*} \hat{c}_i \hat{c}_j^\dagger, \tag{149}$$

The effective two-body exchange rate $g_{c_i c_j}^{\text{eff}}$, can be written as $g_{c_i c_j}^{\text{eff}} = \sqrt{n_s} e^{i\phi_p} g_{c_i c_j s}$, where n_s is the pump strength expressed as a photon number (see Sec. 2.1) and ϕ_p is the pump phase. By design, the $\left(\frac{g}{\Delta}\right)_{\text{wc}}$ coefficients are all around 0.1. Given the SNAIL and router parameters introduced in 4.2.1.2, i.e. $\left(\frac{g}{\Delta}\right)_{\text{ws}} \sim 0.1 - 0.3$ and $g_{sss}/2\pi \sim 100$ MHz , in total we have the cavity-cavity three-wave mixing coefficient of $g_{\text{c}_i\text{c}_j s}/2\pi \sim 0.06 - 0.5$ MHz. The two-step, weak hybridization allows the communication modes live up to 10^4 times longer than the SNAIL mode and 100 times longer than the waveguide modes, greatly decreasing the need for long lifetime components in the router. Given a reasonable photon number of ~ 10, we can expect an iSWAPgate time of ~ 200 ns $- 2$ μs.

One interesting advantage offered by this coupling geometry is that it effectively blocks the direct coupling between the waveguide mode and the computational qubit mode. This is due to the fact that the $\boldsymbol{E}$ field of the waveguide mode, as depicted by the yellow arrows in Figure 31, is perpendicular to the antenna of the transmon qubit (shown in blue in Figure 31), resulting in an extremely weak direct coupling between the two modes. On the other hand, the coaxial communication cavity exhibits a radial $\boldsymbol{E}$ field (depicted in green), enabling it to couple with both the waveguide and the qubit mode.

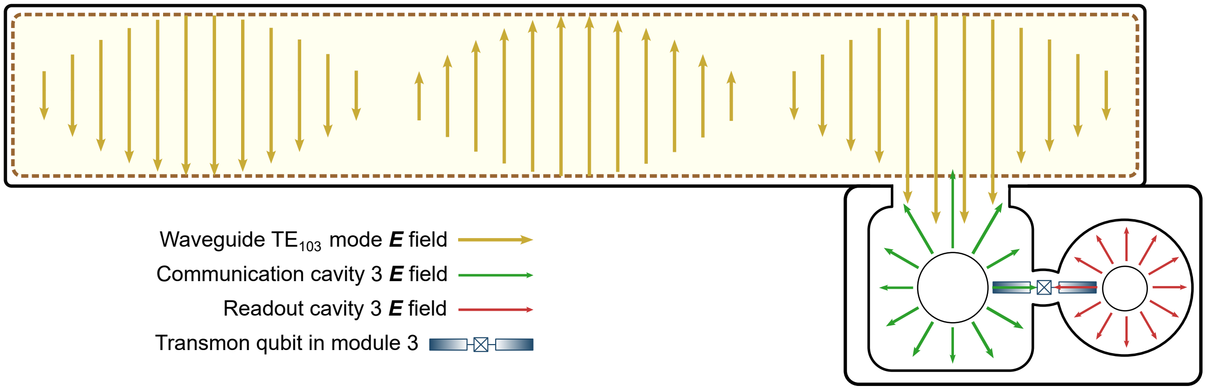

Figure 31: **Example *E* field distribution of the waveguide and module modes.** The yellow vectors represent the electric field vector of the waveguide TE$_{103}$ mode, which overlaps directly with the field of communication mode 3 (depicted as green arrows) at the coupling aperture. The communication cavity mode also couples with the transmon qubit through direct dipole coupling. However, the waveguide mode has very weak direct coupling with the qubit mode as it is perpendicular to the qubit's antenna (shown in blue). The red vectors represent the ***E*** field of the readout mode, which also couples with the qubit, but have near-zero coupling with the waveguide mode.

This advantage enables the design of each module as an independent device that is separated from the router system, and provides great flexibility in choosing the qubit and readout mode frequencies. Thus, to achieve compatibility with the router, only the communication cavity needs to be carefully designed to match with its dedicated waveguide mode, while the qubit and readout cavity can be designed with more freedom as long as the desired χ_{qc} and χ_{qr} are satisfied. This allows the microwave simulation for the whole router + 4 module system can be separated to 5 different parts and done separately.

4.2.2 Measurement system setup

Each mode in the full router + 4 module system has a dedicated control/readout port that is made of a copper coaxial cable soldered onto a custom machined port cap on one end and SMA connector on the other end. Fig. 30c shows the full device with all the ports connected. The device is then put into a cryo-perm magnetic-shielding can (Amumetal 4K) and installed at the base ($\sim 18\,\mathrm{mK}$) plate of a cryogenic set-up, as detailed in Fig. 32.

For controlling and reading out the full device, all pulse sequences are generated by Keysight M3202A (1 GSa/s) and M3201A (500 MSa/s) Arbitrary Waveform Generators (AWGs). The baseband microwave control pulses are generated at an intermediate frequency (IF) of 100 MHz and upconverted to microwave frequencies using IQ mixers. Image rejection (IR) mixers have been used for downconverting the detected signals to 50 MHz, which are then digitized using a control system based on Keysight M3102A Analog-to-Digital converters with a sampling rate of 500 MSa/s and on-board Field-Programmable Gate Arrays (FPGA) for digital signal processing (DSP).

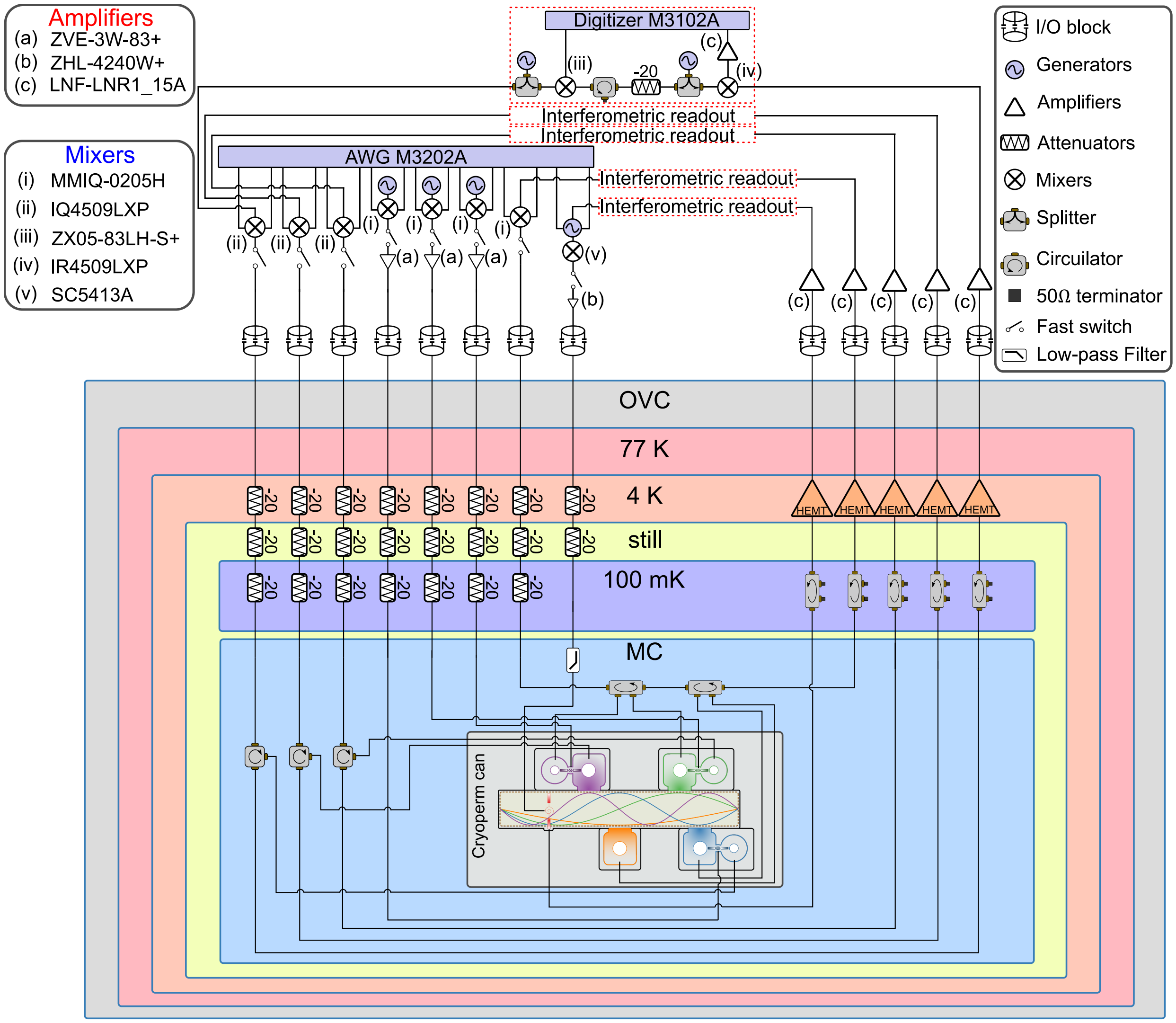

Figure 32: **Fridge wiring and measurement system.**

The SNAIL pump line design aims to deliver sufficient power to the SNAIL mode without overheating the fridge. This requires strong coupling between the pump port and the SNAIL mode, but this can also Purcell limit the lifetimes of the waveguide modes, thereby limiting the communication cavity modes' lifetimes. However, the off-resonance nature of our parametric pumping scheme actually allows us to separate these two constraints in the frequency domain. Specifically, all the possible pumping frequencies we used here are below all the mode frequencies as shown in Fig. 33. This allows us to use a reflective low-pass filter (LPF) on the SNAIL pump port that protects the modes in our device while allowing high-power, low-frequency pumps to pass. Moreover, unlike on-resonance driving schemes that require large amounts of attenuation (usually 20-30 dB) on the mixing chamber (MC) plate to reduce stray photons in the drive lines, the reflective LPF used here also generates much less heat, which also gives more tolerance to strong external pumps, thereby making the parametric pumping scheme even more promising in realizing large-scale/multiplexed qubit controls.

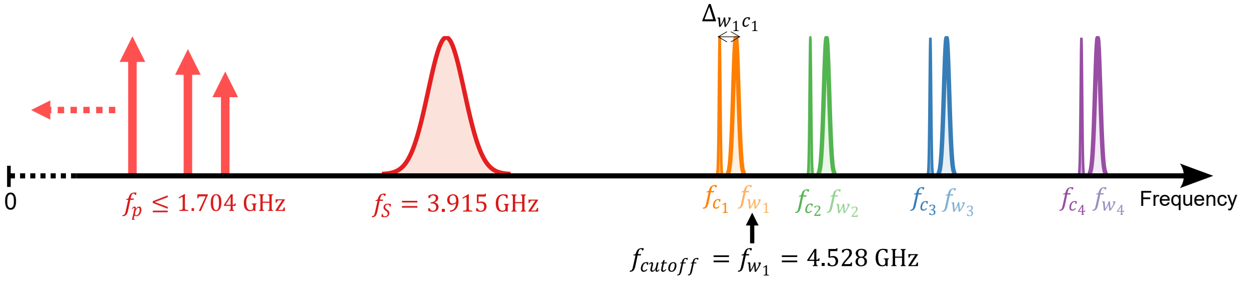

Figure 33: **Frequency spectrum of all linear modes, SNAIL mode, and pumping frequencies..** The maximum pumping frequency on the SNAIL is $f_p^{\max} \approx f_{c_4} - f_{c_1} =$ 1.704 GHz, which is far below the waveguide cutoff frequency $f_{cutoff} = f_{\mathrm{w}1} = 4.528$ GHz. The router then naturally protects pumping tones from propagating into modules. Meanwhile, the frequencies of all other modes don't have to be precisely controlled, so the router can be easily adapted to different modules without fine-tuning. Since the maximum pumping frequency is also lower than the SNAIL frequency $f_p^{\max} < f_s = 3.915$ GHz, a low-pass filter (e.g. Mini-Circuits VLF-2250+) is added to the SNAIL pump port so that strong pumps can be applied to SNAIL while the SNAIL mode lifetimes are protected

4.2.3 Mode characterization

Router mode characterization. The SNAIL mode is characterized by measuring the transmission signal from the SNAIL pump port, shown in yellow in Fig. 34a, to a side probe port (labeled in green) on the waveguide using a network analyzer. The pump port is strongly coupled to the SNAIL with a coupling Q of ~ 2000, while the probe port is much more weakly coupled. In the full router operation experiment, the side port is removed to maximize the mode lifetimes in the router.

By sweeping the bias current applied to the magnet, we can measure how the frequency of the SNAIL and waveguide modes are changed with flux (Fig. 34b).

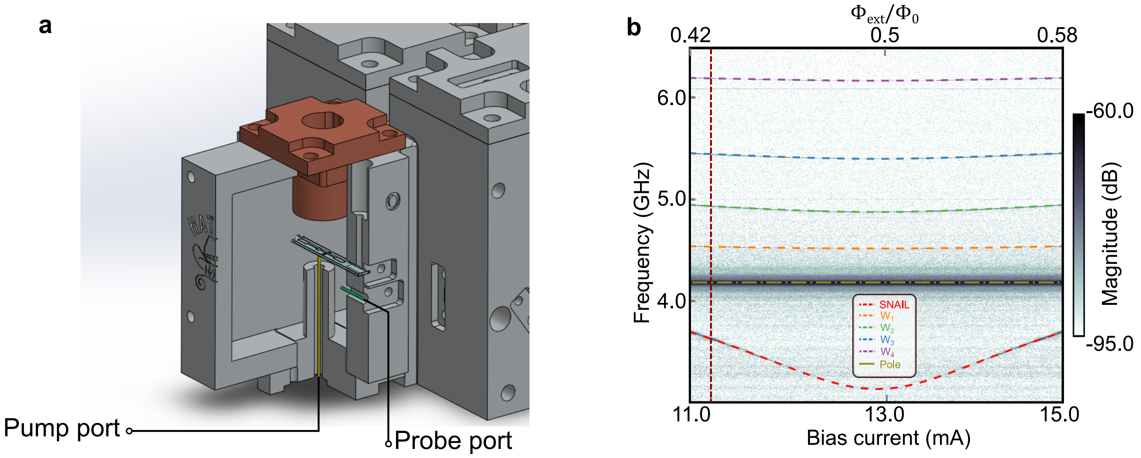

Figure 34: **SNAIL mode characterization setup and flux sweep result.** **a)** CAD drawing that shows the SNAIL pump port and prob port. **b)** Color plot of the magnitude of transmission signal versus the frequency from SNAIL pumping port ($|S_{21}(\omega)|$) for a range of applied coil bias current/applied SNAIL flux. The dotted lines indicate the dressed modes of the waveguide modes and SNAIL, as well as the ‘pole mode’ of the aluminum cylinder containing the drive port. The vertical, dark-red dashed line indicates the operating flux of the SNAIL.

In this setup, the aluminum pole for hosting the SNAIL pump port forms a low Q mode that is also coupled to the waveguide and SNAIL modes and is visible in the transmission measurement (brown dash-dotted line in Fig. 34b). This forms an overall coupling matrix in the router

$$M_{couple} = \begin{bmatrix} f_s & \bar{g}_{p_o s} & \bar{g}_{\mathrm{w}_1 s} & \bar{g}_{\mathrm{w}_2 s} & \bar{g}_{\mathrm{w}_3 s} & \bar{g}_{\mathrm{w}_4 s} \\ \bar{g}_{p_o s} & f_{p_o} & \bar{g}_{p_o \mathrm{w}_1} & \bar{g}_{p_o \mathrm{w}_2} & \bar{g}_{p_o \mathrm{w}_3} & \bar{g}_{p_o \mathrm{w}_4} \\ \bar{g}_{\mathrm{w}_1 s} & \bar{g}_{p_o \mathrm{w}_1} & f_{\mathrm{w}_1} & & & \\ \bar{g}_{\mathrm{w}_2 s} & \bar{g}_{p_o \mathrm{w}_2} & & f_{\mathrm{w}_2} & & \\ \bar{g}_{\mathrm{w}_3 s} & \bar{g}_{p_o \mathrm{w}_3} & & & f_{\mathrm{w}_3} & \\ \bar{g}_{\mathrm{w}_4 s} & \bar{g}_{p_o \mathrm{w}_4} & & & & f_{\mathrm{w}_4} \end{bmatrix}, \tag{150}$$

in which f represent the bare mode frequencies, and $\bar{g} = g/2\pi$ represent the coupling strengths between different modes in frequency units. The subscripts s, p_o, and w_i correspond to the SNAIL mode, the pump port pole, and the waveguide mode i, respectively. Once again, here we omitted the higher frequency waveguide modes in this coupling matrix as they are far detuned from the SNAIL mode.

The observed modes in the measurement are the dressed modes in the system, with frequencies ($\tilde{f}$) corresponding to the eigenvalues of the coupling matrix. By considering the designed SNAIL parameters and the current period and offset in the flux sweep results, we can calculate the bare SNAIL mode frequency f_s as a function of the externally applied flux, and use that to figure out the Kerr-free bias current of the SNAIL (red vertical dashed line in Fig. 34b).

	W_1	W_2	W_3	W_4	S
Frequency (GHz)	4.534	4.936	5.446	6.190	3.915
T_1 (μs)	1.68	0.29	0.28	0.81	
$\bar{g}_{\mathrm{w}s}$ (MHz)	335	417	396	360	

Table 1: **Router mode parameters.**

Also, based on how the waveguide mode frequencies move with the SNAIL mode, we can fit the measured frequencies $\tilde{f}_{\mathrm{w}_i}$ and $\tilde{f}_{p_o}$ as a function of the f_s to extract the coupling coefficients $\bar{g}_{\mathrm{w}_i s}$. The obtained coupling coefficients are summarized in Table 1.The waveguide mode lifetime is measured by driving a coherence state in the waveguide through the SNAIL pump port and measure the power decay from the probe port. The result is also presented in Table 1.

The lifetime of the router mode is primarily limited by two factors: the coupling to the copper intrusion of the bias magnet and the coupling to the drive port. In the full experiment, the loss from the drive port is reduced by the reflective low-pass filter on the pump line (as depicted in Fig. 32). However, we did not directly measure the lifetimes of the waveguide modes with the filter in place, as the same filter makes them unmeasurable through any available port. With the filter added, we believe the major loss sources for the waveguide modes are the seam losses at joints between the waveguide and the communication cavity modes, and the loss due to the copper intrusion.

Module mode characterization. The characterization of the qubit modes in each module follows conventional qubit measurement methods [95]. Through these measurements, we can extract qubit mode parameters, as summarized in Table 2. All values are measured and calibrated at the operation bias point of the SNAIL.

	Q_2	Q_3	Q_4	C_1	C_2	C_3	C_4
f (GHz)	3.067984	4.040709	3.566572	4.477662	4.812500	5.474195	6.180769
T_1 (μs)	60	9.1	8.4	22 (23)	23 (27)	13 (13)	15 (20)
$\mathrm{T}_{2\mathrm{R}}$ (μs)	18	6.3	8.0	44 (45)	46 (47)	22 (11)	25 (23)
$\mathrm{T}_{2\mathrm{E}}$ (μs)	24	7.6	8.0				
$\alpha/2\pi$ (MHz)	-141.3	-118.1	-125.8				
$\chi_{qc}/2\pi$ (MHz)	-0.11	-1.7	-0.86				
Measurement fidelity	93.6%	83.0%	88.0 %				
Single gate error	0.48% ± 0.04%	3.74% ± 0.5%	3.21% ± 0.6%				

Table 2: **Module mode parameters.**

The qubit measurement fidelity is calculated using single-qubit tomography. The single-qubit gate fidelity is measured using interleaved randomized benchmarking[130]. For communication cavities, the coherence times T_1 and T_2 are measured by either (a) using the under-coupled probe port to drive a coherence state and measure the power and voltage decay or (b) swapping single photons from qubits to cavities for variable time. The two times are listed as a (b) in the table. The pure dephasing time T_ϕ can be inferred from these values using $T_2 = 1/[1/(2T_1) + 1/T_\phi]$.

4.2.4 Parametric process tune up

4.2.4.1 C-C exchange interaction via SNAIL

Using the cavity-cavity-SNAIL 3-wave-mixing term introduced in Eq. 147, we can activate exchange interactions between communication cavity pairs, described in Eq. 149, by pumping on the SNAIL mode at the frequency differences between cavities. One interesting property of this exchange interaction is that it exchanges coherent state excitation in a way very similar to Fock state excitation. This allows us to observe the C-C exchange process by simply measuring the voltage leaking out from a weakly coupled port on the cavity, because this voltage, as a complex number, is proportional to the displacement parameter α_{CS} of the coherent state in the cavity.

Figure 35 shows an experimental pulse sequence for swapping coherent states between the module communication modes C_2 and C_4. First, a short on-resonance drive is applied to C_4 through the weakly coupled port, which creates a coherent state in this cavity. Then, a pump tone is applied to the SNAIL mode near the $\mathrm{C}_2 - \mathrm{C}_4$ difference frequency $\omega_p = \omega_{c_4} - \omega_{c_2} + \delta$, where δ is the pump detuning relative to the measured frequency difference between the two cavity modes. Meanwhile, the light in these two cavities is monitored by receiving the I-Q signal leaking out from each cavity's probe port. The amplitude of the coherence state inside the cavity can then be inferred by demodulating the signal at the corresponding cavity frequencies. By sweeping the applied pump frequency and time, we can determine both the swap rate and resonant condition for pumping.

The result of the pump frequency and time 2D sweep is shown in Fig. 35b, from which we can determine the optimal detuning frequency for full photon exchange (vertical dashed line), then we take the line cut at that frequency and plot figure c. There is a good agreement between the envelope of the swap trace (green and purple lines) and the hybridized decay trace, indicating that the state is only swapping between these two cavities without leaking into other modes, and that the fidelity of state exchange is mainly limited by the lifetime of these two cavities.

This same experiment is then performed for the six possible pairs of the four communication modes, and the full iSWAP exchange times are listed in Table 3. We find the fastest

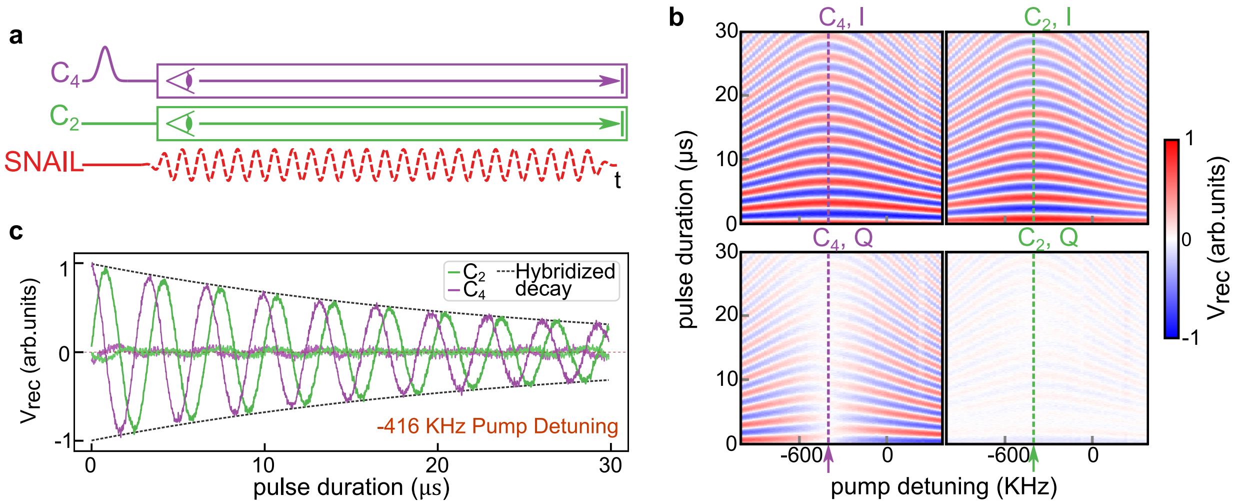

Figure 35: **C-C coherent state exchange.** **a)** Pulse sequence of the coherent exchange experiment. We begin by displacing one cavity to create a coherent state, which we then swap between a pair of cavities by applying a parametric drive to the SNAIL. We continuously monitor the I-Q voltage in each cavity during the swap process. **b)** In-phase (I) and quadrature (Q) received voltage from the two cavities versus pulse duration and pump detuning from the nominal difference frequency. The dashed vertical line denotes the optimal detuning frequency for full photon exchange. **c)** Line-cut of (b) at the optimal full-swap detuning. The grey dashed envelope represents the hybridized T_2 decoherence of the coupled systems, given by $\exp\left(-\bar{\Gamma}_2 t\right)$, where $\bar{\Gamma}_2 = (1/T_{2,\mathrm{C}_2} + 1/T_{2,\mathrm{C}_4})/2$ is the averaged decoherence rate of the two cavities involved (here C_2 and C_4), as the photon being exchanged spends half of its time in each cavity.

full-swap time to be 375 ns, the slowest 1248 ns, and an average swap time of ~ 764 ns. For each pair, the maximum gate speed is measured by increasing the pumping power until we see the mode coherence times substantially differ from their undriven values. On average, the pump frequency required to fully swap light between the two cavities is detuned by several hundred kHz (-416 kHz for the data in Fig. 35), which we attribute to a combination of SNAIL- and communication-mode static and dynamic Kerr effects; that is, the communication-mode frequencies are shifted due to the off-resonance pump on the SNAIL mode. In our pulses, we are only sensitive to changes in the communication modes' frequency difference, so shifts can be positive/negative/zero depending on whether the two modes shift closer together or further apart. This has strong parallels to saturation effects in parametric amplifiers, where the amplifier modes shift with stronger pumping, which complicates amplifier bias and can lead to limitations in power handling in the amplifier as bigger input signals shift the amplifier away from its small-signal frequency [79, 75, 131, 132]. Fortunately, in the case of parametrically controlled iSWAP gate the primary consequence is simply that we must track these shifts and their effects on the qubits' phases in our control electronics.

iSWAP pair	iSWAP time (ns)
$C_1 \leftrightarrow C_2$	1248
$C_1 \leftrightarrow C_3$	651
$C_1 \leftrightarrow C_4$	535
$C_2 \leftrightarrow C_3$	942
$C_2 \leftrightarrow C_4$	832
$C_3 \leftrightarrow C_4$	375

Table 3: **iSWAP exchange times between communication cavity pairs.**

The cavity-cavity exchange interaction demonstrated here is referred as 'beam splitters' gates in other works on cavity-based qubits [50, 48, 58], for their obvious resemblance to the optical component of the same name. However, in our full device operation, the communication cavities serve as intermediary modes that only store (but not compute on) quantum states, and enable the photon exchange between modules via the router controlled exchange interactions. We exclusively use these exchange interactions to swap Fock states fully from a source cavity to a formerly empty target cavity. In this scenario, the gates act as a combination of SWAP and z-rotation for both Fock and coherent states. Thus, in the simple algorithms that I will demonstrate in in Section 4.2.5, we refer to the operation of these exchange interactions as variations of the iSWAP gate, as is typical for gates based on coherent photon exchange[122, 47, 40, 50, 124, 68].

4.2.4.2 Q-C exchange interaction via cross-Kerr 4WM

The intra-module (Q-C) exchange interaction is realized using the cavity-qubit cross-Kerr term that was introduced in Eq. 145, $\chi_{qc}\hat{q}^\dagger\hat{q}\hat{c}^\dagger\hat{c}$. Using this term, we can apply two side-band pumps on the qubit and communication cavity at frequencies: $f_{QSB} = f_q + \Delta$ and $f_{CSB} = f_c + \Delta + \delta$, respectively, as shown in Fig. 36a. The side-band detuning Δ is usually around tens of MHz to avoid activating any on-resonance transitions on the qubit and cavity, and the extra detuning δ is added for compensating pumped induced AC-Stark shifts. These two pumps activate the effective exchange interaction between the qubit and communication cavity[47]:

$$\hat{\mathcal{H}}^{\text{eff}}_{QC}/\hbar = g^{\text{eff}}_{q_i c_i}\hat{q}_i^\dagger\hat{c}_i + g^{\text{eff}*}_{q_i c_i}\hat{q}_i\hat{c}_i^\dagger, \tag{151}$$

This exchange interaction Hamiltonian takes the same form as the $C - C$ exchange interaction in Eq. 149. However, there are two major differences that we need to pay attention to. First, instead of having a beam-splitter like interaction between two linear modes, the qubit mode here is considered as a two-level system, which changes the overall behaviour of the interaction Hamiltonian. However, since our protocols in this experiment only involving swapping light into empty qubits/cavities, states containing two or more photons are never occupied, we only need to consider the sub-space where only the $|e0\rangle \leftrightarrow |g1\rangle$ transition is involved in the qubit-cavity system. In this subspace, the exchange interaction works very similar to an iSWAP gate between the qubit and cavity.

Second, since we are driving on a 4th-order term directly, the AC-stark shift is much stronger than the SNAIL based 3-wave-mixing process. So instead of directly running a pumping frequency sweep around the frequency difference between the two cavity modes as in Fig. 35b, the tune up process is more complicated and involves more steps here.

The overall mode and pump frequency spectrum is shown in Fig. 36a. Under the qubit and cavity side-band pumps, the qubit frequency will shift from f_q to f'_q, while the cavity frequency almost doesn't move ($f'_c \approx f_c$). The two pump frequencies need to satisfy $f_{CSB} - f_{QSB} = f'_c - f'_q = f_c - f_q + \delta$, where δ is the overall frequency shift of both qubit and cavity modes. Since the qubit frequency shift contributes the major part of δ, we first keep track

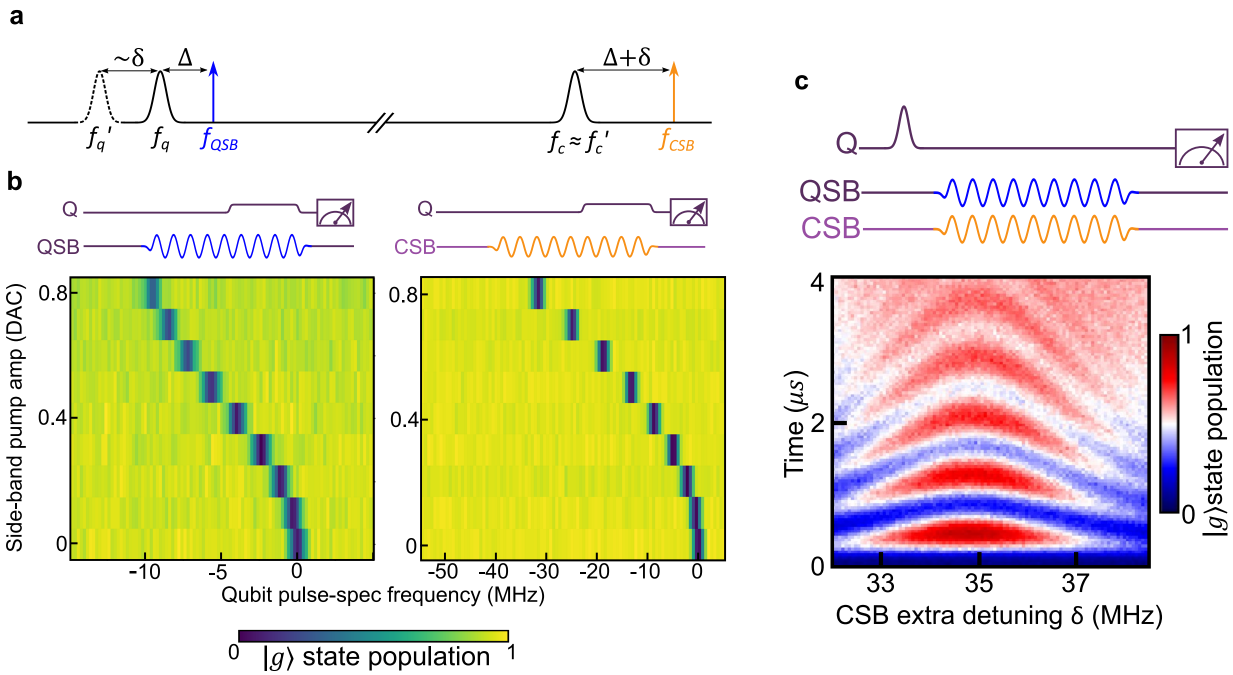

Figure 36: **Tune up Q-C Fock state exchange.** **a)** Spectrum of qubit and communication cavity frequencies and pump tones. Two pump tones, at frequencies f_{QSB} and f_{CSB}, are applied near the qubit and cavity frequencies to generate the exchange interaction between qubit and cavity. The qubit frequency shifts from f_q to f_q' under the pump, while the cavity frequency f_c almost doesn't move. **b)** Pulse sequence and measurement results for calibrating the qubit frequency shifts under individual QSB (left) and CSB (right) pumps. **c)** Pulse sequence and measurement result for the Q-C Fock state exchange experiment. The qubit is first prepared to excited state via a $R_x(\pi)$ pulse at frequency f_q, then two sideband pulses are applied at f_{QSB}, detuned by Δ from f_q, and f_{CSB}, detuned by $\Delta + \delta$ from f_c. Finally, projective measurement is applied to the qubit. Both pulse length and δ are swept to determine an optimized iSWAP gate. The color plot shows the Rabi-like oscillation of the intra-module iSWAP interaction. The vertical axis is the pulse time, the horizontal axis is the CSB extra detuning δ, and the color indicates the $|g\rangle$ state population of qubit.

of the qubit frequency shift by turning on the CSB and QSB pumps individually, and do pulse-spectroscopy on the qubit while each pump is on. Figure 36b shows the qubit frequency shift as a function of the pump amplitudes. From these two experiments, we can pick two pump amplitudes for CSB and QSB, then sum the qubit frequency shifts induced by each pump, this will give us an initial estimate of δ. After that, we prepare the qubit in $|e\rangle$, turn on both pumps at the chosen amplitudes, and fine sweep the extra pump detuning on CSB around this frequency, as well as sweeping the duration of both pumps. This creates the chevron plot shown in Fig. 36c. Form this, we can extract the best detuning frequency δ and the best iSWAP gate time.

This tune up procedure is performed in all three modules that have qubits in them. The shortest iSWAP gate times for each qubit-cavity pair are listed in Table 4. From this we find an averaged intra-module iSWAP gate fidelity of 94%, which is mainly limited by how fast the iSWAP gate is compared to T_2 decoherence of qubit and cavity.

iSWAP pair	iSWAP time (ns)
$Q_2 \leftrightarrow C_2$	1032
$Q_3 \leftrightarrow C_3$	674
$Q_4 \leftrightarrow C_4$	452

Table 4: **Q-C iSWAP gate times.**

4.2.5 Full device operation

With the inter- and intra- module gates all properly tuned up, next we can operate the full router + 4 module device as a prototype modular quantum computer. To recap our device structure, the single-qubit modules 2-4 each consists of one communication cavity C_i, one transmon Q_i, and one readout cavity R_i, while module 1's qubit is omitted. The communication cavities within each module are coupled to the router, allowing for inter-module gates between the communication modes.

For simplicity, our qubit states throughout the system are the Fock states $|0\rangle$ and $|1\rangle$ (or any superposition of $|0\rangle$ and $|1\rangle$), although the communication modes could in principle support a variety of more complex encodings. Here, the communication cavities serve as intermediary modes that only store (but do not compute on) quantum states, and enable the photon exchange between modules via the router controlled exchange interactions.

4.2.5.1 Inter-module Fock state exchange

We first use the module transmons and intra-module iSWAP operations to swap Fock states across the router, transferring single photons between distant qubits as shown in Fig. 37a, b. The protocol begins with all qubits and cavities prepared in their ground states. A $R_x(\pi)$ pulse is first applied to Q_2 which brings it to the excited state. Second, an intra-module iSWAP gate is performed between Q_2 and C_2. This fully swaps the excitation from Q_2 to C_2. Third, the photon is swapped between C_2 and C_4 across the router by pumping on the SNAIL mode, just as demonstrated in Fig. 35. The SNAIL pump duration is varied, which results in an effective Rabi oscillation between the two qubits when the protocol is completed. Finally, we apply two more intra-module iSWAP gates, C_2 to Q_2 and C_4 to Q_4. This fully transfers the states of C_2 and C_4 to their respective module qubits, which are then measured simultaneously using dispersive readout of the readout (R) modes.

The results are shown in Fig. 37c and 37d. The transfer fidelity between Q_4 and Q_2 is 72.5 ± 1.17 %. We perform Lindblad master equation simulations assuming ideal interactions, with the only defect being all modes' measured coherences ; the simulation results (dotted curves) show a good quantitative agreement with our data, indicating that, as with coherent

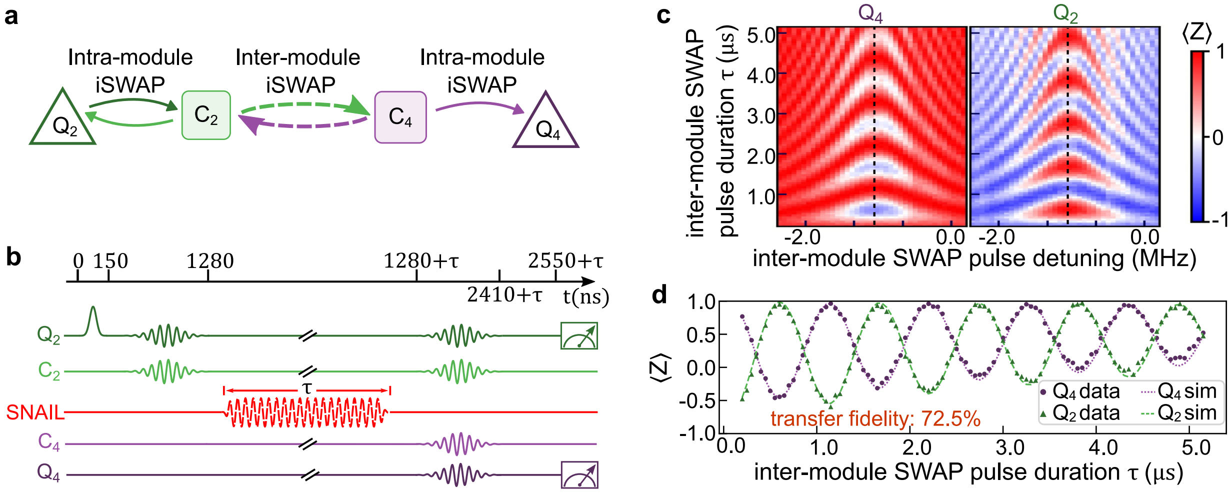

Figure 37: **Intra-module Fock state exchange.** **a)** Illustration of the photon swap protocol, in which a photon originating in Q_2 is fully swapped to C_2, then depending on the variable inter-module pulse duration, routed to Q_4 or returned to Q_2. **b)** Experiment pulse sequence. A photon is created in Q_2, then swapped to C_2. Next, it is swapped (or not) to C_4 with a variable duration, inter-module iSWAP pulse. Finally, the light in $C_{2,4}$ is routed via further intra-module iSWAPs to their respective qubits, which are then measured. The upper black bar indicates the total experimental duration with τ describing the variable, SNAIL actuated inter-module iSWAP. **c)** Measurement result of Q_2 and Q_4 for different SNAIL pump detuning and duration. Here, the color of the 2D sweep indicates the measurement along the qubits' z-axis. **d)** A cut of the swap data along the dotted line indicated in (c). The green triangles and purple circles are Q_2 and Q_4 data, respectively, and the dashed lines are the corresponding simulation results.

state operation, the primary fidelity limit in our system is the ratio of gate time to our modes' coherence times. The uncertainty given for the Fock state transfer fidelity, and all following quoted fidelities, is calculated following the 'bootstrap method' in Ref. [133, 134].

4.2.5.2 Inter-module entanglement generation.

Next, we utilize a $\sqrt{i\text{SWAP}}$ gate, created by shortening the first intra-module iSWAP gate from Fig. 37 by close to 1/2 in duration, to create inter-module Bell states. The $\sqrt{i\text{SWAP}}$ has the effect of taking the single photon in the qubit and coherently 'sharing' it between the qubit and cavity, creating a Bell state between the two modes. Overall, the sequence first creates a Bell pair inside a module, then shifts the communication cavity's component to a qubit in a second module. The quantum circuit is shown in Fig. 38a. Tomography is performed on both qubits, while the communication cavities are not measured. The measurement results are shown in Fig. 38b.

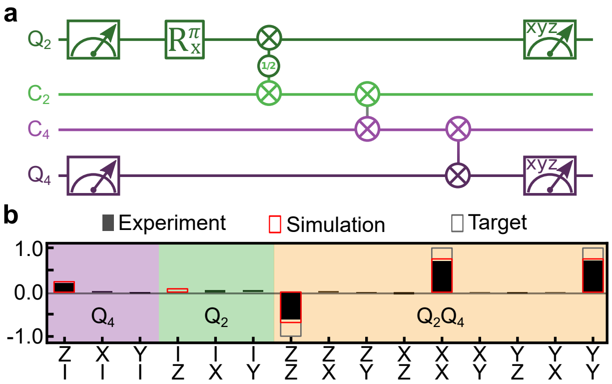

Figure 38: **Inter-module Bell state generation.** **a)** Quantum circuit for generating a Bell state between Q_2 and Q_4. Entanglement is first generated between Q_2 and C_2 using a $\sqrt{i\text{SWAP}}$ gate, then the cavity component is moved to Q_4 using two full-iSWAP gates. **b)** Tomography of the joint Q_2, Q_4 Bloch vector, in which each bar represents a joint measurement of the two qubits in the basis indicated (I indicates no measurement). Here, the black bars indicate the experimental result, the red rectangles are master-equation simulation results, and the gray rectangles represent the pure Bell state. The fidelity to the target Bell state $\frac{1}{\sqrt{2}}(|01\rangle + |10\rangle)$ is $76.9 \pm 0.76\%$, which agrees very well with the simulation prediction of 77.2%.

From this tomographic data, we can reconstruct the density matrix of Q_2 and Q_4, and find we achieve a Bell fidelity of 76.9 ± 0.76 %. The same experiment is performed on the other two qubit pairs $Q_2 - Q_3$ and $Q_4 - Q_3$) with fidelities of 58.7 ± 2.40 % and 68.2 ± 0.83 %, respectively. The results were again compared with Lindblad master equation simulations (red rectangles in Fig. 38b), and show that the dominant source of infidelity remains the modes' lifetimes.

In addition, we attempted a GHZ state preparation experiment between all three qubits in the modules using a similar scheme. The experiment sequence in shown in Fig. 39a, this protocol requires one additional entangling gate: an intra-module CNOT. We achieve this using a state selective qubit $\pi-$pulse [135]. We reconstruct the final state from tomography as shown in Figure 39b, and find a fidelity of 48.9 ± 5.27 %, just below the threshold for provable entanglement. While the result falls below the threshold for provable entanglement, it points to our ability to implement an extensive gate set in the router, and create multi-qubit entanglement.

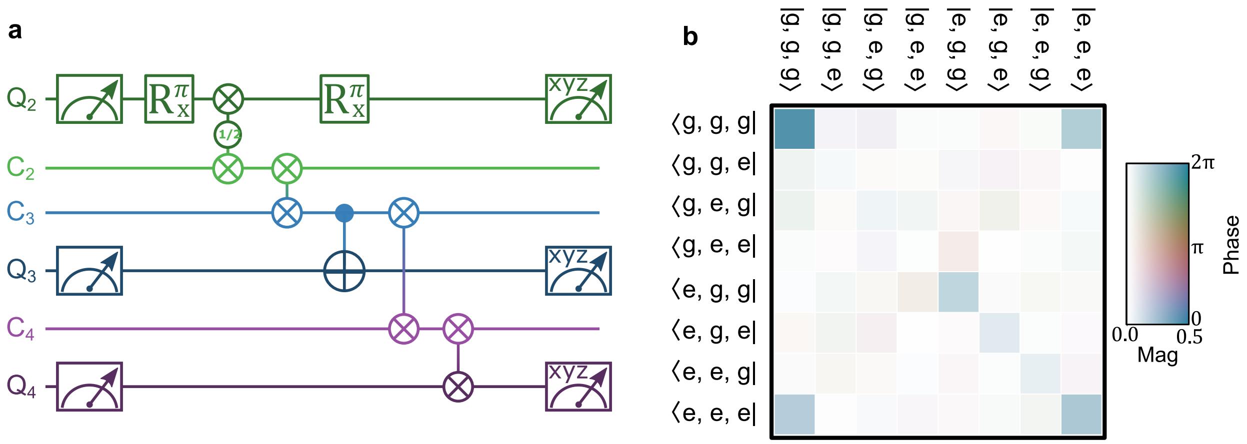

Figure 39: **GHZ state generation experiment. a)** GHZ state generation sequence. First, Q_2 is prepared to excited state, then an intra-module $\sqrt{i\text{SWAP}}$ gate is performed between Q_2 and C_2, which creates a bell state between them. This entanglement is then transferred to C_3 via an inter-module iSWAP gate. After that, an intra-module CNOT is performed between C_3 and Q_3, which entangles Q_2, Q_3 and C_3. In the end, Q_2 state is flipped with a $\pi-$ pulse, and the photon in C_3 is transferred to Q_4 using two iSWAP gate, which creates a GHZ state between Q_2, Q_3 and Q_4. **b)** GHZ state generation density matrix reconstructed from tomography. Here, each element in the density matrix is represented with a color using the Hue-Chroma-Luminance (HCL) color scheme. The amplitude of each element is mapped linearly to the Chroma and Luminance of the color, and the phase (from 0 to 2π) is mapped linearly to the Hue value. This color mapping scheme has the property that elements of the same amplitude are perceived equally by the human eye, so that the small magnitudes fades into the white background to avoid drawing the eye to small, noisy matrix elements. The observed fidelity state is 48.9 ± 5.27 %

4.2.5.3 Parallel operation

Another advantage of our architecture is that we can drive multiple parametric operations in the router simultaneously, which enables parallel operation and efficient ways to create entanglement. We demonstrate the simplest implementation of parallel operations by swapping light between two pairs of modules simultaneously. Here, M_2 and M_4 are treated as one sub-system, while M_3 and M_1 form the second one. We swap a photon from Q_2 to Q_4 and Q_3 to C_1 across the router simultaneously. The gate sequence is shown in Fig. 5a. The two cross-module swap interactions, $C_2 - C_4$ and $C_3 - C_1$, are turned on simultaneously by pumping the SNAIL mode at the two difference frequencies using a room-temperature combiner. The SNAIL pumps are applied for a variable period. The protocol concludes with SWAP gates between all cavity-qubit pairs and measurement of all qubits.

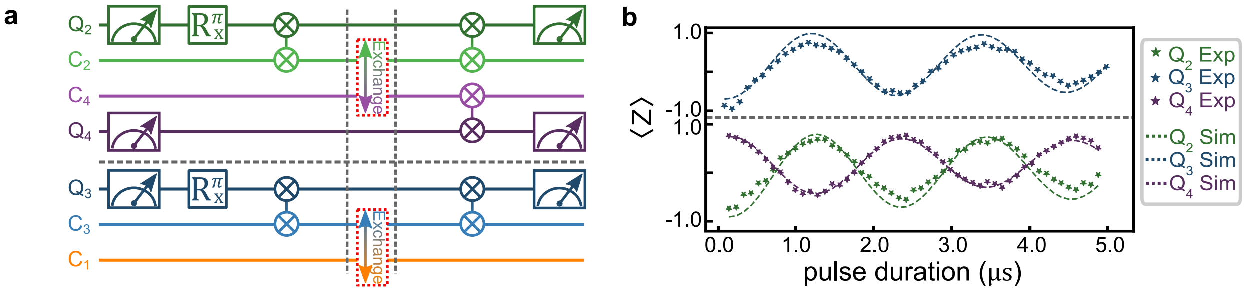

Figure 40: **Parallel photon exchange experiment. a)** Gate sequence for parallel photon exchange over the router. **b)** Photon population of all three qubits vs. router swap time. The dots are experimental results, and the corresponding dashed lines are simulation results.

The results, detailed in Fig. 40, show that Fock states can swap between both pairs of modules simultaneously without interference or enhanced relaxation, as shown by comparison to master equation simulations, provided we do not swap too quickly. The drive frequencies for parallel swap processes in the router need frequency adjustments on the order of ∼100 kHz compared to the single *i*SWAP case, which we attribute to dynamic and static cross-Kerr effects due to the paired SNAIL drives. We reduce the pump strengths, slowing the gates from 600 ns to 1300 ns, as we observe additional decoherence when running two parallel processes at maximum pump strength. We do not believe this is a fundamental limitation, but can be improved in future experiments by optimized SNAIL and router design.

As further proof of the quantum coherence of parallel operations in the router, we repeat the Bell state generation protocol between Q_2 and Q_4 with the $M_1 - M_3$ *i*SWAP activated in parallel. Again, the pump strengths are decreased, slowing the inter-module swap time. We achieve a Bell state fidelity of 68.1 ± 0.79 %, while the simulated fidelity is 68.4 %. Here, the decrease of fidelity compared to the single Bell state generation process (which has a fidelity of 76.9 ± 0.76 %) is due to the longer gate time used for the $C_2 - C_4$ iSWAP in the presence of a parallel iSWAP operation.

4.2.5.4 Multi-parametric interaction

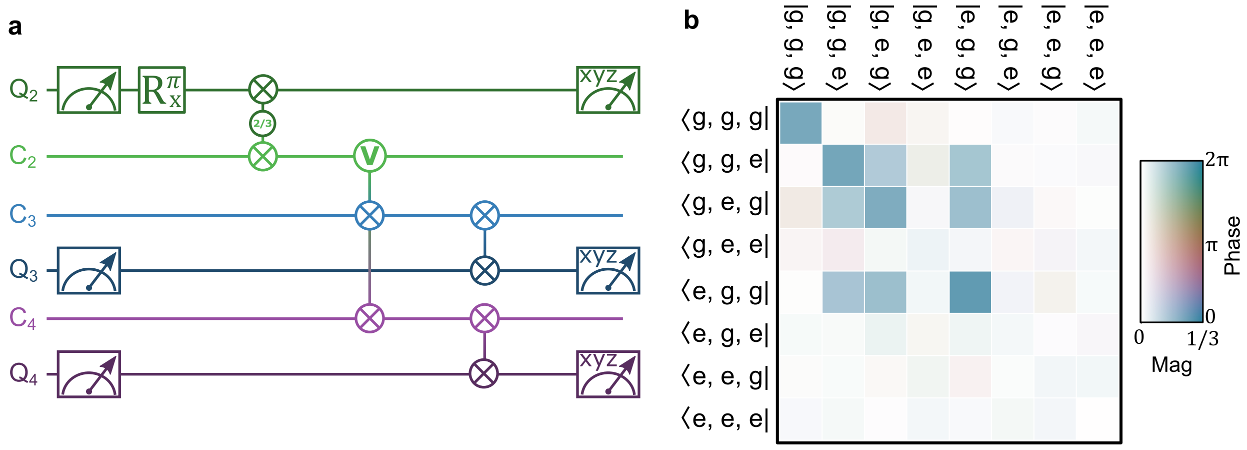

Figure 41: **Multi-parametric operation. a)** W state generation pulse sequence. Together, the $(i\text{SWAP})^{2/3}$ and 'V-iSWAP' gates create a W state distributed across Q_2, C_3, and C_4. The subsequent iSWAPs redirect the latter two components to Q_3 and Q_4, respectively. **b)** W state generation density matrix reconstructed from tomography. Each element in the density matrix is represented by a color using the Hue-Chroma-Luminance (HCL) color scheme. The amplitude of each element is mapped linearly to the Chroma and Luminance of the color, and the phase (from 0 to 2π) is mapped linearly to the Hue value. This color mapping scheme has the property that elements of the same amplitude are perceived equally by the human eye, so that the small magnitudes fades into the white background to avoid drawing the eye to small, noisy matrix elements. The observed fidelity of the state is 53.4 ± 2.56 %

To demonstrate further capabilities of our system, we also explored the use of two simultaneous swap processes that link one 'source' cavity to two 'target' cavities. We refer to such a processes as a 'V-iSWAP'. This form of interaction, for a certain duration, empties the source cavity, coherently and symmetrically swapping its contents into the target cavities. By combining the V-iSWAP with a $(i\text{SWAP})^{2/3}$ gate (which is realized by turning on the $\mathrm{Q}_2 - \mathrm{C}_2$ exchange interaction for $t = \arctan(\sqrt{2})/g^{\text{eff}})$ as shown in Fig. 41a, we can take a single photon from Q_2 and create a W-state shared among the three designated modules. We achieve a fidelity of 53.4 ± 2.56 % for this state. (see state reconstruction in Fig. 41b).

Currently, the utility of the above multi-parametric gates is limited by the slowdown of the gate times compared to individual iSWAPs. However, we believe this kind of multi-parametrically-pumped process should be further investigated, as it could be used to generate other multi-qubit gates in one step. Given the overhead in composing a multi-qubit gate from a series of two-qubit and single-qubit gates (for example, a Toffoli gate can be decomposed into 6 C-NOTs), performing these multi-parametric gates could give better performance in terms of gate fidelity by shortening the overall sequence time/gate count, even if operating at a lower rate.

We also note that in the above multi-parametric experiments, we observe no indication of fridge heating despite two strong pumps being applied to the SNAIL. As discussed earlier in section II, the replacement of attenuation with the reflective LPF at the MC plate gives the parametric pumping scheme an advantage of 20-30 dB in fridge heating tolerance for the same circulating powers at base.

4.2.6 Exchange gate fidelity discussion

4.2.6.1 Estimation of router gate fidelity

In the above discussion, we have listed only state fidelities of combined intra- and inter-module operations. Although our current device setup does not support tomography on the communication modes, the good agreement between our experiment results and the Lindblad master equation simulations (which consider only the measured T_1 decay and T_ϕ dephasing of the involved modes) indicates that our inter-module photon exchange fidelity is only limited by the mode coherence times and the duration of gate operations in the pulse sequence, more importantly, our parametric pumping tone doesn't introduce extra dephasing on any of the modes in the system. Thus, we can estimate the performance of the router itself by considering the gate time ($T^{i,j}_{gate}$) and the averaged decoherence rate ($\bar{\Gamma}_2$) of each communication cavity pair [48] C_i and C_j, i.e. $F^{i,j}_{i\mathrm{SWAP}} \simeq 1 - \bar{\Gamma}^{i,j}_2 * T^{i,j}_{gate}$. Using the values listed in Table 2 and 3, we calculate our best inferred iSWAP exchange fidelity $F^{1,4}_{i\mathrm{SWAP}} = 98.2\%$, the worst $F^{2,3}_{i\mathrm{SWAP}} = 94.7\%$, and the average $F^{avg}_{i\mathrm{SWAP}} = 96.9\%$.

4.2.6.2 Exchange interaction leakage mitigation

Our router design contains intermediate waveguide modes which are close in frequency to the communication cavity modes. Thus, it is possible that when we pump an exchange process between two cavities strongly, their states could leak into to the neighbouring waveguide modes. Here we show how this leakage can be fixed using the idea of "derivative removal by adiabatic gate (DRAG)" [55] at least for moderately long-lived waveguide modes.

Here we only consider the exchange process between two cavity modes c_1 and c_2 with their possible leakage to waveguide modes w_1 and w_2. Following the same derivations as we have done in Sec. 2.1, to see the effect of the leakage to waveguide mode, we write the rotating frame transformation operator in a slightly different way:

$$\begin{aligned} R'(t) = \exp\Big[& i\omega_s \hat{s}^\dagger \hat{s} + i(\omega_{c_1} - \delta/2)\hat{c}_1^\dagger \hat{c}_1 + i(\omega_{c_2} + \delta/2)\hat{c}_2^\dagger \hat{c}_2 \\ & + i(\omega_{c_1} - \delta/2)\hat{\mathrm{w}}_1^\dagger \hat{\mathrm{w}}_1 + i(\omega_{c_2} + \delta/2)\hat{\mathrm{w}}_2^\dagger \hat{\mathrm{w}}_2 \Big], \end{aligned} \tag{152}$$

where $\delta = \omega_{c_1} - \omega_{c_2} - \omega_p$. Then the Hamiltonian after RWA becomes:

$$\begin{aligned} \hat{\mathcal{H}}'^{\mathrm{RWA}}/\hbar = & \frac{\delta}{2}(\hat{c}_1^\dagger \hat{c}_1 - \hat{c}_2^\dagger \hat{c}_2) + (\delta/2 + \Delta_1)\hat{\mathrm{w}}_1^\dagger \hat{\mathrm{w}}_1 + (-\delta/2 + \Delta_2)\hat{\mathrm{w}}_2^\dagger \hat{\mathrm{w}}_2 \\ & + \eta(g_{c_1 c_2 s}\hat{c}_1^\dagger \hat{c}_2 + g_{c_1 \mathrm{w}_2 s}\hat{c}_1^\dagger \hat{\mathrm{w}}_2 + g_{c_2 \mathrm{w}_1 s}\hat{c}_2^\dagger \hat{\mathrm{w}}_1) + \mathrm{h.c.}, \end{aligned} \tag{153}$$

where $\Delta_i = \omega_{\mathrm{w}_i} - \omega_{c_i}$. Here, the cavity-cavity exchange term that we have seen in Eq. 149 still is present in Eq. 153. However, for $\eta g_{c_i w_j} \sim \delta + \Delta_j$ (strong pump), the effects of $\hat{c}_i^\dagger \hat{\mathrm{w}}_j$ terms (waveguide-cavity exchange) can no longer be neglected. To study how this effect can be canceled using DRAG method, we introduce the adiabatic transformation V that allows us to work entirely in the cavity-cavity subspace. This transformation is

$$V(t) = \exp\Bigg\{ \Bigg[-i\,\mathrm{Re}(\eta) \left(i \left(\frac{g_{c_1 \mathrm{w}_2 s}}{\Delta_2 - \delta} \hat{c}_1 \hat{\mathrm{w}}_2^\dagger + \frac{g_{c_2 \mathrm{w}_1 s}}{\Delta_1 + \delta} \hat{c}_2 \hat{\mathrm{w}}_1^\dagger \right) + \mathrm{h.c.} \right) \Bigg] \Bigg\}. \tag{154}$$

After the adiabatic transformation, we have

$$\hat{c}_i \rightarrow \hat{c}_i + \mathrm{Re}(\eta)\zeta_i \hat{\mathrm{w}}_j, \quad \hat{\mathrm{w}}_j \rightarrow \hat{\mathrm{w}}_j - \mathrm{Re}(\eta)\zeta_i \hat{c}_i \tag{155}$$

where $i, j = 1, 2;\ i \neq j;\ \zeta_1 = \frac{g_{c_1 \mathrm{w}_2 s}}{\Delta_2 - \delta};\ \zeta_2 = \frac{g_{c_2 \mathrm{w}_1 s}}{\Delta_1 + \delta}$. After the transformation, the leakage terms: $\hat{c}_1^\dagger \hat{\mathrm{w}}_2$ and $\hat{c}_2^\dagger \hat{\mathrm{w}}_1$ become:

$$\frac{i g_{c_1 \mathrm{w}_2 s} \omega_s}{\omega_d^2 - \omega_s^2} \left(\epsilon^y + \frac{\dot{\epsilon}^x}{\Delta_2 - \delta} \right) \hat{c}_1^\dagger \hat{\mathrm{w}}_2 + \frac{i g_{c_2 \mathrm{w}_1 s} \omega_s}{\omega_d^2 - \omega_s^2} \left(\epsilon^y + \frac{\dot{\epsilon}^x}{\Delta_1 + \delta} \right) \hat{c}_2^\dagger \hat{\mathrm{w}}_1 + h.c., \tag{156}$$

We find these terms can be cancelled under the condition:

$$\epsilon^y = -\frac{\dot{\epsilon}^x}{\Delta_2 - \delta} \text{ and } \epsilon^y = -\frac{\dot{\epsilon}^x}{\Delta_1 + \delta}. \tag{157}$$

Also, ac-Start shift (phase) error can be eliminated with the detuning δ that satisfies:

$$\delta/2 + \mathrm{Re}^2(\eta) \frac{g_{c_1 \mathrm{w}_2 s}^2}{(\Delta_2 - \delta)^2} \left(-\Delta_2 + \frac{3}{2}\delta \right) = 0;\ \delta/2 + \mathrm{Re}^2(\eta) \frac{g_{c_2 \mathrm{w}_1 s}^2}{(\Delta_1 + \delta)^2} \left(\Delta_1 + \frac{3}{2}\delta \right) = 0 \tag{158}$$

Thus, we have eliminated the leakage to the nearest waveguide mode, however, we also notice that this frame induces the term $c_i^\dagger \mathrm{w}_i$ with η^2. This error can also be removed by adding higher transformation to the system, but because of the fact that we drive the system much detuned, this term can be ignored when $\eta << 1$.

4.3 Engineering the coherence time for new module/router design

4.3.1 Upgraded quantum router device design

Mitigating loss due to SNAIL pump port and bias magnet. As discussed in Sec. 4.2.1.2, in our previous router design the two necessary elements for controlling the SNAIL device: the bias magnet and the pump port, were both placed inside the waveguide mode, as shown in Fig. 42a,b. These two elements form lossy modes that limit the coherence of the waveguide mode, thereby in turn limiting the performance of the router controlled operations.

Figure 42c,d depict our updated router design, where the SNAIL chip is relocated to an aluminum tube seamlessly connected to the bottom part of the waveguide body (machined as one monolithic piece). The pump port and the magnet are directly connected only to the SNAIL tube. This tube serves as a high-pass filter with a base mode frequency greater than 20 GHz, efficiently preventing the electromagnetic fields of the waveguide modes we use in the system to propagate into the tube. As a result, the direct couplings between the waveguide modes and the lossy elements are significantly suppressed, which greatly improves the coherence of the waveguide modes and releases the Purcell limits on communication modes due to their coupling with the router. Additionally, the SNAIL device is designed with an asymmetric antenna that extends into the waveguide, which creates sufficiently strong couplings between the SNAIL and the waveguide modes, and gives hybridization strengths that are comparable to our previous router design, i.e., $\left(\frac{g}{\Delta}\right)_{s\mathrm{w}} \sim 0.1 - 0.3$.

Improving router-communication cavity seam quality. Another major source of loss in our previous modular system originated from the seam at the joint of the communication cavity and the router. In the previous design, we used indium wires to seal around this seam, hoping to form a superconducting gasket between the two aluminum bodies, as shown in Fig. 43a. In our upgraded design, the sidewalls of the modules and waveguide are machined with diamond-coated end mills to provide a very smooth initial finish. We then further polish the machined device using sandpapers of progressively finer grits until a mirror-like finish is achieved, as shown in Fig. 43b. Note that the upper piece of the

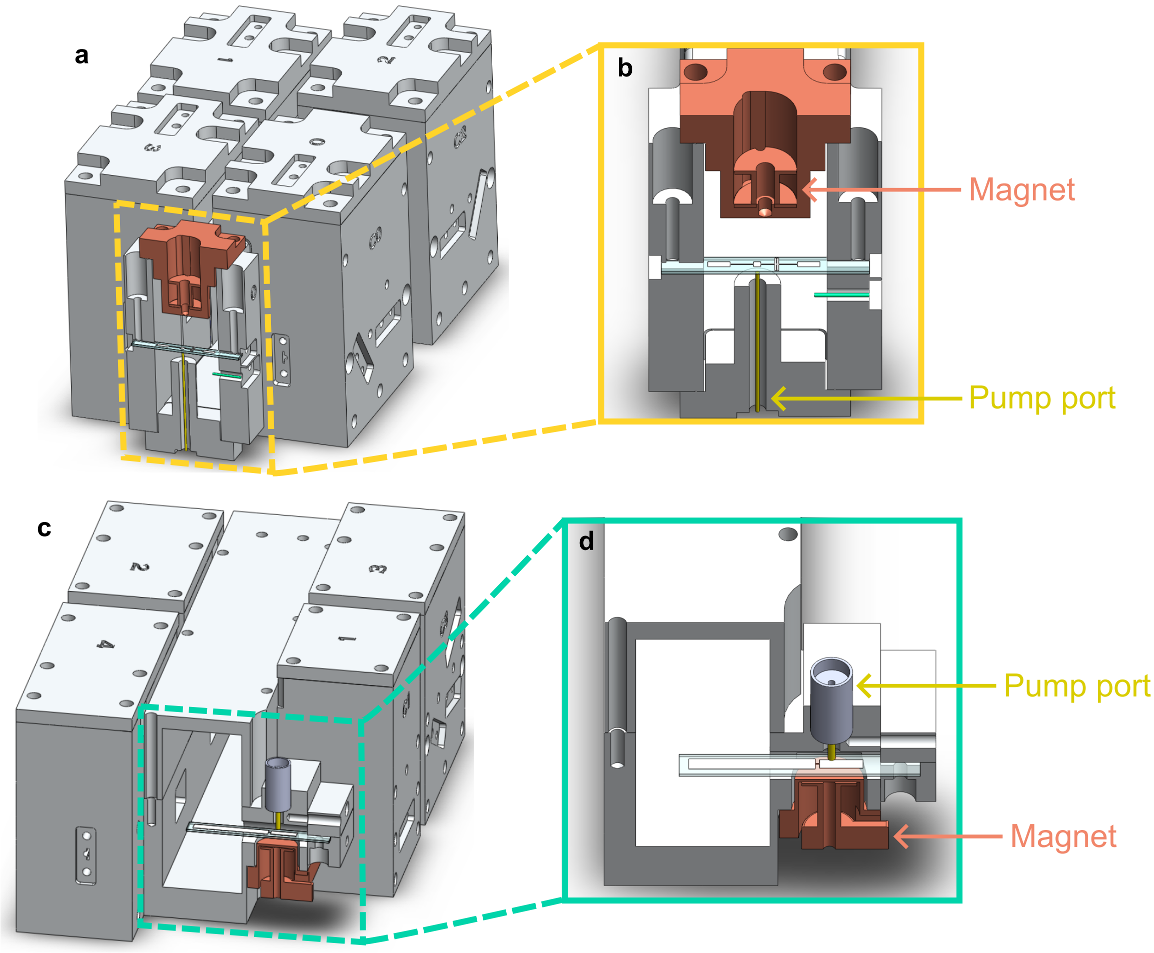

Figure 42: **Upgraded SNAIL port and magnet design.** **a)** and **b)** display the cross-section of the router at the SNAIL pump port in our initial design. Both the pump port and the magnet were positioned within the waveguide, creating low-Q modes that degrade the lifetime of router modes. On the other hand, Figures **c)** and **d)** illustrate our revised design, in which the SNAIL chip is moved to an aluminum tube that integrates seamlessly with the waveguide. As a result, the two loss-inducing control elements have been removed from the waveguide's interior, significantly reducing their direct coupling to the waveguide mode and thereby enhancing the waveguide modes' lifetimes.

waveguide is intentionally machined to be narrower than the bottom piece, and the modules are bolted only with the bottom piece, thus we can avoid potential air gap due to the misalignment between the two parts of the waveguide. This flat, polished aluminum-aluminum surface contact results in much lower loss compared to indium wire sealing (see the discussion on improving seam losses in [136]), as confirmed by our preliminary measurement results.

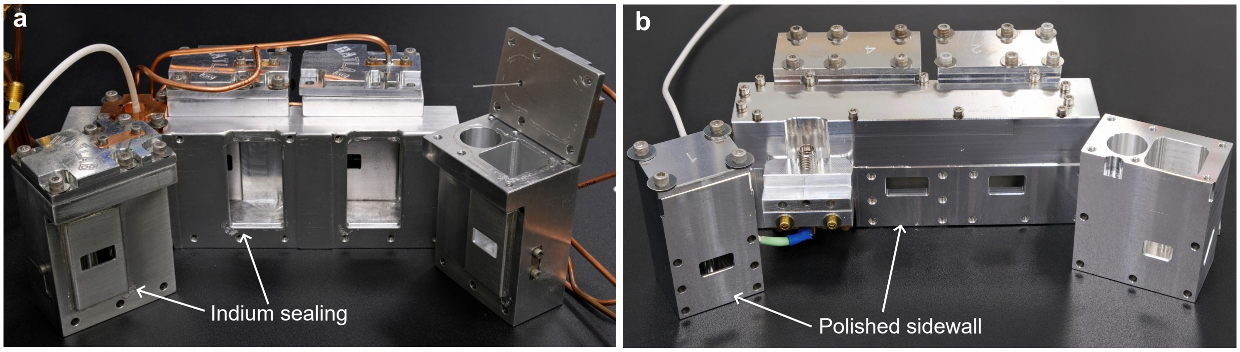

Figure 43: **Upgraded router-module connection. a)** shows the router-module connection interface in our old device, in which the gap between the communication cavity and the waveguide was sealed using indium wires. **b)** presents the new device, in which the waveguide and the cavity both have meticulously polished sidewalls. This improvement results in a significantly higher seam quality compared to our original design.

Preliminary measurement results. We have performed coherence time measurements on the upgraded waveguide + 4 communication cavity device. This measurement is performed without the SNAIL chip present, but with the SNAIL magnet and pump port attached. The measurement results are summarized in Table 5.

	W_1	W_2	W_3	W_4	C_1	C_2	C_3	C_4
f(GHz)	4.300	4.973	5.926	7.033	4.205	4.852	5.830	6.932
$T_1(\mu s)$	1210	736	280	597	290	241	58	85

Table 5: **Upgraded router mode parameters.**

We have achieved coherence times in the range of hundreds of microseconds for both the communication cavities and the waveguide modes, which are much longer than the values we measured in the previous design (Table 1 and 2), affirming the success of the redesign efforts I discuss above. It is noteworthy that all components in the upgraded design are still machined using 6061 alloy aluminum. The measured mode coherence values are comparable to those reported previously using much higher purity aluminum (4N-5N) [129, 137]. This further proves that the seam loss and direct couplings to lossy elements in the system is no longer limiting the mode lifetimes, and we speculate that we have now reached the material loss limitation of the alloy aluminum in our device.

This redesign project has provided us with valuable guidelines for developing future modular superconducting 3D devices, specifically with regards to engineering coupler control elements without introducing extra system loss, and making high quality connections between parts of modular devices. Moving forward, we are working on deploying this upgraded router device for larger-scale modular quantum devices with the expectation of significantly improved coherence and gate performance.

4.3.2 Improving protection against environmental decoherence sources

Besides the improvements in the device design, we have also been putting efforts in engineering better protection for our quantum device against environmental decoherence sources. Multiple previous studies have demonstrated that a significant source of decoherence for superconducting qubits arises from the breaking of Cooper pairs at the Josephson junction via the absorption of high-energy stray photons[138, 103, 139]. These high-energy photons can interact with our qubit device either by direct radiation that penetrate through the multilayered thermal and magnetic field shields that surrounds the sample, or by propagation along the control/readout lines which are directly connected to our device. To better isolate our device from these decoherence channels, we have adopted several improvements both in device packaging and fridge wiring scheme.

Figure 44 shows the upgraded device packaging that we adopted for our four-qubit module device (which I will introduce in Sec. 4.4.1). In this packaging, we connect lab-assembled Eccosorb filters (CR-110) [140], that can effectively block high-energy photons from our device port, with very short microwave cables. We also replaced part of the attenuation we put on the drive line with square-shaped, copper-body ones from Quantum Microwave

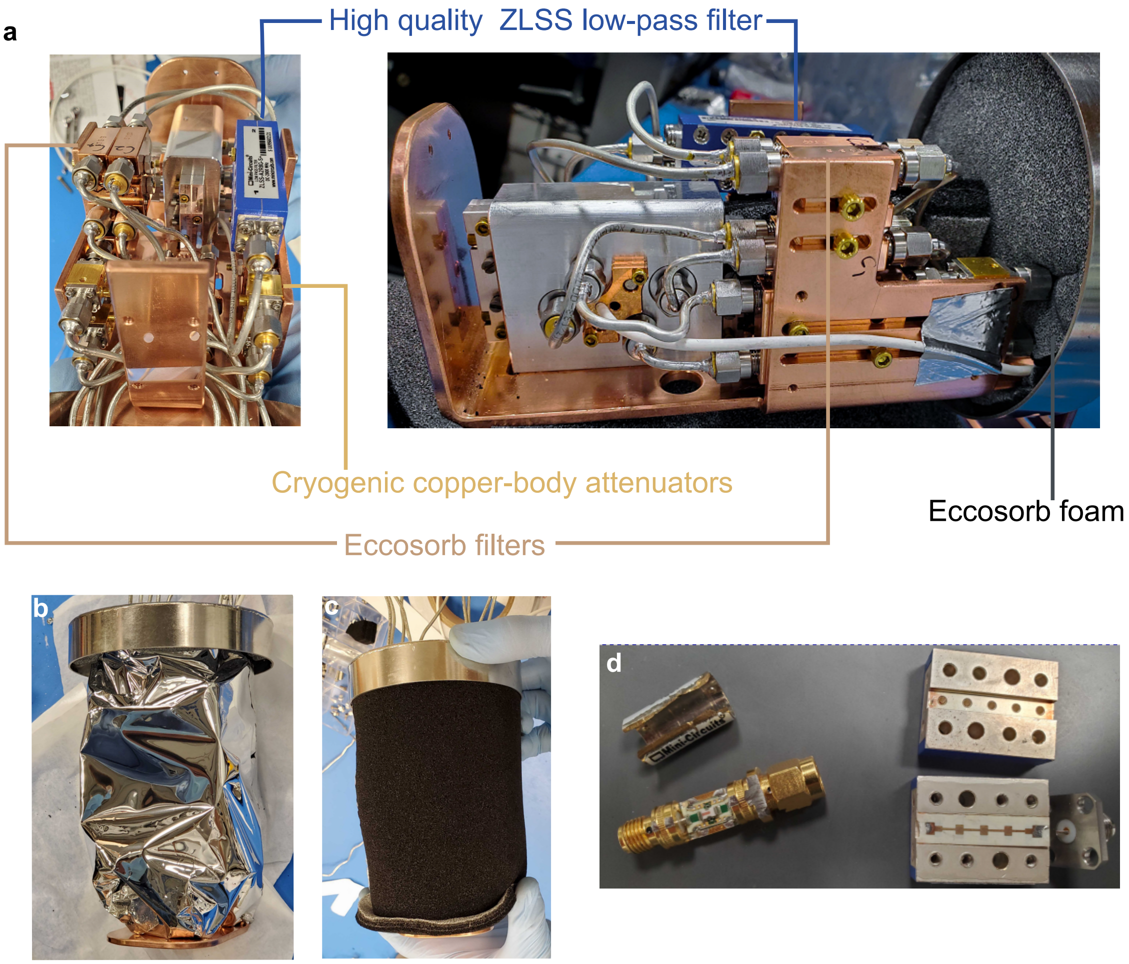

Figure 44: **Upgraded device packaging. a)** Filters and attenuators housed within the cryo-perm (Amumetal A4K) can. Each element is polished on its contact surface with the copper sample holder to ensure good thermal contact. **b)** and **c)** Additional layers of reflective (aluminzed Mylar, McMaster) and absorptive (Eccosorb foam, Digikey) materials within the cryo-perm can, for providing extra protection against high-energy stray photons. **d)** Interior of the Low-Temperature Co-Fired Ceramic (LTCC) filters and suspended substrate filters. The resonator-based suspended substrate has much better overall performance and can be more effectively thermalized with the fridge plate.

so that they can be tightly bolted to the cold sample holder for better dissipation of hot thermal noise. The low-pass filter we used for protecting the over-coupled SNAIL mode is also upgraded from ”low temperature co-fired ceramic” (LTCC) type filters (Fig. 44d left) to ”suspended substrate” type ones (Fig. 44d right), which offer much less refection loss in the stop band and transmission loss in the pass band, and has a solid aluminum body with bolt holes that we can also thermal-anchor well to the fridge plate.

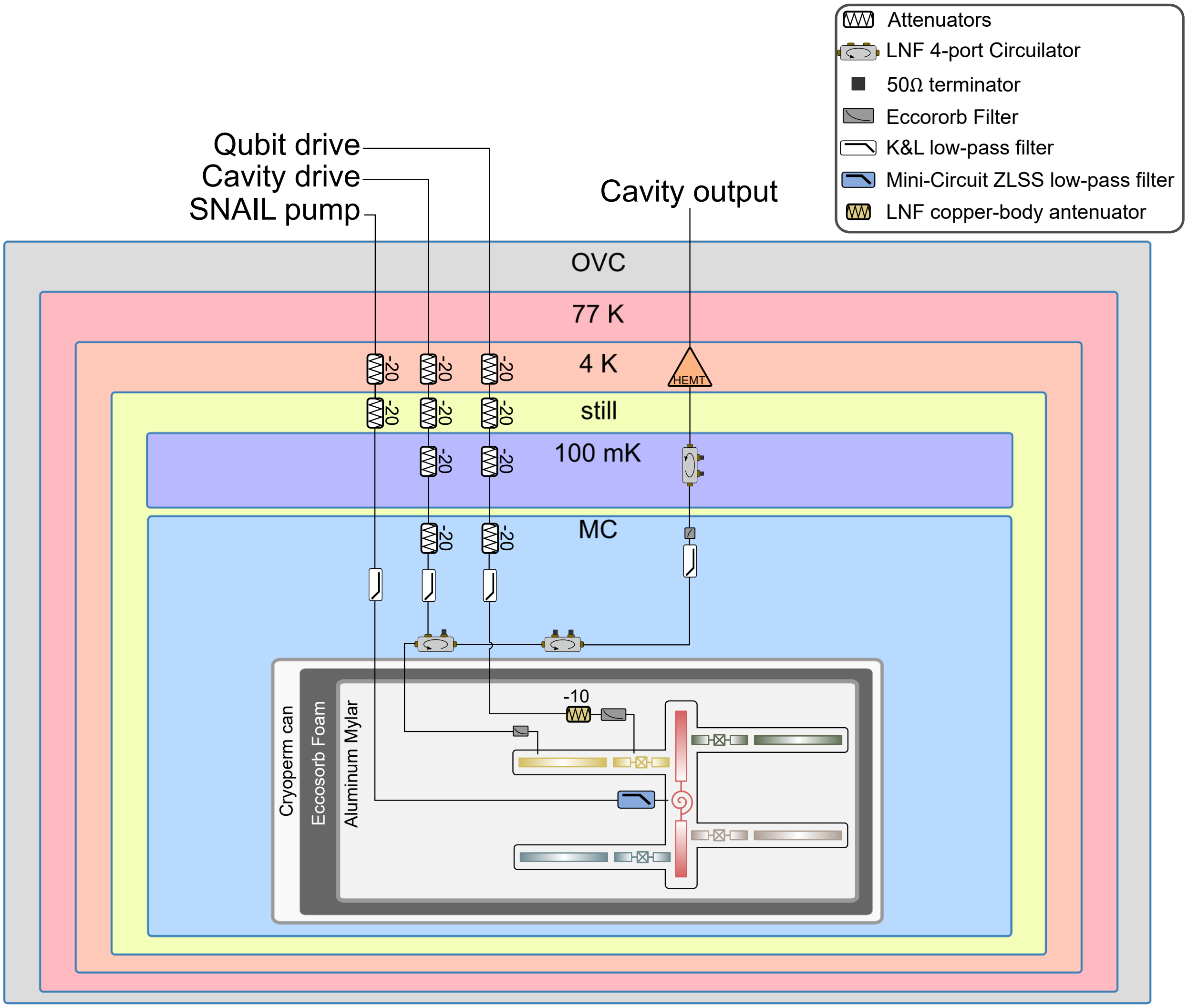

Figure 45: **Upgraded fridge wiring diagram.**

This whole package is then wrapped with layers of aluminum Mylar and Eccosorb foams that acts as extra reflective and absorptive shields against high-energy photons (Fig. 44b, c), and is finally put in a cryo-perm can for magnetic field shielding.

Figure 45 shows a representative example of the enhanced fridge wiring diagram that we now typically use for parametrically controlled quantum devices. In comparison with the wiring scheme we used in the previous experiment (Fig. 32), the incorporation of additional filters and attenuators on the drive line, along with extra insulators on the output line have given us a much better overall device performance in our four-qubit module device, as will be listed in Table 6.

4.4 Expanding modular architecture

4.4.1 The 4-qubit quantum module

In Section 4.2, I've discussed the design and realization of our prototype modular quantum computer based on a quantum state router. The experiments on that device primarily aimed to test the router's functionality as a 4-port device that realizes all-to-all communication among four basic modules, each was designed to host a single transmon qubit. To realize the full modular structure quantum computer as depicted in Fig. 25, the next scaling step is to construct compact quantum modules that can support all-to-all connections with a larger number of qubits.

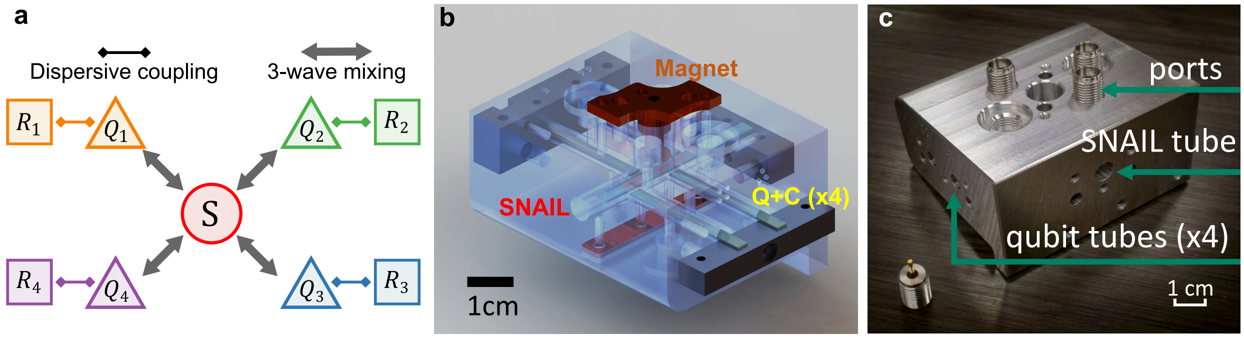

Figure 46: **Schematic and photograph of the 4-qubit module. a)** Coupling scheme of the 4-qubit module. Four transmons qubits ($Q_1 - Q_4$) are directly coupled to a central SNAIL mode (S). Each qubit has a dedicated readout resonator (R). **b)** 3D rendering of the device design. The SNAIL and qubit chips are housed within five individual aluminum tubes. **c)** Photograph of the device.

Based on the methods we have developed in building the quantum state router, one intuitive approach we conceived for connecting multiple qubits in the quantum module is to use a similar SNAIL based three-wave-mixing coupling scheme. However, unlike in the router design where we need the intermediate waveguide modes to distribute the central SNAIL's non-linearity across a large 3D space to accommodate multiple modules, the module design is more straightforward. In the module design, we skip the intermediate modes and directly couple multiple qubits to the SNAIL chip, this not only mitigates the extra frequency crowding issue induced by the intermediate modes, but also aligns with the module's requirement for compactness.

Coupling scheme and gate operations. Figure 46a shows the coupling scheme we designed for our four-qubit quantum module. Four transmon qubits $Q_1 - Q4$ (each with a dedicated readout resonator $(R_1 - R_4)$) are directly coupled to a central SNAIL mode (S), and forms three-wave-mixing Hamiltonian:

$$\hat{\mathcal{H}}^{\mathrm{3wm}}_{Mod}/\hbar = \sum_{i\neq j} g_{q_i q_j s}(\hat{q}_i^\dagger \hat{q}_j \hat{s} + \hat{q}_i \hat{q}_j^\dagger \hat{s}^\dagger). \tag{159}$$

This three-wave-mixing Hamiltonian takes the same form as the one we created between the communication cavity modes and the SNAIL mode in Eq.147, and the interaction coefficient $g_{q_i q_j s}$ also follows similar non-linearity propagation rule: $g_{q_i q_j s} \approx 6 g_{sss}(\frac{g}{\Delta})_{q_i s}(\frac{g}{\Delta})_{q_j s}$. By pumping on the SNAIL mode at the difference of of the two qubits' $|g\rangle \leftrightarrow |e\rangle$ transition frequencies, i.e. $f_p = |f^{ge}_{q_i} - f^{ge}_{q_j}|$, we can activate the $Q - Q$ exchange interaction:

$$\hat{\mathcal{H}}^{\mathrm{eff}}_{qq}/\hbar = g^{\mathrm{eff}}_{q_i q_j} \hat{q}_i^\dagger \hat{q}_j + g^{\mathrm{eff}^*}_{q_i q_j} \hat{q}_i \hat{q}_j^\dagger. \tag{160}$$

Again, this effective Hamiltonian closely resembles the $C - C$ exchange interaction we had in Eq. 149. However, the qubit-qubit exchange interaction here behaves quite differently from the "beam-splitter" gate between cavities, since both modes involved here are actually two-level systems. The time evolution operator of this Hamiltonian can be explicitly written down as a simple 4-by-4 matrix:

$$\hat{U}_{qq}(t) = \exp\left[\frac{i\hat{\mathcal{H}}^{\mathrm{eff}}_{qq} t}{\hbar}\right] = \begin{bmatrix} 1 & 0 & 0 & 0 \\ 0 & \cos(gt) & i\sin(gt)e^{-i\phi_p} & 0 \\ 0 & i\sin(gt)e^{i\phi_p} & \cos(gt) & 0 \\ 0 & 0 & 0 & 1 \end{bmatrix}, \tag{161}$$

in which $g = \mathrm{abs}\left(g^{\mathrm{eff}}_{q_i q_j}\right)$ and $\phi_p = \arg\left(g^{\mathrm{eff}}_{q_i q_j}\right)$. Note that the $|11\rangle\langle 11|$ component in this matrix is constant 1, as a result, instead of having to make the assumption that the $|11\rangle$ state was never occupied as we did in section 4.2, this $Q - Q$ time evolution operator naturally takes the same form as the iSWAP family operators. In particular, the $\sqrt{i\text{SWAP}}$ operator of this family, created by applying the pump for $t = \frac{\pi}{4g}$, is a highly potent universal two-qubit quantum gate [62, 61]. and we can use this $\sqrt{i\text{SWAP}}$ to gate compile arbitrary two-qubit operations in the module system.

In addition, using the $g_{qss}(\hat{q}^\dagger \hat{s}\hat{s} + \hat{q}\hat{s}^\dagger \hat{s}^\dagger)$ three-wave mixing term, we can perform single qubit sub-harmonic gate by driving the SNAIL mode around at half of the qubit mode frequency. The details of this sub-harmonic qubit control scheme have been discussed in Sec. 2.2.1 and Ref. [56]. This allows all the single- and multi-qubit operations within the module to be performed via a single SNAIL port.

Brief overview of the device design. Based on this qubit-SNAIL coupling scheme, we have designed and build our 4-bit module device, as shown in Fig. 46b,c. The device contains one SNAIL chip, and four transmon qubits with stripline readout resonators [91] hosted in five individual aluminum tubes. Each mode has a dedicated control/readout port that are made with commercial SMA waveguide probes. The qubit tubes are positioned perpendicular to the central SNAIL tube, with their openings arranged in a way that they do not directly face each other. This layout effectively limits the direct qubit ZZ interactions, which is usually a challenging engineering problem in such compact multi-qubit devices with all-to-all connectivity. With near-zero direct qubit-qubit coupling, the qubit static ZZ interaction primarily arises from the qubits' mutual coupling to the SNAIL mode. Given our designed hybridization strength of $(\frac{g}{\Delta})_{qs} \sim 0.03$, the qubit cross-Kerr ($ZZ$ interaction) coefficient $\chi_{q_i q_j}$ is on sub-kilohertz level. This result is further validated through our experimental measurements based on conditioned Ramsey experiments.

Preliminary measurement results. We have performed basic characterizations, as well as single and two-qubit gates on this four-qubit quantum module. The result are summarized in in Table 6.

The coherence times and gate fidelities we measured in this device have shown substantial improvements in comparison to those in the prior router experiment. We attribute these improvements to various design adjustments and drive line upgrades, that will be discussed in detail in Sec. 4.3. Currently, we are working on further improve gate fidelities and

	f (GHz)	T_1 (μs)	T_{2R} (μs)	T_{2E} (μs)	Single-qubit gate fidelity	Sub-harmonic gate time (ns)
Q_1	3.871	91.0	32.0	34.0	99.80 %	220
Q_2	4.385	50.3	30.9	39.9	99.84 %	12.1
Q_3	4.863	60.3	17.9	30.3	99.85 %	34.2
Q_4	5.863	68.3	34.5	41.7	99.88 %	38.7
S	4.276	3.03	1.52			

Table 6: **Mode life time and gate fidelities in the four-qubit module.**

mode coherence in this four-qubit module device. Moreover, we are investigating multi-qubit interactions [61] and exploring potential qubit encoding schemes for error-correction [141, 142] algorithms within this system.

4.4.2 Module-router coupling scheme

Figure 47 presents a schematic representation of our proposed future integration of a four-qubit module with the quantum router to construct a 16-qubit modular quantum processor. The coupling of the router-module is realized through an additional stripline resonator that couples with both the SNAIL mode of each module and a designated waveguide mode in the router. This resonator serves as the communication mode between the router and the module, just like the communication cavity we used in section 4.2.

This structure preserves the advantage we had in the router + 4 single-qubit-module device design. Namely, the use of a resonator mode as communication mode accommodates different kind of module encodings, and serves as a separation point between the router and each module. To make each module compatible with the router, only the communication resonator needs to be carefully designed to match with its designated waveguide mode, while the qubit frequencies can be the same for each module without worrying about frequency collision with qubits in other modules, because of their negligible direct coupling with the

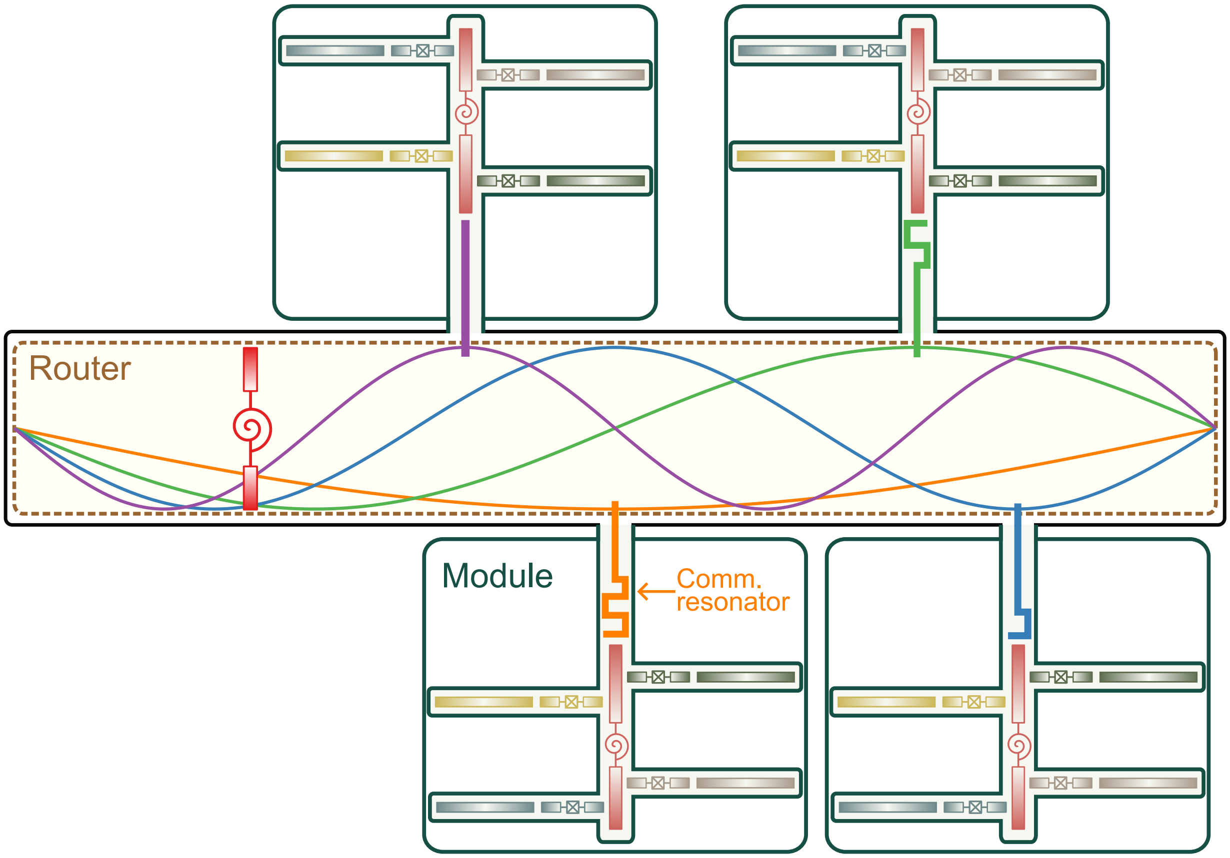

Figure 47: **Schematic of our proposed 16-qubit modular quantum processor.** Our previously designed quantum router is used to couple four 4-qubit modules. Each module has an additional stripline resonator that couples both to the SNAIL mode in the module and an intermediate waveguide mode in the router. This resonator functions as the communication mode between different modules. To make each module be compatible with the router, only the shape of these stripline resonators need to be adjusted to create desired coupling with the waveguide modes and to avoid frequency crowding during the inter-module operations. While the design of the qubit set and SNAIL mode within each module could be the same.

router modes.

To further scale up this modular structure for a greater number of qubits, we need to contemplate the idea of linking multiple routers together, following the similar idea of how each module and the router is linked, and build the whole device in a self-similar, tree-like structure.

4.4.3 Other modular coupling schemes

The aforementioned design scheme provides a realistic approach for the physical realization of the modular structure we originally proposed in Fig. 25. The methods and techniques we have developed in building the router and module system not only facilitate our current design but also pave the way for envisioning the development of modular quantum processors with alternative architectures. It's important to note that the structure depicted in Fig. 47 is not the only blueprint for scaling up a modular system. Moreover, it was not initially apparent whether the original proposal was indeed the most hardware-efficient strategy for executing quantum algorithms. To further investigate these considerations, we have recently initiated a collaborative co-design project with computer scientists, Prof. Alex Jones and his PhD student Evan McKinney, to explore alternative architectural possibilities for modular quantum computers with the focus on optimizing computational efficiency [143].

One of the major results that come out from this co-design project are the "Corral" structure qubit-qubit connection schemes, as depicted in Fig. 48. These connection schemes has the same number of logical qubits (16) as we have in the structure shown in Fig. 47. In Figure 48, the red vertical cylinders represent SNAIL couplers and green/yellow horizontal bars are the qubits coupled between them. The qubit coupling architecture implements an octagonal ring of modules, each consisting of 4 qubits, forming a pattern of fence-post connections. The structure in Fig. 48a is the most straightforward to implement physically - each qubit is coupled to its two nearest adjacent SNAILs, which we denoted as Corral$_{1,1}$, and resulting topology is shown in Fig. 48b. Figure 48c and d shows a slightly modified version, in which the second fence of each module is connected to the second nearest neighbor, which consequently decreases the average distance between all pairs of qubits. Both of these structures can be physically built using the techniques and methods we have developed in the compact 4-qubit module device.

Despite initially appearing similar to a ring, we note that the Corral topoligies actually

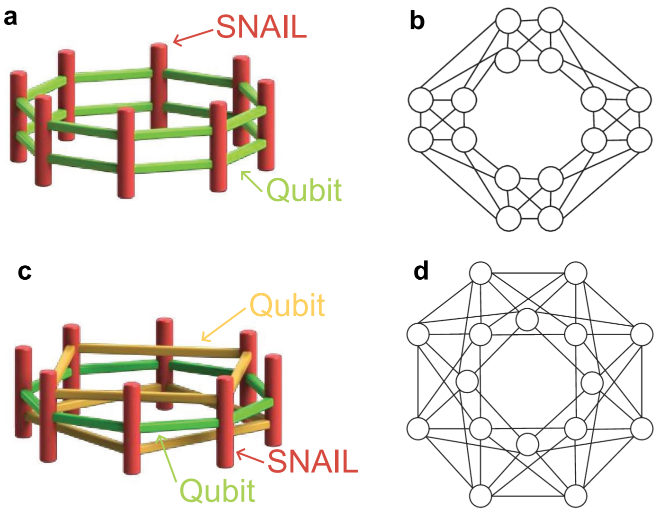

Figure 48: **16-qubit modular device based on the "Corral" architectures. a)** Coupling diagram of the Corral$_{1,1}$ structure. Each red pole represents a SNAIL chip, while the green bars represent qubit chips. **b)** Topology of the Corral$_{1,1}$ structure. **c)** Coupling diagram of the Corral$_{1,2}$ structure. The yellow bars represents qubits that connect between second nearest neighbouring SNAILs, which give shorter averaged qubit-qubit communication distance in the whole device. **d)** Topology of the Corral$_{1,2}$ structure.

exhibit a coupling structure similar to a 4-D hypercube, which has rich local connections and shows even higher operation efficiency in terms of state routing and quantum algorithm decomposition [143]. The Corrals could be further scaled by adding more posts (modules) in the ring; or with more complex designs that connect Corrals with Tree-like modules or layouts with Corrals in a lattice pattern.

In conclusion,our research into the design and realization of the quantum router and module system has helped us gained invaluable experiences in integrating SNAIL couplers and qubits in 3D devices of modular structures. These experiences allow us to venture into increasingly complex qubit connection topoligies, enabling us to move toward the future physical realizations of larger-scale and more computationally efficient modular structure quantum computers.

5.0 Multi-parametric Interactions and Their Applications

The previous chapters have provided a detailed discussion on the theory and physical realization of parametric quantum operations. Most of these discussions focus on performing two-qubit exchange interactions using a three-wave-mixing coupler device, which requires a monochromatic external pump at the frequency difference between the two target modes. Interestingly, when multiple parametric processes are activated simultaneously, they can give rise to entirely new quantum dynamics [144, 145, 146]. In this chapter, will present examples of how multi-parametric interactions can be used to construct innovative multi-qubit gates. Additionally, I will introduce a multi-parametric-based approach to perform longitudinal measurement on the transverse components of a transmon qubit, supported by preliminary experimental data. The gates introduced in this chapter, along with the experiment on parametric qubit measurement, further demonstrate the vast potential of parametric interactions in performing quantum operations that go beyond conventional gate operations.

5.1 Novel multi-qubit gates

5.1.1 Multi-parametric two-qubit gates

In Section 2.2.2, I briefly introduced how the two seemingly different gates, the iSWAP gate and the bSWAP gate, can be converted into one another by simply adding single qubit gates before and after the two-qubit gates. In the language of group theory for gate operations, these two gates areconsidered "locally equivalent" as one gate can be transformed by introducing single qubit gates before and after it into the other [147], as illustrated in Fig. 49a. This local equivalence can be visualized using the mathematical tool known as the "Weyl Chamber" [148, 66]. As depicted in Fig. 49b, each unique type of two-qubit gate can be represented by a specific coordinate (c_1, c_2, c_3) within or on the surface of this chamber,

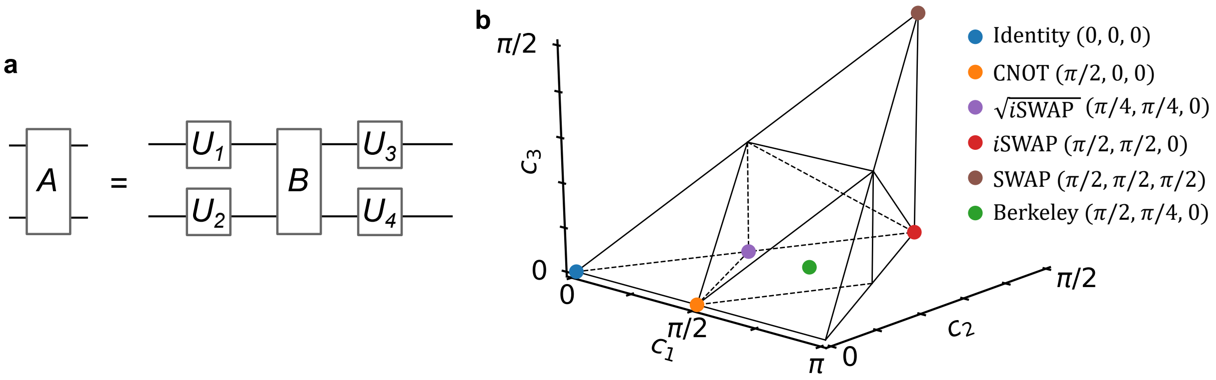

Figure 49: **'Local equivalence' of two qubit gates and the Weyl Chamber.** **a)** Circuit demonstration for the 'local equivalence' of two qubit gates. The two two-qubit gates A and B are 'locally equivalent' if there exist a set of single qubit gates $U_1 - U_4$ such that A can be decomposed into B using this circuit template. **b)** The Weyl Chamber representation for the unique types of two-qubit gates. Each point in this chamber is described by three coordinates (c_1, c_2, c_3), representing a distinct class of two-qubit gates up to local unitary equivalence. The locations of some commonly used two-qubit gates are labeled in the figure.

where locally equivalent 2Q gates, differing only by 1Q gates, are mapped to the same coordinate. For example, the iSWAP and bSWAP gates share the same coordinate $(\frac{\pi}{2}, \frac{\pi}{2}, 0)$. When we tune the duration of the parametric pump, the coordinates of the $(i\text{SWAP})^\alpha$ gates will move along the line connecting the 'Identity' point to the 'iSWAP' gate point, as depicted in Fig. 50. Meanwhile, the coordinates for the $(\text{bSWAP})^\alpha$ gates will move along the same trajectory. However, when both the difference frequency and sum frequency pumps are activated simultaneously, a new system Hamiltonian arises:

$$\hat{\mathcal{H}}_{GC}/\hbar = \eta_c(\hat{\sigma}_{a,+}\hat{\sigma}_{b,-} + \hat{\sigma}_{a,-}\hat{\sigma}_{b,+}) + \eta_g(\hat{\sigma}_{a,+}\hat{\sigma}_{b,+} + \hat{\sigma}_{a,-}\hat{\sigma}_{b,-}), \tag{162}$$

in which η_g and η_c are the coefficients for the bSWAP and iSWAP interactions, respectively. We refer to this Hamiltonian as the 'GC' interaction Hamiltonian, as terms activated by these two pumps resemble the Hamiltonians found in the 'gain' and 'conversion' processes of parametric amplifiers [144, 145, 146]. The time evolution operator of this interaction can be written as:

$$\hat{U}_{gc}(t) = \begin{bmatrix} \cos(\eta_g t) & 0 & 0 & -i\sin(\eta_g t) \\ 0 & \cos(\eta_c t) & -i\sin(\eta_c t) & 0 \\ 0 & -i\sin(\eta_c t) & \cos(\eta_c t) & 0 \\ -i\sin(\eta_g t) & 0 & 0 & \cos(\eta_g t) \end{bmatrix}. \tag{163}$$

Figure 50 shows the Weyl Chamber coordinates of gates produced by turning on the sum and difference frequency pumps for various durations (t) with different relative coefficient ($\frac{\eta_g}{\eta_c}$). The results show that even though the iSWAP/bSWAP family of gates are fundamentally different than the CNOT gate, activating the bSWAP and iSWAP interactions simultaneously with matched coefficients causes the trajectory of the gate's Weyl Chamber coordinates to move along the line connecting the Identity and the CNOT gate. Consequently, a CNOT-equivalent gate can be constructed by implementing the 'GC' interaction with $\eta_c = \eta_g$ and $t = \frac{\pi}{4\eta_g}$. Another noteworthy case is when $\eta_c = 3\eta_g$, and $t = \frac{\pi}{8\eta_g}$. This operation yields a B (Berkeley) gate, which has been demonstrated to be capable of constructing any arbitrary two-qubit quantum gate with a minimal number of both two- and single-qubit gates [149]. In fact, by running the pump duration (t) and the relative coefficient ($\frac{\eta_g}{\eta_c}$), we can produce any gate on the bottom plane of the Weyl Chamber.

5.1.2 Parametric three-qubit gates

The multi-parametric interactions can also be extended to involve more than just two qubits, enabling the creation of multi-qubit gates that act on three or more qubits. Although circuit-based quantum computing only requires a set of universal single- and two-qubit gates to compile an arbitrary quantum algorithm [1], having direct access to gates that manipulate three or more qubits can still be helpful, as these gates can potentially accelerate the execution of quantum circuits by reducing the number of gates needed, and facilitate the generation of highly entangled multi-qubit states in a single operation. They also appear frequently in error correction, for instance using a third, ancillary, qubit to measure the

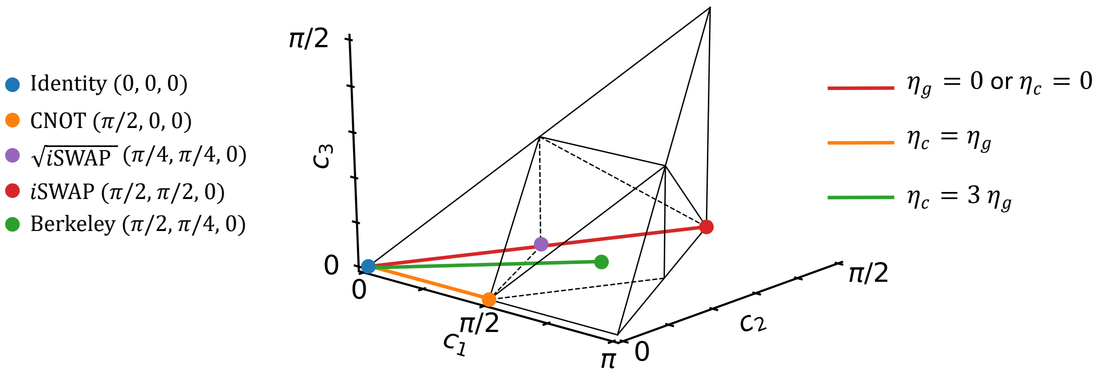

Figure 50: **The trajectories of two-qubit gates' Weyl Chamber coordinates produced by continuous single- and multi-parametric interactions..** For single bSWAP or iSWAP family gates, changing the length of the parametric pump causes trajectory to move along the line connecting the Identity gate and the iSWAP gate. When the bSWAP and iSWAP interactions are turned on simultaneously with matched coefficients (i.e. $\eta_c = \eta_g$), the trajectory produced by different pump lengths aligns with the line connecting the Identity and the CNOT gate. When $\eta_c = 3\eta_g$, the trajectory moves toward the Berkeley gate starting from the Identity gate.

parity of two data qubits. As example demonstrations of this idea, we present two 3-qubit gates realized via multi-parametric pumping.

The "V-SWAP" gate. The "V-SWAP" gate was briefly introduced in Sec. 4.2.5.4. By turning on the exchange interaction between one source qubit mode A and two target qubit modes B and C with matched interaction coefficient η, we get the effective system Hamiltonian:

$$\hat{\mathcal{H}}_{\text{VSWAP}} = \eta(\hat{\sigma}_{a,+}\hat{\sigma}_{b,-} + \hat{\sigma}_{a,-}\hat{\sigma}_{b,+}) + \eta(\hat{\sigma}_{a,+}\hat{\sigma}_{c,-} + \hat{\sigma}_{a,-}\hat{\sigma}_{c,+}), \tag{164}$$

This interaction can be understood as evenly distributing the photon stored in mode A to mode B and C. By turning on this interaction for duration $t = \arccos\left(1/\sqrt{3}\right)/(\sqrt{2}\eta)$, we get the operator for the ‘V-SWAP” gate.

$$\hat{U}_{\text{VSWAP}} = \begin{bmatrix} 1 & 0 & 0 & 0 & 0 & 0 & 0 & 0 \\ 0 & \frac{1}{6}(3+\sqrt{3}) & \frac{1}{6}(-3+\sqrt{3}) & 0 & -\frac{1}{\sqrt{3}} & 0 & 0 & 0 \\ 0 & \frac{1}{6}(-3+\sqrt{3}) & \frac{1}{6}(3+\sqrt{3}) & 0 & -\frac{1}{\sqrt{3}} & 0 & 0 & 0 \\ 0 & 0 & 0 & \frac{1}{\sqrt{3}} & 0 & -\frac{1}{\sqrt{3}} & -\frac{1}{\sqrt{3}} & 0 \\ 0 & \frac{1}{\sqrt{3}} & \frac{1}{\sqrt{3}} & 0 & \frac{1}{\sqrt{3}} & 0 & 0 & 0 \\ 0 & 0 & 0 & \frac{1}{\sqrt{3}} & 0 & \frac{1}{6}(3+\sqrt{3}) & \frac{1}{6}(-3+\sqrt{3}) & 0 \\ 0 & 0 & 0 & \frac{1}{\sqrt{3}} & 0 & \frac{1}{6}(-3+\sqrt{3}) & \frac{1}{6}(3+\sqrt{3}) & 0 \\ 0 & 0 & 0 & 0 & 0 & 0 & 0 & 1 \end{bmatrix} \tag{165}$$

This gate can be used to generate a maximally entangled three-qubit state known as the “W State”. By initializing the system in the simple product state $|100\rangle$ and subsequently applying the VSWAP gate, the system can be prepared to the desired state $\frac{1}{\sqrt{3}}(|100\rangle+|010\rangle+|001\rangle)$ in one step.

The “Δ-SWAP” gate. Another interesting three-qubit gate is the “Δ-SWAP” gate, which can be constructed by simultaneously turning on all three exchange interactions between three mode A, B and C, with matched coefficient η, and a special set of relative pumping phase $\{\phi_{ab} = \pi/2, \phi_{ac} = -\pi/2, \phi_{bc} = \pi/2\}$. The effective Hamiltonian can be written as:

$$\begin{aligned} \hat{\mathcal{H}}_{\Delta\text{SWAP}} = \eta \big[& e^{\pi/2}\hat{\sigma}_{a,+}\hat{\sigma}_{b,-} + e^{-\pi/2}\hat{\sigma}_{a,-}\hat{\sigma}_{b,+} + e^{-\pi/2}\hat{\sigma}_{a,+}\hat{\sigma}_{c,-} \\ & + e^{\pi/2}\hat{\sigma}_{a,-}\hat{\sigma}_{c,+} + e^{\pi/2}\hat{\sigma}_{b,+}\hat{\sigma}_{c,-} + e^{-\pi/2}\hat{\sigma}_{b,-}\hat{\sigma}_{c,+} \big] . \end{aligned} \tag{166}$$

By setting pump duration $t = 2/(3\sqrt{3}\pi)$, we get the operator for the ‘Δ-SWAP” gate.

$$\hat{U}_{\Delta\text{SWAP}} = \begin{pmatrix} 1 & 0 & 0 & 0 & 0 & 0 & 0 & 0 \\ 0 & 0 & 0 & 0 & 1 & 0 & 0 & 0 \\ 0 & 1 & 0 & 0 & 0 & 0 & 0 & 0 \\ 0 & 0 & 0 & 0 & 0 & 0 & 1 & 0 \\ 0 & 0 & 1 & 0 & 0 & 0 & 0 & 0 \\ 0 & 0 & 0 & 1 & 0 & 0 & 0 & 0 \\ 0 & 0 & 0 & 0 & 0 & 1 & 0 & 0 \\ 0 & 0 & 0 & 0 & 0 & 0 & 0 & 1 \end{pmatrix} \tag{167}$$

This gate exhibits a unique behavior: based on the parity of the initial state, it circulates the photon excitation among the three modes in opposite directions. Using this gate, we can generate a "GHZ-like" state in the three mode system by starting from the initial product state $|1\rangle \otimes |0\rangle \otimes \frac{1}{\sqrt{2}}\left(|0\rangle + |1\rangle\right)$, and applying this gate. The final state generated by this gate gives: $\frac{1}{\sqrt{2}}(|001\rangle + |110\rangle)$, which is a "GHZ-like" maximally entangled three qubit state.

5.2 Qubit transverse component readout with a dissipative SNAIL coupler

The aforementioned multi-parametric interaction can also be used to construct a transverse component readout on a qubit. Before we delve into the discussion of this experiment, let us briefly review the existing readout schemes for superconducting qubits (transmons).

Traditionally, the readout of a transmon qubit is performed using the dispersive readout technique [19, 20]. The core Hamiltonian term used in this readout scheme is the qubit-cavity cross-Kerr term:

$$\hat{\mathcal{H}}_{disp,z}/\hbar = \frac{\chi}{2}\hat{\sigma}_z \hat{c}^\dagger \hat{c}, \tag{168}$$

in which $\hat{c}$ and $\hat{c}^\dagger$ are the annihilation and creation operators of a readout cavity that is dispersively coupled to the qubit, while $\hat{\sigma}_z$ denotes the Pauli-Z operator of the qubit. The coefficient χ is generally referred to as the "dispersive shift", which means that different $\hat{\sigma}_z$ eigenvalues of the qubit will change the cavity frequency by χ. Therefore, by applying a near-resonance microwave drive to the cavity mode and monitoring the phase and/or amplitude shift of the returned signal, we can perform a continuous, quantum non-demolition (QND) measurement along the σ_z axis of the qubit. Tomographic measurement along the σ_x and σ_y axes (transverse components) can be done by applying a pre-rotation on the qubit before the σ_z measurement. Alternatively, it is also possible to perform continuous QND measurements on the transverse components of the qubit. In the work presented by Vool et al.[150], this was realized by engineering an effective Hamiltonian term that looks similar to Eq. 168 but with the $\hat{\sigma}_z$ operator replaced by $\hat{\sigma}_x$/ $\hat{\sigma}_y$ operators, allowing for dispersive readout of the corresponding qubit components.

Despite the widespread adoption of the dispersive readout scheme in superconducting

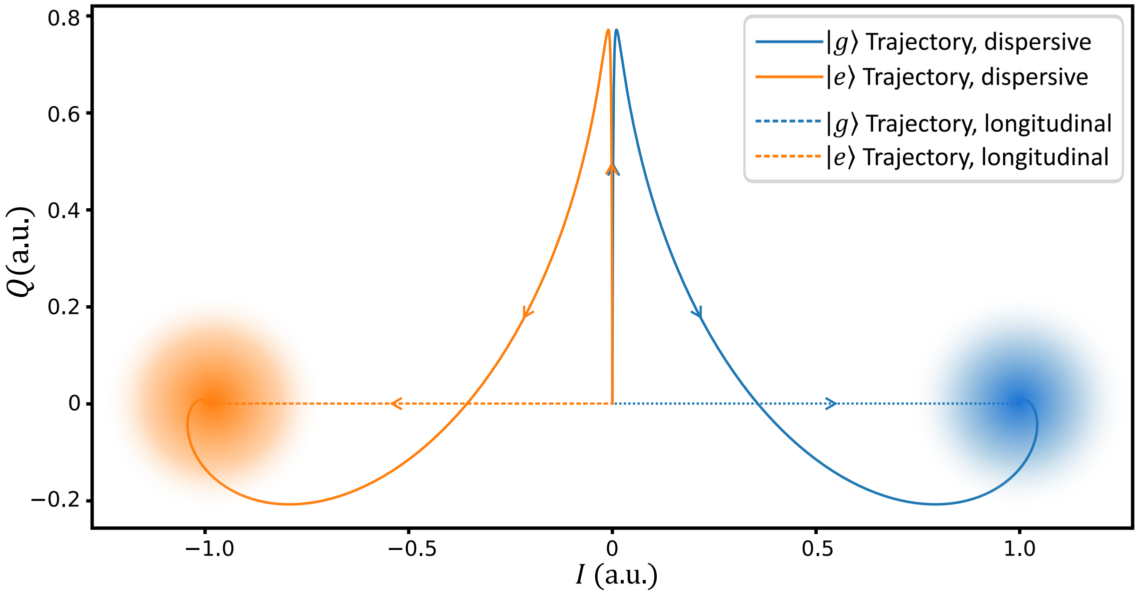

Figure 51: **IQ trajectories for dispersive and longitudinal readout.** Example evolution of the pointer states on the IQ plane for longitudinal (solid lines) and dispersive (dashed lines) readout schemes. Blue and orange correspond to the qubit in $|g\rangle$ and $|e\rangle$ states, respectively. In dispersive readout, the two traces have very small separation at the beginning of the readout. In contrast, the two traces in the longitudinal readout scheme consistently move in opposite directions.

qubit experiments, which has led to progressively higher readout speeds and fidelities [151, 152, 153], this method does come with inherent issues. One of the major challenges is to be able to rapidly populate the cavity photon number at the beginning of the measurement process. As depicted in Fig. 51, the trajectories of the two cavity states that correspond to the two measurement outcomes (also known as the pointer states), do not move toward the steady state along a straight line. Instead, they initially move in the same direction, resulting in minimal information about the qubit state at short measurement times. Accelerating the readout process necessitates either a larger cavity drive amplitude or a stronger coupling to the external port (denoted as κ). However, both parameters cannot be excessively high, since an increased drive amplitude could activate unwanted qubit-cavity transitions [90], while a larger κ could impose a Purcell limit on the qubit's lifetime [154]. Furthermore, the readout term in Eq. 168 is an always-on, non-rotating term. This implies that without careful management [155], stray photons in the cavity can unintentionally readout the qubit, leading to qubit decoherence.

To address these issues, one proposed solution is to construct a different form of qubit-cavity coupling, known as the "longitudinal coupling" [156, 21, 157, 158], in which the qubit is coupled to the cavity field via its longitudinal degree of freedom. This coupling scheme enables a new readout protocol, termed "longitudinal readout"[21], characterized by the core Hamiltonian:

$$\hat{\mathcal{H}}_{long,z}/\hbar = \zeta(t)\hat{\sigma}_z(\hat{c} + \hat{c}^\dagger). \tag{169}$$

In the interaction picture, this Hamiltonian generates an on-resonance drive on the cavity, with the sign of the drive depends on the qubit's $\hat{\sigma}_z$ eigenstate. As illustrated in Fig. 51, the cavity will be displaced to opposite directions when the qubit is in different states. Consequently, the trajectories of the pointer states consistently move in opposing directions, yielding a significantly faster initial readout speed compared to the dispersive readout scheme [21]. The bare longitudinal interaction has been realized experimentally with superconducting circuits [159, 160], while the QND longitudinal readout has also been performed "effectively" using parametric driving methods[161, 162].

Up to this point, we have used the adjectives "transverse" and "longitudinal" in various contexts. It would be beneficial to pause here and provide some clarity regarding these terminologies.

In terms of readout scheme:

- cavity operator for dispersive readout: $c^\dagger c$
- cavity operator for longitudinal readout: $(c + c^\dagger)$

In terms of readout component:

- qubit longitudinal component: $\hat{\sigma}_z$
- qubit transverse components: $\hat{\sigma}_x, \hat{\sigma}_y$

Here in our experiment, by synchronously activating the parametric conversion and 'gain' interactions between a qubit and a lossy SNAIL coupler device, we effectively creates a

longitudinal readout on the **transverse component** of the qubit. The effective readout Hamiltonian is given by:

$$\hat{\mathcal{H}}_{long,xy}/\hbar = \zeta(t)\left[\cos(\theta)\hat{\sigma}_x + \sin(\theta)\hat{\sigma}_y\right](\hat{c} + \hat{c}^\dagger), \tag{170}$$

in which the measurement direction θ is fully controllable by the phase of the parametric pumps, allowing us to measure along any arbitrary axis on the equator of the Bloch sphere. This direct QND measurement along the transverse axes of the qubit is useful in various quantum error correction schemes [30, 81], and has the advantage of being "fast" as an longitudinal readout protocol. Most importantly, in contrast to the previously mentioned dispersive/longitudinal readout experiments on the transverse/longitudinal components of the qubits [150, 163, 161, 162], which all rely on finite cross-Kerr for operation, our readout protocol is fully based on parametric three-wave-mixing processes. Therefore, the measurement can be completely deactivated when the parametric drives are turned off, leading to a substantial reduction in stray cavity photon induced qubit decoherence.

In the following sections, I will provide a concise overview of the theory and the complete experimental protocol for this parametric readout experiment we conducted using a standard transmon qubit and a lossy SNAIL coupler.

5.2.1 Brief theory of the parametric transverse component readout

The basic experiment setup contains a qubit mode Q that is coupled to another mode S with third order non-linearity, as depicted in Fig. 52 The total bare Hamiltonian of the system can be written as:

$$\hat{\mathcal{H}}_0/\hbar = -\frac{\omega_q}{2}\hat{\sigma}_z + \omega_s \hat{s}^\dagger \hat{s} + g_3(\hat{s} + \hat{s}^\dagger)^3 + g_{qs}(\hat{\sigma}_+ \hat{s} + \hat{\sigma}_- \hat{s}^\dagger), \tag{171}$$

in which ω_q and ω_s denote the frequencies of the Q and S modes, respectively. The coefficient g_3 is the strength of the third-order non-linear term, and g_{qs} represents the direct coupling strength between the two modes.

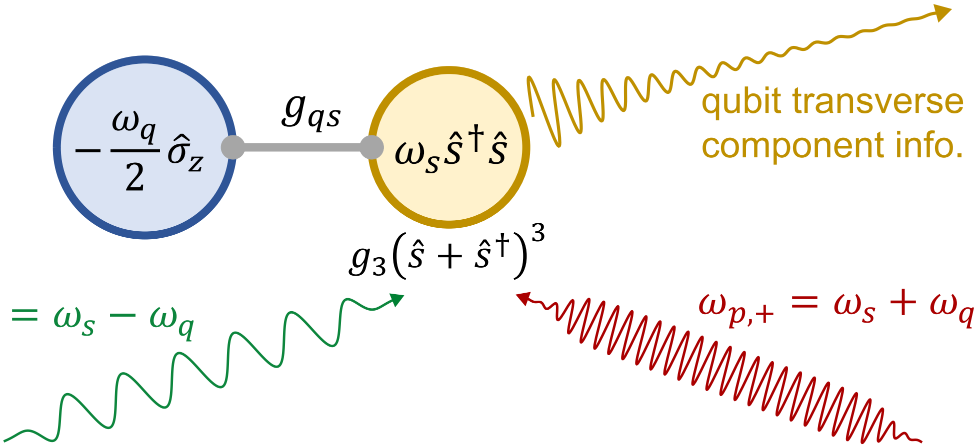

Figure 52: **Coupling scheme for the parametric readout experiment.** A qubit mode, Q, with frequency ω_q is weakly coupled to a non-linear mode, S, that has third order non-linearity. Two pumps are applied to the S mode at frequencies corresponding to the difference and sum of the Q and S mode frequencies. These pumps effectively generate an on-resonance drive on the S mode, with a phase that is dependent on the eigenstate of the qubit's transverse component. Therefore, the qubit's transverse component readout can be performed by collecting and demodulating the output signal from the SNAIL mode.

To activate the parametric measurement process, two external pumps are applied to the S mode at the frequencies $\omega_{p,+} = \omega_s + \omega_q$ and $\omega_{p,-} = \omega_s - \omega_q$ (assuming $\omega_s > \omega_q$). The Hamiltonian terms of these two pumps can be written as:

$$\begin{aligned}\hat{\mathcal{H}}_{p,+}/\hbar &= i\ \varepsilon_{p,+}(t)\cos(\omega_{p,+}t + \phi_{p,+})\left(\hat{s}^\dagger - \hat{s}\right)\\ \hat{\mathcal{H}}_{p,-}/\hbar &= i\ \varepsilon_{p,-}(t)\cos(\omega_{p,-}t + \phi_{p,-})\left(\hat{s}^\dagger - \hat{s}\right),\end{aligned} \tag{172}$$

in which $\varepsilon_{p,\pm}$ and $\phi_{p,\pm}$ are the amplitudes and phases of the two pumps, respectively. Following the full derivations that we have introduced in Sec. 2.1, these two pumps will activate two parametric processes:

$$\begin{aligned}\hat{\mathcal{H}}_G/\hbar &= \zeta_+(t)\left(e^{-i\phi_{p,+}}\hat{\sigma}_-\hat{s}^\dagger + e^{i\phi_{p,+}}\hat{\sigma}_+\hat{s}\right)\\ \hat{\mathcal{H}}_C/\hbar &= \zeta_-(t)\left(e^{-i\phi_{p,-}}\hat{\sigma}_+\hat{s}^\dagger + e^{i\phi_{p,-}}\hat{\sigma}_-\hat{s}\right),\end{aligned} \tag{173}$$

in which $\zeta_\pm(t)$ are the effective interaction strengths. The relationship between $\zeta_\pm(t)$ and the amplitudes and frequencies of each pump can be determined using the formulas presented in Sec. 2.1.4, which gives:

$$\zeta_\pm(t) = 6g_3 \frac{g_{qs}}{\omega_s - \omega_q} \frac{\omega_{p,\pm}}{\omega_{p,\pm}^2 - \omega_s^2} \varepsilon_{p,\pm}(t). \tag{174}$$

We refer to the two processes in Eq. 173 as parametric 'gain' (G) and 'conversion' (C) processes, as they mirror the similar processes of these names in parametric amplifiers [164, 145, 144, 146]. As introduced in Sec. 2.2.2, when the S mode is also a qubit, these two processes correspond to the iSWAP and bSWAP interactions between the Q and S modes, while turning on both pumps simultaneously can create a new family of two-qubit gates [61]. However, when the S mode is a lossy, weakly anharmonic mode, the conversion process will induce a parametric cooling effect that stabilizes the qubit to the $|g\rangle$ state, while the gain process will parametrically heat the qubit and stabilize it to the $|e\rangle$ state [165]. When both processes are activated simultaneously and the pump amplitudes are adjusted such that $\zeta_+ = \zeta_- = \zeta$, the effective system Hamiltonian can be expressed as:

$$\begin{aligned} \hat{\mathcal{H}}^{eff}/\hbar &= \hat{\mathcal{H}}_G/\hbar + \hat{\mathcal{H}}_C/\hbar \\ &= \zeta(t)\left(e^{-i\phi_{p,+}}\hat{\sigma}_-\hat{s}^\dagger + e^{i\phi_{p,+}}\hat{\sigma}_+\hat{s} + e^{-i\phi_{p,-}}\hat{\sigma}_+\hat{s}^\dagger + e^{i\phi_{p,-}}\hat{\sigma}_-\hat{s}\right) \\ &= \zeta(t)\left(e^{i\phi_m}\hat{\sigma}_- + e^{-i\phi_m}\hat{\sigma}_+\right)\left(e^{i\phi_s}\hat{s} + e^{-i\phi_s}\hat{s}^\dagger\right) \\ &= \zeta(t)\left[\cos(\phi_m)\hat{\sigma}_x + \sin(\phi_m)\hat{\sigma}_y\right]\left(e^{i\phi_s}\hat{s} + e^{-i\phi_s}\hat{s}^\dagger\right), \end{aligned} \tag{175}$$

in which we have reorganized the phase terms and defined:

$$\phi_m = (\phi_{p,+} - \phi_{p,-})/2 \tag{176a}$$

$$\phi_s = (\phi_{p,+} + \phi_{p,-})/2 \tag{176b}$$

Thus, by applying the two parametric pumps that activate the gain and conversion (GC) processes with matched coefficients, we create the effective Hamiltonian of longitudinal readout along the transverse axes of the qubit. The qubit measurement direction is controlled by ϕ_m (with the subscription 'm' denotes 'measurement'), while the displacement direction of the S mode is determined by ϕ_s (with the subscription 's' denotes 'signal'). Both ϕ_m and ϕ_s are fully controllable by adjusting the phase of the two pumps: $\phi_{p,+}$ and $\phi_{p,-}$.

5.2.2 Experiment setup

To physically realize the Hamiltonian described in Sec. 5.2.1, we designed and built the device shown in Fig. 53. This device actually uses the same 3D aluminum housing that was designed for our 4-qubit module, which I have introduced in Sec. 4.4.1. The central tube contains a SNAIL device that is used to provide the third-order non-linearity and perform the parametric readout. For the purpose of this experiment, only one of the qubit channels is used. The channel hosts a transmon qubit (Q) fabricated on a sapphire chip. To perform basic qubit characterization and verify the result of the SNAIL-based parametric measurement, a strip-line resonator (R) is fabricated on the same chip as the qubit for performing conventional dispersive readout.

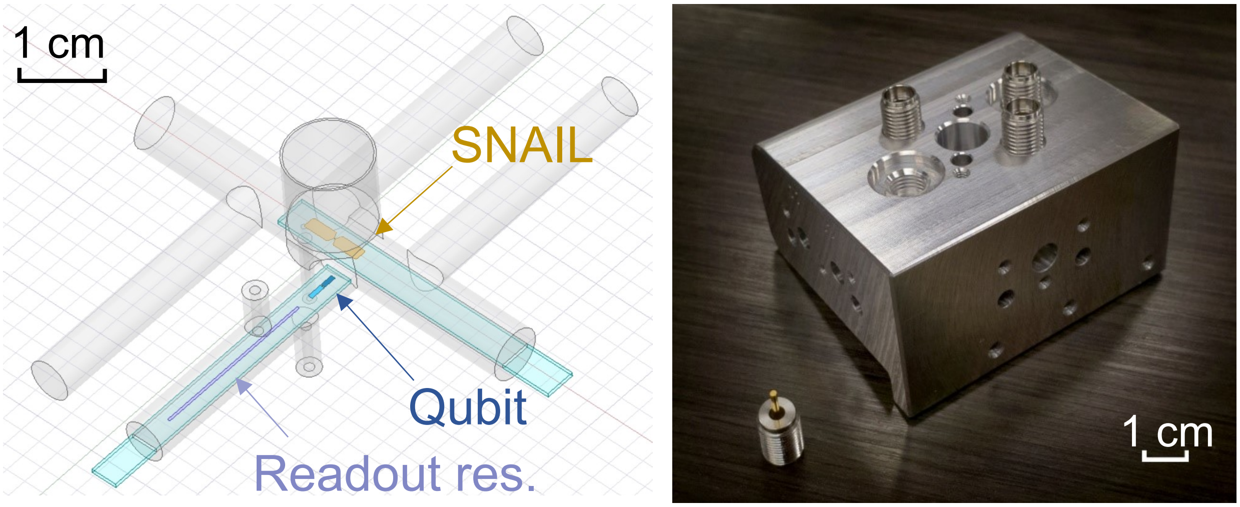

Figure 53: **3D design and picture of the device used in the parametric readout experiment.** The aluminum hosing contains one central channel that hosts a SNAIL chip, and four perpendicular channels for qubit chips. In this experiment, only one qubit channel is used, which hosts a transmon qubit with a stripline readout resonator.

The full device parameters are listed in Table 7. The frequencies of the SNAIL and qubit are carefully designed to ensure that all associated control and readout frequencies fall within the analog bandwidth of the DACs and ADCs on a single Xilinx RFSoC ZCU-216 board. This facilitates straightforward phase synchronization among all the direct digital

		Qubit	SNAIL	Readout resonator
Frequency (GHz)	$\omega/2\pi$	3.544	4.972	5.378
Relaxation time (μs)	T_1	41.2	0.056	0.179
Coherence time (μs)	$T_{2,R}$	32.0		
Anharmonicity (MHz)	α	-181		
Coupling with qubit mode (MHz)	$g/2\pi$		22	71
Cross-Kerr with qubit mode (MHz)	$\chi/2\pi$		≈ -0.09	-0.54
Coupling with port (MHz)	$\kappa_{ext}/2\pi$		2.585	0.791

Table 7: **Parameters for modes in the parametric measurement experiment.**

synthesized (DDS) control and readout channels, which is critical for the success of this experiment, as will be illustrated in Sec. 5.2.6 .

Another parameter that is worth highlighting is that the direct coupling between the qubit and SNAIL is intentionally designed (and measured) to be very small, specifically, $g_{qs}/2\pi = 22.0\,\text{MHz}$, which results in a very small estimated static qubit-SNAIL cross-Kerr $\chi_{qs}/2\pi \approx -90\,\text{kHz}$ (primarily caused by the self-Kerr of the qubit). This value is significantly lower than the typical cross-Kerr used in dispersive readout experiments, suggesting a much reduced decoherence induced by cavity thermal photons. This residual cross-Kerr can be further mitigated either by engineering the SNAIL design [49] or by applying additional external drives [155].

Figure 54 shows the fridge wiring diagram and setup of room temperature electronics for the control and measurement of the parametric readout experiment. The qubit drive, conversion pump, and the gain pump are all generated using direct digital synthesis (DDS) with a ZCU-216 board, which ensures the long-term phase coherence for the multi-parametric operation. The readout resonator drive is generated using an up-conversion circuit with the local oscillator provided by an external SignalCore generator; the same generator is used for the down conversion of the resonator's output signal, thus the phase drift of the generator

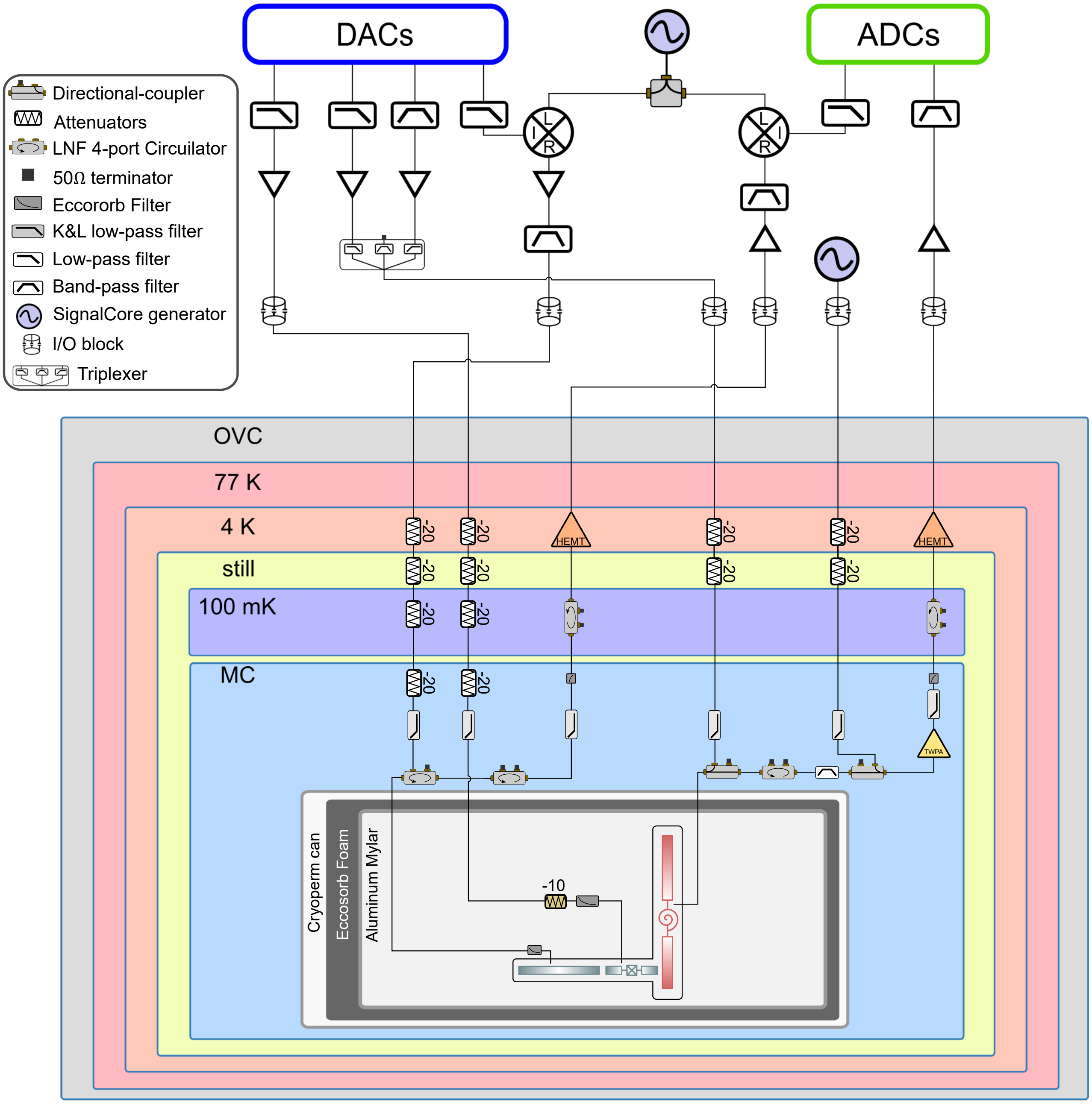

Figure 54: **Fridge wiring diagram and setup of room temperature electronics for control and measurement of the parametric readout experiment.**

is canceled. The output signal from the SNAIL is first amplified using a travelling-wave parametric amplifier (TWPA) at the mixing chamber plate, then further amplified using a conventional HEMT amplifier and another low-noise amplifier at room temperature. We acknowledge Lincoln Lab for providing us with the TWPA, and the QICK team from Fermi Lab, as well as Sara Sussman from Houck group at Princeton for their generous and extremely helpful support on operating the RFSoC board with QICK. The data we acquired in this experiment would not have been possible without all their help.

5.2.3 Tune up matched gain-conversion processes

The first step of tuning up the parametric measurement is to tune up matched gain and conversion processes. As illustrated in Eq. 173 and 174, in the ideal 3-wave mixing process, the interaction coefficients of the two processes (ζ_+ and ζ_-) are independently controlled by the amplitudes of the corresponding pumps (ε_+ and ε_-). Therefore, these two processes can be individually tuned to find the drive amplitudes that yield the same interaction coefficient.

As shown in Fig. 55, in the conversion process, the qubit is first prepared to $|e\rangle$ state using a π pulse, then a pump at frequency $f_{p,-} = f_s - f_q + \delta_-$ is applied on the SNAIL mode. The detuning δ_- is added to compensate for the AC-Stark shift effects during the pump. By sweeping the detuning and length of the pump, and measure the final $\hat{\sigma_z}$ expectation value of the qubit using the readout resonator, we acquire the "Chevron-like" plot that shows the qubit is "cooled" to the ground state when the pump is applied at the right frequency, as shown in Fig. 55b1. We then fit the data from the "on-resonance" trace (i.e. when the pumping frequency matches with the Stark-shifted $Q - S$ frequency difference) to acquire the effective interactions strength ζ_- under this pump, as shown in Fig. 55c1. The fitting function we used is

$$\langle z\rangle = A\cos^2[\zeta_-(t+t_0)]\exp(-t\kappa_{qs}) + A_0, \tag{177}$$

in which t is the independent variable — the length of the pump. The parameters A, A_0 and t_0 are free parameters that are related the state preparation and measurement (SPAM) errors. The decay rate $\kappa_{qs} = 1/2(\kappa_q + \kappa_s)$ is the averaged decay rate of the qubit and the SNAIL.

The similar experiment is performed for the gain process, in which the qubit is prepared to the $|g\rangle$ state, and the pump is applied at frequency $f_{p,+} = f_s + f_q + \delta_+$. The result shows that the qubit is now parametrically heated to the $|e\rangle$ state. We then tune the amplitude of the gain pump to make the resulted interaction coefficient ζ_+ match with the one we acquired from the conversion process, ζ_-. This will give us an initial guess for the pumping condition.

When both the gain and conversion pumps are activated simultaneously, the Stark shift effects induced by both pumps must be taken into account. This will cause the pumping frequencies to shift by an additional $\sim 10\,\mathrm{MHz}$ compared to the conditions found in the individual pump cases. Fortunately, as seen from Eq.174, the effective interaction strength is less sensitive to this relatively small frequency change, given that all the mode frequencies are on the gigahertz level. Therefore, to find the pump condition that yields the matched, on-resonance GC interaction when both pumps are on, we can perform a simple 2D sweep over the frequencies of the two pumps, with fixed pump amplitudes that we've determined from the individual tune-up processes, and a fixed pump length ($3\,\mu$s). The pulse sequence and experiment results are shown in Fig.56. The qubit is first prepared in the $\frac{1}{\sqrt{2}}(|g\rangle + |e\rangle)$ state with a $\pi/2$ pulse, then the gain and conversion pumps are turned on at the amplitudes that we've found in the previous step, and the two frequencies are swept. A final tomography measurement is performed on the qubit using the readout resonator after applying the pumps.

Figure 56b plots the qubit Z component after after the application of the GC pumps. The figure shows that when only one process is resonant, the qubit is either parametrically cooled (blue region) or heated (red region). The central white point in this plot corresponds to when both pumps are tuned on-resonance. At this point, the qubit's Z component is measured to be 0. Meanwhile, in Fig. 56c, the qubit's transverse component is maximized. This indicates that the GC pumps applied a measurement along an axis on the equator of the Bloch sphere, such that the length of the qubit's transverse component is preserved after the measurement. Therefore, the central point of this plot indicates the ideal GC pumping condition (amplitudes and frequencies of the two pumps) for performing the parametric transverse component on the qubit.

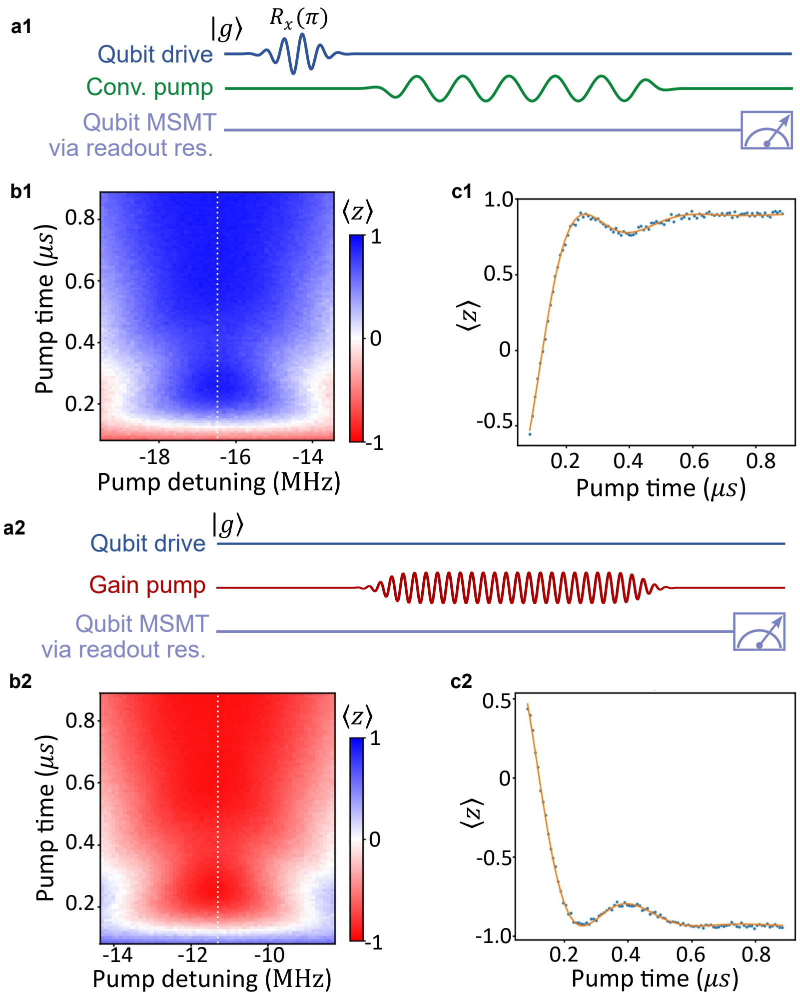

Figure 55: **Tune up individual gain and conversion processes. a1)** Pulse sequence for parametric qubit-SNAIL photon conversion experiment. The qubit starts from $|g\rangle$ state and is prepared to the $|e\rangle$ state with a π pulse. Then, a pump is applied around the frequency difference between the SNAIL and qubit modes. After applying the pump for various lengths of time, the qubit is measured along the z axis using the readout resonator. **b1)** "Chevron-like" plot that shows the "cooling" of the qubit under different pump lengths and frequencies. **c1)** Line-cut of **b1)** at the on-resonance drive frequency. The orange line represents the fitted curve, which is used to extract the interaction coefficient. **a2)-c2)** Experiment sequence and measurement results for the qubit-SNAIL gain process.

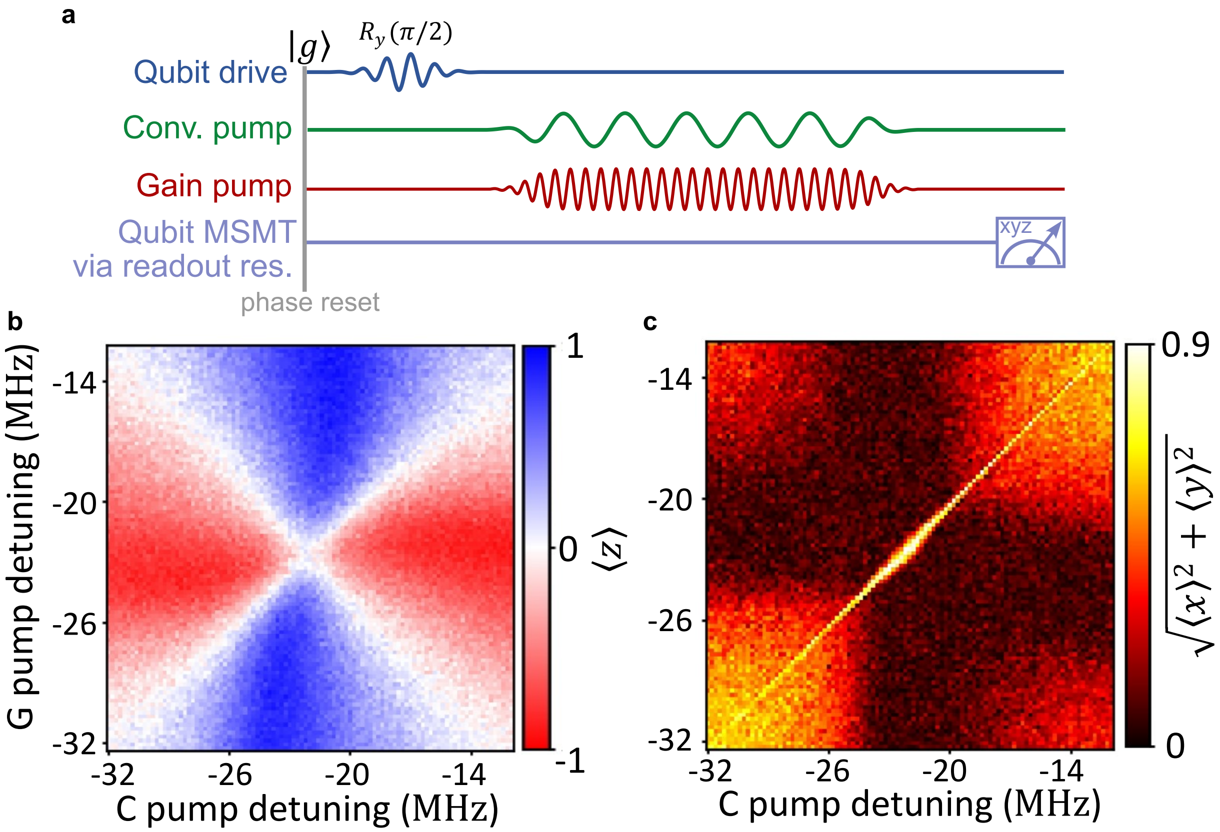

Figure 56: **Tune up of simultaneous gain and conversion processes. a)** Pulse sequence for tuning simultaneous gain-conversion (GC) process. The two pumps are applied at fixed amplitudes and lengths, while the frequencies are swept to find the on-resonance pumping condition. **b)** Qubit z measurement result after the GC pumping. The blue and red region indicates parametric cooling and heating of the qubit when only one pump is on-resonance, while the white region in the middle indicates the optimal combination of pumping frequencies that lock the qubit to a state on the equatorial plane of the Bloch sphere. **c)** Qubit transverse component amplitude, $\sqrt{\langle x\rangle^2+\langle y\rangle^2}$, after applying the GC pumps. The bright region in the middle indicates that the qubit transverse component is preserved during the pump.

5.2.4 Tune up the measurement frame

Once we have the matched gain and conversion coefficients, the next step is to tune up the phase of the measurement. As illustrated in Sec. 3.3.2, the AC-Stark shift effects will introduce additional phase shifts when the two pumps are turned on. In our parametric measurement experiment, there are two phases we need to consider. First, the relationship between the measurement direction and the pump phases in Eq.176a will have a constant offset, $\phi_{m,0}$, that must be calibrated. This ensures clarity about the direction along which we are measuring. Second, after the GC measurement, the qubit's final state will undergo a phase change, $\phi_{m,1}$. This phase change needs to be calibrated and then corrected with a virtual-Z (VZ) gate [94, 95, 56] to ensure that the gates following the parametric measurement will still be performed in the correct frame.

The values of $\phi_{m,0}$ and $\phi_{m,1}$ can be calibrated in a single phase-sweep experiment, as illustrated in Fig. 57a. The pulse sequence is basically the same as in Fig. 56a, with the difference being that we now sweep the phase of the initial preparation pulse on the qubit, ϕ_q. At the beginning of the experiment, the phases of all the drive channels are reset to 0, so the parametric measurement will be performed along direction $\phi_{m,0}$. Taking into account the additional phase shift $\phi_{m,1}$ after the parametric measurement, the final tomography measurement of the qubit will yield:

$$\begin{aligned}
\langle x\rangle &= \cos(\phi_{m,1}+\phi_{m,0})\cos(\phi_q-\phi_{m,0})\\
\langle y\rangle &= \sin(\phi_{m,1}+\phi_{m,0})\cos(\phi_q-\phi_{m,0})\\
\langle z\rangle &= 0.
\end{aligned} \tag{178}$$

A typical measurement result is shown in Fig. 57b. By fitting the $\langle x\rangle$ and $\langle y\rangle$ traces to two sinusoidal functions, we can extract the value of $\phi_{m,0}$ and $\phi_{m,1}$. To correct these two extra phases, we can simply add $2\phi_{m,0}$ to $\phi_{p,-}$, and apply a VZ gate with phase $-\phi_{m,1}$ after the parametric measurement. Consequently, with these phase adjustments, the same experiment produces the results shown in Fig. 58c, which shows that parametric measurement is now aligned with the x axis, and the qubit state after measurement is adjusted back to the measurement axis. It is worth noting that the readout signal coming out from the SNAIL will also carry a constant phase offset, determined by the Stark-shift effects and the values of

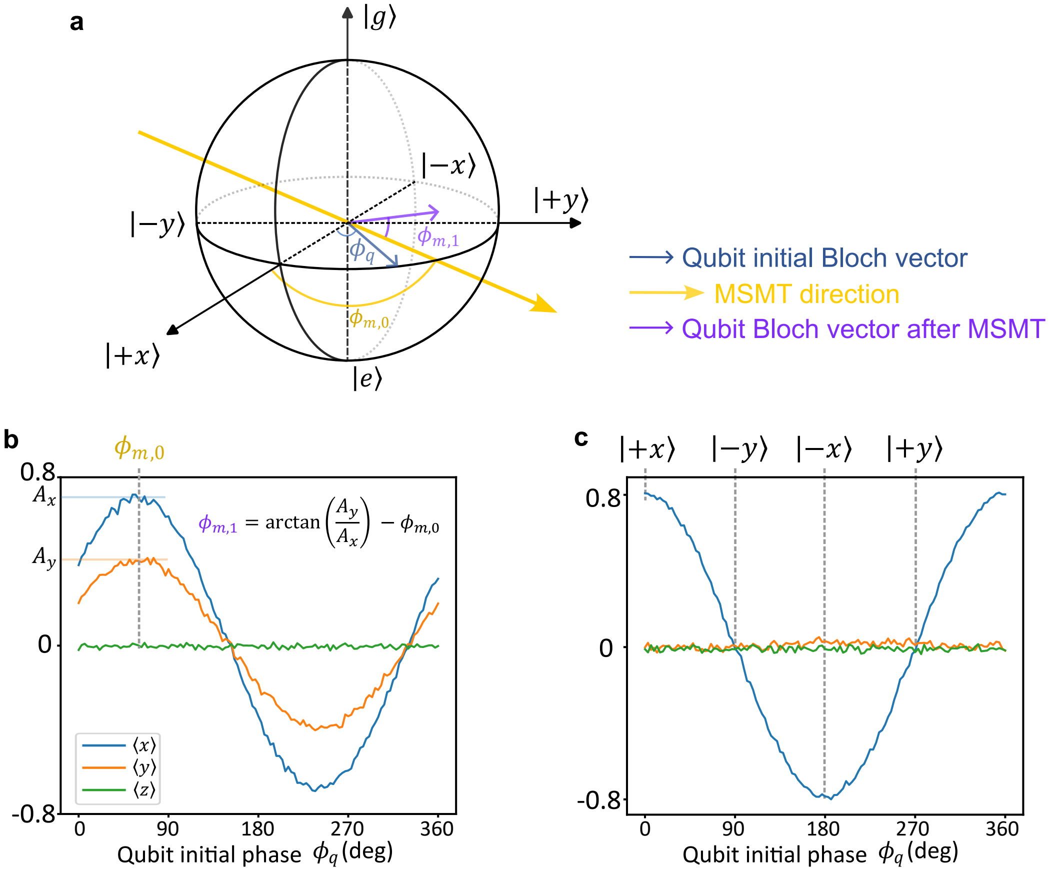

Figure 57: **Tune up phase for parametric measurement.** **a)** Bloch sphere representation for the phase offset of the parametric measurement, $\phi_{m,0}$, and the Stark-shift induced qubit phase change after the GC pumping, $\phi_{m,1}$. **b)** Qubit tomographic measurement result versus the initial phase ϕ_q before calibrating the two phase offsets. **c)** Same experiment as in **b)** but after compensating for the two phase offsets by adjusting the pump phase and applying virtual-Z gates.

$\phi_{p,-}$ and $\phi_{p,+}$. However, this doesn't impact the fact that the two pointer states will always separate in opposite directions. When a phase-sensitive amplifier is used in the readout chain [161], the phase of the readout signal can be adjusted by tuning the values of $\phi_{p,-}$ and $\phi_{p,+}$ to align with the desired amplification direction. Otherwise, this constant phase offset can also be easily compensated in software post-processing.

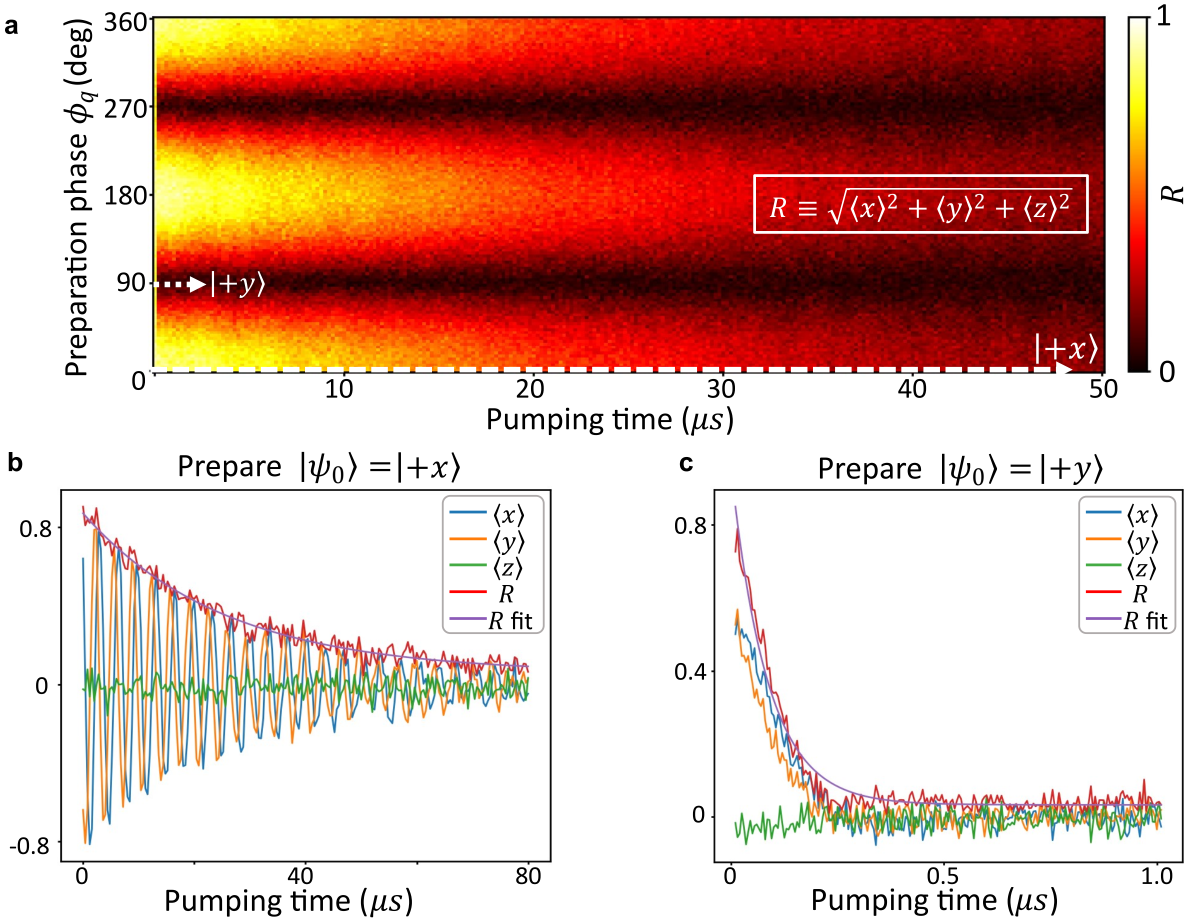

Figure 58: **Examine measurement back action with various pump length. a)** Decay of the qubit's Bloch vector length R as a function of pump length at different initial preparation phases ϕ_q. The measured value of R decays rapidly when the initial phase of the qubit is perpendicular to the measurement direction. In contrast, the decay is much slower when the qubit's initial phase aligns parallel to the measurement direction.. **b)** Qubit tomographic measurement result versus the pump length for $\phi_q = 0$. The decay of R is fitted to a exponential function and we extract a decay rate close to the static T_2 of the qubit, which indicates the quantum non-demolition nature of our parametric measurement. **c)** Qubit tomographic measurement for $\phi_q = 90°$. The qubit undergoes fast decoherence under the pump. From the decay trace we can extract the measurement rate of the parametric readout.

With the measurement direction tuned, we can apply the pump for various lengths of time to examine the back action of our parametric measurement. The results are shown in Fig. 58. The parametric measurement direction is tuned to be along the $+x$ direction. After applying the GC pumps for various lengths of time, the length of the qubit Bloch vector, $R = \sqrt{\langle x\rangle^2 + \langle y\rangle^2 + \langle z\rangle^2}$, is calculated using the final tomography measurement results. When the qubit is prepared in the $|\pm x\rangle$ state, we obtain a decay constant of R that equals to $T_2^{eff} = 27\,\mu$s, which is close to the static T_2 of the qubit, indicating the quantum non-demolition (QND) nature of the parametric measurement. On the other hand, when the qubit is prepared in the $|\pm y\rangle$ state, the decay constant of R is fitted to 77 ns, which indicates a measurement rate of 13 MHz.

5.2.5 Acquire and verify the parametric readout result

The tune-up process described above only involves applying the pumps and measuring the final state of the qubit using the readout resonator. However, the actual result of the parametric readout is carried by the light emanating from the SNAIL mode. Figure. 59a shows the complete experimental sequence, which involves capturing the output signal from the SNAIL and demodulating the measurement results. The qubit is first prepared to $|+x\rangle$, $|+y\rangle$ and $|-x\rangle$ states, then the GC pumps are applied using the amplitude, frequency, and phase parameters that we have tuned in the previous steps. Meanwhile, the out put signal from the SNAIL is sent to the ADC, where demodulation is performed with direct digital synthesised reference signal. After the GC pumping, a tomographic x measurement on the qubit is performed using the readout resonator to verify the final qubit state after the measurement.

Figure 59b shows the acquired signal from the SNAIL when the qubit is prepared to $|+x\rangle$ and $|-x\rangle$ states. The time traces show that the SNAIL is displaced to two opposite directions when the qubit is prepared to the two eigenstates along the parametric measurement axis. By applying a longer pulse ($6\,\mu$s) and integrating the time traces, we can plot the IQ histogram shown in Fig. 60a. The histogram is rotated such that the separation is maximized along the I axis. The two Gaussian distributions centered around the right and left side of the IQ plane correspond to when the qubit is prepared in the $|+x\rangle$ and $|-x\rangle$ states. The qubit

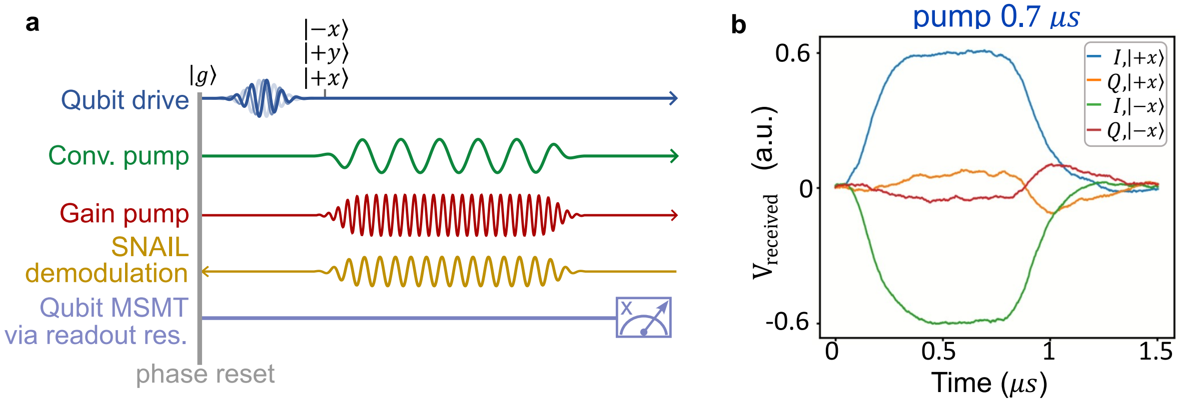

Figure 59: **Full parametric readout experiment.** **a)** Pulse sequence of the parametric readout experiment. The qubit is first prepare to three different states on the equator of the Block sphere using $\pi/2-$pulses of different phases. Then, the gain and conversion pumps are turned on simultaneously, meanwhile, the output signal from the SNAIL is acquired by the digitizer where the digital demodulation is performed. Finally, a traditional tomographic measurement is performed on the qubit using the stripline readout resonator. **b)** The time domain output signal acquired from the SNAIL after demodulation. The result shows that the output signals have a 180° phase difference when the qubit is prepared in the $|+x\rangle$ and $|-x\rangle$ states, indicating that the output signal indeed carries the qubit's state information.

state after the parametric measurement is further examined by calculating the average x component of the qubit, conditioned by the measurement outcome of the final tomographic x measurement [166]. This conditioned map is plotted in Fig. 60b, which shows that the qubit's final state is in the $|+x\rangle$ / $|-x\rangle$ eigenstate when the parametric measurement outcome yields histograms on the right/left.

Using the histogram in Fig. 60a, we can calculate the fidelity of the parametric x measurement. We draw a separation line between the left- and right-displaced Gaussian distributions, and count the possibility of the measured (I, Q) points being on the right(left) side when the qubit was prepared in the $|+x\rangle$ ($|-x\rangle$) state. These possibilities give us the measurement fidelities for the $|+x\rangle$ and $|-x\rangle$ states, which yield $\mathcal{F}_{+x} = 89.2\%$ and $\mathcal{F}_{-x} = 89.3\%$. These

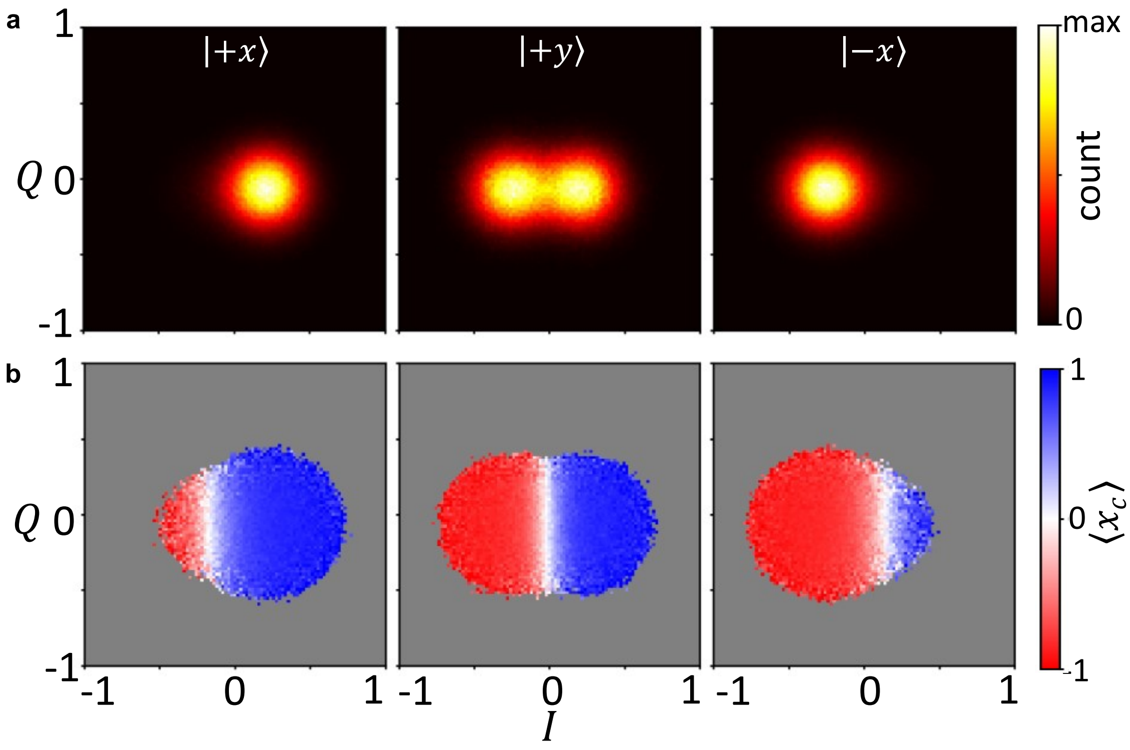

Figure 60: **IQ histogram of the SNAIL measurement result. a)** Integrated IQ histogram of the SNAIL output signal for different qubit initial states. The result shows that the SNAIL mode is displaced to opposite directions when the qubit is prepared to the two eigenstates of the $\hat{\sigma}_x$ operator. **b)** Conditioned $\hat{\sigma}_x$ measurement result from the final qubit tomography measurement. When the SNAIL is displaced to the right/left, the qubit stay at the $|+x\rangle$ / $|-x\rangle$ state after the parametric measurement, which proves the QNDness of the parametric measurement.

fidelities are on par with previously reported continuous x measurements on transmon qubits using different methods [150]. The infidelity of the measurement is mostly dominated by the separation of the two Gaussian distributions. By projecting the two 2D Gaussian distributions onto the I axis and fitting them to two 1D Gaussian functions, we extract a separation of 2.65σ, which gives a separation fidelity of 90.7%. To achieve larger separation between the two Gaussian distributions, we need to population the SNAIL with higher averaged photon numbers. In our current setup, this is limited by the finite self-Kerr of the SNAIL mode at our operation bias, where the system is most sustainable under the GC pumps. Moving forward, we are working on repeating the experiment with arrayed SNAIL devices [79, 76], in which the self-Kerr is greatly suppressed and hopefully can provide us with better readout fidelity.

The protocol presented here also has the prospect of measuring multi-qubit operators by coupling more than one qubit to a single SNAIL. For example, using the fifth order term of the SNAIL, we can perform joint $\sigma_x\sigma_x$ measurements of two qubits, which is very desirable in surface code error correction schemes. Moreover, the effective Hamiltonian constructed in Eq. 175 also has applications in other quantum operations, including multi-parametric amplification [145, 144, 146], qubit bath engineering [165], and logical qubit operations in various innovative quantum error corrections schemes [141, 167].

5.2.6 Stable phase coherence control with the RFSoC board

The success of the parametric measurement experiment relies strongly on the ability to generate stable phase coherence signals for the qubit drive, the parametric pumps and the reference tones for the SNAIL signal demodulation. Following the protocol introduced in Sec. 3.3.2 and using the phase relation in Eq. 176, we find that to maintain a stable phase for the parametric measurement experiment, the following conditions must be satisfied:

$$\begin{aligned} \phi_q - (\phi_{p,+} - \phi_{p,-})/2 &= \text{const} \\ \phi_{s,r} - (\phi_{p,+} + \phi_{p,-})/2 &= \text{const}, \end{aligned} \tag{179}$$

in which ϕ_q is the phase of the qubit drive channel, $\phi_{p,+}$ and $\phi_{p,-}$ are the phases of the gain and conversion pumps, respectively. Phase $\phi_{s,r}$ is the phase of the reference tone for SNAIL signal demodulation.

We have performed this parametric measurement experiment using two signal generation approaches: 1) mixer-based setup with low-frequency AWGs and signal generators, and 2) direct digital synthesized (DDS) signals with an RFSoC board controlled with "Qick" [85]. Maintaining the phase coherence condition described in Eq. 179 within a short time period (tens of seconds) is achievable in both setups, although the mixer-based up-/down-conversion circuits are more complex to set up and require careful selection of the local oscillator (LO) frequencies, while the DDS pulses simply requires a FPGA-controlled phase reset on all channels at the beginning of each experiment. However, maintaining long-term phase stability (over hours) is significantly more challenging in the mixer-based setup, due to the difficulty in preserving relative phase stability between different LO channels. To test the phase stability of the two different hardware setups, we repeated the phase calibration experiment in Fig. 57 for ten hours with fixed control parameters set in the software.

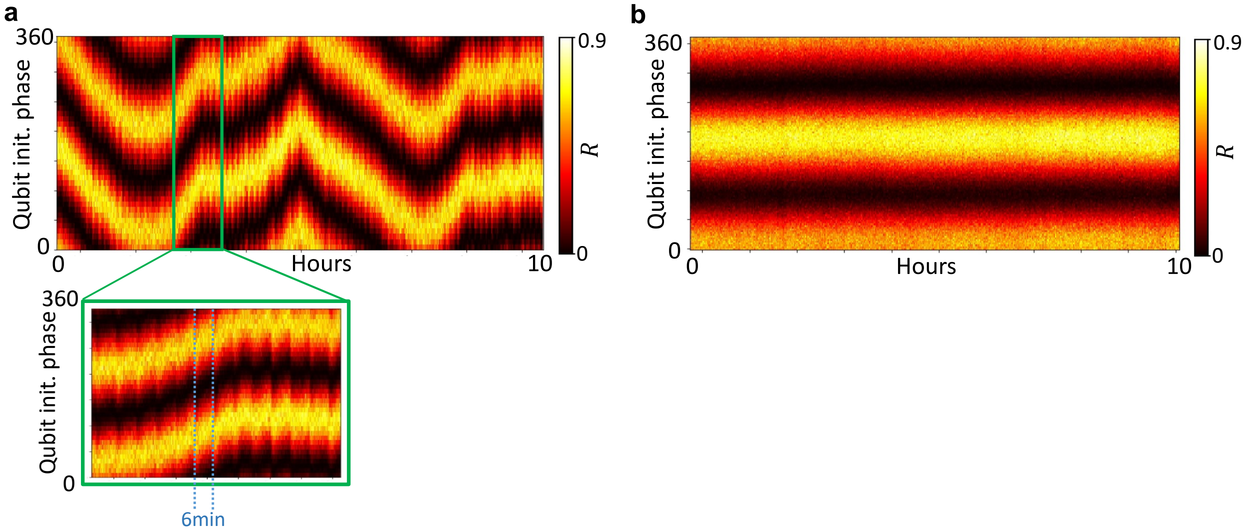

Figure 61: **Long time-scale phase stability using different hardware setups .** **a)** Phase stability data obtained from running the phase calibration experiment using a mixer-based control circuit for a duration of 10 hours. The phase exhibits a 6-minute period drift caused by imperfections in the phase lock loop of the signal generators, and also shows a larger overall phase drift over several hours due to temperature fluctuations. **b)** Phase stability data of the same experiment obtained with a a QICK-controlled RFSoC board. The phase remained stable throughout the entire 10-hour experiment.

Figure 61a shows the phase stability of the mixer-based setup. Although all the signal generators and AWG channels used were locked to an external 10 MHz Rubidium clock, we still observed a $\sim$ 6min-period phase drift due to the imperfections of the phase-lock-loop in the signal generators, as well as an overall slow drift that we attribute to changes in room temperatures over time [168, 56]. Such drift makes all experimental studies extremely tedious, as re-calibration is required every few minutes. In contrast, Fig. 61b shows the same experiment performed using a QICK-controlled RFSoC board, where all the drives were generated using direct digital synthesis with phase reset on each repetition. The measurement phase remained stable over the entire 10-hour experiment, which allows long-time averaging and greatly simplifies the phase calibration process.

6.0 Conclusions and Perspectives

With the key concept of parametric interactions as the central theme, this thesis has provided a thorough discussion of the theory, realization and applications of parametric interactions in superconducting quantum systems. The theoretical derivation in Ch. 2 provides a comprehensive illustration of charge-pumped parametric interactions. Through careful calculation and analysis, we revealed the power of these interactions to facilitate universal single- and two-qubit gates with full microwave control.

Chapter 3 discussed the indispensable role of FPGA-based microwave electronics for real-time quantum control. In this discussion, we introduced and compared the two kinds of control systems - mixer-based and direct-digital synthesised (DDS) pulse generation and readout schemes. It became evident that the more recent RFSoC devices offer significant benefits for controlling superconducting quantum devices, due to their simplicity of the hardware setup and ability to maintain long-term relative phase coherence.

Utilizing these parametric interactions, I have conducted two major experiments. Namely, the realization of quantum state router, and parametric readout on the transverse component of a transmon qubit. These experiments serve as demonstrative examples that shows the power and versatility of parametric interactions. The protocols and results presented here have important implications for future development of coupler devices for superconducting quantum computing, enabling novel modular quantum processor designs with innovative topologies, and potentially inspiring other uses of parametric interactions in the manipulation of superconducting quantum systems.

In our extensive journey of designing and implementing modular quantum processors, we've gained invaluable experiences into simulating, fabricating, and controlling parametrically coupled multi-mode systems. However, the most profound lesson we've learned is the versatility of parametric interactions. They offer flexibility not just in the variety of operations they can perform, but also in enabling novel coupling architectures. While industry giants like IBM and Google have made significant progress in integrating an increasing number of qubits using the surface code structure, we, as academic researchers, can enrich the field by venturing beyond established paradigms. It's crucial that we explore innovative qubit connection architectures, and the parametric coupling scheme offers many opportunities in this area. For example, the single-qubit subharmonic gate introduced in Sec. 2.2.1 stands as a neat recent outcome of adopting this strategy, which provides non-traditional high-performance single-qubit gates by exploiting the intrinsic non-linearity of the transmon qubit itself.

Finally, I leave the reader with a brief discussion of two areas where I feel there are both great opportunities and pressing need for further work. First, how we can use my results to further-scale up modular quantum processors, and second, addressing one of the skeletons in the closet of parametric driving: understanding and controlling their speed limits.

6.1 Perspectives

6.1.1 Scaling up modular quantum processors

The quantum router and module experiments demonstrated in Ch. 4 has shown the effectiveness of the parametric coupler devices in achieving dense all-to-all couplings between multiple modes, while effectively limiting cross-talk effects. However, extending such coupling to a much larger number of modes ($\gtrsim 10$) presents challenges. A significant issue is frequency crowding, since each parametric operation needs to be addressed by a unique sum/difference frequency. The router-module coupling scheme depicted in Fig. 47 solves this problem by segmenting large multi-mode devices into smaller clusters of all-to-all coupled devices. These smaller devices then use intermediate communication modes to exchange quantum information via the router. Although our first generation quantum router and module experiments have been successful and indicate the feasibility of this coupling scheme, we shouldn't restrict our focus solely to this architecture. The parametric coupling strategy offers a plethora of possibilities for establishing qubit-to-qubit connections. For instance, the designs in Fig. 48 leverage a similar direct coupling between qubits and SNAIL couplers, but create multi-mode systems with higher qubit communication efficiency than the router-module design, although it is not as clear how to chop the corral into smaller circuits to allow it to be fully modular.

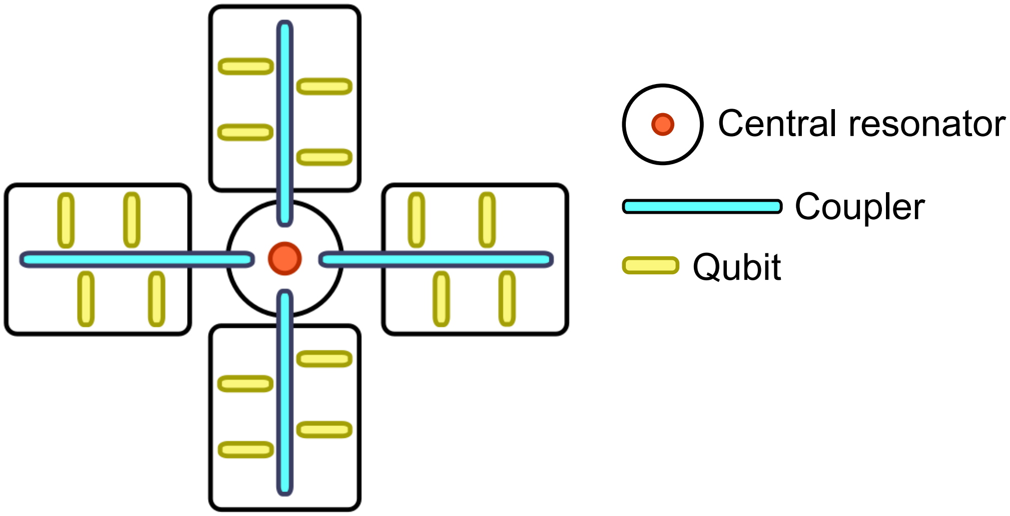

Figure 62: **A 16-bit coupling scheme with potentially identical qubit sets in each module.** Four 4-bit modules are coupled to one central cavity mode. Each module uses a central SNAIL coupler (highlighted in blue) to perform intra-module gates between the qubits (marked in yellow). The exchange interaction between qubits of different modules can be activated by applying two pumps on two SNAILs, which can directly perform gates between the target qubits and only virtually occupy the central cavity mode. The decision of which SNAILs to pump gives us the precision to select the specific qubits on which to perform the gate. As a result, qubit sets in different modules can share the same frequency without the concern of frequency crowding.

Moreover, we can also think about mitigating the frequency crowding issue using innovative ways of applying the parametric pumps. For instance, Fig. 62 presents an alternative multi-mode coupling scheme based on parametric interactions. Unlike the coupling scheme in Fig. 47, which requires intermediate communication modes to separate the intra- and inter-module operations, this approach directly links the couplers of each module to a mutual "virtual transfer station" mode. To activate an intra-module qubit-qubit exchange interaction, one simply needs to apply pumps to the coupler modes of the two modules. Each pump should be applied at a frequency that is detuned from the difference between the target qubit mode and the “transfer station” mode, creating a direct parametric exchange interaction between the target qubits without occupying the central mode. This method enables the execution of real all-to-all gates across all 16 modes in the four modules. More importantly, selecting which intra-module interaction to activate is determined by deciding which two couplers to pump. Therefore, this design allows for identical qubit sets across different modules, substantially reducing the frequency crowding overhead.

6.1.2 Is there a boundary for parametric quantum operations?

The parametric interaction is used extensively in the experiments introduced in this thesis. The simplified theory based on the truncated Hamiltonian introduced in Ch. 2 seems to indicate that faster parametric operations can be realized by simply applying stronger pumps. However, in practice we do encounter limitations on stronger parametric pumps. One obvious practical limitation is that the cooling power of dilution refrigerator sets the cap for the maximum power we can apply on the pump lines. This limitation is more like a engineering problem that can be solved by improving the cooling power of the fridge and carefully engineering the pump line design, as introduced in Ch. 4. On the other hand, as the pump gets stronger, we have also observed other unexpected effects that can decrease the fidelity of parametric quantum operations, which includes: 1) the desired interaction strength stops increasing monotonically as we increase the strength of the pump, 2) the coherence time of the modes in the system begin to decrease as the pump gets stronger, and 3) at even stronger pump power, a ‘break down’ behaviour is observed, where all the modes in the system are suddenly heated to high-photon-number states with a small increase of pump power, as shown in Fig. 63.

These effects appear to be more closely related to the intrinsic quantum dynamics of the system when exposed to a strong external pump, which are actually more concerning. However, it remains uncertain whether any of these effects suggest a fundamental limitation to parametric operations. For instance, the reduced speed of parametric gates as pump power increases might be attributable to the fifth-order effect in the SNAIL coupler device. This issue might be addressable by creating an array of SNAIL loops to suppress higher-

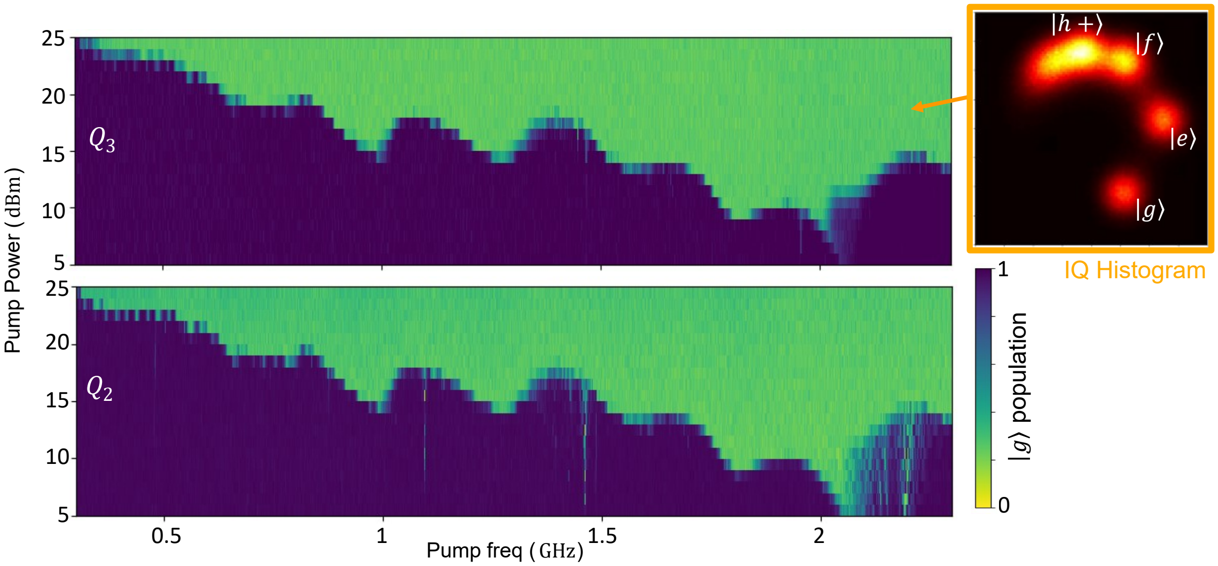

Figure 63: **Breakdown behaviour of qubit-SNAIL system under strong external pump.** This data was obtained in our four-qubit module device that has been introduced in Ch. 4. We prepare two qubits Q_2 and Q_3 in their ground states and apply pumps on the SNAIL at different frequencies and amplitudes. Under each pumping frequency, there is a critical pump power that suddenly heats both qubits to a high-photon-number state. The similarity of the two qubits' behaviour indicates that there is probably a "break down" behaviour happening in the SNAIL coupler at the critical pump power, which leads to the catastrophic reaction of the whole system.

order nonlinear terms [79]. Nevertheless, the decoherence of the qubit and the observed breakdown behavior still needs further investigation. Understanding the dynamics of these effects requires us to conducting theoretical studies and comparing the theoretical results with the observed effects. This behavior has been seen before in semi-classical devices, where it was associated with chaos and limit cycles, closely related to the classical behavior of Kerr oscillators [169]. However, in our quantum system it is unclear how these concepts cross over. In previous work in our laboratory, we explored similar concepts in two-mode Josephson frequency comb devices[170, 171] A deeper understanding of these dynamics and how the concepts apply in semi-classical and more fully quantum systems is an area of active research in the lab and with our theory collaborators, and should pave the way for the design of improved coupler devices. This, in turn, can help sidestep these problems, pushing the boundary for higher fidelity parametric operations.

Appendix A General formula for displacement transformation in a non-linear oscillator under parametric pumping

The derivation presented here is adapted from a calculation note shared by Prof. Roger Mong. We consider a general oscillator mode A, with frequency ω_a and non-linear interaction term $g(\hat{a}, \hat{a}^\dagger)$, under an external parametric pump $f(t)$. The total system Hamiltonian can be written as:

$$\hat{\mathcal{H}}/\hbar = \omega_a \hat{a}^\dagger \hat{a} + g(\hat{a}, \hat{a}^\dagger) + f(t)\hat{a}^\dagger + f^*(t)\hat{a} \tag{180}$$

Note that the pumping term $f(t)\hat{a}^\dagger + f^*(t)\hat{a}$ is written in a generalized form to accommodate either flux coupling or charge coupling between the external pump and the quantum mode A. For example, in the case of charge coupling as shown in Eq. 43, we have $f(t) = \varepsilon(t)e^{-i\omega_p t} - \varepsilon^*(t)e^{i\omega_p t}$.

Our goal is to eliminate the f terms via a unitary transformation-specifically with a displacement operator:

$$\hat{U}_D = \exp\bigl(za^\dagger - z^* a\bigr). \tag{181}$$

Using the Baker–Campbell–Hausdorff (BCH) formula, we can calculate the transformation of the photon annihilation and creation operators, which gives:

$$\begin{aligned} \hat{U}_D \ \hat{a} \ \hat{U}_D^\dagger &= \hat{a} - z, \\ \hat{U}_D \ \hat{a}^\dagger \ \hat{U}_D^\dagger &= \hat{a}^\dagger - z^*. \end{aligned} \tag{182}$$

The time derivative of $\hat{U}_D$ is a bit more complicated to calculate. We need to first use a derived form of the BCH formula (know as the Zassenhaus formula) to rewrite $\hat{U}_D$ as:

$$\hat{U}_D = e^{-\frac{1}{2}|z|^2} e^{z\hat{a}^\dagger} e^{-z^*\hat{a}}. \tag{183}$$

Then we can take the time derivative of each exponent term, and keep in mind the commutation relation $[\hat{a}, \hat{a}^\dagger] = 1$. We have:

$$
\begin{aligned}
\frac{d}{dt}\hat{U}_D &= (-|z||\dot{z}|)e^{-\frac{1}{2}|z|^2}e^{z\hat{a}^\dagger}e^{-z^*\hat{a}} \\
&+ e^{-\frac{1}{2}|z|^2}(\dot{z}\hat{a}^\dagger)e^{z\hat{a}^\dagger}e^{-z^*\hat{a}} \\
&+ e^{-\frac{1}{2}|z|^2}e^{z\hat{a}^\dagger}(-\dot{z}^*\hat{a})e^{-z^*\hat{a}} \\
&= \left[-|z||\dot{z}| + \dot{z}\hat{a}^\dagger + e^{z\hat{a}^\dagger}(-\dot{z}^*\hat{a})e^{-z\hat{a}^\dagger}\right] e^{-\frac{1}{2}|z|^2}e^{z\hat{a}^\dagger}e^{-z^*\hat{a}} \\
&= \left[-|z||\dot{z}| + \dot{z}\hat{a}^\dagger - \dot{z}^*(\hat{a} - z)\right]\hat{U}_D \\
&= \left[-i|z|^2\frac{d\arg(z)}{dt} + \dot{z}\hat{a}^\dagger - \dot{z}^*\hat{a}\right]\hat{U}_D
\end{aligned}
\tag{184}
$$

Using Eq. 182 and the final result in Eq. 184, we can calculate the system Hamiltonian after the displacement transformation, which can be written as:

$$
\begin{aligned}
\hat{\mathcal{H}}'/\hbar &= \hat{U}_D\hat{\mathcal{H}}\hat{U}_D^\dagger/\hbar + i\dot{\hat{U}}_D\hat{U}_D^\dagger \\
&= \omega_a\hat{a}^\dagger\hat{a} + \left[-\omega_a z + i\dot{z} + f(t)\right]\hat{a}^\dagger + \left[-\omega_a z^* - i\dot{z}^* + f^*(t)\right]\hat{a} \\
&+ |z|^2\left[\omega_a + \partial_t\arg(z)\right] + g(\hat{a} + z, \hat{a}^\dagger + z^*).
\end{aligned}
\tag{185}
$$

For a given pumping function $f(t)$, to transfer away the pumping terms, we need to find a time-dependent function $z(t)$ such that:

$$
f(t) = \omega_a z(t) - i\dot{z}(t) \tag{186}
$$

Generally, the parametric pumps are applied with constant carrier frequencies, so $f(t)$ can be written as:

$$
f(t) = \sum_{\Omega\neq\omega_a} f_\Omega\, e^{i\Omega t}, \tag{187}
$$

where f_Ω is the amplitude of the frequency component Ω. Let

$$
z(t) = \sum_{\Omega\neq\omega_a} z_\Omega\, e^{i\Omega t}. \tag{188}
$$

Then Eq. 186 can be solved with Fourier decomposition, and we get the final solution for $z(t)$ that can be used in the displacement transformation to eliminate the pumping terms.

$$
z(t) = \sum_{\Omega\neq\omega_a} \frac{f_\Omega}{\Omega + \omega_a}\, e^{i\Omega t} \tag{189}
$$

Appendix B Systematic approach for enumerating the potential parametric interactions in a multi-mode system with n^{th} order non-linearity

Consider a system that consists of a central coupler mode C, and $(N-1)$ linear modes $A_1, \ldots, A_{N-1}$ coupled to C. The C mode has a frequency of ω_c and has n^{th} order non-linearity. Each linear mode A_i has a frequency of ω_i and is coupled to the C mode with a hybridization strength of $\lambda_i = g_{c,a_i}/(\omega_i - \omega_c)$. Following the calculation in Sec. 2.1, the interaction picture Hamiltonian for the system under external pump can be written as:

$$\hat{\mathcal{H}}_I/\hbar = g_n \left(\hat{c}e^{-i\omega_c t} + \sum_{i=1}^{N-1} \lambda_i \hat{a}_i e^{-i\omega_i t} + \eta e^{-i\omega_p t} + h.c. \right)^n , \tag{190}$$

in which ω_p is the pumping frequency, and the effective pump photon term η follows the same definition as in Eq. 50. The expansion of Eq. 190 contains a vast collection of possible n-wave mixing parametric processes that can be activate by the external pump. Our goal here is to systematically enumerate all the potential parametric processes and their corresponding pump frequencies. To achieve this, we introduce the following formalism:

- Generally, a n-wave mixing parametric process should involve k $(1 \leq k \leq n-1)$ pumping terms η, and $\ell \equiv (n-k)$ mode operators. Therefore, we can categorize the n-wave mixing processes based on the number of "pump photons" involved. Namely, we denote the interactions that involve k pumping photons as 'η^k interactions'.
- An η^k interaction term from the expansion of Eq. 190 can be generally written as:

$$\eta^k e^{-ik\omega_p t} \; \hat{o}_1 \hat{o}_2 \ldots \hat{o}_\ell \; e^{i\omega_{\text{rot}}^{(\ell)} t}, \tag{191}$$

  in which each mode operator $\hat{o}_i$ is picked from the collection of all the annihilation and creation operators for the modes in the system[1], i.e.,

$$\hat{o}_i \in \{\hat{c}, \hat{c}^\dagger, \hat{a}_1, \hat{a}_1^\dagger, \ldots, \hat{a}_{N-1}, \hat{a}_{N-1}^\dagger\} \tag{192}$$

---

[1] Note that the coupler mode itself can also get involved in a parametric transition, e.g., pumping at $\omega_p = (\omega_c - \omega_{a_1})/2$ will activate the exchange interaction between the C and A_1 mode

Each operator carries a phase that is oscillating at its (positive or negative) mode frequency, these frequencies form the collection

$$\boldsymbol{\Omega} = \{\mp\omega_c, \mp\omega_1, \ldots, \mp\omega_{N-1}\}. \tag{193}$$

The sum of the rotating frequency for each operator gives the total rotating frequency of the mode operators $\omega_{\mathrm{rot}}^{(\ell)}$.

- Thus, all the possible ℓ-variable sums of the rotating frequencies drawn from $\boldsymbol{\Omega}$ form the collection of the possible overall rotating frequencies of the ℓ operators.

$$\omega_{\mathrm{rot}}^{(\ell)} \in \boldsymbol{\Omega}_{\mathrm{rot}}^{(\ell)} = \left\{ \sum_{i=1}^{\ell} \omega_{m_i} \,\middle|\, \omega_{m_i} \in \boldsymbol{\Omega}, m_i \leq m_{i+1} \text{ for } m_i \in [1, \ldots, 2N] \right\}, \tag{194}$$

in which $\boldsymbol{\Omega}_{\mathrm{rot}}^{(\ell)}$ denotes the collection of all possible $\omega_{\mathrm{rot}}^{(\ell)}$ values. The additional constraint $m_i \leq m_{i+1}$ ensures that we only select the unique combinations from the rotating frequency set $\boldsymbol{\Omega}$, e.g., $\omega_a + \omega_b$ and $\omega_b + \omega_a$ are considered as the same element in $\boldsymbol{\Omega}_{\mathrm{rot}}^{(2)}$. The size of $\boldsymbol{\Omega}_{\mathrm{rot}}^{(l)}$ is $|\boldsymbol{\Omega}_{\mathrm{rot}}^{(l)}| = \binom{2N+\ell-1}{\ell}$.

- In the η^k interaction, the effective pumping frequency is $k\omega_p$. Each parametric transition corresponds to a pumping frequency that can compensate the overall rotating frequency of the mode operators, i.e.

$$k\omega_p = \omega_{\mathrm{rot}}^{(\ell)} = \omega_{\mathrm{rot}}^{(n-k)} \tag{195}$$

Note that the overall rotating frequency set $\boldsymbol{\Omega}_{\mathrm{rot}}^{(n-k)}$ contains pairs of values that are opposites in sign, e.g. $(\omega_1 - \omega_2)$ and $(\omega_2 - \omega_1)$, these frequencies corresponds to pairs of Hermitian conjugate terms, e.g. $\hat{a}_1^\dagger \hat{a}_2$ and $\hat{a}_1 \hat{a}_2^\dagger$. Therefore, the rotating frequency ω_{rot} only need to iterate through the positive elements in $\boldsymbol{\Omega}_{\mathrm{rot}}^{(n-k)}$ (denoted as $\boldsymbol{\Omega}_{\mathrm{rot},+}^{(n-k)}$). Consequently, we have the collection of the possible parametric transition frequencies for the n-wave mixing, η^k interactions:

$$\omega_p^{(n,k)} \in \boldsymbol{\Omega}_p^{(n,k)} = \left\{ \omega_{\mathrm{rot}}/k \,\middle|\, \omega_{\mathrm{rot}} \in \boldsymbol{\Omega}_{\mathrm{rot},+}^{(n-k)} \right\} \tag{196}$$

Finally, the collection of all the transition frequencies enabled by a n^{th} order non-linear term can be calculated by combing all the $\boldsymbol{\Omega}_p^{(n,k)}$ sets for k in $[1, \ldots, n-1]$

$$\boldsymbol{\Omega}_p^{(n)} = \boldsymbol{\Omega}_p^{(n,1)} \cup \boldsymbol{\Omega}_p^{(n,2)} \cup \cdots \cup \boldsymbol{\Omega}_p^{(n,n-1)} \tag{197}$$

Following this formalism, we can systematically identify and list all the possible parametric transitions and their corresponding pumping frequencies given a n^{th} order non-linear term. An example result has been provided in Sec. 2.3.2. It is important to note that the above calculation assumes a monochromatic (single frequency) external pump. When multiple pumps are applied at different frequencies, the same parametric processes can also be activated as long as the overall rotating frequencies of the pumping terms match with the transition frequencies. In that case, the above approach can still be used to identify the transition frequencies for each parametric process (as in Eq. 194), and the pumping frequencies just need to satisfy $\sum_j \pm\omega_{p,j} = \omega_{\text{rot}}^{(\ell)}$. Moreover, this protocol also assumes that all the involved modes have evenly spaced energy levels or simply are two-level systems. When the modes have anharmonicity, the possible transition spectrum becomes even more complex and significantly more non-trivial to track [89, 90].

Bibliography

[1] Michael A Nielsen and Isaac Chuang. Quantum computation and quantum information, 2002.

[2] Peter W Shor. Polynomial-time algorithms for prime factorization and discrete logarithms on a quantum computer. *SIAM review*, 41(2):303–332, 1999.

[3] Lov K Grover. A fast quantum mechanical algorithm for database search. In *Proceedings of the twenty-eighth annual ACM symposium on Theory of computing*, pages 212–219, 1996.

[4] Frank Arute, Kunal Arya, Ryan Babbush, Dave Bacon, Joseph C Bardin, Rami Barends, Rupak Biswas, Sergio Boixo, Fernando GSL Brandao, David A Buell, et al. Quantum supremacy using a programmable superconducting processor. *Nature*, 574(7779):505–510, 2019.

[5] Richard P Feynman et al. Simulating physics with computers. *Int. j. Theor. phys*, 21(6/7), 2018.

[6] Iulia M Georgescu, Sahel Ashhab, and Franco Nori. Quantum simulation. *Reviews of Modern Physics*, 86(1):153, 2014.

[7] Peter W Shor and John Preskill. Simple proof of security of the bb84 quantum key distribution protocol. *Physical review letters*, 85(2):441, 2000.

[8] Bruce E Kane. A silicon-based nuclear spin quantum computer. *nature*, 393(6681):133–137, 1998.

[9] Anasua Chatterjee, Paul Stevenson, Silvano De Franceschi, Andrea Morello, Nathalie P de Leon, and Ferdinand Kuemmeth. Semiconductor qubits in practice. *Nature Reviews Physics*, 3(3):157–177, 2021.

[10] David J Wineland, Murray Barrett, Joseph Britton, J Chiaverini, B DeMarco, Wayne M Itano, B Jelenković, Christopher Langer, Dietrich Leibfried, V Meyer, et al. Quantum information processing with trapped ions. *Philosophical Transactions of the Royal Society of London. Series A: Mathematical, Physical and Engineering Sciences*, 361(1808):1349–1361, 2003.

[11] Hartmut Häffner, Christian F Roos, and Rainer Blatt. Quantum computing with trapped ions. *Physics reports*, 469(4):155–203, 2008.

[12] Shantanu Debnath, Norbert M Linke, Caroline Figgatt, Kevin A Landsman, Kevin Wright, and Christopher Monroe. Demonstration of a small programmable quantum computer with atomic qubits. *Nature*, 536(7614):63–66, 2016.

[13] Mark Saffman. Quantum computing with atomic qubits and rydberg interactions: progress and challenges. *Journal of Physics B: Atomic, Molecular and Optical Physics*, 49(20):202001, 2016.

[14] Pieter Kok, William J Munro, Kae Nemoto, Timothy C Ralph, Jonathan P Dowling, and Gerard J Milburn. Linear optical quantum computing with photonic qubits. *Reviews of modern physics*, 79(1):135, 2007.

[15] Han-Sen Zhong, Hui Wang, Yu-Hao Deng, Ming-Cheng Chen, Li-Chao Peng, Yi-Han Luo, Jian Qin, Dian Wu, Xing Ding, Yi Hu, et al. Quantum computational advantage using photons. *Science*, 370(6523):1460–1463, 2020.

[16] John Clarke and Frank K Wilhelm. Superconducting quantum bits. *Nature*, 453(7198):1031–1042, 2008.

[17] Michel H Devoret and Robert J Schoelkopf. Superconducting circuits for quantum information: an outlook. *Science*, 339(6124):1169–1174, 2013.

[18] Jens Koch, M Yu Terri, Jay Gambetta, Andrew A Houck, David I Schuster, Johannes Majer, Alexandre Blais, Michel H Devoret, Steven M Girvin, and Robert J Schoelkopf. Charge-insensitive qubit design derived from the cooper pair box. *Physical Review A*, 76(4):042319, 2007.

[19] Approaching unit visibility for control of a superconducting qubit with dispersive readout. *Physical review letters*, 95(6):060501, 2005.

[20] Jay Gambetta, Alexandre Blais, Maxime Boissonneault, Andrew A Houck, DI Schuster, and Steven M Girvin. Quantum trajectory approach to circuit qed: Quantum jumps and the zeno effect. *Physical Review A*, 77(1):012112, 2008.

[21] Nicolas Didier, Jérôme Bourassa, and Alexandre Blais. Fast quantum nondemolition readout by parametric modulation of longitudinal qubit-oscillator interaction. *Physical review letters*, 115(20):203601, 2015.

[22] Bernard Yurke, LR Corruccini, PG Kaminsky, LW Rupp, AD Smith, AH Silver, RW Simon, and EA Whittaker. Observation of parametric amplification and deamplification in a josephson parametric amplifier. *Physical Review A*, 39(5):2519, 1989.

[23] Jose Aumentado. Superconducting parametric amplifiers: The state of the art in josephson parametric amplifiers. *IEEE Microwave magazine*, 21(8):45–59, 2020.

[24] TC White, JY Mutus, I-C Hoi, R Barends, B Campbell, Yu Chen, Z Chen, B Chiaro, A Dunsworth, E Jeffrey, et al. Traveling wave parametric amplifier with josephson junctions using minimal resonator phase matching. *Applied Physics Letters*, 106(24), 2015.

[25] RC Bialczak, M Ansmann, M Hofheinz, M Lenander, E Lucero, M Neeley, AD O'Connell, D Sank, H Wang, M Weides, et al. Fast tunable coupler for superconducting qubits. *Physical review letters*, 106(6):060501, 2011.

[26] NE Frattini, U Vool, S Shankar, A Narla, KM Sliwa, and MH Devoret. 3-wave mixing Josephson dipole element. *Applied Physics Letters*, 110(22):222603, 2017.

[27] Vasili K Semenov and Dmitri V Averin. Sfq control circuits for josephson junction qubits. *IEEE transactions on applied superconductivity*, 13(2):960–965, 2003.

[28] Edward Leonard Jr, Matthew A Beck, J Nelson, Brad G Christensen, Ted Thorbeck, Caleb Howington, Alexander Opremcak, Ivan V Pechenezhskiy, Kenneth Dodge, Nicholas P Dupuis, et al. Digital coherent control of a superconducting qubit. *Physical Review Applied*, 11(1):014009, 2019.

[29] Yulin Wu, Wan-Su Bao, Sirui Cao, Fusheng Chen, Ming-Cheng Chen, Xiawei Chen, Tung-Hsun Chung, Hui Deng, Yajie Du, Daojin Fan, et al. Strong quantum computational advantage using a superconducting quantum processor. *Physical review letters*, 127(18):180501, 2021.

[30] Sebastian Krinner, Nathan Lacroix, Ants Remm, Agustin Di Paolo, Elie Genois, Catherine Leroux, Christoph Hellings, Stefania Lazar, Francois Swiadek, Johannes Herrmann, et al. Realizing repeated quantum error correction in a distance-three surface code. *Nature*, 605(7911):669–674, 2022.

[31] Jerry Chow, Oliver Dial, and Jay Gambetta. Ibm quantum breaks the 100-qubit processor barrier. *IBM Research Blog*, 2021.

[32] Heike Riel. Quantum computing technology and roadmap. In *ESSDERC 2022-IEEE 52nd European Solid-State Device Research Conference (ESSDERC)*, pages 25–30. IEEE, 2022.

[33] Antonis Kyprianidis, Francisco Machado, William Morong, Patrick Becker, Kate S Collins, Dominic V Else, Lei Feng, Paul W Hess, Chetan Nayak, Guido Pagano, et al. Observation of a prethermal discrete time crystal. *Science*, 372(6547):1192–1196, 2021.

[34] David P DiVincenzo. The physical implementation of quantum computation. *Fortschritte der Physik: Progress of Physics*, 48(9-11):771–783, 2000.

[35] Alexandre Blais, Steven M Girvin, and William D Oliver. Quantum information processing and quantum optics with circuit quantum electrodynamics. *Nature Physics*, 16(3):247–256, 2020.

[36] Alexandre Blais, Arne L Grimsmo, Steven M Girvin, and Andreas Wallraff. Circuit quantum electrodynamics. *Reviews of Modern Physics*, 93(2):025005, 2021.

[37] Radoslaw C Bialczak, Markus Ansmann, Max Hofheinz, Erik Lucero, Matthew Neeley, Aaron D O'Connell, Daniel Sank, Haohua Wang, James Wenner, Matthias Steffen,

et al. Quantum process tomography of a universal entangling gate implemented with josephson phase qubits. *Nature Physics*, 6(6):409–413, 2010.

[38] Alexandre Blais, Alexander Maassen van den Brink, and Alexandre M Zagoskin. Tunable coupling of superconducting qubits. *Physical review letters*, 90(12):127901, 2003.

[39] Fei Yan, Philip Krantz, Youngkyu Sung, Morten Kjaergaard, Daniel L Campbell, Terry P Orlando, Simon Gustavsson, and William D Oliver. Tunable coupling scheme for implementing high-fidelity two-qubit gates. *Physical Review Applied*, 10(5):054062, 2018.

[40] David C McKay, Stefan Filipp, Antonio Mezzacapo, Easwar Magesan, Jerry M Chow, and Jay M Gambetta. Universal gate for fixed-frequency qubits via a tunable bus. *Physical Review Applied*, 6(6):064007, 2016.

[41] AO Niskanen, Khalil Harrabi, F Yoshihara, Y Nakamura, S Lloyd, and Jaw Shen Tsai. Quantum coherent tunable coupling of superconducting qubits. *Science*, 316(5825):723–726, 2007.

[42] Yao Lu, Aniket Maiti, John WO Garmon, Suhas Ganjam, Yaxing Zhang, Jahan Claes, Luigi Frunzio, SM Girvin, and Robert J Schoelkopf. A high-fidelity microwave beamsplitter with a parity-protected converter. *arXiv preprint arXiv:2303.00959*, 2023.

[43] Alexandru Petrescu, Camille Le Calonnec, Catherine Leroux, Agustin Di Paolo, Pranav Mundada, Sara Sussman, Andrei Vrajitoarea, Andrew A Houck, and Alexandre Blais. Accurate methods for the analysis of strong-drive effects in parametric gates. *Physical Review Applied*, 19(4):044003, 2023.

[44] GS Paraoanu. Microwave-induced coupling of superconducting qubits. *Physical Review B*, 74(14):140504, 2006.

[45] Chad Rigetti and Michel Devoret. Fully microwave-tunable universal gates in superconducting qubits with linear couplings and fixed transition frequencies. *Physical Review B*, 81(13):134507, 2010.

[46] Jerry M Chow, Antonio D Córcoles, Jay M Gambetta, Chad Rigetti, Blake R Johnson, John A Smolin, Jim R Rozen, George A Keefe, Mary B Rothwell, Mark B Ketchen, et al. Simple all-microwave entangling gate for fixed-frequency superconducting qubits. *Physical review letters*, 107(8):080502, 2011.

[47] Anirudh Narla, Shyam Shankar, Michael Hatridge, Zaki Leghtas, Katrina M Sliwa, Evan Zalys-Geller, Shantanu O Mundhada, Wolfgang Pfaff, Luigi Frunzio, Robert J Schoelkopf, et al. Robust concurrent remote entanglement between two superconducting qubits. *Physical Review X*, 6(3):031036, 2016.

[48] Yvonne Y Gao, Brian J Lester, Yaxing Zhang, Chen Wang, Serge Rosenblum, Luigi Frunzio, Liang Jiang, SM Girvin, and Robert J Schoelkopf. Programmable interference between two microwave quantum memories. *Physical Review X*, 8(2):021073, 2018.

[49] Atsushi Noguchi, Alto Osada, Shumpei Masuda, Shingo Kono, Kentaro Heya, Samuel Piotr Wolski, Hiroki Takahashi, Takanori Sugiyama, Dany Lachance-Quirion, and Yasunobu Nakamura. Fast parametric two-qubit gates with suppressed residual interaction using the second-order nonlinearity of a cubic transmon. *Physical Review A*, 102(6):062408, 2020.

[50] Luke D Burkhart, James D Teoh, Yaxing Zhang, Christopher J Axline, Luigi Frunzio, MH Devoret, Liang Jiang, SM Girvin, and RJ Schoelkopf. Error-detected state transfer and entanglement in a superconducting quantum network. *PRX Quantum*, 2(3):030321, 2021.

[51] Benjamin J Chapman, Stijn J de Graaf, Sophia H Xue, Yaxing Zhang, James Teoh, Jacob C Curtis, Takahiro Tsunoda, Alec Eickbusch, Alexander P Read, Akshay Koottandavida, et al. A high on-off ratio beamsplitter interaction for gates on bosonically encoded qubits. *arXiv preprint arXiv:2212.11929*, 2022.

[52] Chao Zhou, Pinlei Lu, Matthieu Praquin, Tzu-Chiao Chien, Ryan Kaufman, Xi Cao, Mingkang Xia, Roger SK Mong, Wolfgang Pfaff, David Pekker, et al. Realizing all-to-all couplings among detachable quantum modules using a microwave quantum state router. *npj Quantum Information*, 9(1):54, 2023.

[53] Michel H Devoret et al. Quantum fluctuations in electrical circuits. *Les Houches, Session LXIII*, 7(8):133–135, 1995.

[54] Uri Vool and Michel Devoret. Introduction to quantum electromagnetic circuits. *International Journal of Circuit Theory and Applications*, 45(7):897–934, 2017.

[55] F. Motzoi, J. M. Gambetta, P. Rebentrost, and F. K. Wilhelm. Simple Pulses for Elimination of Leakage in Weakly Nonlinear Qubits. *Physical Review Letters*, 103(11):110501, September 2009.

[56] Mingkang Xia, Chao Zhou, Chenxu Liu, Param Patel, Xi Cao, Pinlei Lu, Boris Mesits, Maria Mucci, David Gorski, David Pekker, and Michael Hatridge. Fast superconducting qubit control with sub-harmonic drives. *arXiv preprint arXiv:2306.10162*, 2023.

[57] Lucas Verney, Raphaël Lescanne, Michel H Devoret, Zaki Leghtas, and Mazyar Mirrahimi. Structural instability of driven josephson circuits prevented by an inductive shunt. *Physical Review Applied*, 11(2):024003, 2019.

[58] Wolfgang Pfaff, Christopher J Axline, Luke D Burkhart, Uri Vool, Philip Reinhold, Luigi Frunzio, Liang Jiang, Michel H Devoret, and Robert J Schoelkopf. Controlled

release of multiphoton quantum states from a microwave cavity memory. *Nature Physics*, 13(9):882–887, 2017.

[59] Matthew Reed. *Entanglement and quantum error correction with superconducting qubits*. Lulu. com, 2013.

[60] Sebastian Krinner, Simon Storz, Philipp Kurpiers, Paul Magnard, Johannes Heinsoo, Raphael Keller, Janis Luetolf, Christopher Eichler, and Andreas Wallraff. Engineering cryogenic setups for 100-qubit scale superconducting circuit systems. *EPJ Quantum Technology*, 6(1):2, 2019.

[61] Evan McKinney, Chao Zhou, Mingkang Xia, Michael Hatridge, and Alex K Jones. Parallel driving for fast quantum computing under speed limits. In *Proceedings of the 50th Annual International Symposium on Computer Architecture*, pages 1–13, 2023.

[62] Cupjin Huang, Tenghui Wang, Feng Wu, Dawei Ding, Qi Ye, Linghang Kong, Fang Zhang, Xiaotong Ni, Zhijun Song, Yaoyun Shi, et al. Quantum instruction set design for performance. *Physical Review Letters*, 130(7):070601, 2023.

[63] Norbert Schuch and Jens Siewert. Natural two-qubit gate for quantum computation using the xy interaction. *Physical Review A*, 67(3):032301, 2003.

[64] Marco Roth, Marc Ganzhorn, Nikolaj Moll, Stefan Filipp, Gian Salis, and Sebastian Schmidt. Analysis of a parametrically driven exchange-type gate and a two-photon excitation gate between superconducting qubits. *Physical Review A*, 96(6):062323, 2017.

[65] Stefano Poletto, Jay M Gambetta, Seth T Merkel, John A Smolin, Jerry M Chow, AD Córcoles, George A Keefe, Mary B Rothwell, JR Rozen, DW Abraham, et al. Entanglement of two superconducting qubits in a waveguide cavity via monochromatic two-photon excitation. *Physical review letters*, 109(24):240505, 2012.

[66] Jun Zhang, Jiri Vala, Shankar Sastry, and K Birgitta Whaley. Geometric theory of nonlocal two-qubit operations. *Physical Review A*, 67(4):042313, 2003.

[67] Robert R Tucci. An introduction to cartan's kak decomposition for qc programmers. *arXiv preprint quant-ph/0507171*, 2005.

[68] Youngkyu Sung, Leon Ding, Jochen Braumüller, Antti Vepsäläinen, Bharath Kannan, Morten Kjaergaard, Ami Greene, Gabriel O Samach, Chris McNally, David Kim, et al. Realization of high-fidelity cz and z z-free iswap gates with a tunable coupler. *Physical Review X*, 11(2):021058, 2021.

[69] Swarnadeep Majumder, Leonardo Andreta de Castro, and Kenneth R Brown. Real-time calibration with spectator qubits. *npj Quantum Information*, 6(1):1–9, 2020.

[70] Sebastian Krinner, Stefania Lazar, Ants Remm, Christian K Andersen, Nathan Lacroix, Graham J Norris, Christoph Hellings, Mihai Gabureac, Christopher Eichler, and Andreas Wallraff. Benchmarking coherent errors in controlled-phase gates due to spectator qubits. *Physical Review Applied*, 14(2):024042, 2020.

[71] X Dai, DM Tennant, R Trappen, AJ Martinez, D Melanson, MA Yurtalan, Y Tang, S Novikov, JA Grover, SM Disseler, et al. Calibration of flux crosstalk in large-scale flux-tunable superconducting quantum circuits. *PRX Quantum*, 2(4):040313, 2021.

[72] Nic Ezzell, Bibek Pokharel, Lina Tewala, Gregory Quiroz, and Daniel A Lidar. Dynamical decoupling for superconducting qubits: a performance survey. *arXiv preprint arXiv:2207.03670*, 2022.

[73] Vinay Tripathi, Huo Chen, Mostafa Khezri, Ka-Wa Yip, EM Levenson-Falk, and Daniel A Lidar. Suppression of crosstalk in superconducting qubits using dynamical decoupling. *Physical Review Applied*, 18(2):024068, 2022.

[74] Pranav Mundada, Gengyan Zhang, Thomas Hazard, and Andrew Houck. Suppression of qubit crosstalk in a tunable coupling superconducting circuit. *Physical Review Applied*, 12(5):054023, 2019.

[75] V.V. Sivak, N.E. Frattini, V.R. Joshi, A. Lingenfelter, S. Shankar, and M.H. Devoret. Kerr-Free Three-Wave Mixing in Superconducting Quantum Circuits. *Phys. Rev. Applied*, 11(5):054060, May 2019. Publisher: American Physical Society.

[76] Nicholas E Frattini. *Three-wave mixing in superconducting circuits: stabilizing cats with SNAILs*. PhD thesis, Yale University, 2021.

[77] Simon E. Nigg, Hanhee Paik, Brian Vlastakis, Gerhard Kirchmair, S. Shankar, Luigi Frunzio, M. H. Devoret, R. J. Schoelkopf, and S. M. Girvin. Black-Box Superconducting Circuit Quantization. *Phys. Rev. Lett.*, 108(24):240502, June 2012. Publisher: American Physical Society.

[78] Zlatko K Minev, Zaki Leghtas, Shantanu O Mundhada, Lysander Christakis, Ioan M Pop, and Michel H Devoret. Energy-participation quantization of Josephson circuits. *npj Quantum Information*, 7(1):1–11, 2021.

[79] NE Frattini, VV Sivak, A Lingenfelter, S Shankar, and MH Devoret. Optimizing the nonlinearity and dissipation of a SNAIL parametric amplifier for dynamic range. *Physical Review Applied*, 10(5):054020, 2018.

[80] VV Sivak, A Eickbusch, B Royer, S Singh, I Tsioutsios, S Ganjam, A Miano, BL Brock, AZ Ding, L Frunzio, et al. Real-time quantum error correction beyond break-even. *arXiv preprint arXiv:2211.09116*, 2022.

[81] Suppressing quantum errors by scaling a surface code logical qubit. *Nature*, 614(7949):676–681, 2023.

[82] Yehan Liu. *Quantum feedback control of multiple superconducting qubits.* PhD thesis, Yale University, 2016.

[83] Yilun Xu, Gang Huang, Jan Balewski, Ravi Naik, Alexis Morvan, Bradley Mitchell, Kasra Nowrouzi, David I Santiago, and Irfan Siddiqi. Qubic: An open-source fpga-based control and measurement system for superconducting quantum information processors. *IEEE Transactions on Quantum Engineering*, 2:1–11, 2021.

[84] Lorenzo Leandro. Time to result: Randomized benchmarking with advanced quantum control, Oct 2022.

[85] Leandro Stefanazzi, Kenneth Treptow, Neal Wilcer, Chris Stoughton, Collin Bradford, Sho Uemura, Silvia Zorzetti, Salvatore Montella, Gustavo Cancelo, Sara Sussman, et al. The qick (quantum instrumentation control kit): Readout and control for qubits and detectors. *Review of Scientific Instruments*, 93(4):044709, 2022.

[86] Kun Hee Park, Yung Szen Yap, Yuanzheng Paul Tan, Christoph Hufnagel, Long Hoang Nguyen, Karn Hwa Lau, Stavros Efthymiou, Stefano Carrazza, Rangga P Budoyo, and Rainer Dumke. Icarus-q: A scalable rfsoc-based control system for superconducting quantum computers. *arXiv preprint arXiv:2112.02933*, 2021.

[87] Douglas Allan, Ehinomen Atimati, Kenny W Barlee, Lewis J Brown, James Craig, Graeme Fitzpatrick, Joshua Goldsmith, Andrew Maclellan, Lewis D McLaughlin, Blair McTaggart, et al. Software defined radio with zynq ultrascale+ rfsoc, 2023.

[88] Steven W Smith et al. The scientist and engineer's guide to digital signal processing, 1997.

[89] Jayameenakshi Venkatraman, Xu Xiao, Rodrigo G Cortiñas, Alec Eickbusch, and Michel H Devoret. Static effective hamiltonian of a rapidly driven nonlinear system. *Physical Review Letters*, 129(10):100601, 2022.

[90] Ross Shillito, Alexandru Petrescu, Joachim Cohen, Jackson Beall, Markus Hauru, Martin Ganahl, Adam GM Lewis, Guifre Vidal, and Alexandre Blais. Dynamics of transmon ionization. *Physical Review Applied*, 18(3):034031, 2022.

[91] Christopher James Axline. *Building blocks for modular circuit QED quantum computing.* PhD thesis, Yale University, 2018.

[92] Marlan O Scully and M Suhail Zubairy. Quantum optics, 1999.

[93] Baleegh Abdo, Flavius Schackert, Michael Hatridge, Chad Rigetti, and Michel Devoret. Josephson amplifier for qubit readout. *Applied Physics Letters*, 99(16):162506, 2011.

[94] David C McKay, Christopher J Wood, Sarah Sheldon, Jerry M Chow, and Jay M Gambetta. Efficient z gates for quantum computing. *Physical Review A*, 96(2):022330, 2017.

[95] Pinlei Lu. *Parametric controls for modular quantum computing and quantum devices.* PhD thesis, University of Pittsburgh, 2022.

[96] Christopher Chamberland, Guanyu Zhu, Theodore J Yoder, Jared B Hertzberg, and Andrew W Cross. Topological and subsystem codes on low-degree graphs with flag qubits. *Physical Review X*, 10(1):011022, 2020.

[97] Eric Dennis, Alexei Kitaev, Andrew Landahl, and John Preskill. Topological quantum memory. *Journal of Mathematical Physics*, 43(9):4452–4505, 2002.

[98] Austin G Fowler, Matteo Mariantoni, John M Martinis, and Andrew N Cleland. Surface codes: Towards practical large-scale quantum computation. *Physical Review A*, 86(3):032324, 2012.

[99] Rami Barends, Julian Kelly, Anthony Megrant, Andrzej Veitia, Daniel Sank, Evan Jeffrey, Ted C White, Josh Mutus, Austin G Fowler, Brooks Campbell, et al. Superconducting quantum circuits at the surface code threshold for fault tolerance. *Nature*, 508(7497):500–503, 2014.

[100] Christopher Monroe, Robert Raussendorf, Alex Ruthven, Kenneth R Brown, Peter Maunz, L-M Duan, and Jungsang Kim. Large-scale modular quantum-computer architecture with atomic memory and photonic interconnects. *Physical Review A*, 89(2):022317, 2014.

[101] Alysson Gold, JP Paquette, Anna Stockklauser, Matthew J Reagor, M Sohaib Alam, Andrew Bestwick, Nicolas Didier, Ani Nersisyan, Feyza Oruc, Armin Razavi, et al. Entanglement across separate silicon dies in a modular superconducting qubit device. *npj Quantum Information*, 7(1):142, 2021.

[102] Nicholas LaRacuente, Kaitlin N Smith, Poolad Imany, Kevin L Silverman, and Frederic T Chong. Short-range microwave networks to scale superconducting quantum computation. *arXiv preprint arXiv:2201.08825*, 2022.

[103] Matt McEwen, Lara Faoro, Kunal Arya, Andrew Dunsworth, Trent Huang, Seon Kim, Brian Burkett, Austin Fowler, Frank Arute, Joseph C Bardin, et al. Resolving catastrophic error bursts from cosmic rays in large arrays of superconducting qubits. *Nature Physics*, 18(1):107–111, 2022.

[104] CD Wilen, S Abdullah, NA Kurinsky, C Stanford, L Cardani, G d'Imperio, C Tomei, L Faoro, LB Ioffe, CH Liu, et al. Correlated charge noise and relaxation errors in superconducting qubits. *Nature*, 594(7863):369–373, 2021.

[105] J. I. Cirac, P. Zoller, H. J. Kimble, and H. Mabuchi. Quantum State Transfer and Entanglement Distribution among Distant Nodes in a Quantum Network. *Phys. Rev. Lett.*, 78(16):3221–3224, April 1997. Publisher: American Physical Society.

[106] H. J. Kimble. The quantum internet. *Nature*, 453(7198):1023–1030, June 2008. Number: 7198 Publisher: Nature Publishing Group.

[107] Christopher Monroe and Jungsang Kim. Scaling the ion trap quantum processor. *Science*, 339(6124):1164–1169, 2013.

[108] Christopher R Monroe, Robert J Schoelkopf, and Mikhail D Lukin. Quantum connections. *Scientific American*, 314(5):50–57, 2016.

[109] Chin-Wen Chou, Hugues De Riedmatten, Daniel Felinto, Sergey V Polyakov, Steven J Van Enk, and H Jeff Kimble. Measurement-induced entanglement for excitation stored in remote atomic ensembles. *Nature*, 438(7069):828–832, 2005.

[110] David L Moehring, Peter Maunz, Steve Olmschenk, Kelly C Younge, Dzmitry N Matsukevich, L-M Duan, and Christopher Monroe. Entanglement of single-atom quantum bits at a distance. *Nature*, 449(7158):68–71, 2007.

[111] Stephan Ritter, Christian Nölleke, Carolin Hahn, Andreas Reiserer, Andreas Neuzner, Manuel Uphoff, Martin Mücke, Eden Figueroa, Joerg Bochmann, and Gerhard Rempe. An elementary quantum network of single atoms in optical cavities. *Nature*, 484(7393):195–200, 2012.

[112] Julian Hofmann, Michael Krug, Norbert Ortegel, Lea Gérard, Markus Weber, Wenjamin Rosenfeld, and Harald Weinfurter. Heralded entanglement between widely separated atoms. *Science*, 337(6090):72–75, 2012.

[113] Hannes Bernien, Bas Hensen, Wolfgang Pfaff, Gerwin Koolstra, Machiel S Blok, Lucio Robledo, TH Taminiau, Matthew Markham, Daniel J Twitchen, Lilian Childress, et al. Heralded entanglement between solid-state qubits separated by three metres. *Nature*, 497(7447):86–90, 2013.

[114] Nicolas Roch, Mollie E Schwartz, Felix Motzoi, Christopher Macklin, Rajamani Vijay, Andrew W Eddins, Alexander N Korotkov, K Birgitta Whaley, Mohan Sarovar, and Irfan Siddiqi. Observation of measurement-induced entanglement and quantum trajectories of remote superconducting qubits. *Physical review letters*, 112(17):170501, 2014.

[115] Christian Dickel, JJ Wesdorp, NK Langford, S Peiter, Ramiro Sagastizabal, Alessandro Bruno, Ben Criger, F Motzoi, and L DiCarlo. Chip-to-chip entanglement of transmon qubits using engineered measurement fields. *Physical Review B*, 97(6):064508, 2018.

[116] Philipp Kurpiers, Marek Pechal, Baptiste Royer, Paul Magnard, Theo Walter, Johannes Heinsoo, Yves Salathé, Abdulkadir Akin, Simon Storz, J-C Besse, et al. Quantum communication with time-bin encoded microwave photons. *Physical Review Applied*, 12(4):044067, 2019.

[117] Christopher J Axline, Luke D Burkhart, Wolfgang Pfaff, Mengzhen Zhang, Kevin Chou, Philippe Campagne-Ibarcq, Philip Reinhold, Luigi Frunzio, SM Girvin, Liang Jiang, et al. On-demand quantum state transfer and entanglement between remote microwave cavity memories. *Nature Physics*, 14(7):705–710, 2018.

[118] P. Campagne-Ibarcq, E. Zalys-Geller, A. Narla, S. Shankar, P. Reinhold, L. Burkhart, C. Axline, W. Pfaff, L. Frunzio, R. J. Schoelkopf, and M. H. Devoret. Deterministic remote entanglement of superconducting circuits through microwave two-photon transitions. *Phys. Rev. Lett.*, 120:200501, May 2018.

[119] Philipp Kurpiers, Paul Magnard, Theo Walter, Baptiste Royer, Marek Pechal, Johannes Heinsoo, Yves Salathé, Abdulkadir Akin, Simon Storz, J-C Besse, et al. Deterministic quantum state transfer and remote entanglement using microwave photons. *Nature*, 558(7709):264–267, 2018.

[120] N. Leung, Y. Lu, S. Chakram, R. K. Naik, N. Earnest, R. Ma, K. Jacobs, A. N. Cleland, and D. I. Schuster. Deterministic bidirectional communication and remote entanglement generation between superconducting qubits. *npj Quantum Inf*, 5(1):1–5, February 2019.

[121] Paul Magnard, Simon Storz, Philipp Kurpiers, Josua Schär, Fabian Marxer, Janis Lütolf, T Walter, J-C Besse, M Gabureac, K Reuer, et al. Microwave quantum link between superconducting circuits housed in spatially separated cryogenic systems. *Physical Review Letters*, 125(26):260502, 2020.

[122] Adam J Sirois, MA Castellanos-Beltran, MP DeFeo, L Ranzani, F Lecocq, RW Simmonds, JD Teufel, and J Aumentado. Coherent-state storage and retrieval between superconducting cavities using parametric frequency conversion. *Applied Physics Letters*, 106(17):172603, 2015.

[123] Sumeru Hazra, Anirban Bhattacharjee, Madhavi Chand, Kishor V Salunkhe, Sriram Gopalakrishnan, Meghan P Patankar, and R Vijay. Ring-resonator-based coupling architecture for enhanced connectivity in a superconducting multiqubit network. *Physical Review Applied*, 16(2):024018, 2021.

[124] Youpeng Zhong, Hung-Shen Chang, Audrey Bienfait, Etienne Dumur, Ming-Han Chou, Christopher R. Conner, Joel Grebel, Rhys G. Povey, Haoxiong Yan, David I. Schuster, and Andrew N. Cleland. Deterministic multi-qubit entanglement in a quantum network. *Nature*, 590(7847):571–575, February 2021. Number: 7847 Publisher: Nature Publishing Group.

[125] Brian Vlastakis, Gerhard Kirchmair, Zaki Leghtas, Simon E. Nigg, Luigi Frunzio, S. M. Girvin, Mazyar Mirrahimi, M. H. Devoret, and R. J. Schoelkopf. Deterministically Encoding Quantum Information Using 100-Photon Schrödinger Cat States. *Science*, 342(6158):607–610, November 2013. Publisher: American Association for the Advancement of Science Section: Report.

[126] Marios H. Michael, Matti Silveri, R. T. Brierley, Victor V. Albert, Juha Salmilehto, Liang Jiang, and S. M. Girvin. New Class of Quantum Error-Correcting Codes for a Bosonic Mode. *Phys. Rev. X*, 6(3):031006, July 2016. Publisher: American Physical Society.

[127] Daniel Gottesman, Alexei Kitaev, and John Preskill. Encoding a qubit in an oscillator. *Phys. Rev. A*, 64(1):012310, June 2001. Publisher: American Physical Society.

[128] David M Pozar. *Microwave engineering.* John wiley & sons, 2011.

[129] Matthew Reagor, Wolfgang Pfaff, Christopher Axline, Reinier W Heeres, Nissim Ofek, Katrina Sliwa, Eric Holland, Chen Wang, Jacob Blumoff, Kevin Chou, et al. Quantum memory with millisecond coherence in circuit qed. *Physical Review B*, 94(1):014506, 2016.

[130] Julian Kelly, Rami Barends, Brooks Campbell, Yu Chen, Zijun Chen, Ben Chiaro, Andrew Dunsworth, Austin G Fowler, I-C Hoi, Evan Jeffrey, et al. Optimal quantum control using randomized benchmarking. *Physical review letters*, 112(24):240504, 2014.

[131] Luca Planat, Rémy Dassonneville, Javier Puertas Martínez, Farshad Foroughi, Olivier Buisson, Wiebke Hasch-Guichard, Cécile Naud, R. Vijay, Kater Murch, and Nicolas Roch. Understanding the Saturation Power of Josephson Parametric Amplifiers Made from SQUID Arrays. *Phys. Rev. Applied*, 11(3):034014, March 2019.

[132] Chenxu Liu, Tzu-Chiao Chien, Michael Hatridge, and David Pekker. Optimizing Josephson-ring-modulator-based Josephson parametric amplifiers via full Hamiltonian control. *Phys. Rev. A*, 101(4):042323, April 2020.

[133] Mark EJ Newman and Gerard T Barkema. *Monte Carlo methods in statistical physics.* Clarendon Press, 1999.

[134] Peter Young. *Everything you wanted to know about data analysis and fitting but were afraid to ask.* Springer, 2015.

[135] DI Schuster, Andrew Addison Houck, JA Schreier, A Wallraff, JM Gambetta, A Blais, L Frunzio, J Majer, B Johnson, MH Devoret, et al. Resolving photon number states in a superconducting circuit. *Nature*, 445(7127):515–518, 2007.

[136] Chan U Lei, Lev Krayzman, Suhas Ganjam, Luigi Frunzio, and Robert J Schoelkopf. High coherence superconducting microwave cavities with indium bump bonding. *Applied Physics Letters*, 116(15):154002, 2020.

[137] M Kudra, J Biznárová, A Fadavi Roudsari, JJ Burnett, D Niepce, S Gasparinetti, B Wickman, and P Delsing. High quality three-dimensional aluminum microwave cavities. *Applied Physics Letters*, 117(7):070601, 2020.

[138] K Serniak, M Hays, G De Lange, S Diamond, Sh Shankar, LD Burkhart, L Frunzio, M Houzet, and MH Devoret. Hot nonequilibrium quasiparticles in transmon qubits. *Physical review letters*, 121(15):157701, 2018.

[139] Chuan-Hong Liu, David C Harrison, Shravan Patel, Christopher D Wilen, Owen Rafferty, Abigail Shearrow, Andrew Ballard, Vito Iaia, Jaseung Ku, Britton LT Plourde, et al. Quasiparticle poisoning of superconducting qubits from resonant absorption of pair-breaking photons. *arXiv preprint arXiv:2203.06577*, 2022.

[140] Mark Halpern, Herbert P Gush, Edward Wishnow, and Vittorio De Cosmo. Far infrared transmission of dielectrics at cryogenic and room temperatures: glass, fluorogold, eccosorb, stycast, and various plastics. *Applied Optics*, 25(4):565–570, 1986.

[141] Ziqian Li, Tanay Roy, David Rodriguez Perez, Kan-Heng Lee, Eliot Kapit, and David I Schuster. Autonomous error correction of a single logical qubit using two transmons. *arXiv preprint arXiv:2302.06707*, 2023.

[142] James D Teoh, Patrick Winkel, Harshvardhan K Babla, Benjamin J Chapman, Jahan Claes, Stijn J de Graaf, John WO Garmon, William D Kalfus, Yao Lu, Aniket Maiti, et al. Dual-rail encoding with superconducting cavities. *arXiv preprint arXiv:2212.12077*, 2022.

[143] Evan McKinney, Mingkang Xia, Chao Zhou, Pinlei Lu, Michael Hatridge, and Alex K Jones. Co-designed architectures for modular superconducting quantum computers. In *2023 IEEE International Symposium on High-Performance Computer Architecture (HPCA)*, pages 759–772. IEEE, 2023.

[144] T-C Chien, O Lanes, C Liu, X Cao, P Lu, S Motz, G Liu, D Pekker, and M Hatridge. Multiparametric amplification and qubit measurement with a kerr-free josephson ring modulator. *Physical Review A*, 101(4):042336, 2020.

[145] Anja Metelmann and Aashish A Clerk. Nonreciprocal photon transmission and amplification via reservoir engineering. *Physical Review X*, 5(2):021025, 2015.

[146] A Metelmann, O Lanes, TZ Chien, A McDonald, M Hatridge, and AA Clerk. Quantum-limited amplification without instability. *arXiv preprint arXiv:2208.00024*, 2022.

[147] Yuriy Makhlin. Nonlocal properties of two-qubit gates and mixed states, and the optimization of quantum computations. *Quantum Information Processing*, 1:243–252, 2002.

[148] S Balakrishnan and R Sankaranarayanan. Characterizing the geometrical edges of nonlocal two-qubit gates. *Physical Review A*, 79(5):052339, 2009.

[149] Jun Zhang, Jiri Vala, Shankar Sastry, and K Birgitta Whaley. Minimum construction of two-qubit quantum operations. *Physical review letters*, 93(2):020502, 2004.

[150] U Vool, S Shankar, SO Mundhada, N Ofek, A Narla, K Sliwa, E Zalys-Geller, Y Liu, L Frunzio, RJ Schoelkopf, et al. Continuous quantum nondemolition measurement of the transverse component of a qubit. *Physical review letters*, 117(13):133601, 2016.

[151] Evan Jeffrey, Daniel Sank, JY Mutus, TC White, J Kelly, R Barends, Y Chen, Z Chen, B Chiaro, A Dunsworth, et al. Fast accurate state measurement with superconducting qubits. *Physical review letters*, 112(19):190504, 2014.

[152] Theodore Walter, Philipp Kurpiers, Simone Gasparinetti, Paul Magnard, Anton Potočnik, Yves Salathé, Marek Pechal, Mintu Mondal, Markus Oppliger, Christopher Eichler, et al. Rapid high-fidelity single-shot dispersive readout of superconducting qubits. *Physical Review Applied*, 7(5):054020, 2017.

[153] Johannes Heinsoo, Christian Kraglund Andersen, Ants Remm, Sebastian Krinner, Theodore Walter, Yves Salathé, Simone Gasparinetti, Jean-Claude Besse, Anton Potočnik, Andreas Wallraff, et al. Rapid high-fidelity multiplexed readout of superconducting qubits. *Physical Review Applied*, 10(3):034040, 2018.

[154] AA Houck, JA Schreier, BR Johnson, JM Chow, Jens Koch, JM Gambetta, DI Schuster, L Frunzio, MH Devoret, SM Girvin, et al. Controlling the spontaneous emission of a superconducting transmon qubit. *Physical review letters*, 101(8):080502, 2008.

[155] Cristóbal Lledó, Rémy Dassonneville, Adrien Moulinas, Joachim Cohen, Ross Shillito, Audrey Bienfait, Benjamin Huard, and Alexandre Blais. Cloaking a qubit in a cavity. *arXiv preprint arXiv:2211.05758*, 2022.

[156] Andrew J Kerman. Quantum information processing using quasiclassical electromagnetic interactions between qubits and electrical resonators. *New Journal of Physics*, 15(12):123011, 2013.

[157] P-M Billangeon, Jaw Shen Tsai, and Y Nakamura. Circuit-qed-based scalable architectures for quantum information processing with superconducting qubits. *Physical Review B*, 91(9):094517, 2015.

[158] Susanne Richer and David DiVincenzo. Circuit design implementing longitudinal coupling: A scalable scheme for superconducting qubits. *Physical Review B*, 93(13):134501, 2016.

[159] Denis Vion, A Aassime, Audrey Cottet, Pl Joyez, H Pothier, C Urbina, Daniel Esteve, and Michel H Devoret. Manipulating the quantum state of an electrical circuit. *Science*, 296(5569):886–889, 2002.

[160] Tanay Roy, Suman Kundu, Madhavi Chand, Sumeru Hazra, N Nehra, R Cosmic, A Ranadive, Meghan P Patankar, Kedar Damle, and R Vijay. Implementation of pairwise longitudinal coupling in a three-qubit superconducting circuit. *Physical Review Applied*, 7(5):054025, 2017.

[161] S Touzard, A Kou, NE Frattini, VV Sivak, S Puri, A Grimm, L Frunzio, S Shankar, and MH Devoret. Gated conditional displacement readout of superconducting qubits. *Physical review letters*, 122(8):080502, 2019.

[162] Joni Ikonen, Jan Goetz, Jesper Ilves, Aarne Keränen, Andras M Gunyho, Matti Partanen, Kuan Y Tan, Dibyendu Hazra, Leif Grönberg, Visa Vesterinen, et al. Qubit measurement by multichannel driving. *Physical review letters*, 122(8):080503, 2019.

[163] Shay Hacohen-Gourgy, Leigh S Martin, Emmanuel Flurin, Vinay V Ramasesh, K Birgitta Whaley, and Irfan Siddiqi. Quantum dynamics of simultaneously measured non-commuting observables. *Nature*, 538(7626):491–494, 2016.

[164] Baleegh Abdo, Archana Kamal, and Michel Devoret. Nondegenerate three-wave mixing with the josephson ring modulator. *Physical Review B*, 87(1):014508, 2013.

[165] Xi Cao, Maria Mucci, and et. al. Bath-engineering qubit systems with 3-wave mixing. *In preparation*, 2023.

[166] Michael Hatridge, Shyam Shankar, Mazyar Mirrahimi, F Schackert, K Geerlings, T Brecht, KM Sliwa, B Abdo, Luigi Frunzio, Steven M Girvin, et al. Quantum back-action of an individual variable-strength measurement. *Science*, 339(6116):178–181, 2013.

[167] Alexander Grimm, Nicholas E Frattini, Shruti Puri, Shantanu O Mundhada, Steven Touzard, Mazyar Mirrahimi, Steven M Girvin, Shyam Shankar, and Michel H Devoret. Stabilization and operation of a kerr-cat qubit. *Nature*, 584(7820):205–209, 2020.

[168] Harrison Ball, William D Oliver, and Michael J Biercuk. The role of master clock stability in quantum information processing. *npj Quantum Information*, 2(1):1–8, 2016.

[169] R Vijay, MH Devoret, and I Siddiqi. Invited review article: The josephson bifurcation amplifier. *Review of Scientific Instruments*, 80(11), 2009.

[170] Pinlei Lu, Tzu-Chiao Chien, Xi Cao, Olivia Lanes, Chao Zhou, Michael J Hatridge, Saeed Khan, and Hakan E Türeci. Nearly quantum-limited josephson-junction frequency-comb synthesizer. *Physical Review Applied*, 15(4):044031, 2021.

[171] Saeed Khan and Hakan E Türeci. Frequency combs in a lumped-element josephson-junction circuit. *Physical review letters*, 120(15):153601, 2018.